

NOTE TO USERS

This reproduction is the best copy available.

UMI[®]



Study of Bond Coating Pre-oxidation Heat Treatments for High Temperature Thin Film Sensors in Gas Turbine Engine Applications

by

Philipp Puetz

A Thesis submitted to
the Faculty of Graduate Studies and Research
in partial fulfilment of
the requirements for the degree of
Master of Applied Science

Ottawa-Carleton Institute for
Mechanical and Aerospace Engineering

Department of Mechanical and Aerospace Engineering

Carleton University

Ottawa, Ontario, Canada

January 2010

Copyright ©

2010 - Philipp Puetz



Library and Archives
Canada

Bibliothèque et
Archives Canada

Published Heritage
Branch

Direction du
Patrimoine de l'édition

395 Wellington Street
Ottawa ON K1A 0N4
Canada

395, rue Wellington
Ottawa ON K1A 0N4
Canada

Your file *Votre référence*
ISBN: 978-0-494-63812-5
Our file *Notre référence*
ISBN: 978-0-494-63812-5

NOTICE:

The author has granted a non-exclusive license allowing Library and Archives Canada to reproduce, publish, archive, preserve, conserve, communicate to the public by telecommunication or on the Internet, loan, distribute and sell theses worldwide, for commercial or non-commercial purposes, in microform, paper, electronic and/or any other formats.

The author retains copyright ownership and moral rights in this thesis. Neither the thesis nor substantial extracts from it may be printed or otherwise reproduced without the author's permission.

AVIS:

L'auteur a accordé une licence non exclusive permettant à la Bibliothèque et Archives Canada de reproduire, publier, archiver, sauvegarder, conserver, transmettre au public par télécommunication ou par l'Internet, prêter, distribuer et vendre des thèses partout dans le monde, à des fins commerciales ou autres, sur support microforme, papier, électronique et/ou autres formats.

L'auteur conserve la propriété du droit d'auteur et des droits moraux qui protègent cette thèse. Ni la thèse ni des extraits substantiels de celle-ci ne doivent être imprimés ou autrement reproduits sans son autorisation.

In compliance with the Canadian Privacy Act some supporting forms may have been removed from this thesis.

Conformément à la loi canadienne sur la protection de la vie privée, quelques formulaires secondaires ont été enlevés de cette thèse.

While these forms may be included in the document page count, their removal does not represent any loss of content from the thesis.

Bien que ces formulaires aient inclus dans la pagination, il n'y aura aucun contenu manquant.


Canada

The undersigned recommend to
the Faculty of Graduate Studies and Research
acceptance of the Thesis

**Study of Bond Coating Pre-oxidation Heat Treatments for
High Temperature Thin Film Sensors in Gas Turbine Engine
Applications**

Submitted by **Philipp Puetz**
in partial fulfilment of the requirements for the degree of
Master of Applied Science

X. Huang, Supervisor

L.R. Zhao, Supervisor

M. Yaras, Department Chair

Carleton University

2010

Abstract

The application of thin film sensors on hot section components of gas turbine engines requires the formation a specific and complex layered structure to be functional, reliable, and durable. In the case of conducting substrates, such as the nickel- or cobalt-based superalloys, an electrically-insulating layer (typically aluminum oxide) is required between the sensing layer elements and the substrate. In this work, test specimens consisting of an MCrAlY-coated nickel-base substrate were subjected to selected vacuum and air furnace heat treatments in order to observe the effects of the heat treatments on the test specimen structure, particularly in terms of superficial thermally-grown oxide (TGO) formation. Three different MCrAlY materials were applied to the Hastelloy-X substrate, with each coat material deposited by a different process. FeCrAlY, NiCrAlY, and CoNiCrAlY were applied by magnetron sputtering physical vapour deposition (MS-PVD), air plasma spray (APS) deposition, and high-velocity oxy-fuel spray (HVOF) deposition, respectively. The surfaces and cross-sectional features of the test specimens were examined using SEM and EDS analysis, together with the support of XRD analysis. Of the heat-treated bond coat-substrate combinations tested, the HVOF CoNiCrAlY-coated test specimens subjected to an air furnace heat treatment of 1100°C for 1 hour yielded the most suitable surface condition that could be processed further into a thin film sensor assembly prototype. The surface of this specimen consisted of a 1 μm -thick aluminum oxide TGO layer featuring the fewest distributed transition metal oxide clusters.

Acknowledgments

- To my thesis supervisors Xiao Huang and Linruo Zhao for their guidance and support in performing this work. A thank you also to the National Research Council Canada's Institute for Aerospace Research (NRC-IAR) for their financial contribution towards my research assistantship.
- To Qi Yang for sharing his wealth of knowledge regarding PVD and thermal spray coatings, XRD data interpretation advice, and the countless hours spent in front of the Philips scanning electron microscope with me.
- To Robert McKellar for entertaining my many questions regarding the technical and practical aspects of both CA-PVD and MS-PVD processes, as well as making possible several opportunities to experience some of the practical aspects for myself.
- To Olga Lupandina for always selflessly making available her time to provide invaluable knowledge and advice pertaining to metallographic test specimen preparation and to help fixing unserviceable equipment.
- To Dave Chow, Ryan MacNeil, Dave Morphy, Pascale Lafleur, Luc Lafleur, and John MacMillan for their help in carrying out my experimental work in task including equipment training and setup, vacuum furnace programming, test specimen substrate machining, and generally providing their technical knowledge.

- To Xiaomei Du of NRC's Institute for Chemical Process and Environmental Technology (NRC-ICPET) for her time to perform the XRD measurements for this work in the constraints of a demanding time-frame.
- To the Northwest Mettech Corporation and Rogerio Lima of NRC's Industrial Materials Institute (NRC-IMI) for providing the APS NiCrAlY- and HVOF CoNiCrAlY-coated test specimens, respectively, for this work.
- To Dongfang Yang of NRC's Industrial Materials Institute (NRC-IMI) for sharing his expertise in thin film sensor technology and providing me with images of NRC's thin film sensor prototypes.
- To Kirsten Plante, Heather Clarke-Thomas, Cory Kendall, and Norbert Puetz, who generously provided their time and patience to read, correct, and provide feedback to my thesis chapter drafts.

Table of Contents

Abstract	iii
Acknowledgments	iv
Table of Contents	vi
List of Tables	ix
List of Figures	x
Nomenclature	xi
1 Introduction	1
2 Literature Review	4
2.1 Typical Constituents of Modern Gas Turbine Engine Hot Section Components	5
2.1.1 Structural Materials	11
2.1.2 Bond Coat (BC)	13
2.1.3 Top Coat (TC)	28
2.2 Thin Film Sensors	30
2.2.1 Advantages of Thin Film Sensors Over Conventional Sensors .	31
2.2.2 Thin Film Sensor Applications in Gas Turbine Engines	33

2.2.3	Thin Film Sensor Operational Requirements	36
2.2.4	Typical Thin Film Sensor Assembly Layout	37
2.2.5	NASA's Thin Film Sensor Experiences	43
3	Research Objectives	46
4	Materials and Experimental Procedures	47
4.1	Test Specimen Structure	48
4.1.1	Hastelloy-X Substrate	49
4.1.2	MCrAlY Bond Coat Materials	51
4.2	Bond Coat Deposition Processes	55
4.2.1	Physical Vapour Deposition (PVD)	57
4.2.2	Thermal Spray Deposition	65
4.3	Surface Processing	73
4.3.1	Pre-deposition	73
4.3.2	Post-deposition	74
4.4	Pre-oxidation Heat Treatments	75
4.5	Test Specimen Evaluation	77
4.5.1	Microscopic Evaluation	78
4.5.2	X-ray Diffraction (XRD) Analysis	83
5	Results and Discussion	87
5.1	Hastelloy-X Substrate	90
5.1.1	As-received Condition	91
5.1.2	Vacuum Furnace Heat Treatments	93
5.1.3	Air Furnace Heat Treatments	96
5.1.4	XRD Results	99
5.2	PVD FeCrAlY Bond Coat Deposition	102

5.2.1	Cathodic Arc PVD	102
5.2.2	Magnetron Sputtering PVD	107
5.3	Magnetron Sputtering PVD FeCrAlY	118
5.3.1	As-deposited Condition	118
5.3.2	Vacuum Furnace Heat Treatments	122
5.3.3	Air Furnace Heat Treatments	146
5.3.4	XRD Results	161
5.4	Air Plasma Spray Deposited NiCrAlY	164
5.4.1	As-deposited Condition	164
5.4.2	Vacuum Furnace Heat Treatments	168
5.4.3	Air Furnace Heat Treatments	186
5.4.4	XRD Results	201
5.5	High-velocity Oxy-fuel Sprayed CoNiCrAlY	203
5.5.1	As-deposited Condition	203
5.5.2	Vacuum Furnace Heat Treatments	207
5.5.3	Air Furnace Heat Treatments	227
5.5.4	XRD Results	241
6	Conclusions and Recommendations	243
6.1	Conclusions	243
6.1.1	MS-PVD FeCrAlY	243
6.1.2	APS NiCrAlY	244
6.1.3	HVOF CoNiCrAlY	244
6.2	Recommendations for Future Work	245
	List of References	247
	Appendix A Hastelloy-X Substrate Coupon Drawing	255

List of Tables

1	Desirable features of an oxidation/corrosion resistant coating. Adapted from [22]).	16
2	Ductile-to-brittle transition temperatures at 1% strain to crack for various aluminide an overlay coating systems. Adapted from [16]).	23
3	Summary of NASA thin film sensor assembly manufacturing processes [40–44, 51, 52].	42
4	Selected Hastelloy-X material properties (adapted from [59]).	51
5	Summary of MCrAlY feedstock materials used for bond coat deposition.	56
6	Advantages and disadvantages to CA-PVD [67–69].	60
7	CA-PVD processing parameter ranges for FeCrAlY coating trials.	60
8	Advantages and disadvantages to MS-PVD [67].	65
9	MS-PVD processing parameter ranges for FeCrAlY+Al coating trials.	66
10	Advantages and disadvantages to thermal spray processes [67].	69
11	APS processing parameters for NiCrAlY coating runs.	71
12	HVOF processing parameters for CoNiCrAlY coating runs.	72
13	Summary of temperatures and hold times for furnace pre-oxidation heat treatment trials.	77
14	Summary of analysis techniques performed on test specimens.	79
15	EDS surface area scan data for region shown in Figure 39a (in wt%).	91

16	EDS surface area scan data for region shown in Figure 40a and spot scan data for location marked in Figure 40b (in wt%).	95
17	EDS surface area scan data for region shown in Figure 42a (in wt%).	98
18	EDS spot scan data for region shown in Figure 43b (in wt%).	98
19	Magnetron sputtering PVD process parameters for successful coating runs.	111
20	EDS surface area scan data for region shown in Figure 48 (in wt%). .	116
21	Cross-sectional EDS area scan data for the locations shown in Figures 49a with select cross-sectional views shown in Figures 49b-d (in wt%).	116
22	EDS spot scan data for locations shown in Figure 50 (in wt%).	117
23	EDS surface area scan data for region shown in Figure 51a (in wt%).	120
24	EDS surface area scan data for the cross-sectional area shown in Figure 52 (in wt%).	121
25	EDS surface area scan data for locations shown in Figure 54 (in wt%).	125
26	EDS surface area scan data for region shown in Figure 56a (in wt%).	126
27	EDS surface area scan data for region shown in Figure 58a (in wt%).	129
28	EDS spot scan data for locations shown in Figure 59 (in wt%).	131
29	EDS surface area scan data for region shown in Figure 60a (in wt%).	133
30	EDS spot scan data for locations shown in Figure 61 (in wt%).	134
31	EDS surface area scan data for region shown in Figure 62a (in wt%).	136
32	EDS spot scan data for locations shown in Figure 63 (in wt%).	137
33	EDS surface area scan data for region shown in Figure 64a (in wt%).	139
34	EDS spot scan data for locations shown in Figure 65 (in wt%).	139
35	A summary of MS-PVD FeCrAlY-coated test specimen surface after VHT.	143
36	A summary of MS-PVD FeCrAlY-coated test specimen cross-sections after VHT.	145

37	EDS surface area scan data for region shown in Figure 67a (in wt%).	149
38	EDS spot scan data for locations shown in Figure 68 (in wt%).	149
39	EDS surface area scan data for region shown in Figure 69 (in wt%). .	151
40	EDS spot scan data for location shown in Figure 71 (in wt%).	152
41	EDS area scan data for both 'light' and 'dark' oxides shown in Figures 73a and b, respectively, (in wt%).	156
42	EDS spot scan data for locations shown in Figure 74 (in wt%).	156
43	A summary of MS-PVD FeCrAlY-coated test specimen surface condi- tion after AHT.	159
44	A summary of MS-PVD FeCrAlY-coated test specimen cross-sections after AHT.	160
45	EDS surface area scan data for region shown in Figure 76a (in wt%), with comparison to the nominal NiCrAlY powder (Sulzer Metco AMDRY 962) composition.	166
46	EDS area scan data for region shown in Figure 77a and EDS spot scan data for locations shown in Figure 77b (in wt%), with the nominal NiCrAlY powder (AMDRY 962) composition for comparison.	167
47	EDS surface area scan data for region shown in Figure 78a (in wt%).	169
48	EDS surface area scan data for region shown in Figure 80 (in wt%). .	172
49	EDS spot scan data for locations shown in Figure 81b (in wt%). . . .	173
50	EDS spot scan data for location shown in Figure 82b (in wt%). . . .	173
51	EDS surface area scan data for region shown in Figure 83a (in wt%).	174
52	EDS spot scan data for location shown in Figure 84b (in wt%). . . .	175
53	EDS surface area scan data for region shown in Figure 85a (in wt%).	176
54	EDS surface area scan data for region shown in Figure 87 (in wt%). .	178
55	EDS surface area scan data for region shown in Figure 89a (in wt%).	181

56	A summary of APS NiCrAlY-coated test specimen surface conditions after VHT.	183
57	A summary APS NiCrAlY-coated test specimen cross-sections after VHT.	185
58	EDS spot scan data for locations shown in Figure 93a (i) and Figure 93b (ii) (in wt%).	187
59	EDS spot scan data for locations shown in Figure 95 (in wt%).	190
60	EDS surface area scan data for region shown in Figure 96 (in wt%).	192
61	EDS spot scan data for region shown in Figure 97 (in wt%).	193
62	EDS spot scan data for regions shown in Figure 98 (in wt%).	194
63	EDS spot scan data for regions shown in Figure 99 (in wt%).	194
64	EDS spot scan data for regions shown in Figure 101 (in wt%).	196
65	A summary of APS NiCrAlY-coated test specimen surfaces after AHT.	199
66	A summary of APS NiCrAlY-coated test specimen cross-sections after AHT.	200
67	EDS surface area scan data for region shown in Figure 104a (in wt%), with comparison to the nominal CoNiCrAlY powder (Sulzer Metco AMDRY 4700) composition.	204
68	EDS area scan data for region shown in Figure 105a and EDS spot scan data for locations shown in Figure 105b (in wt%), with the nominal CoNiCrAlY powder (AMDRY 4700) composition for comparison.	206
69	EDS surface area scan data for region shown in Figure 106a (in wt%).	208
70	EDS spot scan data for location shown in Figure 107 (in wt%).	209
71	EDS surface area scan data for region shown in Figure 108a (in wt%).	211
72	EDS spot scan data for location shown in Figure 109 (in wt%).	212
73	EDS spots can data for locations shown in Figure 110 (in wt%).	213
74	EDS surface area scan data for region shown in Figure 111a (in wt%).	214

75	EDS surface area scan data for region shown in Figure 113a (in wt%).	218
76	EDS surface area scan data for region shown in Figure 115 (in wt%).	218
77	EDS surface area scan data for region shown in Figure 117a (in wt%).	220
78	A summary of HVOF CoNiCrAlY-coated test specimen surface condition after VHT.	224
79	A summary of HVOF CoNiCrAlY-coated test specimen cross-sections after VHT.	226
80	EDS spot scan data for locations shown in Figure 121 (in wt%). . . .	228
81	EDS spot scan data for location shown in Figure 122b (in wt%). . . .	228
82	EDS surface area scan data for region shown in Figure 123 (in wt%).	232
83	EDS spot scan data for locations shown in Figure 124 (in wt%). . . .	232
84	EDS spot scan data for location shown in Figure 125b (in wt%). . . .	234
85	EDS spot scan data for locations shown in Figure 127 (in wt%). . . .	237
86	EDS spot scan data for location shown in Figure 128 (in wt%). . . .	237
87	A summary of HVOF CoNiCrAlY-coated test specimen surfaces after AHT.	239
88	A summary of HVOF CoNiCrAlY-coated test specimen cross-sections after AHT.	240

List of Figures

1	A prototype of a NRC-designed palladium-13%chromium strain gauge sensor manufactured onto an IN625 substrate using pulsed laser deposition and femtosecond laser patterning. (Image courtesy of D.F.Yang, NRC-IMI)	3
2	Combustion chamber assembly [5].	5
3	Turbine assembly [5].	6
4	Exhaust pipe assembly [5].	6
5	Trends in engine turbine inlet temperatures compared with high-temperature material developments [9].	9
6	Historical evolution of turbine entry temperatures for both aeroengines and industrial gas turbines [4].	9
7	By-pass air cooling arrangements in gas turbine aeroengines [5]. . . .	10
8	Schematic cross-section of a typical thermal barrier coating (TBC) system showing the relative temperature gradient between the hot gases and the internal cooling passage surfaces in the superalloy blade material [10].	10
9	Alloying elements present in nickel-base superalloys [12].	12
10	Fractured cross-section of oxide scales after oxidation of a FeCrAl foil in a conventional muffle furnace at 900°C for 300 hours [27].	18
11	Various examples of α -Al ₂ O ₃ morphologies presented in literature. . .	19

12	The surface scale morphology of an EB-PVD deposited CoNiCrAlY bond coat material after a heat treatment in air at 1100°C for 25 hours, showing presence of θ -Al ₂ O ₃ [17].	19
13	Surface morphology of oxide layers after oxidation in air of a FeCrAl alloy at 900°C for 300 hours. The platelets correspond to γ -Al ₂ O ₃ . [27].	20
14	Oxide stability maps for 1000°C isothermal oxidation in air [16]. . . .	23
15	Five of the major failure categories documented in literature for TBC systems [31].	26
16	Various NASA applications of thin film sensors [39,40].	32
17	Cross-sectional layouts of NASA thin film sensor assemblies for the instrumentation of hot section gas turbine engine components. [39]. .	39
18	Cross-sectional layout of ONERA thin film sensor assemblies for the instrumentation of hot section gas turbine engine components. [43]. .	40
19	Flat substrate prototype of NASA platinum/platinum-13%rhodium thin film thermocouple sensor [41].	40
20	Layout of ONERA's prototype thin film strain gauge-instrumented turbine blade [43].	41
21	Test specimens: MCrAlY-coated Hastelloy-X substrates.	49
22	Rolls-Royce/Allison T56 combustor can liner.	52
23	Relative oxidation and corrosion resistance of various diffusion and overlay bond coat materials [20,22].	55
24	Schematic diagram of the cathodic arc PVD process. Adapted from [69].	61
25	Sulzer Metaplas Type MR303 coating system with Metaplas Ionon MZR304/33 deposition chamber.	62
26	FeCrAlY feedstock cathode.	62
27	Schematic of the magnetron sputtering PVD process. Adapted from [69].	64
28	Teer Coatings Limited UDP 650/4 magnetron sputtering coating system.	64

29	Configuration of the MS-PVD coating system to accommodate hybrid Fe-CrAlY+Al target arrangement: (i) backing Al target, (ii) magnetically-adhered FeCrAlY disks (inside oval-shaped 'race track'), and (iii) substrate holder facing hybrid target arrangement.	67
30	MS-PVD FeCrAlY-coated test specimen.	68
31	Typical thermally-sprayed coating microstructure, containing: (a) unmelted particles, (b) oxides, (c) debris, (d) fine particles, and (e) porosity. Adapted from [37].	68
32	A schematic of a typical air plasma spray (APS) process [71].	72
33	A schematic of a typical high-velocity oxy-fuel (HVOF) process [71].	73
34	Oxy-Gon model C700 vacuum furnace.	78
35	Lindberg model 51232 box furnace with Lindberg model 59554 furnace controller.	80
36	Philips XL30S FEG SEM with Phoenix EDS detector system.	84
37	Hitachi S-570 tungsten filament thermionic emission gun SEM with Link Systems LX-5 model 5697 EDS detector system.	85
38	Characterizing pear-shaped ionization diagram for relative penetration volumes for various incident energy beam types. Adapted from [76].	86
39	Hastelloy-X substrate material in as-received condition, etched with a mild acid solution to expose grain boundaries.	92
40	Surface features on the Hastelloy-X substrate material after a VHT of 1000°C for 15 hours.	94
41	A cross-sectional SE micrograph showing the microstructure of the Hastelloy-X substrate material after VHT of 1100°C for 1 hour. The brightening effect visible along the specimen surface is attributed to an edge effect.	94

42	Surface features on the Hastelloy-X substrate material after an AHT of 1000°C for 10 hours.	97
43	Cross-sectional features on the TGO layer on the Hastelloy-X substrate material after an AHT of 1000°C for 10 hours.	97
44	XRD spectra for the bare Hastelloy-X test specimens in the following conditions: AHT of 1000°C for 10 hours (followed by complete oxide scale removal), VHT of 1100°C for 1 hour, and AHT of 1050°C for 5 hours.	101
45	A sputter-polished section of the FeCrAlY cathode material showing the as-cast microstructure.	105
46	Comparison of a severely degraded FeCrAlY cathode to a fresh cathode. Arc-striking mechanism of the CA-PVD coater is shown in the foreground (images courtesy of Q.Yang/R.McKellar, NRC).	106
47	Comparison of geometry changes in the hybrid FeCrAlY+Al target with use (images courtesy of Q.Yang/R.McKellar, NRC).	110
48	A high-magnification SE micrograph showing the surface texture of the MS-PVD deposited FeCrAlY coating for sample number M081119a.	114
49	Cross-sectional BSE micrographs showing the different coating microstructures as a function of distance across the substrate width, showing selected views. Average coating thickness is 20 μm	115
50	A high-magnification BSE micrograph showing a detailed view of the light (i) and dark (ii) coating constituents present in the as-deposited MS-PVD FeCrAlY layer. Markers also indicate EDS spot scan locations.	116
51	Surface features of the as-deposited MS-PVD FeCrAlY (M090225a).	120
52	A cross-sectional BSE micrograph showing the coating microstructure of the as-deposited MS-PVD FeCrAlY layer (M090225a). Average coating thickness is 30 μm	120

53	Surface features of the MS-PVD deposited FeCrAlY bond coat after VHT of 1000°C for 10 hours.	123
54	A BSE micrograph showing the two predominant surface oxide constituents typically present on the FeCrAlY layer as a result of a VHT of 1000°C for 10 hours: (i) a 'light' iron- and chromium-rich component and (ii) a 'dark' aluminum-rich component. Markers also show EDS spot scan locations.	124
55	A cross-sectional BSE micrograph showing the formation of three different layers as a result of a VHT of 1000°C for 10 hours: (i) the porous top layer (former BC layer), (ii) an interdiffusion layer, and (iii) an Cr-rich tcp (σ) phase region above (iv) the Hastelloy-X substrate. Also shown is (v) the diffusion of heavier elements to the Hastelloy-X grain boundaries, (vi) voids, and (vii) tungsten-rich patches that are frequently present in the substrate material.	124
56	Surface features of the MS-PVD FeCrAlY coated test specimen after VHT of 1000°C for 15 hours.	127
57	A cross-sectional BSE micrograph showing the formation of three different layers as a result of a VHT of 1000°C for 15 hours: (i) a porous top layer, (ii) an interdiffusion layer, and (iii) a Cr-rich tcp phase layer between the interdiffusion layer and (iv) substrate material. Light-shaded particles (v) in the substrate material are tungsten-rich. . . .	127
58	Surface features of the MS-PVD FeCrAlY-coated test specimens after VHT of 1050°C for 5 hours.	130

59	A cross-sectional BSE micrograph showing the four layers present in the MS-PVD FeCrAlY-coated test specimen after VHT of 1050°C for 5 hours: (i) a porous top layer, (ii) an interdiffusion layer, and (iii) a Cr-rich tcp-phase layer between the interdiffusion layer and (iv) the Hastelloy-X substrate material. Markers also indicate EDS spot scan locations.	130
60	Surface features of the MS-PVD FeCrAlY-coated test specimen after VHT of 1050°C for 10 hours.	133
61	A cross-sectional BSE micrograph showing the formation of three different layers in the MS-PVD FeCrAlY-coated test specimen as a result of a VHT of 1050°C for 10 hours: (i) a porous top layer, (ii) an interdiffusion layer, and (iii) σ -phase layer that forms between the interdiffusion layer and (iv) the Hastelloy-X substrate material. . . .	134
62	Surface features of the MS-PVD FeCrAlY-coated test specimen after VHT of 1100°C for 1 hour.	136
63	A cross-sectional BSE micrograph showing the formation of three different layers in the MS-PVD FeCrAlY-coated test specimen as a result of a VHT of 1100°C for 1 hour: (i) a porous top layer, (ii) an interdiffusion layer, and (iii) a σ phase-containing layer that forms between the interdiffusion layer and the Hastelloy-X substrate material. Markers also indicate EDS spot scan locations.	137
64	Surface features of the MS-PVD FeCrAlY-coated test specimen after VHT of 1100°C for 5 hours.	139

65	A cross-sectional BSE micrograph showing the formation of three different layers in the MS-PVD FeCrAlY-coated test specimen as a result of a VHT of 1100°C for 5 hours: (i) a porous top layer, (ii) an interdiffusion layer, and (iii) a Cr-rich σ phase-containing layer that forms between the diffusion layer and the Hastelloy-X substrate material. Markers also indicate EDS spot scan locations.	140
66	EDS area scan data for the MS-PVD FeCrAlY-coated test specimen surface composition (in wt%) as a function of specimen condition. . .	144
67	Surface features of the MS-PVD FeCrAlY-coated test specimen after an AHT of 1000°C for 10 hours.	148
68	A cross-sectional BSE micrograph showing the formation of three different layers in the MS-PVD FeCrAlY-coated test specimen as a result of a AHT of 1000°C for 10 hours: (i) a porous top layer, (ii) an interdiffusion layer, and (iii+iv) σ phase-containing layer that forms between the interdiffusion layer and the (v) Hastelloy-X substrate material. Note the presence of a largely continuous, sub- μm TGO surface layer. Markers also indicate EDS spot scan locations.	148
69	Surface features of the MS-PVD FeCrAlY-coated test specimen after an AHT of 1050°C for 5 hours. Note the presence of bubbling along coating ridges with some cracking along the highest points of the bubbles.	151
70	Detailed views of the TGO layer surface features on the MS-PVD FeCrAlY-coated test specimen after an AHT of 1050°C for 5 hours. .	152
71	Cross-sectional SE micrographs of the MS-PVD FeCrAlY-coated test specimen as a result of a AHT of 1050°C for 5 hours.	152
72	Surface features of the MS-PVD FeCrAlY-coated test specimen after an AHT of 1100°C for 1 hour. Note the presence of bubbling along coating ridges with some cracking along the highest points of the bubbles.	154

73	High-magnification SE micrographs showing details of both light and dark phases present on the surface of the MS-PVD FeCrAlY-coated test specimen after an AHT of 1100°C for 1 hour.	155
74	A cross-sectional SE micrograph showing the formation of three different layers in the MS-PVD FeCrAlY-coated test specimen as a result of a AHT of 1100°C for 1 hour: (i) a porous top layer, (ii) an inter-diffusion layer, and (iii) a σ phase-containing layer that forms between the diffusion layer and the Hastelloy-X substrate material. Marker also indicates EDS spot scan location.	155
75	XRD spectra for the MS-PVD deposited FeCrAlY-coated Hastelloy-X test specimens in the following conditions: as-deposited, VHT of 1100°C for 1 hour, and AHT of 1050°C for 5 hours.	163
76	SE micrographs showing the surface condition of the as-deposited APS NiCrAlY coated specimen.	165
77	Cross-sectional BSE micrographs showing the microstructural details of the as-deposited APS NiCrAlY-coated test specimen.	166
78	Surface features of the APS NiCrAlY-coated test specimen after VHT of 1000°C for 10 hours.	169
79	Cross-sectional microstructural features of the APS NiCrAlY-coated test specimen after VHT of 1000°C for 10 hours.	170
80	A SE micrograph showing the typical surface features of the APS NiCrAlY-coated test specimen after VHT of 1000°C for 15 hours. . .	172
81	High-magnification micrographs showing the surface morphology of the two TGO constituents typically present on the APS NiCrAlY-coated test specimen surface after a VHT of 1000°C for 15 hours.	172

82	Cross-sectional microstructural features of the APS NiCrAlY-coated test specimen after VHT of 1000°C for 15 hours. The sample was mounted face-to-face to ensure TGO retention throughout the metallographic preparation process.	173
83	Surface features of the APS NiCrAlY-coated test specimen after VHT of 1050°C for 5 hours.	175
84	Cross-sectional microstructural features of the APS NiCrAlY-coated test specimen after VHT of 1050°C for 5 hours.	175
85	Surface features of the APS NiCrAlY-coated test specimen after VHT of 1050°C for 10 hours.	177
86	Cross-sectional microstructural features of the APS NiCrAlY-coated test specimen after VHT of 1050°C for 10 hours. The sample was mounted face-to-face to ensure TGO retention throughout the metallographic preparation process.	177
87	A SE micrograph showing the surface features of the APS NiCrAlY-coated test specimen after VHT of 1100°C for 1 hour.	179
88	Cross-sectional microstructural features of the APS NiCrAlY-coated test specimen after VHT of 1100°C for 1 hour.	179
89	Surface features of the APS NiCrAlY-coated test specimen after VHT of 1100°C for 5 hours.	180
90	Cross-sectional microstructural features of the APS NiCrAlY-coated test specimen after VHT of 1100°C for 5 hours.	181
91	EDS area scan data for the APS NiCrAlY-coated test specimen surface composition (in wt%) as a function of specimen condition.	184
92	Surface features of the APS NiCrAlY-coated test specimen after an AHT of 1000°C for 10 hours.	188

93	High-magnification SE micrographs providing detailed views of the surface morphology of the two predominant oxide phases that are typically found on the surface of the APS NiCrAlY-coated test specimen after an AHT of 1000°C for 10 hours.	188
94	A BSE micrograph showing the typical cross-sectional microstructural features of the APS NiCrAlY-coated test specimen after an AHT of 1000°C for 10 hours, showing (i) a largely continuous oxide layer that is sporadically broken by (ii) outcroppings of a second oxide phase.	189
95	High-magnification micrographs providing a detailed view of the three different oxide phases typically present on the surface of the APS NiCrAlY-coated test specimen after an AHT of 1000°C for 10 hours. Markers also indicate EDS spot scan locations.	189
96	A SE micrograph showing the distribution of oxide phases on the surface of the APS NiCrAlY-coated test specimen after an AHT of 1050°C for 5 hours: (i) a globular oxide islands in a matrix consisting of (ii) a whisker-shaped oxide phase.	192
97	A high-magnification SE micrograph showing the surface morphology of the aluminum-rich, whisker-shaped oxide phase that is present on the surface of the APS NiCrAlY-coated test specimen after an AHT of 1050°C for 5.	193
98	High-magnification SE micrographs showing the surface morphology of the two variants of the globular, nickel-rich oxide phase that are typically present on the surface of the APS NiCrAlY-coated test specimen after an AHT of 1050°C for 5 hours. Markers show EDS spot scan measurement locations.	193

99	A SE micrograph showing the typical cross-sectional microstructural features of the APS NiCrAlY-coated test specimen after an AHT of 1050°C for 5 hours, showing (i) a largely continuous oxide layer that is sporadically broken by (ii) outcroppings of a second oxide phase. Markers also indicate EDS spot scan locations.	194
100	Surface features of the APS NiCrAlY-coated test specimen after an AHT of 1100°C for 1 hour.	196
101	High-magnification SE micrographs showing the surface morphology of the three different oxide morphologies that are typically present on the surface of the APS NiCrAlY-coated test specimen after an AHT of 1100°C for 1 hour. Markers also indicate EDS spot scan locations.	197
102	High-magnification SE micrographs providing a detailed view of the two TGO constituents typically present in the cross-section of the APS NiCrAlY-coated test specimen after an AHT of 1100°C for 1 hour: (a) an aluminum-rich layer that is frequently interrupted by (b) nickel- and chromium-rich mixed-oxide clusters.	197
103	XRD spectra for the APS-sprayed NiCrAlY-coated Hastelloy-X test specimens in the following conditions: as-deposited, VHT of 1100°C for 1 hour, and AHT of 1050°C for 5 hours.	202
104	SE micrographs showing the surface condition of the as-deposited HVOF NiCrAlY-coated specimen.	205
105	Cross-sectional BSE micrographs showing the microstructural details of the as-deposited HVOF CoNiCrAlY-coated test specimen.	205
106	Typical surface features present on the HVOF CoNiCrAlY-coated test specimen after a VHT of 1000°C for 10 hours.	208

107	A cross-sectional BSE micrograph showing the typical microstructural features of the HVOF CoNiCrAlY-coated test specimen after a VHT of 1000°C for 10 hours. Note the presence of (i) a discontinuous, sub-micron TGO layer on the BC surface. Marker also indicates EDS spot scan location.	209
108	Typical surface features present on the HVOF CoNiCrAlY-coated test specimen after a VHT of 1000°C for 15 hours.	211
109	A SE micrograph providing a detailed view of the TGO particles present on the HVOF CoNiCrAlY-coated test specimen after a VHT of 1000°C for 15 hours. Marker (i) indicates EDS spot scan location.	212
110	A cross-sectional BSE micrograph showing the typical microstructural features of the HVOF CoNiCrAlY-coated test specimen after a VHT of 1000°C for 15 hours. Note the presence of (i+ii) a largely continuous, sub-micron TGO layer on the BC surface. Markers also indicate EDS spot scan location. The sample was mounted face-to-face to ensure TGO retention throughout the metallographic preparation process.	212
111	Typical surface features present on the HVOF CoNiCrAlY-coated test specimen after a VHT of 1050°C for 5 hours.	215
112	A cross-sectional, high-magnification BSE micrograph showing the typical microstructural features present in the HVOF CoNiCrAlY-coated test specimen after a VHT of 1050°C for 5 hours. The sample was mounted face-to-face to ensure TGO retention throughout the metallographic preparation process.	215
113	Typical surface features present on the HVOF CoNiCrAlY-coated test specimen after a VHT of 1050°C for 10 hours.	217

114	Cross-sectional micrographs showing the typical microstructural features present in the HVOF CoNiCrAlY-coated test specimen after a VHT of 1050°C for 10 hours.	217
115	Typical surface features present on the HVOF CoNiCrAlY-coated test specimen after a VHT of 1100°C for 1 hour, showing (i) porosity in the BC layer.	219
116	Cross-sectional micrographs showing the typical microstructural features present in the HVOF CoNiCrAlY-coated test specimen after a VHT of 1100°C for 1 hour.	219
117	Typical surface features present on the HVOF CoNiCrAlY-coated test specimen after a VHT of 1100°C for 5 hours.	221
118	A cross-sectional BSE micrograph showing the typical microstructural features present in the HVOF CoNiCrAlY-coated test specimen after a VHT of 1100°C for 5 hours.	221
119	EDS area scan data for the HVOF CoNiCrAlY-coated test specimen surface composition (in wt%) as a function of specimen condition. . .	225
120	Typical surface features present on the HVOF CoNiCrAlY-coated test specimen after an AHT of 1000°C for 10 hours.	229
121	High-magnification micrographs providing detailed views of the three oxide phases typically found on the surface of the the HVOF CoNiCrAlY-coated test specimen after an AHT of 1000°C for 10 hours. Markers also indicate EDS spot scan locations.	229
122	Typical cross-sectional microstructural features present in the HVOF CoNiCrAlY-coated test specimen after an AHT of 1000°C for 10 hours.	230
123	A SE micrograph showing the typical surface features present on the HVOF CoNiCrAlY-coated test specimen after an AHT of 1050°C for 5 hours.	232

124	High-magnification micrographs providing detailed views of the two oxide phases typically found on the surface of the the HVOF CoNiCrAlY-coated test specimen after an AHT of 1050°C for 5 hours. Markers also indicate EDS spot scan locations.	233
125	Typical cross-sectional microstructural features present in the HVOF CoNiCrAlY-coated test specimen after an AHT of 1050°C for 5 hours.	233
126	A SE micrograph showing the typical surface features present on the HVOF CoNiCrAlY-coated test specimen after an AHT of 1100°C for 1 hour: (i) globular, mixed-oxide islands in widely interspersed in (ii) a dense, nodular oxide matrix.	236
127	High-magnification micrographs providing detailed views of the two oxide phases typically found on the surface of the the HVOF CoNiCrAlY-coated test specimen after an AHT of 1100°C for 1 hour. Markers also indicate EDS spot scan locations.	236
128	A cross-sectional SE micrograph showing the typical microstructural features present in the HVOF CoNiCrAlY-coated test specimen after an AHT of 1100°C for 1 hour, indicating the presence of (i) a continuous TGO layer with an average thickness of 1 μm . Marker also indicates spot scan location.	237
129	XRD spectra for the HVOF-sprayed CoNiCrAlY-coated Hastelloy-X test specimens in the following conditions: as-deposited, VHT of 1100°C for 1 hour, and AHT of 1050°C for 5 hours.	242

Nomenclature

AHT	air furnace heat treatment
APS	air plasma spray
BC	bond coat
bcc	body-centred cubic
BSE	backscattering electron
CA-PVD	cathodic arc physical vapour deposition
CSM	Coating and Surface Modifications
CTE	coefficient of thermal expansion
CVD	chemical vapour deposition
DBTT	ductile-to-brittle transition temperature
DE	deposition efficiency
DS	directionally solidified
EDPHM	engine diagnostic and prognostic health management

EDS	energy dispersive spectrometry
EB-PVD	electron beam physical vapour deposition
FEG	field emission gun
GADDS	general area detector diffractometer software
GTL	Gas Turbine Laboratories
hcp	hexagonal close-packed
HIP	hot isostatic pressing
HP	high pressure
HVOF	high-velocity oxy-fuel
IAR	Institute for Aerospace Research
ICPET	Institute for Chemical Process and Environmental Technology
IGT	industrial gas turbine
IMI	Industrial Materials Institute
LP	low pressure
MCT	Materials and Component Technologies
MS-PVD	magnetron sputtering physical vapour deposition

NASA	National Aeronautics and Space Administration (United States of America)
NIF	New Initiative Fund
NRC	National Research Council (Canada)
ONERA	Office National d'Études et Recherches Aérospatiales (France)
PDF	powder diffraction file
PM	powder metallurgy
PVD	physical vapour deposition
RE	reactive elements
sccm	standard cubic centimetres per minute
SE	secondary electron
SEM	scanning electron microscope
SNECMA	Société Nationale d'Étude et de Construction de Moteurs d'Aviation (France)
SSME	Space Shuttle main engine
SX	single crystal
TBC	thermal barrier coating

TC	top coat
tcp	topologically close-packed
TGO	thermally-grown oxide
TIT	turbine inlet temperature
TS	thermal spray
VAR	vacuum arc remelt
VPS	vacuum plasma spray
VHT	vacuum furnace heat treatment
wt%	weight percent
XRD	x-ray diffraction
YSZ	yttrium oxide-stabilized zirconium oxide

Chapter 1

Introduction

In the aerospace propulsion sector, particularly in the civil air transport branch, there has been increased customer demand to find ways to decrease the total cost of ownership of gas turbine engines. In order to answer this demand, engine manufactures are beginning to invest in the development of intelligent engine diagnostic and prognostic health management (EDPHM) systems [1, 2]. These systems will contribute to the decrease in total ownership cost through improvements in safety and reliability, optimized fuel consumption, and decreased maintenance cost of the whole engine fleet. The EDPHM systems will serve to detect and isolate deteriorating components in real time to save the engine operator from costly repairs as a result of complete component failure which may compromise the reliability and safety of the engine. These systems will also be capable of predicting when components require replacement in order to streamline maintenance scheduling [1, 2].

The most critical components in a gas turbine aeroengine are found in the hot section, which consists of components downstream of the combustor inlet. Components in this section are subjected to extreme conditions that push the capabilities of the most sophisticated materials used to manufacture these complex components. The extreme conditions in the hot section are a consequence of extreme temperature,

pressure, and vibration, in combination with high fluid flow rates, a highly corrosive, oxidative and abrasive combustion gas atmosphere, and in the case of rotating machinery, high centripetal loading.

This exceedingly hostile environment requires durable and reliable high-performance sensor systems that are capable of providing the desired information from the critical components over extended periods of time. High temperature thin film sensors, such as the NRC-designed palladium-13%chromium strain gauge (Figure 1) will be implemented on critical structures in the gas turbine to monitor various aspects of the instrumented component in order to aid in the fulfillment of functions associated with the implementation of a EDPHM system [1, 2].

This thesis presents an experimental investigation into the effects of selected vacuum furnace and air furnace heat treatments on a nickel-based superalloy substrate onto which a MCrAlY overlay bond coat has been applied. This thesis is presented in the following order:

- Chapter 2** Literature Review
- Chapter 3** Research Objectives
- Chapter 4** Materials and Experimental Procedures
- Chapter 5** Results and Discussion
- Chapter 6** Conclusions and Recommendations

This work is a contribution to a New Initiatives Fund (NIF) project at the National Research Council Canada (NRC) whose aim is to develop high temperature thin film sensors for gas turbine engines. The project is led by the Materials and Components Technologies (MCT) group of NRC's Institute for Aerospace Research (IAR), in collaboration with IAR's Gas Turbine Laboratory (GTL) and the Coating and Surface Modifications (CSM) group of NRC's Industrial Materials Institute (IMI).

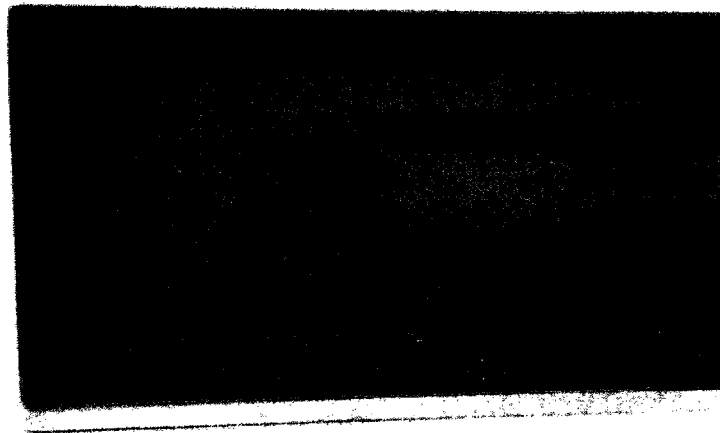


Figure 1: A prototype of a NRC-designed palladium-13%chromium strain gauge sensor manufactured onto an IN625 substrate using pulsed laser deposition and femtosecond laser patterning. (Image courtesy of D.F. Yang, NRC-IMI)

Chapter 2

Literature Review

In this chapter, the typical constituents of modern gas turbine engine hot section components are reviewed, including an overview of nickel-base superalloy structural materials, and thermal barrier coating (TBC) systems that consist of both a bond coat (BC) and a ceramic insulating top coat (TC) layer. As a primary focus of this thesis work, the following aspects of the bond coat are described in greater detail: bond coat function, aluminum oxide as the preferred thermally-grown oxide (TGO), MCrAlY overlay coating materials and their oxide formation characteristics, typical bond coat failure modes, and pre-oxidation heat treatments. Thin film sensor technology is introduced, followed by a brief comparison between conventional sensors and thin film sensors, highlighting the advantages of the latter. Two applications of thin film sensor instrumentation of hot section components in gas turbine engines are described, together with the operational requirements of the sensor systems in these applications. These are followed by an overview of typical sensor layouts that have already been applied to hot-section components in previous research, together with the various microfabrication processes used to manufacture these sensor assemblies. This chapter is concluded with a synopsis of the National Aeronautical and Space Administration's (NASA) extensive experiences with the application of thin film sensors in the instrumentation of hot section turbomachinery components.

2.1 Typical Constituents of Modern Gas Turbine Engine Hot Section Components

The hot section of a typical gas turbine engine consists of all components that are downstream of the gas path from the air intake and compressor assembly: the combustor, turbine and exhaust (see Figures 2, 3, and 4). These components are regularly subjected to service conditions that include exposure to a harsh combustion product atmosphere in temperatures that exceed 1000°C . These conditions have led to the development of special nickel- and cobalt-base, high-temperature superalloys for use in the manufacture of such components to withstand these conditions and to meet expected service lifetimes that range between 10,000 hours (for civil aeroengine applications) to 100,000 hours (for industrial/power generation applications) [3,4].

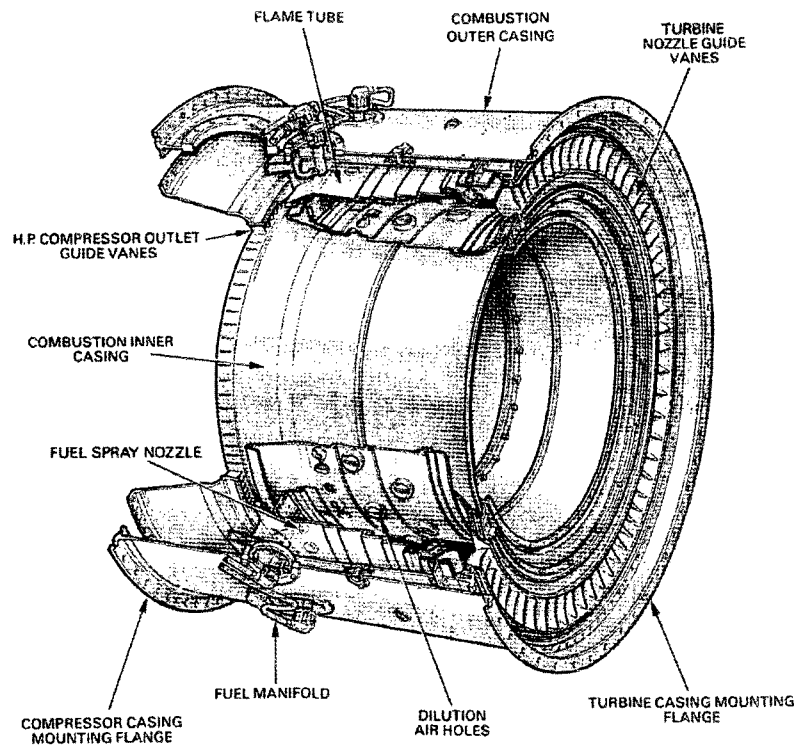


Figure 2: Combustion chamber assembly [5].

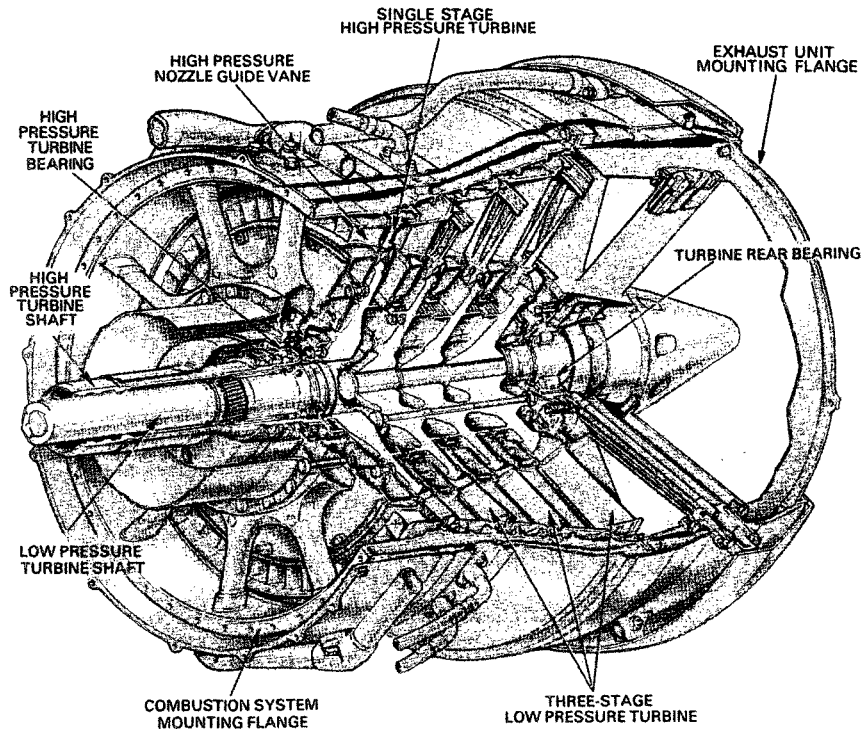


Figure 3: Turbine assembly [5].

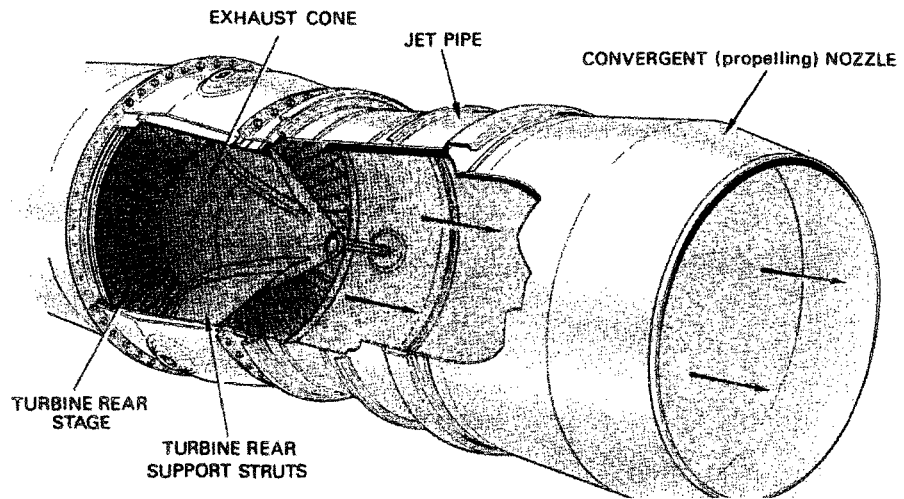


Figure 4: Exhaust pipe assembly [5].

The hottest temperatures in a gas turbine engine are found in the combustor section, in which the temperature of combustion gases are typically about 1800–2000°C, resulting in severe thermal loading of the affected components. Approximately 40–80% of the total air mass flow entering the combustor is used for film or transpiration cooling of the combustor walls as well as combustion gas dilution, allowing for turbine inlet temperatures (TITs) exceeding 1500°C [5]. While TITs are lower than the average temperatures experienced in the combustor, rotating turbine components such as the turbine blades are also subject to high centripetal loading, placing not only thermal stresses on the component, but also internal forces due to the rotation of the component. Nickel-base superalloys developed since the 1940s (Figure 5), have enabled the TITs to increase from approximately 760°C in the beginnings of gas turbine technology to nearly 1500°C in modern gas turbine engines (Figure 6).

The requirement to withstand such conditions has resulted in the development of directionally solidified (DS) and single crystal (SX) processed superalloys to achieve desirable material properties in major loading direction of the blade. Even with DS and SX superalloys, the maximum operating temperature is limited by incipient melting, and is restricted to a maximum material temperature of about 1050°C with occasional excursions to 1200°C [3]. Two major technological advances have made long-term, higher-temperature operation a possibility: blade cooling and thermal barrier coating systems [3].

Blade cooling is achieved by diverting some of the compressed air from the compressor section of the engine and forcing it through internal passages and around the vane and blade airfoil surfaces (see Figure 7). Blade cooling significantly decreases the average temperature experienced by the airfoil material by approximately 200–300°C, allowing for the operation of the blades and vanes at combustion gas temperatures exceeding 1300°C [6].

Increasing the flow of diverted compressed air for cooling negatively affects the

overall efficiency of the engine: thus, a supplementary solution is required to decrease the average operating temperature of the structural material [7]. This need led to the introduction of an overlaid ceramic top coat (TC) layer to act as a thermal barrier between the structural blade or vane alloy and the combustion gas environment. TCs consist of a thin (100–400 micron thickness) ceramic layer that acts as a thermally-insulating layer (Figure 8), reducing the average metal skin temperature experienced by the structural material by another 150–200°C. This reduction in skin temperature permits for an increase in the allowable turbine inlet temperature to above 1500°C [7,8].

There is, however, a significant difference in thermal expansion coefficient between the structural, metallic superalloy material and the insulating ceramic TC material, resulting in significant stresses between substrate and TC. The resulting stresses between substrate and TC can lead to premature coating failures, compromising the component service life. In addition, improvements in mechanical properties as a result of superalloy composition changes have come at the cost of a general decrease in corrosion resistance of the structural superalloys. These problems have been mitigated through the application of an intermediary bond coat (BC) layer, the purpose of which is to restore and improve the corrosion and oxidation resistance by acting as a diffusion barrier as well as a strain accommodation layer between superalloy and the ceramic top coat. Both the bond coat and the top coat form the essential elements of the thermal barrier coating (TBC) system (Figure 8).

The following subsections provide greater detail into the three different integral components that make up the hot section components found in modern gas turbine engines, with emphasis on the bond coat layer as it is the focus of the presented thesis work.

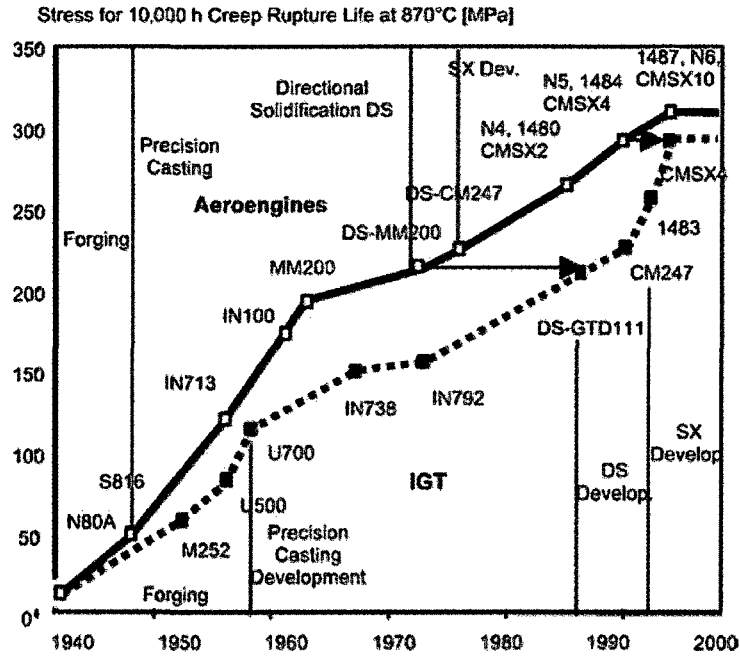


Figure 5: Trends in engine turbine inlet temperatures compared with high-temperature material developments [9].

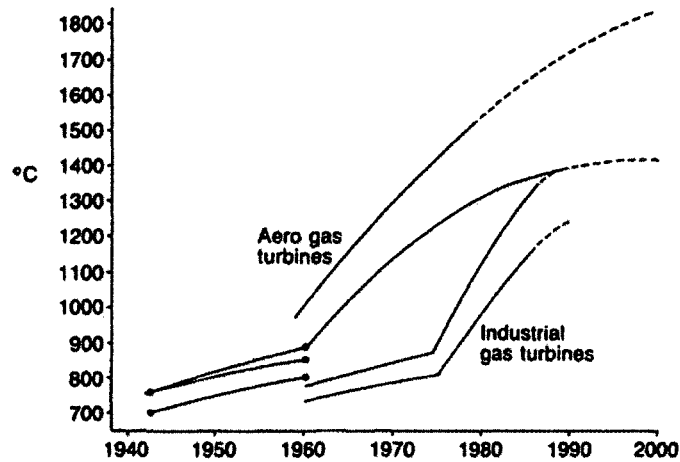
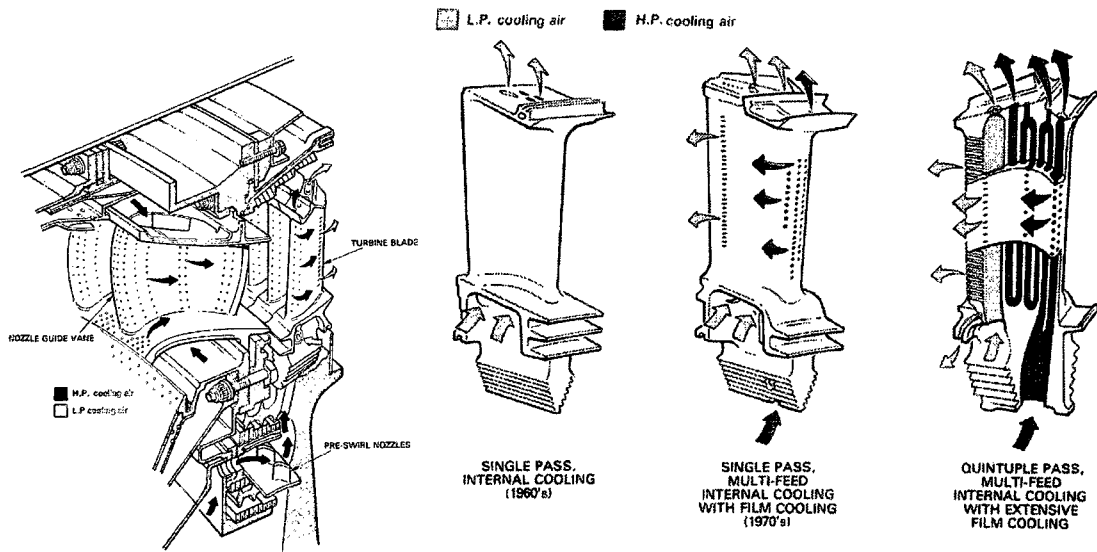


Figure 6: Historical evolution of turbine entry temperatures for both aeroengines and industrial gas turbines [4].



(a) General blade and vane cooling overview.

(b) Rotating blade cooling schemes.

Figure 7: By-pass air cooling arrangements in gas turbine aeroengines [5].

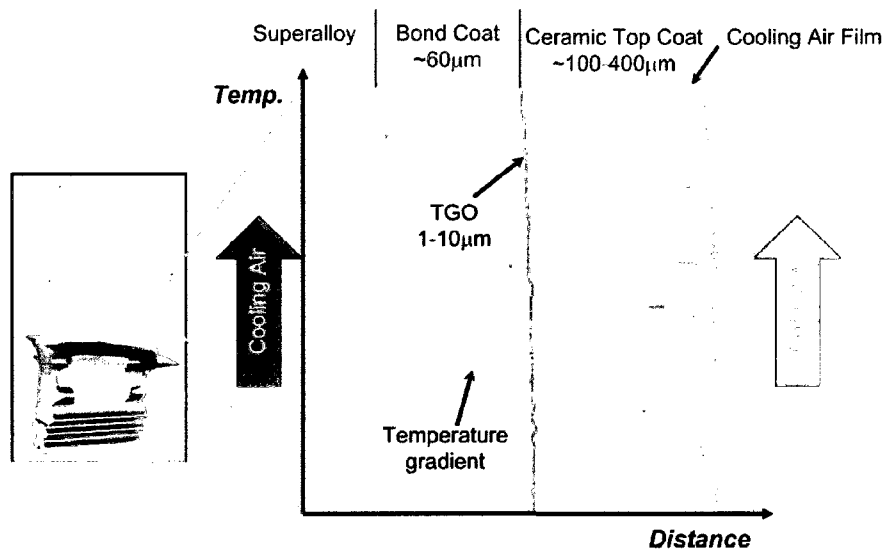


Figure 8: Schematic cross-section of a typical thermal barrier coating (TBC) system showing the relative temperature gradient between the hot gases and the internal cooling passage surfaces in the superalloy blade material [10].

2.1.1 Structural Materials

Hot section components found in modern Western gas turbine engine designs are typically manufactured from nickel-base superalloys that exhibit a superior combination of strength, creep resistance, and toughness at high temperatures, in addition to providing for excellent resistance to corrosion and oxidation that is necessary for operation while being subjected to harsh operating conditions. While there exist several applications of cobalt-base superalloys for vanes and ferritic and austenitic steels for turbine disks, the majority of the components are manufactured from nickel-base superalloys [5]. In a modern Western gas turbine aeroengine, nickel-base superalloys contribute, on average, between 40–50% of the total weight of the engine [3]. Depending on the design loading conditions of the component, they may be cast as single crystals (SX) for highly-loaded rotating components such as early-stage, high-pressure turbine blades, or directionally solidified (DS) and even polycrystalline for components with lower loadings. Rotating turbine disks, into which the turbine blades are installed or bonded, are manufactured through wrought processes such as forging, using vacuum-arc remelted (VAR) ingots or consolidated superalloy powder metallurgy (PM) preforms [3, 11].

Nickel superalloys are composed mainly of face-centred cubic (fcc) nickel with up to a 40 wt% combination of five to ten other alloying components. All nickel superalloy compositions are based on the binary nickel-aluminum system where strengthening of the alloy is due primarily to the precipitation of a Ni_3X (γ') phase [3, 8]. Refractory elements such as molybdenum, tungsten, niobium, and rhenium are added to act as solid solution strengtheners, while aluminum, titanium, tantalum, and niobium are added to form $\text{Ni}_3(\text{Al}, \text{Ti}, \text{Ta}, \text{Nb})$ γ' phases [12, 13] (see Figure 9). Alloying elements such as chromium, yttrium, and lanthanum are added to augment oxidation

IIA	IIIA	IVB	Element						
	B 0.097	C 0.077	Atomic Radius (nm)						
	Al 0.143		IVA	VA	VIA	VIIA	VIIIA	VIIIA	VIIIA
		Ti 0.147	V 0.132	Cr 0.125		Fe 0.124	Co 0.125	Ni 0.125	
	Y 0.181	Zr 0.158	Nb 0.143	Mo 0.136		Ru 0.134			
		Hf 0.159	Ta 0.147	W 0.157	Re 0.138				

γ' former
 Minor alloying additions
 γ former

Figure 9: Alloying elements present in nickel-base superalloys [12].

and/or corrosion resistance, leading to the formation of a slow-growing and adherent aluminum oxide layer [3]. Minor alloying additions of ductility-enhancing boron, carbon, hafnium, and zirconium are included to promote the formation of carbides and borides that tend to locate in the grain boundaries of polycrystalline alloys. These borides and carbides work to impede grain boundary sliding and to minimize damage accumulation as a result of high temperature creep [3, 14]. Detrimental to the mechanical properties of nickel-base superalloys is the formation of topologically close-packed (tcp) phases that deplete the microstructure of strengthening refractory elements and act as crack initiation sites under cyclic loading conditions. Precipitation reactions for TCP phases are typically quite slow and are only apparent after considerable component service life [3].

The following sub-section describes the bond coat layer of the thermal barrier coating system, the intermediary layer between the structural alloy and the thermally-insulating ceramic top coat layer, part of whose function is to provide protection of the structural superalloy from oxidation and hot corrosion.

2.1.2 Bond Coat (BC)

The bond coat is one of two principal components of a thermal barrier coating system that is applied directly over the structural alloy surface of the hot section component. The function of the bond coat is two-fold: to afford the superalloy substrate with hot corrosion and oxidation resistance and to act as a strain accommodation layer between the superalloy substrate and the overlaid ceramic thermal barrier coating (TBC) layer. To perform these two essential functions, the bond coat must exhibit sufficient oxidation and corrosion resistance, interface stability, coating adhesion, and mechanical strength. A listing of desirable coating properties and requirements is listed in Table 1.

The following sub-sections will describe how the properties of bond coat materials allow the coatings to perform their intended function, followed by the reasoning behind attempting to form a TGO that consists primarily of α -aluminum oxide. MCrAlY materials are explored further by describing their composition and the mechanisms of TGO formation and relating these to the desirable features of an oxidation/corrosion resistant coating listed in Table 1. Finally, bond coat failure modes are briefly summarized, together with an introduction to pre-oxidation heat treatments and their potential to increase coating system lifetime.

Bond Coat Function

In order to provide adequate oxidation resistance, the bond coat must develop a barrier to oxygen diffusion into the superalloy, as well as outward diffusion of the superalloy elemental constituents. The bond coat is designed to develop such a barrier through the formation of an adherent, dense, and stable thermally-grown oxide (TGO) layer. The bond coat should form this thin, protective oxide on first contact with the oxidizing environment, and the oxide scale must have good adhesion to the parent

bond coat and overlying ceramic top coat (TC) layer, allowing for long-term coating adhesion through an extensive service life consisting of cyclic thermal and mechanical loading that is typical in gas turbine engine operation [15].

A successful bond coat will be one that exhibits the necessary thermal and chemical compatibility with the substrate material in order to maintain the desired composition, microstructure and physical properties over the lifetime of the coating system. This requires that the TGO exhibits slow growth, minimal misfit strain between the BC and the TC, and a high creep strength with suitable ductility [15]. Misfit strain can be minimized by selecting a bond coat material whose coefficient of thermal expansion (CTE) best matches both the superalloy substrate and the TC layer [7,8,16].

As the TBC system's overall durability and reliability are explicitly linked to the oxidation behaviour of the bond coat, it is essential that it forms a continuous, dense, stable, and adherent oxide layer [10,17–19]. In the event of TGO spallation, it is important that the oxide layer regrows quickly to re-form the diffusion barrier. In the case of aluminum oxide-forming bond coat alloys, the bond coat alloy must contain more than the critical content of aluminum required for aluminum oxide formation, in order to generate and maintain a dense and effective oxide layer. This TGO regeneration capability, in turn, is determined through a variety of metallurgical factors such as the concentration of alloying elements and alloy structure, as well as oxidation conditions such as temperature and oxygen partial pressure. The coating composition must be formulated in such a way to ensure that the primary oxidation product is the desired, protective, thermodynamically stable oxide phase, and not a transitional, non-protective oxide phase that may have a tendency to compete with the desired oxide phase at the operational temperature range of the coated component [10].

This TGO-regeneration property is also essential for hot corrosion resistance.

Since the dissolution of protective oxides due to the continuous deposition of low-melting point constituents from the combustion product atmosphere causes hot corrosion damage, a rapid and continuous re-growth of a protective TGO is required. These low-melting point deposits are combustion process by-products as a result of maritime operating environments and fuel impurities, which form compounds containing sodium, various halides, vanadium and sulfur [20]. While unable to prevent this corrosion process entirely, fuel additives have been successfully used to reduce the detrimental effects [21].

If left without a functionally protective TGO, the underlying structural superalloy will suffer rapid degradation, possibly resulting in catastrophic failure of the coated component. While all of the requirements for a successful bond coat, listed in Table 1, cannot be satisfied simultaneously, a trade-off between the different aspects must be considered for each substrate/bond coat/ceramic top coat combination. In the following sub-section, aluminum oxide is presented as the preferred TGO in gas turbine engine hot section components, together with the reasoning behind the selection, which is based on oxide formation, its physical and chemical properties, and the characteristics of its formation.

Aluminum Oxide as Preferred TGO

In general, high-temperature materials based on iron-, nickel-, and cobalt-based alloys have been designed to form protective scales of either chromium oxide (Cr_2O_3), aluminum oxide (Al_2O_3), or silicon dioxide (SiO_2) when exposed to oxidizing conditions [23]. These particular oxides have been shown to be thermodynamically stable up to approximately 900°C , have high melting points, and exhibit slow transport processes for diffusing elements. At temperatures above 900°C , however, Cr_2O_3 has the tendency to react further with oxygen to form volatile CrO_3 , severely limiting

Table 1: Desirable features of an oxidation/corrosion resistant coating. Adapted from [22]).

Oxidation/Corrosion Resistance	<ul style="list-style-type: none"> • Low rates of scale formation • Uniform surface attack • Thermodynamically stable surface oxide • Ductile surface scales • Adherent surface scales • High concentration of scale forming elements within the coating to act as scale reformation reserves
Interface Stability	<ul style="list-style-type: none"> • Low rate of diffusion across interface at operating temperatures • Limited compositional changes across interface • Absence of embrittling phase formation during service
Good Adhesion	<ul style="list-style-type: none"> • Matched coating and substrate properties to minimize coating mismatch and stress generation at coating/substrate interface • Optimum surface condition before coating • Minimization of growth stresses during coating formation
Mechanical Strength	<ul style="list-style-type: none"> • Coating must withstand all stress (creep, fatigue, and impact loading) generated at component surface during service • Well matched thermal expansion coefficients between coating and substrate to minimize thermal stressing and thermal fatigue

the lifetime of Cr_2O_3 -forming alloys. While both Al_2O_3 and SiO_2 are able to withstand higher temperatures up to around 1200–1300°C, SiO_2 formers are limited to environments with adequate oxygen activity due to the propensity to form volatile SiO at low oxygen activities [8, 23]. In addition, silicon has significant adverse effects on the mechanical properties of iron-, nickel-, and cobalt-based alloys, limiting the amount that can be added to the composition of a particular high-temperature alloy to increase corrosion resistance. Silicon is also significantly less capable in developing a healing TGO layer than aluminum, as SiO_2 tends to form at a slower rate and develops less efficiently than Al_2O_3 in the early stages of oxidation, leading to a higher proportion of transient oxidation phases [23].

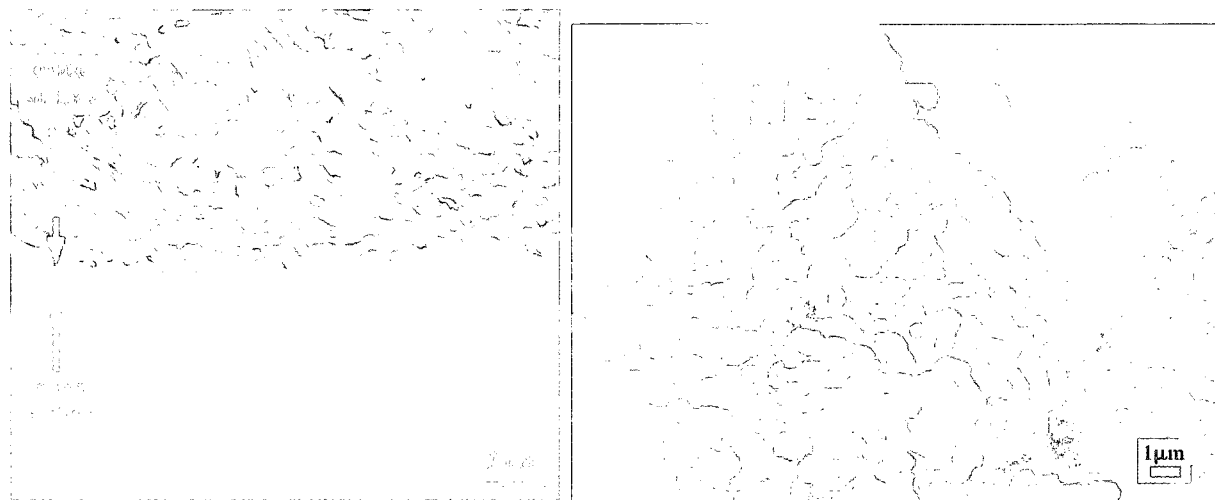
In practice, bond coat materials that have shown the most promise are those that form a slow-growing, non-porous, and adherent α -aluminum oxide TGO layer [10, 15, 24]. While the thermodynamically stable alpha-phase of aluminum oxide is desired as the primary TGO constituent, there are several transient phases of aluminum oxide with different crystal structures that have also been shown to exist: γ - Al_2O_3 (cubic spinel structure), δ - Al_2O_3 (tetragonal structure), and θ - Al_2O_3 (monoclinic structure) [25]. These metastable aluminum oxide structures form blade or whisker-type surface morphologies and tend to grow at a significantly faster rate than the α - Al_2O_3 structure. Figure 10 shows the formation of an aluminum oxide TGO on a FeCrAl alloy containing α -, γ -, and θ - Al_2O_3 phases. In this case, it appears that both the γ - and θ - Al_2O_3 phases grow on the exposed surface while the sub-TGO surface component comprises largely of the α - Al_2O_3 phase. Figure 11 shows close-up views of α - Al_2O_3 surface features, while Figure 12 and Figure 13 show a close-up view of θ - and γ - Al_2O_3 phases, respectively. All transitional aluminum oxide phases can be converted to the α -phase through heat treatment; however, this phase change can be accompanied by a significant volume change. For example, during the transformation from θ - Al_2O_3 to α - Al_2O_3 , a volume decrease of 8-13% occurs, and this volume



Figure 10: Fractured cross-section of oxide scales after oxidation of a FeCrAl foil in a conventional muffle furnace at 900°C for 300 hours [27].

decrease has the potential to cause crack formation that can result in TGO scale spallation [10]. The α -phase of aluminum oxide possesses a dense, hexagonal close-packed (hcp), rhombohedral crystal structure with nearly no defects, and does not undergo phase transition between room temperature and its melting point, avoiding potentially detrimental volume changes that could lead to excessive stresses in the coating resulting in oxide layer spallation [26]. Although the effects of minor alloying elements in the bond coat material on the rates of aluminum oxide transformation to the stable α -phase are unclear, however, there have been studies that suggest that chromium and titanium additions accelerate this transformation [10].

In the following sub-section, aluminum oxide-forming MCrAlY overlay bond coat materials are introduced, highlighting their metallurgical structure and composition, methods of coating deposition, and mechanisms of TGO formation.



(a) New oxide formation along the grain boundaries of initially formed α - Al_2O_3 TGO [15]. (b) Several agglomerates of α - Al_2O_3 after heating in air to 1500°C [28].

Figure 11: Various examples of α - Al_2O_3 morphologies presented in literature.

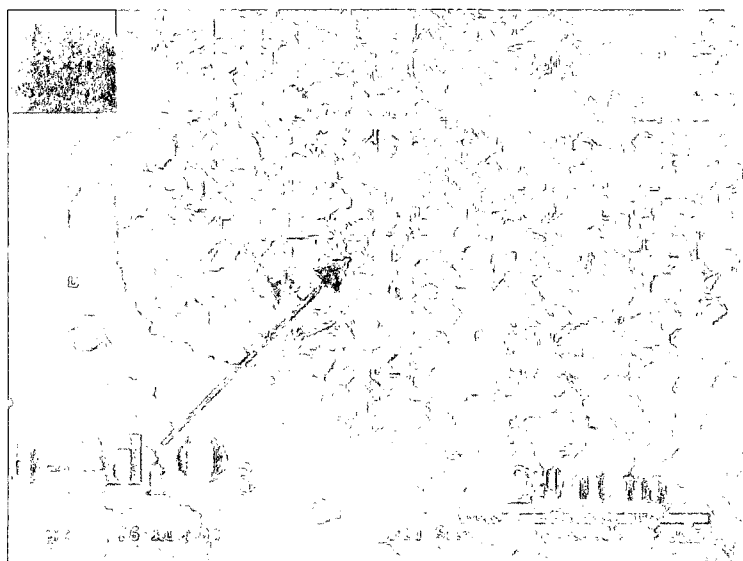


Figure 12: The surface scale morphology of an EB-PVD deposited CoNiCrAlY bond coat material after a heat treatment in air at 1100°C for 25 hours, showing presence of θ - Al_2O_3 [17].



Figure 13: Surface morphology of oxide layers after oxidation in air of a FeCrAl alloy at 900°C for 300 hours. The platelets correspond to γ -Al₂O₃. [27].

MCrAlY Bond Coat Materials

Commercially applied bond coats are typically one of two types that derive from purposely-designed, stand-alone, oxidation and corrosion protection coatings that have been previously developed for hot section gas turbine components. These two different coating types are the single β -phase, platinum-modified aluminide diffusion coatings and two-phase, γ - β MCrAlY overlay coatings [10,24]. Diffusion-type coatings are generally applied through electroplating and chemical vapour deposition (CVD) processes such as pack cementation, while overlay coatings may be applied through a variety of physical vapour deposition (PVD) and thermal spray (TS) processes such as electron beam physical vapour deposition or magnetron sputtering deposition, and plasma spray or high-velocity oxy-fuel spray deposition, respectively [8, 16]. Tests have shown that overlay coatings provide superior protection over aluminized diffusion coatings, partly due to the substantially increased ductility in MCrAlY-type coatings [16], as evident from ductile-to-brittle transition temperatures (DBTT) listed in Table 2. The focus in this sub-section centres on MCrAlY materials, as the bond

coat materials used in this work fall under this bond coat material type.

MCrAlY materials are intermetallic alloys where the M can represent either iron, nickel, cobalt, or a combination of nickel and cobalt [8]. Modern MCrAlY materials used as bond coats on high-temperature gas turbine components, however, employ either nickel, cobalt, or both nickel and cobalt in combination. MCrAlY coatings of this type generally comprise of a brittle β -NiAl (or β -CoAl) phase in a γ -nickel (or γ -cobalt) matrix containing chromium in solid solution [8, 10, 16].

MCrAlY coatings are secondary aluminum oxide formers that generally develop chromium oxide scales on the external surface of the coating and subsequently form an aluminum oxide layer underneath the chromium oxide layer during prolonged exposure to an oxidizing environment [29]. For binary Ni-Al or Co-Al alloys, substantial amounts of aluminum are required to form and maintain a surface scale of aluminum oxide. The addition of approximately 10% of Cr, however, decreases the amount of aluminum needed to form and maintain the aluminum oxide surface scale to about 5% [8, 16]. This effect is evident in Figure 14, which shows the oxygen stability maps for both the NiCrAl and CoCrAl alloy systems for isothermal oxidation at 1000°C.

The active element additions, such as yttrium, decrease the oxidation/corrosion kinetics and enhance the adhesion of the protective oxide scale. These active elements have been shown to significantly reduce the grain boundary diffusion coefficient of aluminum in the aluminum oxide TGO, and for this reason, tend to reduce the amount of aluminum outwards transport through the aluminum oxide scale, resulting in an overall reduction of TGO thickening [30]. Yttrium is also added to improve the adhesion of the TGO, primarily by acting as a solid state gettering site for sulphur, which diffuses up from the superalloy substrate. Sulphur is considered a deleterious impurity that negatively impacts mechanical properties and oxidation resistance [3, 31]. Other active elements such as hafnium, tantalum, or silicon could be added in addition to yttrium. These elements, however, function via different mechanisms,

with the effectiveness of each addition often varying with temperature. Since turbine vanes and blades operate over a range of temperatures, it can be most beneficial to include multiple active elements within an overlay system in order to take advantage of their synergistic effects, thereby maximizing the oxidation/corrosion resistance [8,16].

The formation of a protective TGO as a result of isothermal oxidation on a bare bond coat alloy surface can be categorized into three distinct stages: a transient stage, a steady-state stage, and a breakaway stage. In the transient stage, all possible (thermodynamically stable) oxide phases can be formed, depending on the alloy composition and the oxidation conditions. The steady-state stage consists of the transformation of the bulk of the transitional oxides to a long-term phase. The breakaway stage consists of the failure of the steady-state scale, consisting of the long-term phase constituent, that leads to the subsequent formation of oxides that offer lesser protection to the substrate. The time required to reach this breakaway stage is the limit to the useful lifetime of the TBC system, after which failure of the entire coating system occurs [10]. The transient oxidation stage is particularly significant for multiphase MCrAlY-type alloys, as the different phases tend to have varying aluminum contents. Exposure of these varying phases to high-temperature air environments typically results in the formation of a transient and heterogeneous scale, which consists of a variety of oxides such as stable and metastable aluminum oxides, chromium oxide and various spinels. While stable α -Al₂O₃ eventually becomes the dominant oxide in the TGO layer, the stresses resulting from the transformation of transitional oxides to the alpha phase can again lead to crack formation and TBC system failure [10,17–19].

In the following sub-section, the major bond coat failure modes that have been most commonly reported in literature are described briefly.

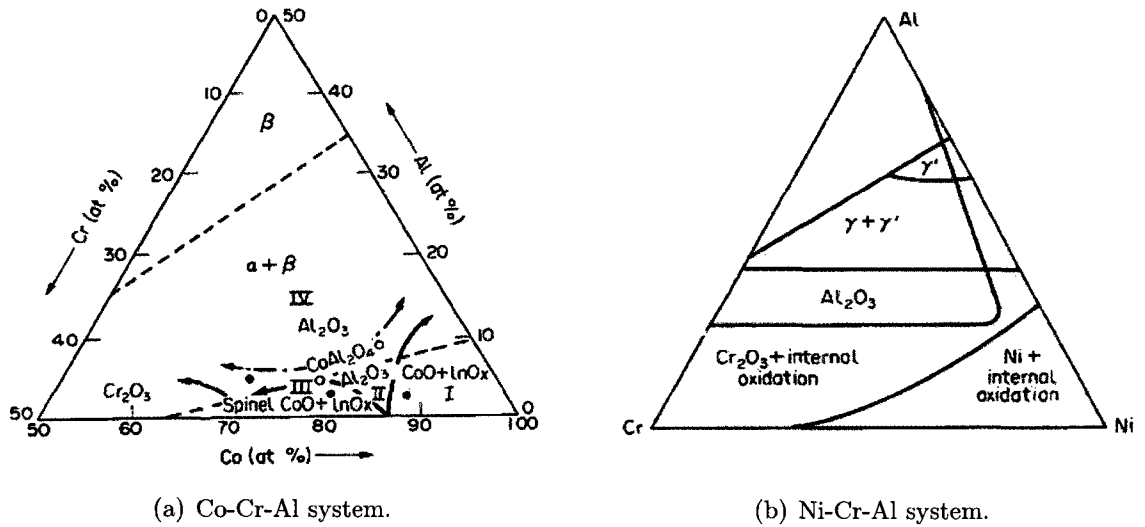


Figure 14: Oxide stability maps for 1000°C isothermal oxidation in air [16].

Table 2: Ductile-to-brittle transition temperatures at 1% strain to crack for various aluminide an overlay coating systems. Adapted from [16]).

Material	DBTT at 1% strain to crack (°C)
Ni-35Al	740
Co-35Al	970
PtAl ₂	870-1070
Ni ₂ Al ₃	570-710
NiAl	868-1060
Ni ₃ Al	730-900
Co-15Cr-9Al-Y	230-250
Co-18Cr-11Al-Y	440-470
Co-20Cr-12.5Al-Y	660-680
Co-23Cr-12Al-Y	740
Co-27Cr-12Al-Y	910
Ni-38Cr-11Al-Y	430

Bond Coat Failure Modes

The failure modes experienced by a particular bond coat depend largely on its type, method of deposition, elemental composition, and the application in which the coated component is used. A component that is part of a propulsion system or peak power generation system will experience a greater number of thermal cycles (startup-operation-shutdown), whereas full-time power generation systems operate predominantly in an isothermal mode for long periods of time (few thermal cycles) [31]. Figure 15 shows a schematic representation of five of the major failure categories that have been most commonly suggested and described in literature. Evident from Figure 15 is that all five failure categories lead to the spallation of the TGO and the overlaid ceramic insulation layer, resulting in the loss of thermal and oxidation/corrosion protection afforded to the structural component alloy by the TBC system as a whole.

- Category 1 failure occurs due to aluminum depletion from the bond coat as a result of excessive spallation-TGO regrowth cycles. The lack of aluminum activity leads to the formation of porous, non-protective spinels that ultimately cause spallation from inside the TGO [16,31].
- Category 2 failure occurs by the outward diffusion of nickel from the bond coat (or potentially even the superalloy substrate) leading to the formation of spinels that, in turn, lead to coat spallation.
- Category 3 failure is thought to be caused by imperfections in the TGO that act as local stress raisers, leading to an increased propensity for crack formation when a critical stress level is achieved [10,31].
- Category 4 failure is referred to as 'rumpling' or 'ratcheting' of the TGO, which is a displacement instability caused by exposure to thermal cycling events at high temperatures. Thermal cycling at high temperatures causes an increase

in TGO thickness, resulting in misfit strains in both TGO-bond coat and TGO-ceramic insulating layer interfaces. Excessive strains lead to crack nucleation and propagation, leading to spallation [10, 15, 31].

- Lastly, category 5 failure is prompted by foreign object damage by an impacting particle that is thought to lead to the formation of an area of increased temperature exposure, ultimately leading to crack formation and coating spallation [31].

In the following sub-section, the concept of pre-oxidation heat treatments to generate a TGO on top of the bond coat before the component enters into service is introduced. The pre-oxidation heat treatments are intended to delay the onset of some of the failure modes listed above, allowing for improved TBC system lifetimes and increasing component life as a result.

Pre-oxidation Heat Treatments

It has been suggested that pre-oxidation heat treatments in a low-pressure oxygen environment could serve to preferentially form a largely continuous aluminum oxide TGO between the bond coat and the ceramic insulating top coat before the coated component is placed into service. This would be in contrast to the preferential formation of chromium oxide, spinels ($\text{Ni}(\text{Cr},\text{Al})_2\text{O}_4$), and nickel oxide (NiO) that has been shown to form alongside the aluminum oxide TGO in thermally-sprayed TBC systems. This pre-oxidation heat treatment could occur either between bond coat deposition and TC deposition, or after deposition of both bond coat and TC layer, but before the component is put into service. As TBC system failure is almost exclusively linked to the excessive growth of the TGO, forming a continuous diffusion barrier of aluminum oxide before putting the component into service would significantly delay the oxidation reaction kinetics from the onset of oxidation and subsequently increase

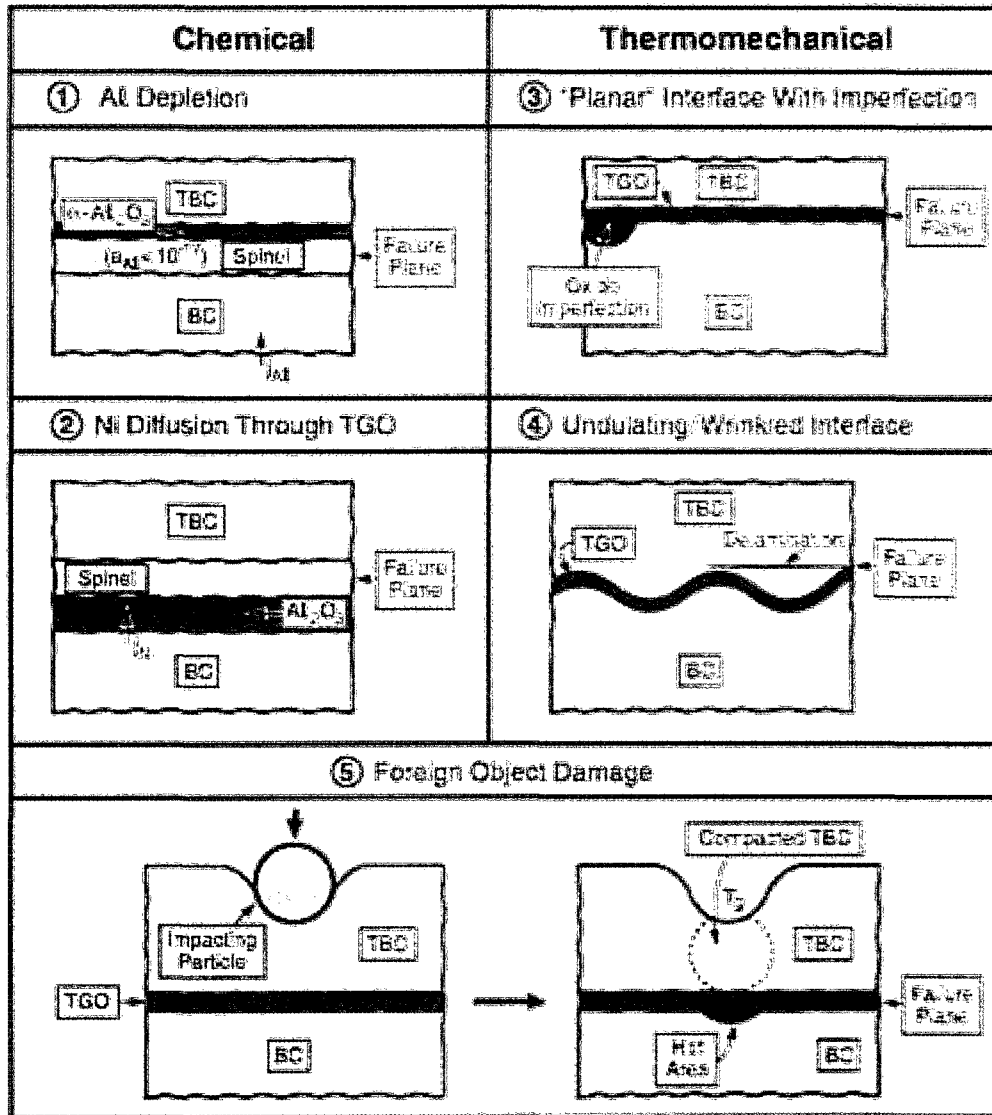


Figure 15: Five of the major failure categories documented in literature for TBC systems [31].

the component's service lifetime.

The following experimental work [32–36] suggests that significant gains in overall lifetime of the TBC system can be achieved through pre-oxidation heat treatments. For MCrAlY-type materials, it has been shown that a layer of metastable θ -Al₂O₃ forms in the earlier stages of oxidation, at temperatures below about 1100°C. This is followed by a transformation to α -Al₂O₃ after an extended period of exposure at high temperature [23].

Previous research into bond coat pre-oxidation heat treatments [32–36] has suggested that a nearly or fully continuous α -Al₂O₃ TGO of approximately 1–3 μ m in thickness can be formed by subjecting bond-coated substrates to a pre-oxidation heat treatment. The heat treatment temperatures ranged between 1000–1100°C and were performed in both vacuum and air furnace environments.

Lih et al described an optimal pre-oxidizing vacuum furnace heat treatment of 1000°C for 50 hours for a NiCrAlY (AMDRY 962 or similar) coated Mar-M247 substrate resulting in the formation of a 'healing layer' of predominantly protective aluminum oxide of 2–3 μ m average thickness, resulting in a significant increase in coating system life in cyclic oxidation conditions as compared to as-deposited (not pre-oxidation heat treated) samples [32].

Nijdam et al has suggested heating for 1–5 minutes at 1100°C in an inert atmosphere as a pre-oxidation heat treatment, followed by 2–4 hours at 1100°C and an oxygen partial pressure of 100 Pa for a NiCoCrAlY bond coated Rene N5 substrate alloy.

Heating in an inert atmosphere allows for the development of an aluminum-rich layer on the bond coat surface. During the pre-oxidation heat treatment, the oxygen partial pressure must be maintained high enough to allow for beneficial yttrium-rich peg formation that results in mechanical keying of the TGO to the bond coat, as well as to improve the nucleation of θ -Al₂O₃ (instead of α -Al₂O₃) at the bond coat surface.

Through prolonged oxidation, the transformation from the θ - Al_2O_3 to α - Al_2O_3 will achieve a larger grain size and, for this reason, the TGO will grow at a relatively low rate, leading to longer coating system lifetimes [33].

Chen et al suggest a pre-oxidation treatment for CoNiCrAlY/8 wt%-YSZ-coated Inconel 625 disks consisting of a 45 minute heating at 1050°C and an oxygen partial pressure of 0.01–0.1 Pa to promote the growth of a nearly continuous aluminum oxide layer between the bond coat layer and the thermally-insulating top coat layer. With these heat treatment conditions, the formation of nickel-aluminum oxides and nickel oxides was suppressed. This would allow for the formation of a TGO consisting primarily of aluminum oxide, which is thought to contribute to a higher cyclic oxidation lifetime of the coating system [34].

The following sub-section introduces the thermally-insulating, ceramic top coat (TC) layer that completes the TBC system. Application techniques of TC layers is briefly described, together with a description of the material requirements of an ideal TC layer. Yttrium oxide-stabilized zirconium oxide (YSZ), the most common industrially applied TC layer material, is described in terms of physical properties, material structure, and limits to its application as a result of some of these properties.

2.1.3 Top Coat (TC)

A ceramic top coat layer is generally the uppermost layer in the thermal barrier coating system structure. Commercially, the thermal insulation layer is typically applied over the bond coat via thermal spray processes such as air plasma spraying (APS) and vacuum plasma spraying (VPS), or through electron beam physical vapour deposition (EB-PVD) [10,37]. The function of the thermally-insulating top coat layer is to reduce the effective surface temperature of the substrate material as a result of exposure to the hot combustion gas environment.

To perform this function, it must be made of a material that has excellent high-temperature microstructural stability, low thermal conductivity, and good chemical compatibility and adherence to the underlying TGO. The TC layer is designed to include a microstructure that provides low in-plane stiffness and strain tolerance through spatially configured porosity [10, 15]. The preferred material for use as a thermally-insulating TC layer in modern gas turbine hot section components is yttrium oxide-stabilized zirconium oxide (YSZ) due to its low and stable thermal conductivity over a wide temperature range. Zirconium oxide experiences a phase transformation from cubic to tetragonal ($\sim 2370^\circ\text{C}$), followed by a martensitic transformation from tetragonal to monoclinic upon cooling (between 1170 and 950°C) [16]. The transformation from tetragonal to monoclinic is accompanied by undesirable microcracking due to a 4–5% volume change [10, 16]. The addition of a stabilizing dopant such as yttrium oxide (Y_2O_3) to zirconium oxide depresses the phase transformation temperature and promotes the formation and retention of a metastable, non-transforming tetragonal (t') phase through quenching from high temperature. The optimal composition of 7 wt% yttrium oxide-stabilized zirconium oxide (7-YSZ) has been shown to achieve the greatest number of thermal cycles until coating spallation failure [15, 38].

As higher engine operating temperatures are pursued, there are several factors that will limit the use of YSZ as a TC material. The toughness of the YSZ coating is dependant on its structure; cubic structures exhibit very low fracture toughness ($\sim 6 \text{ J/m}^2$), while the partially stabilized tetragonal compositions such as 7-YSZ have much higher fracture toughness ($\sim 300 \text{ J/m}^2$) [15]. To avoid microcracking, which ultimately leads to coating failure through spallation, YSZ compositions are selected so that they allow for a t' phase that is stable below the desired component operating temperature. Depending on the operating temperature for a particular application, however, the quantity of the stabilizer solute required to ensure that enough t' phase remains upon

cooling of the top coat may exceed the solubility limit for that stabilizer [10, 15]. While remaining to be synthesized in practice, research into the ternary $\text{ZrO}_2\text{-YO}_{1.5}\text{-TaO}_{2.5}$ system has shown the potential of achieving a tetragonal phase that does not decompose below 1500°C and has a toughness that is greater than or at least equal to that of the 7-YSZ composition [15].

In summary, this section has outlined the three typical main constituents of modern gas turbine engine hot section components, which include the component's structural material, the bond coat, and the thermally-insulating top coat. The bond coat, the primary focus of this thesis work, is further described in terms of coating function, aluminum oxide TGO growth, MCrAlY materials, failure modes, and pre-oxidation heat treatments. The following section introduces thin film sensor technology with a focus on its application in the instrumentation of hot section components. The section begins with a general overview of thin film sensor technology, followed by two potential applications of thin film sensor systems in gas turbine engines (aero-engine testing and engine health monitoring), together with the particular operating requirements of these sensor systems. Typical thin film sensor assembly layouts for instrumented hot section components are described, followed by an overview of the National Aeronautical and Space Administration's (NASA) experiences with thin film sensor technology on hot section components.

2.2 Thin Film Sensors

Thin film sensors are electrically-based measurement devices with an overall thickness of only a few micrometers, which are applied to the surface of a component where various physical properties are of interest. These sensors may be applied to numerous substrate materials of diverse shapes and sizes. In general, the gauge layer consists of a metallic compound with material properties suited to measuring a particular

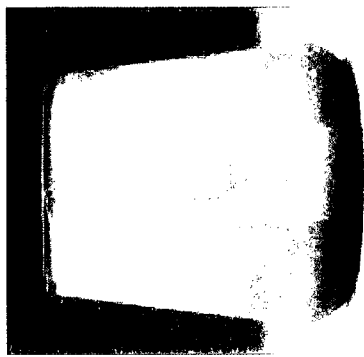
physical property of the substrate component being tested. The sensors' gauge material configuration is sensitive to the condition that is to be measured and produces a change in electrical potential, resulting in a potential difference when the measured condition changes in the sensors' immediate vicinity. This electrical signal can then be extracted from the component-mounted sensor through various means, and analyzed by test instrumentation or by feedback control hardware.

This section outlines the advantages of thin film sensors over conventional sensors that are currently employed, followed by a description of two thin film sensor applications in gas turbine engines: gas turbine aeroengine test instrumentation and engine health monitoring, followed by the operational requirements of the thin film sensors in these two related applications. Additionally, typical thin film sensor assembly layouts for use in hot section component instrumentation applications are reviewed. This is followed by a summary of the National Aeronautical and Space Administration's (NASA) experiences and problems with thin film sensors that have been designed for aerospace propulsion applications. Figure 16 shows a wide variety of thin film sensor types that been developed by NASA for various applications.

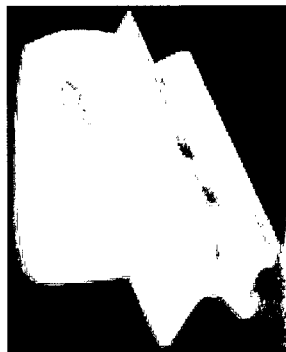
2.2.1 Advantages of Thin Film Sensors Over Conventional Sensors

Thin film sensors offer several advantages over conventional sensors, predominantly due to their comparably smaller physical dimensions. Reduced sensor size can lead to simpler and more cost-effective installation on a component, and provides a more accurate sampling of the particular property the sensor is designed to measure.

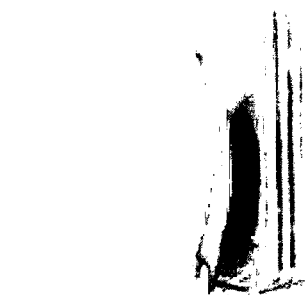
Thin film sensors are intended to be applied to the instrumented component in such a way as to avoid significant component modification, minimizing or eliminating altogether the introduction of flaws or stress concentrations into the component that



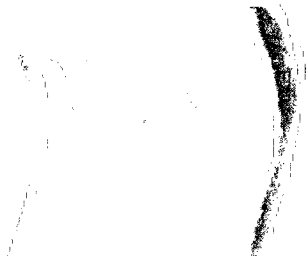
(d) Thermocouple on SiC/SiC combustor liner.



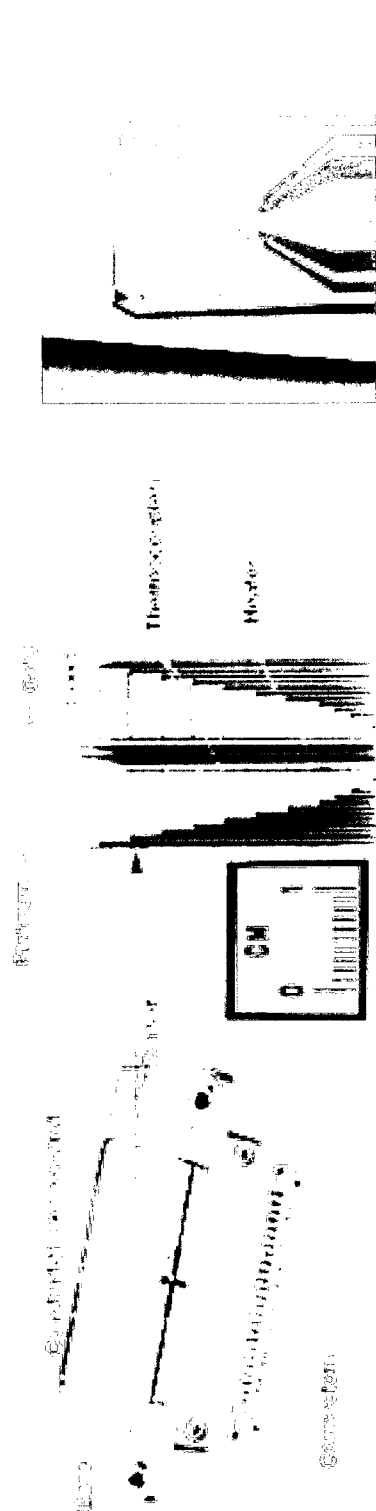
(e) PdCr dynamic strain gauge on silicon nitride turbine blade.



(b) Thermocouple on SSME turbopump blade.



(a) Heat flux sensor on SSME turbopump blade.



(c) Large-size thermocouple boundary layer rake for flow sensing.



(f) Multifunctional sensor consisting of Pt rosettes, a type-R thermopile heat flux sensor and thermocouple.

Figure 16: Various NASA applications of thin film sensors [39, 40].

will weaken the structure and compromise its performance [41,42]. To ensure reasonable measurement accuracy, conventional sensors may require extensive modification of the instrumented component to properly mount the sensor, depending on their placement on a component or assembly.

Due to their relatively small size, with sensor thicknesses measured on the micron scale, thin film sensors add negligible mass to the component being instrumented. The minute size of the sensor system is intended to cause minimal interference to the operational thermal, strain, and vibrational phenomena to which the instrumented component is usually subjected to, while providing accurate sensing of the desired point of instrumentation [41,43,44]. Due to their size and nature of their installation, these sensors have also shown promising response times, on the order of milliseconds [44].

An added benefit of the microfabrication techniques used to produce thin-film sensor technology is the ability to manufacture a large quantity of sensors onto a transfer substrate, where each of the individual sensors can be separated and packaged individually [41].

2.2.2 Thin Film Sensor Applications in Gas Turbine Engines

Due to the substantial benefits achievable through the application of thin film sensors over conventional sensors, as described in the previous sub-section, two key applications have been suggested for use in gas turbine aeroengines: engine testing and certification, and real-time engine health monitoring.

The increased level of competition in today's gas turbine aeroengine industry has led the manufactures to become interested in exploring and developing the implementation of thin film sensors in engine test instrumentation as a way to decrease the cost of engine testing and to qualify engines more quickly.

Environmental, commercial viability, and budgetary pressures have also led gas

turbine aeroengine operators, such as commercial airlines and military operators alike, to express interest in the application of similarly-placed thin film sensors for a long-term engine health monitoring. These thin film sensor systems allow for real-time monitoring and of engine operating parameters, permitting the optimization of fuel usage, the facilitation of maintenance scheduling, and an improvement in the safe operation of gas turbine engines in practice.

The first application can be seen as a precursor to the second application, relying on a maturation and commercialization of the thin film sensor technology in order to make it viable for long-term, reliable, and affordable implementation in gas turbine engines.

Gas Turbine Aeroengine Testing

Before certification, all new gas turbine aeroengine designs are subjected to validation testing. These tests are used to certify the flight worthiness of the engine, as well as to confirm overall engine performance criteria [45]. The cost of engine development and certification is on the order of hundreds of millions of dollars per engine program, taking 18 to 36 months to complete, and requiring up to six complete engines for testing.

Currently, these engine tests require instrumentation with between 1000 and 3000 individual sensors that are placed in areas of interest on the test engine. The requirement for a large quantity of sensors is partly due to poor sensor reliability, requiring sensor redundancy, and limited operational lifetimes of the individual sensors themselves [45]. The added cost of instrumentation (including labour and components) is substantial, amounting to approximately 25% of the cost to manufacture each engine. The installation of a typical conventional strain gauge is estimated to require eight hours of highly skilled labour.

An evolving gas turbine propulsion market is forcing competitors to employ novel

solutions to manufacture engines that have consistently improved reliability and efficiency at a competitive price. The efforts of cost reduction on the test and evaluation component of an engine development program are characterized by fewer engine tests while increasing the quantity of test data extracted per test and a reduction to the total number of sensors required [45]. The implementation of non-intrusive, durable and reliable thin film sensors are a viable contribution to this goal.

Engine Health Monitoring

Substantial cost savings can be achieved as a result of the implementation of an intelligent control system technology in a modern gas turbine engine system, using real-time signals from a thin film sensor-instrumented engine.

This intelligent control system serves to reduce component life cycle costs and optimize engine performance by providing real-time diagnostics and prognostics of engine operating parameters [46–48]. The system’s diagnostics action will serve to identify failing components or sub-systems in the engine while the prognostics action serves to predict impending failure in these same components or sub-systems. The system’s prognostics action might also be used to delay or prevent the failure of these components by implementing a control function. This control function makes use of engine system feedback to optimize engine operational performance, maximize system efficiency, and reduce the requirement for system maintenance [49].

Using a gas-path performance analysis based on data collected from thin film sensor-instrumented components, real-time operating parameters can then be compared to a historical baseline model for that particular engine. This data could then be analyzed for potential engine faults or performance deterioration, indicating a requirement for component repair or replacement, or even complete engine removal from service [50].

Current health management techniques of existing aircraft fleets often rely on a

'total accumulated cycles' system in which the aircraft components are permanently removed from service either after a set number of operating cycles or based on a time limit derived from statistically-generated fleet data. A system based on real-time monitoring of component usage to estimate remaining component lifetime allows for on-condition maintenance, providing for longer service lifetime per component and lower overall engine life cycle costs in comparison to current methods [50].

The additional cost of monitoring engine parameters, however, does not consist of the sensor cost alone, but it also includes the expense of ancillary equipment associated with the thin film sensor installation, such as lead wire routing, as well as signals processing hardware and software [47]. For this reason, there is a motivation toward the development of non-intrusive, reliable, durable, multifunctional smart sensors that provide a wealth of information for complete engine diagnostics, prognostics and active control. The greatest impediment thus far to real-time estimation of health parameters in flight, however, is simply the non-existence of engine sensors that are able to provide the required data in a reliable manner for the duration of the instrumented component's service life [47]. The following sub-section describes some of the operational conditions faced by thin film sensor systems that are intended for use in the instrumentation of hot section components in gas turbine engines.

2.2.3 Thin Film Sensor Operational Requirements

The operational conditions inside a modern gas turbine engine are extreme and require the utmost in hardware performance capability. Thin film sensors mounted along the gas path inside the combustor and turbine section must withstand temperatures approaching 1500°C, which may be coupled with high centripetal loadings due to the substantial rotational speeds for the turbomachinery. Surface-mounted thin film sensors will come into contact with an erosive combustion gas stream yielding flow velocities in the range of 30–60 m/s, in addition to the aerodynamic forces and particle

impingement that accompany this flow [6]. Sensors must also be resistant to the degradative effects as a result of long-term immersion in a harsh, high-temperature, oxygen-rich, combustion product atmosphere. The thin film sensor system must be able to transfer the signal generated by the sensor to the measurement circuit outside the core of the engine. This resistance entails the transfer of the signal from the static or rotating component on which the sensor is mounted, through an environment that contains a significant presence of relative motion between metal bodies as well as other sources of electrical noise. In the case of engine testing, a lifetime of just a few hundred hours might be acceptable, however, the application of a continuous component monitoring sensor on a hot section component in a gas turbine engine, will require a highly reliable operational life similar to that of the component (10,000–100,000 hours).

2.2.4 Typical Thin Film Sensor Assembly Layout

In this sub-section, the constituents of typical thin film sensor prototype layer assemblies developed by both the American National Aeronautical and Space Administration (NASA) and the French Office National d'Études et Recherches Aéropatiales (ONERA) are presented. Both prototype installations involve the placement of a thin film thermocouple or strain gauge sensor onto hot section components in aerospace propulsion applications. Finally, a table summarizing the typical steps of a NASA thin film sensor assembly procedure using various microfabrication techniques is listed.

Depending on the nature of the sensor and the substrate material, the sensor assembly will consist of several thin material film layers that perform essential functions to allow for the desired sensor operation. Since thin-film sensors typically generate electrical signals, it is required to electrically insulate the sensing layer from a conductive substrate to prevent a shorting connection to ground. For this reason, a ceramic

layer with adequate resistivity and stability at high temperatures is commonly overlaid onto a conductive substrate to act as an electrical isolator.

Aluminum oxide (Al_2O_3) is preferred as a base coat for thin film sensor applications due to its high stability at elevated temperatures, with a bulk material melting temperature of 2054°C and a resistivity of approximately $5\text{E}7\Omega\text{-cm}$ at 1100°C [40,42]. In the case of instrumenting modern hot section components made of nickel-base superalloys (such as combustor liners or turbine blades/vanes), there generally exists a layer structure consisting of the substrate that is usually coated with an aluminum oxide TGO-forming bond coat layer. In this case, the aluminum oxide TGO would serve two functions: both as a diffusion barrier and an electrically-insulating layer. While hot section components usually include a ceramic, thermally-insulating top coat layer as well, NASA and ONERA thin film sensor prototypes have only considered a conductive MCrAlY bond coat material layer on top of a superalloy structural blade material substrate. Typical cross-sections of the thin film sensor layer structure are shown in Figures 17 and 18 [39,43]. Both NASA and ONERA prototypes make use of an aluminum oxide insulating layer. If the sensor is to be placed onto a non-conductive substrate material, this step can be omitted.

The next layer consists of the sensor's gauge material, the sensing layer. This is the layer in the sensor assembly that generates the electrical signal that will later be processed by the sensor system's measurement circuit. The exact patterning of the sensor layer will depend upon the type of sensor being applied and the physical property that is to be measured. Provisions must also be made to allow the sensor signal to be transferred to lead wires followed by trunk signal wires that complete the circuit to the test instrumentation. For both NASA and ONERA prototypes, this has been typically done by extending the sensor material layer away from the sensing location and providing an enlarged area for sensor signal extraction through means of clamping or physical/chemical bonding of a lead wire to the sensing material layer

[41, 43]. A final layer of insulating material such as aluminum oxide, if required, may be deposited as a top coat onto the sensing layer in order to provide supplementary protection from oxidation and erosion due to environmental conditions.

Figure 19 presents an example of NASA's thin film thermocouple prototype mounted to a flat substrate, showing the enlarged lead pad areas for sensor signal extraction at the far left and the platinum versus platinum-rhodium thermocouple junction at the far right. A schematic representation of ONERA's thin film strain gauge installation onto a turbine blade is shown in Figure 20. To note in this installation is the extension of the platinum 'tracks' from the NiCr strain gauge, down to the root of the blade where it is bonded with ceramic cement to 70 μm nickel trunk wires. These trunk wires, which are spot-welded to the rear face of the blade and led off to the measurement circuit, are sheathed in stainless steel casing that is filled with magnesium oxide powder insulation.

Due to the necessity of producing multilayer thin films and features on the micron scale, thin film sensor microfabrication techniques are typically developed from experiences in the semiconductor microelectronics industry. These microfabrication processes include physical vapour deposition (PVD), photolithography, and parallel-gap welding. Table 3 provides a summary of typical multi-step manufacturing processes used by NASA for their thin film sensor prototypes.

2.2.5 NASA's Thin Film Sensor Experiences

The majority of published research regarding thin film sensors for aerospace propulsion applications has been performed by the National Aeronautical and Space Administration (NASA). This research began in the early 1980s with simple thin film sensor prototypes on flat substrates made of the nickel-base superalloy Mar-M246 (Figure 19). These assemblies were subjected to extreme thermal shock conditions in NASA's hydrogen-oxygen rocket lab facility, experiencing temperatures of 900–1100°C for

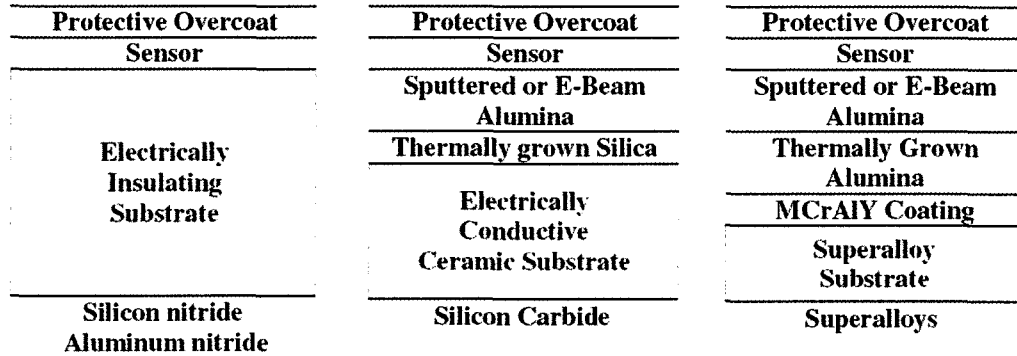


Figure 17: Cross-sectional layouts of NASA thin film sensor assemblies for the instrumentation of hot section gas turbine engine components. [39].

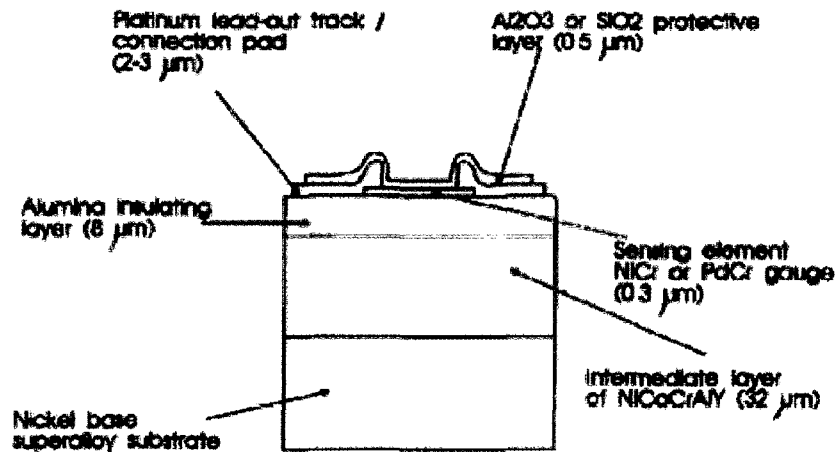


Figure 18: Cross-sectional layout of ONERA thin film sensor assemblies for the instrumentation of hot section gas turbine engine components. [43].

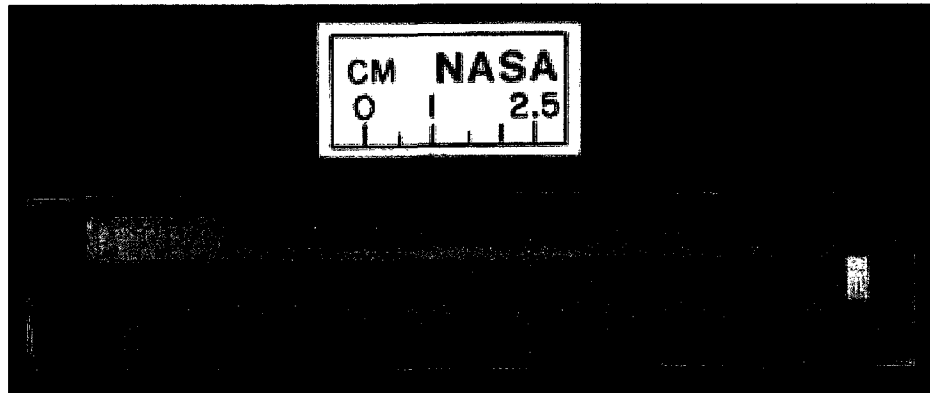


Figure 19: Flat substrate prototype of NASA platinum/platinum-13%rhodium thin film thermocouple sensor [41].

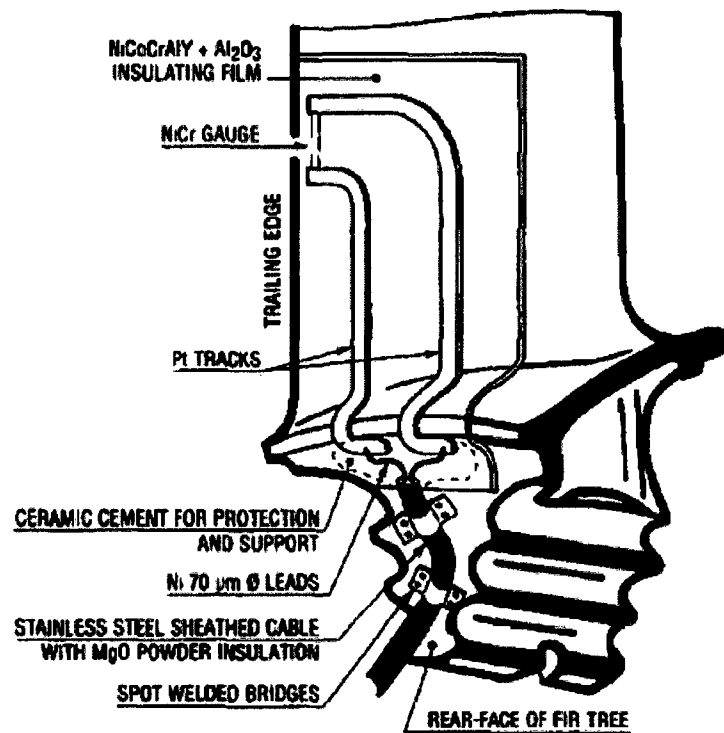


Figure 20: Layout of ONERA's prototype thin film strain gauge-instrumented turbine blade [43].

Table 3: Summary of NASA thin film sensor assembly manufacturing processes [40–44, 51, 52].

Manufacturing Step	Process(es) Used	Notes
1. Bond coat deposition	<ul style="list-style-type: none"> • PVD (magnetron sputtering, electron beam) 	<ul style="list-style-type: none"> • Optional glass peening operation to increase bond coat density • Optional grit-blasting of deposited BC surface to increase mechanical interlink between BC layer and TGO
2. Bond coat pre-oxidation heat treatment	<ul style="list-style-type: none"> • Heat treatment in air at 1100°C to produce Al₂O₃ TGO layer of approximately 1–3μm 	<ul style="list-style-type: none"> • Thorough cleaning in microsoap and de-ionized water before pre-oxidation heat treatment.
3. Deposition of additional Al ₂ O ₃ layer	<ul style="list-style-type: none"> • PVD (magnetron sputtering, electron beam) 	<ul style="list-style-type: none"> • To ensure good sensor performance, the Al₂O₃ layer must be free of macroscopic defects such as pores and discontinuities
4. Sensor layer deposition	<ul style="list-style-type: none"> • PVD (magnetron sputtering, electron beam) • Shadow mask stencilling process, photolithography 	<ul style="list-style-type: none"> • Deposition of 3–4μm thick sensing layer • Substrate holder was cooled to 0°C • Oxygen-enhanced sputtering mode used for first 0.1–0.2μm
5. Deposition of protective Al ₂ O ₃ overcoat	<ul style="list-style-type: none"> • PVD (magnetron sputtering, electron beam) 	<ul style="list-style-type: none"> • A protective layer of approximately 2–3μm can increase sensor survivability by protecting against the high-temperature, oxidative environment and erosion
6. Sensor assembly annealing heat treatment	<ul style="list-style-type: none"> • Heat treatment in vacuum furnace at 1000°C for 20 hours 	<ul style="list-style-type: none"> • Relieve any stresses remaining from the manufacturing process
7. Bonding measurement circuit lead wires to the sensing layer	<ul style="list-style-type: none"> • Parallel-gap welding • High-temperature cement application with strain-relief loops • Rokide flame spraying • ARCJoint process 	<ul style="list-style-type: none"> • To ensure durable connection between sensor and measurement circuit through temperature, pressure, and vibrational transients

short periods of time without any temperature ramping [41]. This thin film thermocouple concept was further developed for installation onto a Space Shuttle Main Engine turbopump blade (Figure 16a) and exposed to a simulated hydrogen/oxygen-rich atmosphere in NASA's Turbine Blade Testing Facility that is capable of producing a temperature of 930°C at the blade row inlet, with combustion gas pressures up to 16.5 MPa [53]. Further research into thin film sensors then branched out to non-metallic substrate types such as hydridopolysilazane fibre / silicon carbide ceramic matrix composite panels and cylinders, silicon nitride turbine blades (Figure 16c), and silicon carbide combustion liners (Figure 16d) [42, 54]. The majority of these components were evaluated in a jet fuel-fired burner rig, producing gas temperatures around 1500°C at combustion gas pressures between 0.7–2 MPa [42]. Most recently, the limitation of gauge material accuracy at extreme temperatures has led NASA to investigate the development of ceramic gauge material layers, albeit without much success [55].

Overall, NASA test results for the metallic, thin film thermocouple concepts indicated that overall structural strength and adhesion of the sensor layers to the substrate were adequate for their intended design purposes in all but the most extreme environmental conditions, such as those simulated in the hydrogen-oxygen rocket lab facility.

Regardless of sensor materials or sensor layer fabrication techniques used, however, the greatest issue regarding NASA's thin film thermocouple sensor designs was the recurrent problem of poor bonding between the lead wires and sensor lead pads, resulting in an intermittent or complete loss of the sensor signal. This loss of signal was attributed to the cyclic conditions of high pressure, high temperature and intense vibration to which the sensor system was subjected during testing, resulting in separation of the lead wires from the sensor lead pads [42, 44, 53].

Another technical issue regarding NASA thin film thermocouple design was drift

in the sensor signal that occurred during repeated, lengthy exposure to high temperature environments. This drift was thought to be caused by the degradation of the sensor layer material as a result of interdiffusion between the sensor elements and the protective oxide scale, the exposure to erosive, high velocity combustion product particulates, and the oxidation of the rhodium components in the gauge material [56]. It was observed that sensor drift varies with sensor film thickness and lead wire diameter, the temperature gradient between the thin film and the lead wire, and the absolute temperature of the substrate material [42, 51]. The problem of sensor drift will effectively limit the useful lifetime of a sensor at particular environmental and temperature conditions, especially in long-term monitoring applications.

Fluid machinery components, such as those found in hot sections of gas turbine engines, depend on complex geometry to perform their intended duties. As a result, they are often formed into complex shapes that vary greatly in all three dimensions, further complicating line-of-site material deposition techniques that are currently used to deposit the individual sensor layers onto the instrumented component's surface. To this end, patterning techniques, such as photolithography or other similar processes, must be refined in conjunction with advances in thin film deposition technologies to allow for the fabrication of sensor layer assemblies on a wide variety of complex components at an affordable cost.

In summary, thin film sensor technology for use in the instrumentation of hot section components in gas turbine engines is still very much in its infancy. Thin film deposition processes, such as sputtering and electron beam physical vapour deposition, have been proven in laboratory settings to produce adherent sensor layer structures on a variety of metallic and non-metallic substrates that survive the harsh conditions. Key issues, however, such as sensor fabrication and installation cost, together with a deficiency in reliable sensor signal extraction from the sensor, and the long-term effects of sensor gauge material degradation as a result of exposure in harsh

combustion gas environments, must still be resolved before this technology can make the transition from research into industrial applications.

Chapter 3

Research Objectives

The objectives of the presented work are the following:

1. Observe the effects of selected vacuum furnace and air furnace heat treatments on MCrAlY-coated nickel-base superalloy substrate. The nickel-base superalloy is Hastelloy-X alloy. The three different applied MCrAlY coating types include FeCrAlY, NiCrAlY, and CoNiCrAlY, that are deposited with magnetron sputtering physical vapour deposition (MS-PVD), air plasma spray (APS) deposition, and high-velocity oxy-fuel (HVOF) spray deposition, respectively.
2. Assess the heat treated test specimens in terms of their suitability to host the installation of a thin film sensor that is currently being developed by the National Research Council (NRC).

Chapter 4

Materials and Experimental Procedures

To study the effect of pre-oxidation heat treatments on the formation of surface oxides, three different MCrAlY coatings were deposited onto a nickel-base superalloy substrate and subjected to a set of isothermal heat treatments in both vacuum and atmospheric air furnace environments.

This chapter describes the materials and experimental procedures used in this work, beginning with a description of the test specimen structure. The specimens tested consisted of a nickel-base superalloy substrate of Hastelloy-X that was coated with one of three MCrAlY-type overlay bond coats, which were applied by one of three deposition processes (Figure 21). The Hastelloy-X substrate material, as well as the three MCrAlY materials (FeCrAlY, NiCrAlY, and CoNiCrAlY) are described, as well as a listing of feedstock materials used in this work.

The test specimen description is followed by the introduction to the deposition processes used to apply the MCrAlY materials; cathodic arc and magnetron sputtering physical vapour deposition (PVD), and air plasma spray and high-velocity oxy-fuel spray (both thermal spray) processes. Individual deposition processes are introduced according to their basic principle of deposition, followed by a more detailed examination of the nuances of each deposition process used in this work. Coating equipment and processing parameters used for this work are listed.

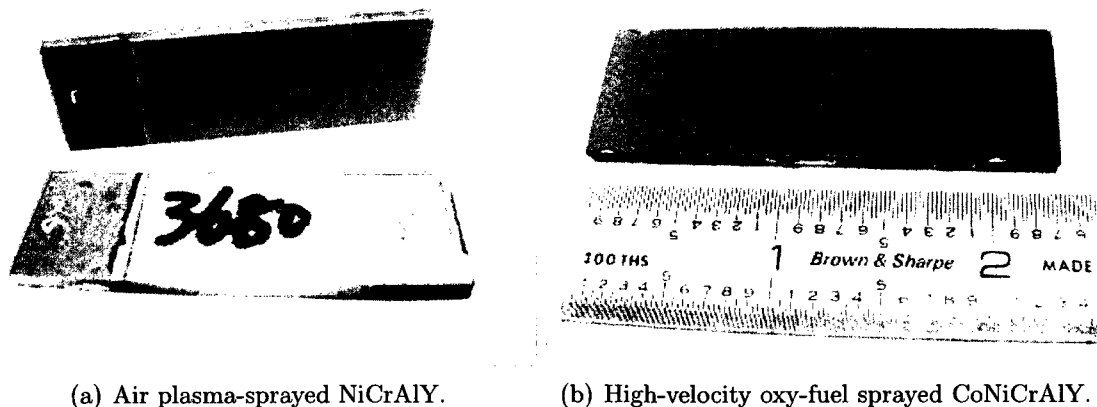
Before and after bond coat deposition, surface processing procedures were applied to both the substrate surface and coated surface, respectively, to promote improved substrate-coating adhesion during bond coat deposition, and to encourage the formation of a uniform and continuous thermally-grown oxide (TGO) during a post-deposition heat treatment. These surface processing procedures are described, together with a rationale explaining the desired result.

After bond coat deposition and surface processing procedures were completed, the test specimens were subjected to a set of isothermal heat treatments in both an atmospheric air furnace and a vacuum furnace. These pre-oxidation heat treatments were designed to investigate the formation of oxides on the three different MCrAlY-coated samples, with the objective of establishing a protective surface oxide consisting of α -Al₂O₃. Heat treatment equipment used in this work, as well as the heat treatment conditions, are listed.

The test specimens were examined in both initial and heat-treated conditions and were analyzed with a variety of techniques. These included microscopic analysis (optical and scanning electron microscopy) for surface and cross-sectional morphological features, as well as energy dispersive spectroscopy and x-ray diffraction analysis to examine the compositional element distribution in the test specimens. A complete listing of equipment used in the examination of the test specimens is provided, together with those required for sample sectioning and preparation for microscopic analysis.

4.1 Test Specimen Structure

The specimens tested consisted of a nickel-base superalloy substrate of Hastelloy-X that was coated with one of three MCrAlY-type overlay bond coats, which were applied by one of three deposition processes. The MCrAlY bond coats consisted of



(a) Air plasma-sprayed NiCrAlY.

(b) High-velocity oxy-fuel sprayed CoNiCrAlY.

Figure 21: Test specimens: MCrAlY-coated Hastelloy-X substrates.

FeCrAlY, NiCrAlY, and CoNiCrAlY, and were deposited by magnetron sputtering PVD, air plasma spray, and high-velocity oxy-fuel spray, respectively. This section begins with a description of the Hastelloy-X substrate material, including the reasoning for its selection, the specifications of the substrate coupons, a listing of relevant materials properties, and a brief listing of common commercial uses of Hastelloy-X in high-temperature applications. This is followed by a description of the three MCrAlY overlay materials used in this work, beginning with a historical development of FeCrAlY alloys from binary FeAl alloys, the use of FeCrAlY materials as overlay bond coats and their theoretical advantages over other MCrAlY materials, and the findings of some preliminary FeCrAlY coating work. A relative comparison between NiCrAlY and CoCrAlY materials is presented, followed by a description of the feedstock materials used in this work.

4.1.1 Hastelloy-X Substrate

The substrate selected for this study was the Hastelloy-X alloy (Haynes International). This substrate alloy was selected to match the one used as the structural material of the combustor liner found in the Rolls-Royce/Allison T56 turboshaft engine (Figure

22), the same component is to host the installation and testing of a thin film thermocouple sensor. This sub-section begins with a brief description of the dimensions of the Hastelloy-X coupons that serve as the substrate for the subsequent MCrAlY bond coat material, followed by an outline of pertinent material properties of Hastelloy-X, together with the common uses of Hastelloy-X in various commercial applications.

Hastelloy-X is a solid solution strengthened, nickel-base superalloy that exhibits good oxidation resistance up to 1200°C, and good mechanical properties in high temperature, corrosive environments up to 871°C. Chromium, molybdenum, and tungsten act as the primary solid solution strengtheners. Nominal alloy composition and selected physical properties are listed in Table 4. Wrought products are generally delivered in the solution heat treated condition, consisting of heating the entire component to a uniform temperature of 1177°C, followed by a rapid cooling process to avoid carbide formation. This solution heat treatment results in the optimum mechanical and corrosion resistance properties for most applications [57].

Due to its ability to withstand high temperature oxidizing, reducing, carburizing and nitriding environments, the Hastelloy-X alloy has been used in the gas turbine industry in components such as combustor liners, transition pieces between combustor and first stage stationary inlet airfoils, afterburner spray bars and flame holders, and exhaust ducts [11, 57, 58].

Rectangular Hastelloy-X substrate coupons were fabricated from a 3.5 in diameter, solution heat treated bar into strips with the nominal dimensions of .787 in (20.00 mm) x 2.362 in (60.00 mm) x .110 in (2.80 mm), with a surface finish of 16 microinch (0.4064 μm) (See appendix A, drawing 20062).

Table 4: Selected Hastelloy-X material properties (adapted from [59]).

Nominal Chemical Composition	Ni	47 wt.% (bal.)
	Cr	22 wt.%
	Fe	18 wt.%
	Mo	9 wt.%
	Co	1.5 wt.%
	W	0.6 wt.%
	C	0.10 wt.%
	Mn	1 wt.% (max.)
	Si	1 wt.% (max.)
	B	0.008 wt.% (max.)
Density	8.22 g/cm ³	(at 22°C)
Melting Range	1260-1355°C	
Electrical Resistivity	1.18x10 ⁻³ Ω-cm	(at 22°C)
Thermal Conductivity	9.1-27.2 W/m-K	(between 21-927°C)
Mean Coefficient of Thermal Expansion	16.6x10 ⁻⁶ m/m-°C	(between 26-982°C)

4.1.2 MCrAlY Bond Coat Materials

In this study, the following three different MCrAlY materials were deposited onto the Hastelloy-X substrate: FeCrAlY, NiCrAlY, and CoNiCrAlY. The following subsection will begin with an outline of the origin of MCrAlY materials, with the evolution of FeCrAlY from simple FeAl binary alloys. The use of FeCrAlY as an overlay bond coat material is then described, highlighting the theoretical advantages of its ferritic body-centred cubic (bcc) structure over the intermetallic face-centred cubic (fcc) structure of the other MCrAlY materials. Additionally, the general results of some FeCrAlY coating studies are presented. This is followed by a brief relative comparison between the properties of NiCrAlY and CoCrAlY alloys for use as high-temperature bond coat materials in gas turbine engine hot section components.



Figure 22: Rolls-Royce/Allison T56 combustor can liner.

Finally, the feedstock materials used in the deposition of the three different MCrAlY bond coat materials used in this work are briefly described, together with a listing of their nominal material compositions.

FeCrAlY materials were developed from FeAl binary alloys that were identified in the 1930s to possess superior oxidation resistance [60]. Chromium was added to FeAl alloys to increase oxidation and corrosion resistance, forming FeCrAl alloys. FeCrAl alloys, such as Fecralloy (Resistalloy International), are commonly used as structural materials for heating elements, hot-zone furnace components, and more recently, in automobile catalysts and industrial gas heaters [61,62]. Oxidation resistance of these alloys is provided through the formation of a slow-growing, protective aluminum oxide or chromium oxide surface scale. The addition of reactive elements (RE), such as yttrium, to form FeCrAlY alloys further improves aluminum oxide scale adherence. RE additions perform this function by acting to getter sulphur impurities present in the alloy to prevent sulphur segregation as well as to suppress outward cationic

transport through the alumina scale [62, 63].

The use of a FeCrAlY overlay coating originated from a General Electric nuclear program [63], and was further investigated by Pratt and Whitney for use on hot-section gas turbine components. The alloy was observed to possess superior aluminum oxide scale adherence during cyclic oxidation, however the coating was deemed not useful in practice at high temperatures due to the formation of a coating-substrate reaction, resulting in the formation of a detrimental NiAl layer between the coating and the substrate alloy.

Additional studies were performed by Burman et al [64] into the use FeCrAlY as a bond coat material, deposited by two different methods: physical vapour deposition and vacuum plasma spray. FeCrAlY possesses a ferritic body-centred cubic (bcc) structure, giving it an inherent advantage in ductility over the intermetallic face-centred cubic (fcc) structures of both NiCrAlY and CoCrAlY coatings [64, 65]. This increased ductility in the bcc FeCrAlY material could theoretically increase the fatigue resistance of the bond coat material at the substrate-bond coat and bond coat-ceramic top coat interfaces. It has also been shown that FeCrAlY alloys have approximately 30% lower coefficients of thermal expansion (CTE) than the intermetallic, fcc-structured MCrAlY materials, making them more compatible with the ceramic, thermally insulating top layer. In addition, the increased ductility of the FeCrAlY bond coat material allows for the inclusion of a greater proportion of oxides into the coating than other intermetallic, fcc-structured MCrAlY materials. This greater proportion of oxides in the coating increases the diffusion distances, yielding longer coating lifetimes, while remaining sufficiently ductile to achieve acceptable thermal fatigue properties [65]. It was discovered, however, that eventual and inevitable nickel diffusion from a nickel-base superalloy substrate into a ferritic FeCrAlY results in a detrimental phase change from a ferritic bcc structure to an intermetallic fcc

structure, leading to a decrease in coating ductility [64]. Despite the purported advantages in the application of FeCrAlY for use as a high-temperature, hot corrosion- and oxidation-resistant bond coat, there is very little literature regarding FeCrAlY in use as an overlay coating, let alone use of FeCrAlY as a coating in general. The majority of available literature refers to FeCrAlY in the form of a structural alloy used for non-aerospace applications.

The vast majority of overlaid MCrAlY corrosion/oxidation resistant bond coats for high-temperature applications in modern gas turbine engine hot section components fall under the category consisting of NiCrAlY, CoCrAlY, and CoNiCrAlY materials. NiCrAlY alloys exhibit superior coating ductility but lack the hot corrosion resistance in comparison to CoCrAlY alloys [63]. CoCrAlY alloys have been shown to have very good hot corrosion and oxidation resistance, however, these same compositions have proven to be unsuitable for turbomachinery airfoils in high performance commercial and military gas turbine aeroengines due to their poor coating ductility (See Table 2). In an attempt to merge the desired properties of good coating ductility and high hot corrosion and oxidation resistance, CoNiCrAlY alloys were developed [16, 22, 63]. A wide variety of commercially available CoNiCrAlY compositions exist (see Figure 23), which contain minor additions of tantalum, tungsten, titanium, niobium, rhenium, and zirconium, that can be tailored and optimized to satisfy varying coating requirements [63]. Both the NiCrAlY and CoNiCrAlY coatings selected for this work are commonly used in the aerospace industry to protect hot-section components from hot corrosive and oxidizing operating environments and were intended to serve as a baseline comparison to the FeCrAlY coating.

The NiCrAlY powder used in this work (Sulzer Metco's AMDRY 962) is typically used in aerospace applications, such as gas turbine blades or valve systems requiring protection from hot corrosion and oxidizing environments at high temperatures, and are post-deposition heat treated before service. This protective overlay coating is

specified by a number of gas turbine manufacturers that includes General Electric, SNECMA, Turbomeca, Volvo, and Williams [66]. The CoNiCrAlY powder used in this work (Sulzer Metco's AMDRY 4700) is typically used in aerospace applications suitable for HVOF processing, on components that will be used in hot corrosive and oxidizing environments. In particular, this protective overlay coating is specified by Rolls-Royce [66]. The nominal compositions of all feedstock materials used in this work, obtained from the individual feedstock material suppliers, are listed in Table 5.

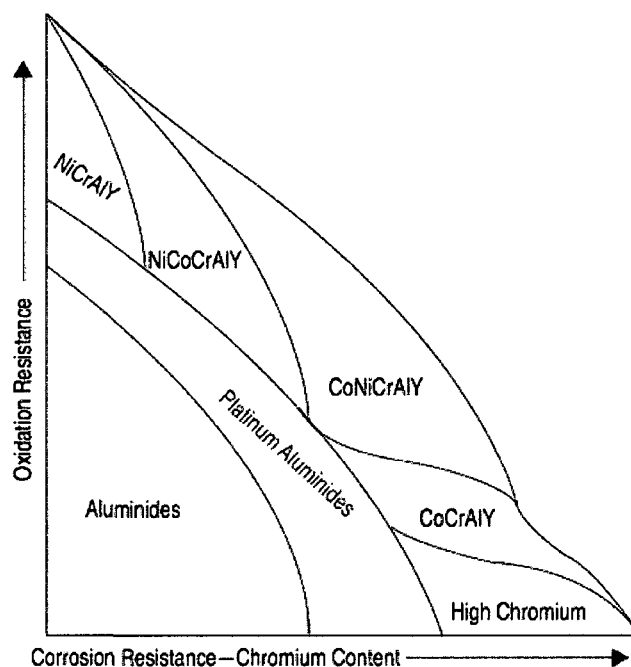


Figure 23: Relative oxidation and corrosion resistance of various diffusion and overlay bond coat materials [20, 22].

4.2 Bond Coat Deposition Processes

The MCrAlY overlay bond coats were applied to the Hastelloy-X substrate using three different deposition processes. The FeCrAlY coating was deposited using magnetron sputtering physical vapour deposition, whereas the NiCrAlY and CoNiCrAlY coatings

Table 5: Summary of MCrAlY feedstock materials used for bond coat deposition.

MCrAlY Type	Alloying Element Concentration (wt.%)						Supplier	Form/Application	Notes
	Fe	Co	Ni	Cr	Al	Y			
FeCrAlY	70.0	-	-	22.6	5.9	0.6	<ul style="list-style-type: none"> Sophisticated Alloys Inc. (Butler, PA, USA) 	<ul style="list-style-type: none"> cathodes, CA-PVD / MS-PVD 	<ul style="list-style-type: none"> Vacuum-cast and HIPed
NiCrAlY (AMDRY 962)	-	-	67.0	22.0	10.0	1.0	<ul style="list-style-type: none"> Sulzer Metco (Westbury, NY, USA) 	<ul style="list-style-type: none"> alloy powder, APS 	<ul style="list-style-type: none"> Spheroidal, gas atomized, 56-106 μm average particle diameter
CoNiCrAlY (AMDRY 4700)	-	38.5	32.0	21.0	8.0	0.5	<ul style="list-style-type: none"> Sulzer Metco (Westbury, NY, USA) 	<ul style="list-style-type: none"> alloy powder, HVOF 	<ul style="list-style-type: none"> Spheroidal, gas atomized, 56-106 μm average particle diameter

were deposited by air plasma spray and high-velocity oxy-fuel processes, respectively, which are both thermal spray processes. It was also attempted to deposit the FeCrAlY layer using cathodic arc physical vapour deposition, and a description of this process is included for this reason.

In this section, the individual deposition processes are introduced according to basic principle of deposition (physical vapour deposition and thermal spray deposition), with an overview of the mechanisms of operation common to each category. This is followed by a more detailed examination of the nuances of each deposition process used in this work, describing the function, advantages and disadvantages of the process, and a listing of equipment and operating parameters used during bond coat deposition.

4.2.1 Physical Vapour Deposition (PVD)

Physical vapour deposition (PVD) consists of a broad category of vacuum deposition processes where thin films, with coating thickness ranging from several nanometres to several microns, are deposited onto a substrate through the vapourization of a target material.

Vapourization can be accomplished through a variety of methods such as evaporative heating, energized particle/photon impingement or physical particle sputtering, all of which result in the ejection of particles from the target surface that are transported through a vacuum and deposited onto the substrate surface [67]. The source material that is to be vapourized and deposited may be solid or liquid, but most commonly the former.

A vacuum environment in the deposition chamber is manipulated by varying the atmospheric gas particle density to prevent or promote particle collisions, to control the partial pressures of the environment gases, and to control gas flow [68]. Deposition of pure elements or compounds is achieved in high vacuum conditions with an

inert atmosphere while reactive compounds such as oxides, nitrides or carbides can be synthesized through the addition of appropriate reactive gases in the deposition chamber atmosphere [67].

PVD vacuum processes were originally developed to be used to exploit the electrical and optical properties of thin films, but recent focus has shifted to further exploration into the exploitation of the mechanical and tribological properties of thin films as well [68]. A large variety of individual PVD processes exist, as well as hybrids of these individual processes, however only the relevant processes used in this work for the deposition of the FeCrAlY bond coat (cathodic arc and magnetron sputtering PVD) are described and discussed further.

Cathodic Arc PVD (CA-PVD)

In cathodic arc vapour deposition, target material vapourization is achieved through the generation of an electric arc between an anode and a cathode, where the target is the cathodic electrode [67]. These electric arcs are formed as a result of the passage of a high-current, low-voltage electrical current through a low-pressure gas vacuum that contains a vapour cloud of cathodic electrode materials, as shown in a schematic representation of the CA-PVD process (Figure 24). The arc is generated between the two electrodes by briefly touching them together and then separating them by a set distance. These arcs may be random or controlled and are affected by ambient gas pressure and composition, the selection of cathode material and degree of impurities that it contains, and the presence of magnetic fields.

The cathode and anode are heated through ion and electron bombardment respectively, resulting in the ejection of molten droplets or solid particles. A large fraction of the vapourized particles are ionized during arc vapourization [67, 69]. In the cathodic arc process, vapourization occurs through arc erosion on the cathode surface. The cathode may be molten or solid, however, a solid cathode system (cold cathode)

requires water cooling.

To obtain adherent and dense films, the cathodic arc source can be used to generate superfluous amounts of film ions and reactive gas ions that are used to sputter clean the substrate surface, as well as implant film atoms into the surface of the substrate [67]. Additionally, cathodic arc deposition can be performed in a low-pressure gas environment for both compound film generation through activated reactive evaporation (such as evaporation of titanium in a low-pressure nitrogen environment to form titanium nitride), as well as using the gas atmosphere to scatter the evaporant ions during their approach to the substrate to achieve a more uniform coating on geometrically complex substrates [69]. The advantages and disadvantages of CA-PVD are summarized in Table 6.

Cathodic arc coating trials were performed at NRC-IAR's PVD facility using Fe-CrAlY cathodes (Table 5) in a Sulzer-Metaplas (Bergisch Gladbach, Germany) Type MR303 coating system, together with a 273 litre Metaplas-Ionon Model MZR 304/33 deposition chamber, as shown in Figure 25. The cylindrical FeCrAlY cathodes (Figure 26) were 63 mm in diameter and 32 mm high and were manufactured by Sophisticated Alloys (Butler, PA, USA). An extensive combination of operating conditions for this coating apparatus were tested in attempts to produce a suitable bond coat deposition, with parameter ranges listed in Table 7.

Magnetron Sputtering PVD (MS-PVD)

In contrast to cathodic arc PVD, which makes use of an electric arc to vapourize the target material, sputter deposition makes use of the non-thermal physical sputtering phenomenon in which the target material particles are ejected into a plasma cloud from the target surface through momentum transfer with energetic bombarding particles. These energetic particles are typically gaseous ions that are accelerated from the plasma cloud into the target material [67]. The particles used to cause target

Table 6: Advantages and disadvantages to CA-PVD [67–69].

Advantages	<ul style="list-style-type: none"> • Large portion of vapourized material is positively ionized, allowing use of a negative bias on the substrate to accelerate positive ions toward the substrate, increasing adhesion strength of coating • Higher vapourization and deposition rates than for physical evaporation and sputtering • High evaporation flux from cathode, resulting in greater resistance to cathode surface poisoning by reactive gases
Disadvantages	<ul style="list-style-type: none"> • Production of macroparticles from solid cathodes due to intense arcing, resulting in coating defects such as bumps and pinholes (Particles can be reduced by controlling arc travel using magnetic fields and filtering at a price of severe decrease in deposition rate) • Arc instability due to random arc travel in relation to cathode surface

Table 7: CA-PVD processing parameter ranges for FeCrAlY coating trials.

Base pressure:	2.9x10 ⁻³ –7.3x10 ⁻³ mtorr (3.9x10 ⁻⁴ –9.7x10 ⁻⁴ Pa)
Operating pressure:	7.5–26.3 mtorr (1.0–3.5 Pa)
Arc current:	15–18 A

evaporation can be generated through two methods: ion beam; and glow discharge (or magnetron) sputtering. In both methods, the inert bombardment ions (such as ionized helium or argon) are generated in a glow-discharge plasma. Sputter deposition can be performed in a variety of vacuum levels, from low plasma pressures of less than 5 mtorr (0.67 Pa), to higher pressures of 5–30 mtorr (0.67–4 Pa) [67]. In higher plasma pressures, energetic particles ejected or reflected from the sputtering target are slowed down through collisions with the gaseous phase before reaching the substrate surface.

In the specific example of planar magnetron sputtering, the physical sputtering PVD process that was used in this work, the plasma region can be electromagnetically

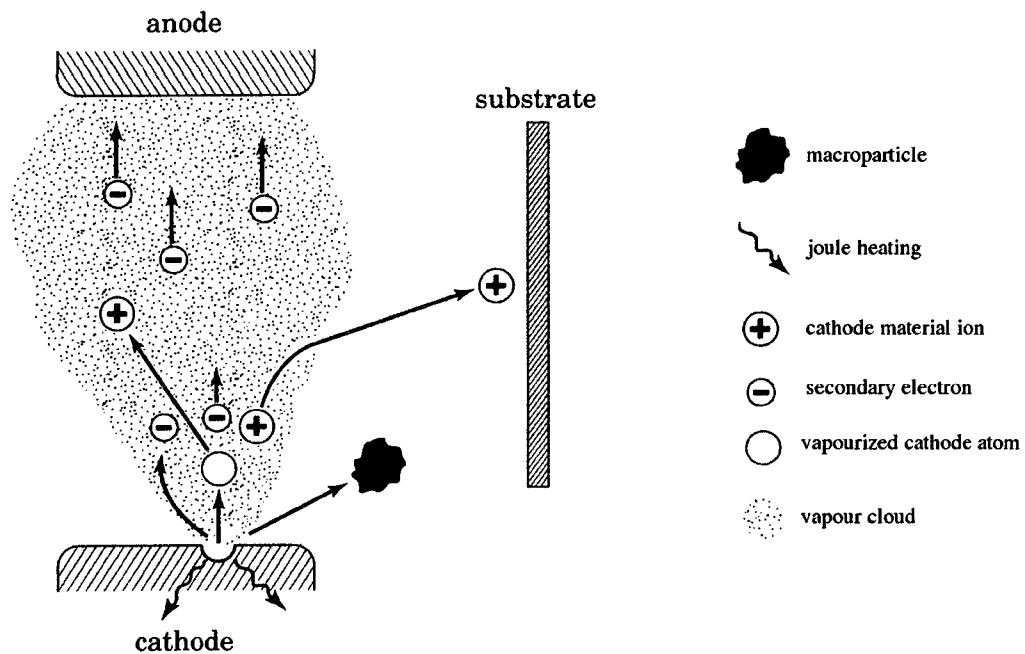


Figure 24: Schematic diagram of the cathodic arc PVD process. Adapted from [69].

confined to areas near the sputtering surface (See Figure 27) [67]. This combination of electrical and magnetic confinement leads to the trapping of charged particles at the target surface, yielding greater vapourization rates and a decreased distance to accelerate the positive ions to the target. These improvements allow sputtering to occur at lower pressures and voltages with higher deposition rates [68].

In sputtering deposition processes, the sputtering target is cooled in order to decrease the amount of radiant heat in the reaction chamber, allowing for the coating of thermally sensitive substrates as well as avoiding diffusion in alloy targets that could alter their composition [67].

Sputtering can be used to process a large variety of materials from pure elements to alloys or compounds, where the composition of the deposited material is that of the bulk composition of the sputter target. This is possible because diffusion in the target does not occur and each atom layer must be removed before the next can be sputtered.

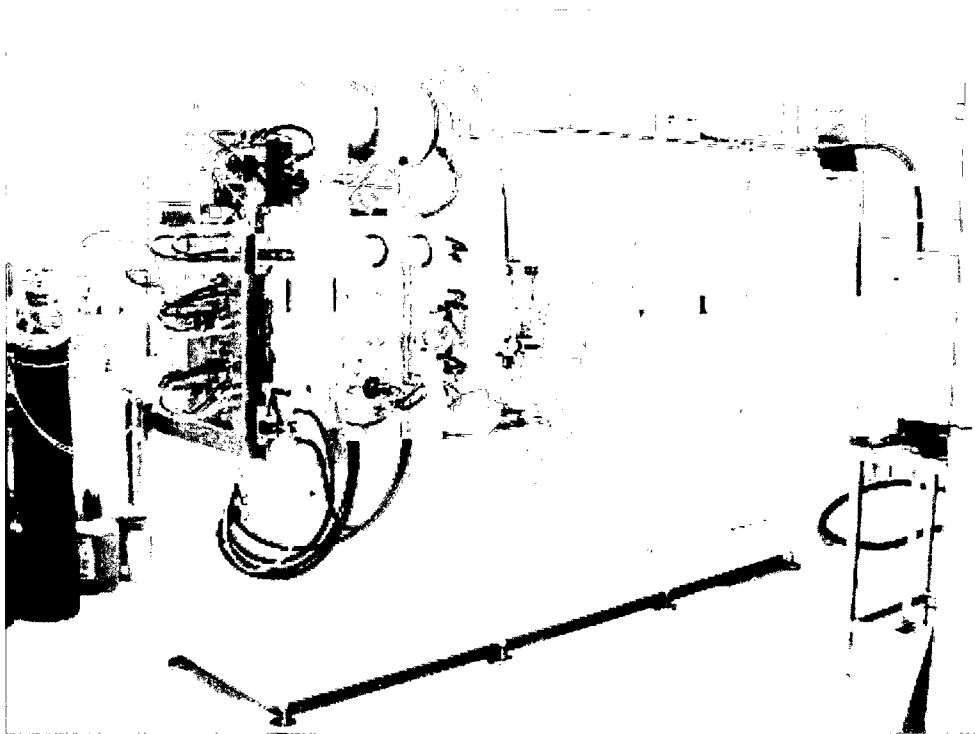


Figure 25: Sulzer Metaplas Type MR303 coating system with Metaplas Ionon MZR304/33 deposition chamber.



Figure 26: FeCrAlY feedstock cathode.

To increase the chemical sensitivity of the target material, the phenomenon of plasma activation is used through the addition of reactive gas, or gases, to the plasma [67]. The advantages and disadvantages of MS-PVD are summarized in Table 8.

Magnetron sputtering trials were performed at NRC-IAR's PVD facility using a hybrid FeCrAlY+Al target in a Teer Coatings Limited (Worcestershire, UK) UDP vacuum sputtering system (Figure 28), model UDP 650/4, using argon as the plasma-forming gas. A schematic diagram of the magnetron configuration in this type of magnetron sputtering system is shown in Figure 29a. This system has been upgraded with a Polycold water vapour cryopump refrigeration system (model PFC-400ST) to improve the coating-to-substrate adhesion. A hybrid target system was devised in order to re-use the FeCrAlY cathodes from the cathodic arc coating trials and avoid purchasing a FeCrAlY sputtering target to fit the coater. The circular 63 mm cathodic arc targets were sectioned into 3 mm-thick wafers and then placed in various configurations onto a backing sputtering target made of pure aluminum (see Figure 29b). The magnetic field of the magnetron provided sufficient attraction to retain the ferromagnetic FeCrAlY wafers against the aluminum target. The FeCrAlY wafers were spatially arranged to ensure their proximity to the race track profile in which the magnetic field impinges the argon ions into the target surface to sputter the target ions. Although the UDP 650/4 coater incorporates four magnetrons (as shown in Figure 29a) which allows for the deposition of up to four different materials simultaneously, only one active magnetron with the hybrid FeCrAlY+Al target configuration was used, and the substrate holder was held in a fixed position directly in front of the active magnetron.

An extensive combination of operating conditions for this coating apparatus were attempted to produce a suitable bond coat deposition, with parameter ranges listed in Table 9. An example of a MS-PVD FeCrAlY-coated test specimen is shown in Figure 30.

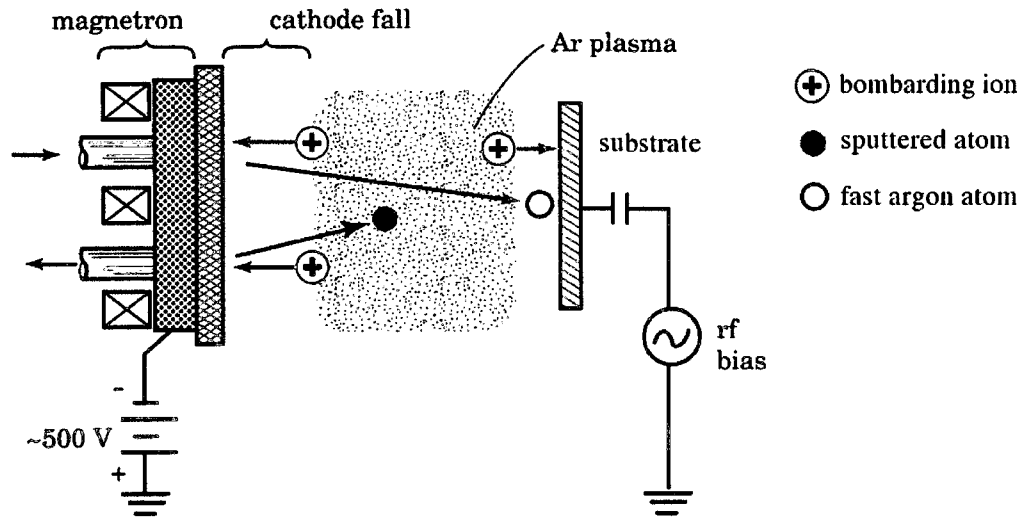


Figure 27: Schematic of the magnetron sputtering PVD process. Adapted from [69].

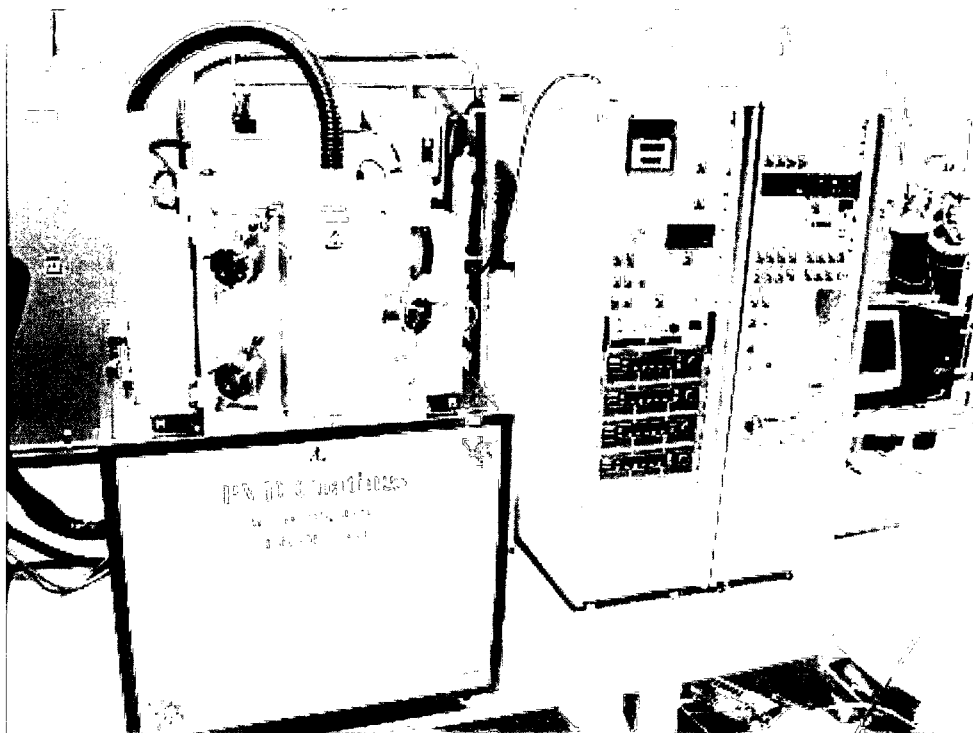


Figure 28: Teer Coatings Limited UDP 650/4 magnetron sputtering coating system.

Table 8: Advantages and disadvantages to MS-PVD [67].

Advantages	<ul style="list-style-type: none"> • Theoretically, any element, alloy, or compound, can be sputter-deposited • Stable vapourization process: long usage life; high material utilization of sputtering targets • Targets can be sputtered (vapourized) from any orientation • Due to inherent process stability, sputtering parameters can be easily reproduced • Low radiant heating in comparison to other PVD processes • Inherent kinetic energy distribution of sputtered atoms allowing for film deposition that avoids causing sub-surface damage • Substrate surface preparation can be incorporated into deposition process (sputter cleaning)
Disadvantages	<ul style="list-style-type: none"> • Energy inefficient • High cost of sputtering targets • Low vapourization rates in comparison to other PVD processes • Cooling requirement due to significant conversion of sputtering energy into heat in the target material • Impingement of detrimental shortwave radiation and high-energy particles onto substrate • Contamination of coating due to gaseous inclusions in plasma-based sputtering

4.2.2 Thermal Spray Deposition

In contrast to physical vapour deposition, which is an atomistic deposition process, thermal spray deposition relies on the deposition of much larger, macroscopic particles. Thermal spray deposition describes a vast range of processes for applying metallic or non-metallic coatings onto a substrate. Common to all methods is the use of an energy source, either through gas combustion or by electrical means, to melt or partially melt the coating feedstock material that is delivered in a powder, wire, or rod form. This heated coating feedstock material is accelerated toward the substrate using process gases or atomization jets. The impact of the heated coating material

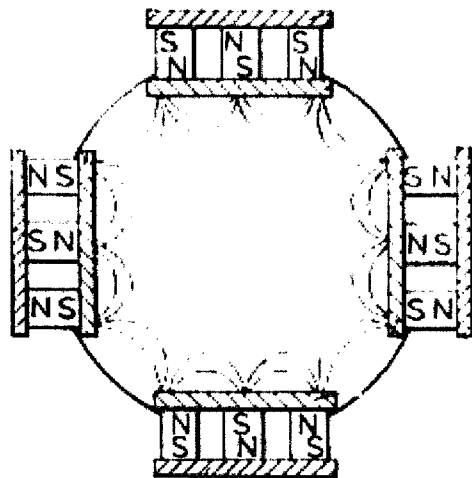
Table 9: MS-PVD processing parameter ranges for FeCrAlY+Al coating trials.

Base pressure:	8.0x10 ⁻⁴ –1.0x10 ⁻² mtorr (1.1x10 ⁻⁴ –1.3x10 ⁻³ Pa)
Operating pressure:	1.9–7.5 mtorr (0.25–1 Pa)
Magnetron current:	0.25–2 A
Substrate bias:	20–25 V
Sputtering gas (Ar) flow rate:	25–50 sccm
Number of FeCrAlY wafers on Al sputtering target:	2–8

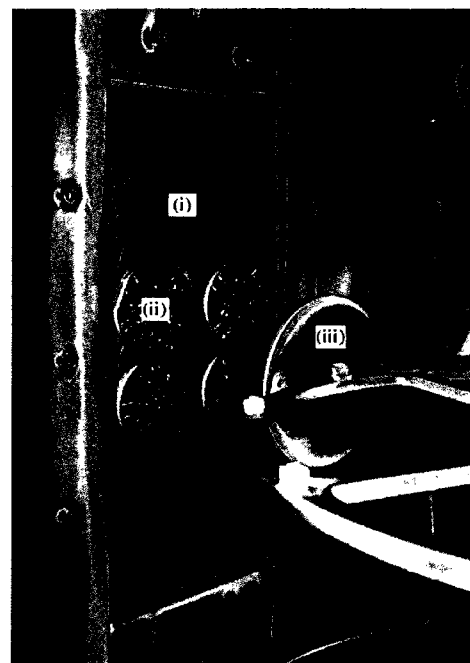
against the substrate results in bonding to the surface and subsequent buildup of coating thickness.

The deposited particles are typically lamellar, also known as 'splats' [37]. Thermal spray coatings consist of uniform, fine-grained, polycrystalline deposits that contain porosity between 0 and 10% by volume. Sprayed particles are subject to various degrees of melting from fully melted splat particles to partially melted particles that may contain oxides from reactions with the air atmosphere. An illustration of the typical constituents of a thermally-sprayed coating microstructure is shown in Figure 31. Due to a high cooling rate of the sprayed particles, the coatings have sub-micron grain sizes, which can be altered using post-spray heat treatments [37].

The levels of porosity and non-melted inclusions are a function of the particular thermal spray process, as well as the spraying parameters and the coating feedstock material used. The quantity of oxides present in the coating can be controlled by varying particle velocity, as well as reducing the oxygen content in the spraying environment. Typical tensile strengths of sprayed coatings range between 10 and 60% of the cast or wrought material properties and are largely dependant on the spraying process used, where higher oxide fractions and lower coating density lead to lower



(a) Magnetron arrangement in the UDP 650/4 MS-PVD coater [70]



(b) Hybrid FeCrAlY+Al magnetron sputtering target arrangement.

Figure 29: Configuration of the MS-PVD coating system to accommodate hybrid Fe-CrAlY+Al target arrangement: (i) backing Al target, (ii) magnetically-adhered FeCrAlY disks (inside oval-shaped 'race track'), and (iii) substrate holder facing hybrid target arrangement.

strengths [37].

Spraying in a controlled environment (vacuum or inert-gas environment), in combination with a post-spray heat treatment, can result in coating tensile strengths that approach near 100% of the wrought or cast strengths. Coating build-up thickness is limited due to the accumulation of residual stresses from rapid splat solidification [37]. The advantages and disadvantages of thermal spray processes are listed in Table 10.

The following sections provide a more detailed overview of the particular thermal spray processes used to deposit MCrAlY coatings onto the Hastelloy-X substrates in this work: air plasma spraying (APS) and high-velocity oxy-fuel (HVOF) spraying.

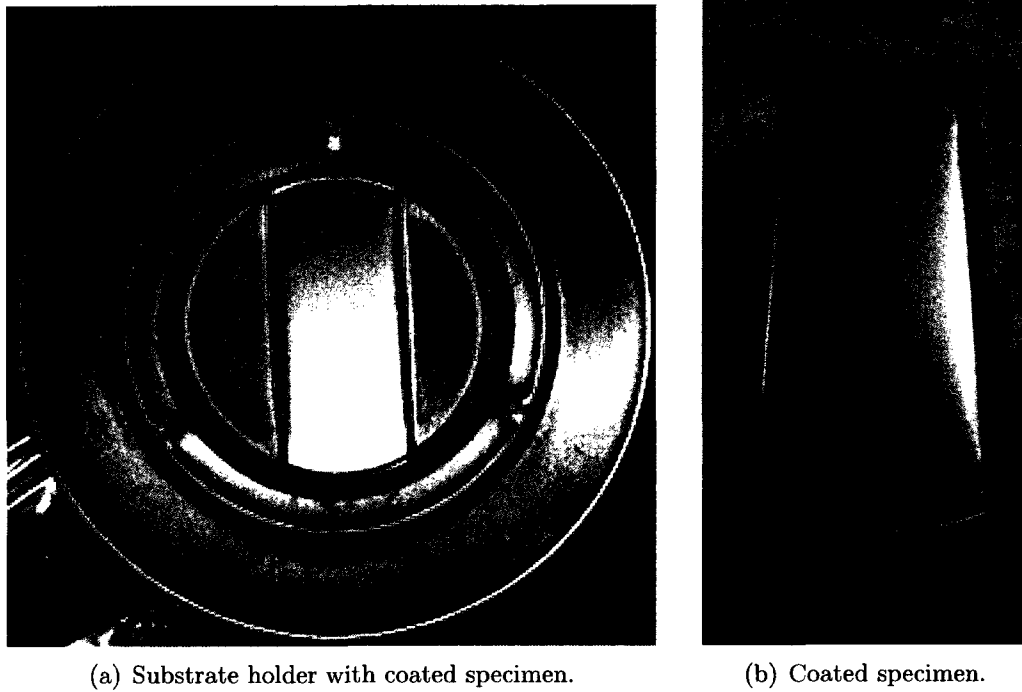


Figure 30: MS-PVD FeCrAlY-coated test specimen.

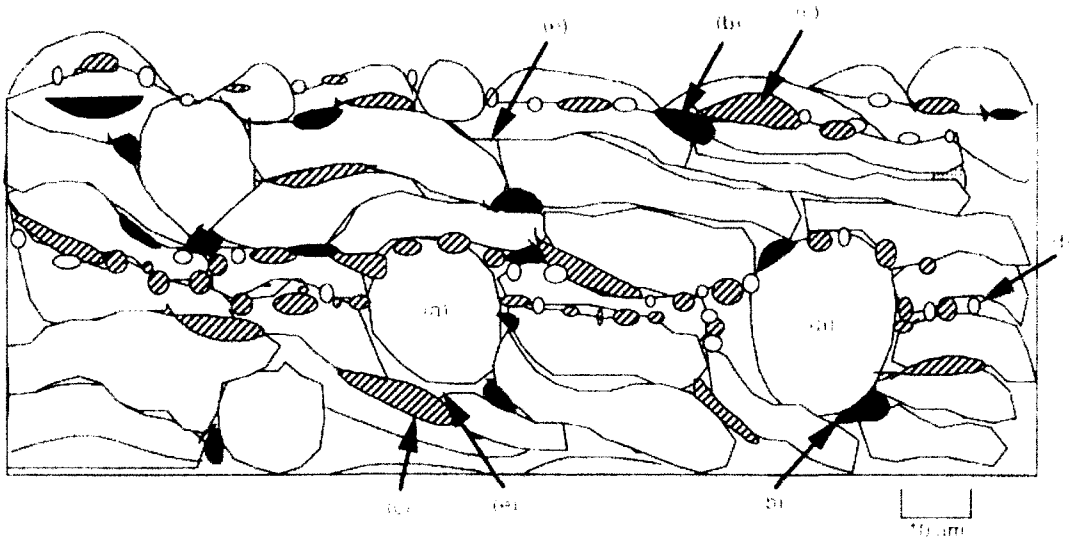


Figure 31: Typical thermally-sprayed coating microstructure, containing: (a) unmelted particles, (b) oxides, (c) debris, (d) fine particles, and (e) porosity. Adapted from [37].

Table 10: Advantages and disadvantages to thermal spray processes [67].

Advantages	<ul style="list-style-type: none"> • Generally more economical than PVD methods • Ability to produce coatings in a broad range of thicknesses from a wide variety of materials, relative to PVD methods • Capable of coating substrates without significant heat input, allowing the application of coating materials to components that have already been machined and heat treated to finished product form without causing dimensional or microstructural changes • Thermally-sprayed coatings can, in most instances, be stripped and re-coated without causing dimensional or microstructural distortion to the substrate component, after the original coating's service lifetime has expired
Disadvantages	<ul style="list-style-type: none"> • Coating process is line-of-sight, meaning that the coating flux can only be applied in a linear fashion, requiring that the application device has direct access to the area that is to be coated • Generally, thermal spray coatings exhibit lower bond strength and higher porosity than those achieved through other coating processes such as PVD

Air Plasma Spray (APS)

The plasma spray process uses electric power to generate plasma in order to melt the feedstock coating material, which is then transferred, via plasma jet, to the substrate. The plasma that is used to melt the feedstock material is typically generated by direct current electric arcs or induction-coupled devices [37]. Plasma spray processes can be further classified into those that are performed in an air environment and those that are performed in a controlled environment, such as a vacuum plasma spray or low-pressure plasma spray.

Air plasma spray (APS), the process used in this work, is one of the simpler and more cost-effective thermal spray coating processes. It offers a large degree of flexibility by allowing the application of a wide variety of materials due to the use of an inert carrier gas, with high gas velocity, and extremely high temperatures. The APS process can furnish plasma jet temperatures of up to 15,273°C, and plasma jet

velocities in the range of 300-1000 m/s, with power inputs between 40-100 kW [37]. Appreciable coating densities (between 90–95%) and bond strengths are achievable due to large degrees of particle melting and high particle velocity, resulting in a superior quality coating microstructure. While oxide content can be minimized in comparison to other atmospherically sprayed processes, some oxide content will always be present in an APS coating.

A typical plasma spray gun (Figure 32) consists of a tungsten cathode with an axially aligned anodic nozzle that is water-cooled to maximize gun component lifetimes. The gases used for plasma generation are fed into the rear of the gun where they are released into the arc chamber through a vortex-generating gas ring. The spin imparted by the gas ring provides arc stabilization at the cathode tip while rotating the arc root at the anode, thereby minimizing anode erosion. The plasma-generating gases are then passed around and through the arc, allowing the heated gases to expand radially and axially, accelerating toward the converging/diverging nozzle.

Plasma-sprayed samples were provided courtesy of Northwest Mettech Corporation (Vancouver, BC, Canada). Processing was performed using the Axial III Plasma Spray System which features a spray nozzle with three coaxial electrodes that are capable of producing a supersonic powder jet, using the processing parameters listed in Table 11.

High-Velocity Oxy-Fuel (HVOF)

Unlike plasma spray processes, which use an electrically-generated plasma to melt the coating feedstock material, the high-velocity oxy-fuel (HVOF) deposition process is a continuous, steady-state process which uses high-volume combustible gases to melt the feedstock material. An illustration of a typical HVOF gun configuration is shown in Figure 33. In an expansion nozzle, oxygen and a torch fuel are combined and the mixture is ignited, resulting in high pressures that force the combustion gases

Table 11: APS processing parameters for NiCrAlY coating runs.

Total nozzle flow rate:	350 lpm
N₂ proportion:	10%
H₂ proportion	20%
Ar proportion	70%
Carrier gas flow rate:	12 lpm
Powder feed rate:	80 g/min
Nozzle diameter:	0.375 in (0.95 cm)
Spray distance:	15 cm
Turn table rotational speed:	356 rpm
Average coating thickness:	.010 in (254 μ m)

through the nozzle. Torch fuels can be either gaseous (propylene, propane, hydrogen, or natural gas) or liquid (kerosene). Coating feedstock powders are injected into the combustion air stream in the nozzle via a carrier gas such as nitrogen. The combustion gases uniformly heat the powder as it leaves the gun nozzle and is propelled toward the surface of the substrate at velocities between 1,525 and 1,825 metres per second. There exist two classes of high-velocity combustion spray devices: high velocity devices operating at 241 kPa and 527 MJ heat input and hypervelocity devices that operate in excess of 620 kPa and approximately 1 GJ of heat input [37]. The high particle velocities ensure that full melting of the coating material particles is not required. Instead, the partially-melted powder particles flatten plastically as they impact the workpiece surface. As a result, coatings have predictable compositions that are homogeneous and have a fine granular structure.

HVOF coatings exhibit superior coating properties to plasma-sprayed coatings due to their greater density and adhesion as a result of high particle impact velocities. HVOF coatings also have lower oxide contents due to the lower average particle temperatures that reduce the proportion of particle melting and oxidation as compared

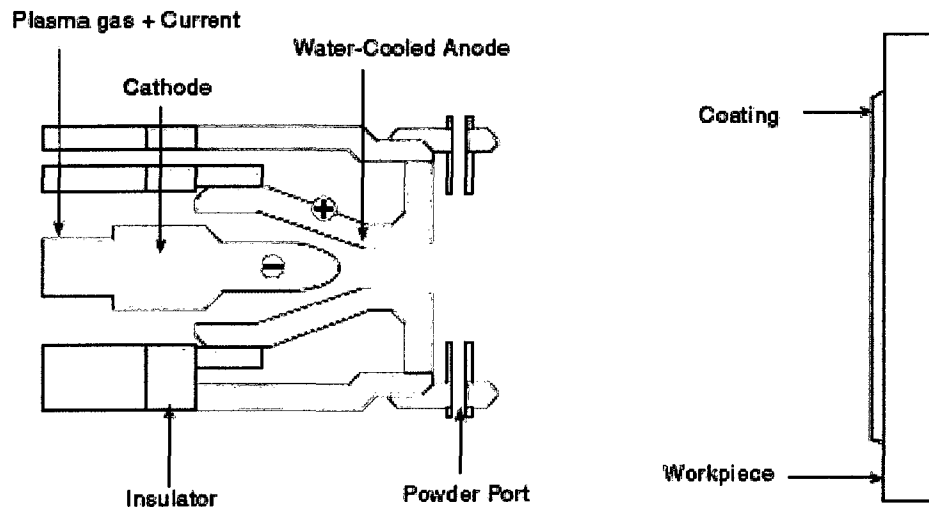


Figure 32: A schematic of a typical air plasma spray (APS) process [71].

to the APS process. Higher particle impact velocities also tend to result in generation of beneficial compressive stresses in the component at the cost of deposition efficiency (DE). The deposition efficiency is an idealized measure of the proportion of particles that have been injected into the spray jet in comparison to the amount that adheres the substrate, without considering overspray [37].

The HVOF-sprayed samples were provided courtesy of NRCs Institute Materials Institute (NRC-IMI, Boucherville, QC). HVOF-processing was performed using a Sulzer Metco (Westbury, NY, USA) DJ2600-hybrid hypervelocity HVOF system, using the processing parameters listed in Table 12.

Table 12: HVOF processing parameters for CoNiCrAlY coating runs.

H₂ flow rate:	684 lpm
O₂ flow rate:	231 lpm
Shroud gas (N₂) flow rate:	330 lpm
Spray distance:	10 in (25.4 cm)
Average coating thickness:	92 μm

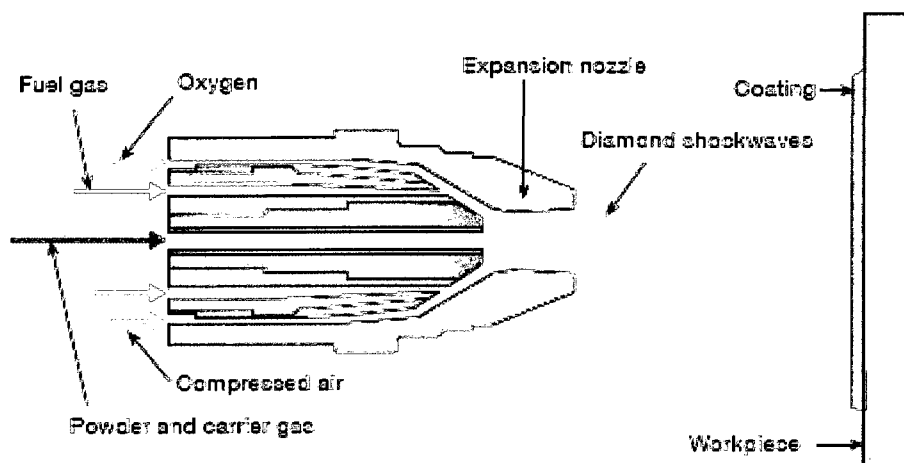


Figure 33: A schematic of a typical high-velocity oxy-fuel (HVOF) process [71].

4.3 Surface Processing

Surface processing was applied to both the substrate surface before MCrAlY bond coat deposition for all test specimens and post-deposition for all thermally-sprayed test specimens. In general, the aim of these surface processing treatments was to promote improved substrate-coating adhesion during bond coat deposition, and to encourage the formation of a uniform and continuous thermally-grown oxide (TGO) during a post-deposition heat treatment. The following sub-sections describe the pre-deposition and post-deposition surface modification procedures applied to the test specimens.

4.3.1 Pre-deposition

Pre-deposition surface treatments for the the deposition surfaces on the Hastelloy-X substrate were selected to suit the type of deposition process. For PVD processes, where the deposition process is atomistic in nature, two surface conditions were used: 1200 grit silicon carbide ground finish, and 1 μm diamond polish finish. By providing a fine surface finish, it was expected to produce a bond coat layer whose own surface

condition was very similar to that of the substrate. By extension, it was thought that a smooth bond coat surface would encourage the formation of a uniform and continuous thermally-grown oxide consisting primarily of α -Al₂O₃. This TGO would form a base layer for the deposition of additional aluminum oxide, which acts as both a diffusion barrier and an electrically-insulating barrier to the thin film sensor, as described in the **Literature Review** chapter. Ground and polished substrates were ultrasonically cleaned in acetone, then in anhydrous ethyl alcohol for 10 minutes each. Substrates were then air-dried and immediately mounted in the sample holder to be loaded into the coating chamber for subsequent bond coat deposition.

Unlike the PVD processes, the thermal spray deposition process requires a coarse substrate surface finish as coating adhesion is due primarily to mechanical interlocking rather than atomic cohesion. In the high-temperature aerospace coating industry, aluminum oxide particle grit blasting is commonly used to prepare the substrate surfaces for thermally sprayed components [72]. In this work, all NiCrAlY samples were grit blasted with aluminum oxide particles of #54 mesh size prior to air plasma spray processing. Half of the substrates for the CoNiCrAlY-coated samples was ground to 1200 grit using silicon carbide paper prior to coating, while the other half was grit blasted with aluminum oxide particles of #24 mesh size prior to HVOF processing. Unlike for PVD processes, the resulting post-deposition coating surface condition is independent of the substrate surface. For this reason, they require an additional post-deposition surface modification procedure in an attempt to achieve the same desired post-heat treatment TGO properties as for the PVD-deposited test specimens. This post-deposition surface modification is described in the following sub-section.

4.3.2 Post-deposition

In addition to the pre-deposition surface modification of the Hastelloy-X substrate, an additional post-deposition surface treatment of the MCrAlY coating surface was

applied prior to heat treatment for the thermally sprayed samples (APS-NiCrAlY and HVOF-CoNiCrAlY). This consisted of grinding the coated sample surface to a 1200 grit finish with silicon carbide paper to encourage a uniform TGO scale growth during the subsequent heat treatment. Again, a reasonably smooth TGO surface finish would facilitate the deposition of the sensor layer materials on top of the TGO, as with the pre-deposition surface modification of the PVD-processed samples. Applying this surface treatment to the samples processed by both thermal spray methods also negates the influence of the as-deposited surface condition on the resulting oxide formation during heat treatments, thus allowing for some level of comparison between the two different methods. The ground samples were ultrasonically cleaned in acetone, then anhydrous ethyl alcohol for 10 minutes each before the pre-oxidation heat treatments.

4.4 Pre-oxidation Heat Treatments

The MCrAlY-coated Hastelloy-X substrates were subjected to a set of isothermal heat treatments in both an atmospheric air furnace and a vacuum furnace. A summary of temperatures and hold times is listed in Table 13. Heat treatment temperatures and hold times for the selected heat treatments were chosen to maintain a reasonable similar Larson-Miller parameter value for all heat treatments. The pre-oxidation heat treatments were designed to investigate the formation of oxides on the three different MCrAlY-coated samples with the objective of establishing a protective surface oxide consisting of α -Al₂O₃. This thermally-grown α -Al₂O₃ was intended as a base for the deposition of additional Al₂O₃, and also to act as an electrically-insulating layer for the thin film sensor to be deposited on its surface.

As previously stated in the **Literature Review** chapter, an ideal protective oxide for high-temperature hot section components is a highly stable and continuous, slow

growing, free from defects such as cracks and pores, and remains adherent and coherent with the substrate or thermally-insulating top coat. α - Al_2O_3 has been shown to satisfy most of these requirements, and MCrAlY overlay materials have been designed to form a thermally grown oxide (TGO) layer consisting primarily of α - Al_2O_3 , which acts as a corrosion and oxidation barrier to the underlying substrate material [25]. Critical factors in achieving an oxide scale comprising largely of α - Al_2O_3 are the magnitude of the heat treatment temperature and the oxygen partial pressure of the oxidizing environment. In order to ensure the preferential formation of α - Al_2O_3 , both the pre-oxidation temperature and the oxygen partial pressure of the oxidizing atmosphere must be sufficiently high enough to promote the formation of stable α - Al_2O_3 , rather than the transient oxides of aluminum (γ -, θ -, and δ - Al_2O_3), chromium oxides and other spinels [25].

For heat treatment, the bare Hastelloy-X substrate material and the MCrAlY-coated Hastelloy-X test specimens were sectioned into smaller pieces, measuring approximately 20 mm x 20 mm x 2.8 mm, to maximize the number of specimens available. This sample size was also suitable for use in the x-ray diffractometer, described in a later sub-section. PVD-coated substrates were sectioned using a Buehler Isomet 2000 precision saw with a Beta Diamond sectioning blade. The samples were positioned so that the coating surface faced into the blade rotation. The coating surface was protected from sample holding clamp abrasion with cotton wadding. The bare Hastelloy-X substrate test specimens and thermal spray-coated specimens were cut using a Buehler Samplemet II abrasive cutter with a Buehler abrasive cut-off wheel for non-ferrous materials. Prior to heat treatment, all specimens were ultrasonically cleaned in acetone, then anhydrous ethyl alcohol for 10 minutes each.

In this study, vacuum heat treatments (VHTs) were performed in a programmable Oxy-Gon (Oxy-Gon Industries, NH, USA) furnace, model C700 (Figure 34), operating at a pressure between 10^{-5} and 10^{-6} torr (1.33×10^{-4} – 1.33×10^{-3} Pa). Samples were

Table 13: Summary of temperatures and hold times for furnace pre-oxidation heat treatment trials.

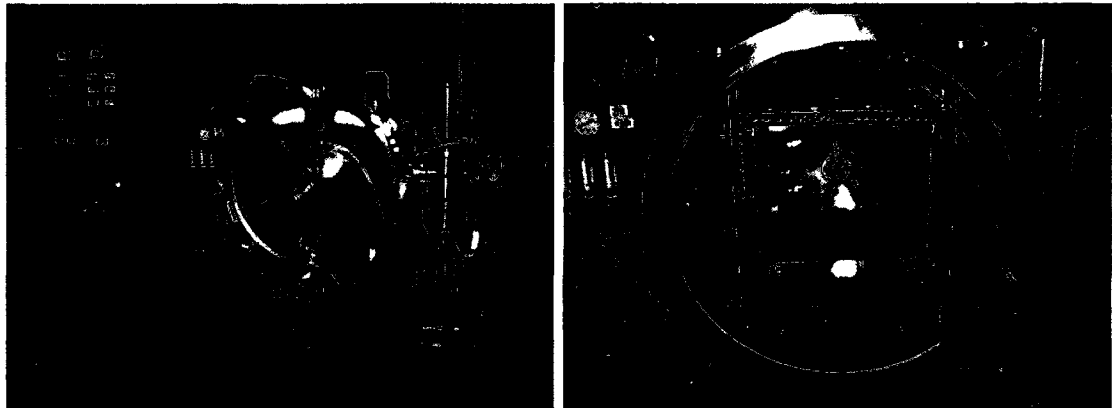
	Vacuum Furnace	Air Furnace
1000°C	10 hours, 15 hours	10 hours
1050°C	5 hours, 10 hours	5 hours
1100°C	1 hour, 5 hours	1 hour

placed on an Al_2O_3 block inside the vacuum chamber. Prior to the VHT thermal profile, the vacuum chamber was pumped down to operating pressure and then back-filled with argon gas three times. After the completion of the isothermal VHT heat treatment, samples were allowed to furnace-cool at a sufficiently slow cooling rate as to prevent fracturing of the Al_2O_3 sample-holding block.

Isothermal air furnace oxidation heat treatments (AHTs) were performed in a 1200°C-capable Lindberg box furnace (Lindberg/MPH, MI, USA), model 51232, controlled by a Lindberg model 59554 automatic power control console (Figure 35). Temperature was recorded using a PC running NightWatch thermocouple data recording software. After completion of the isothermal AHT heat treatment, the samples were allowed to furnace cool prior to removal from the furnace.

4.5 Test Specimen Evaluation

As-received and heat-treated Hastelloy-X substrate material, together with as-deposited and heat treated MCrAlY-coated substrates were analyzed with a variety of techniques, a summary of which is provided in Table 14. Initial observations of surface features were made using optical microscopy; in-depth observations regarding surface morphology and compositional information were performed using a scanning electron microscope (SEM) coupled with an energy dispersive spectroscopy (EDS) sensor. Before cross-sectioning and mounting the samples, a representative set was



(a) Vacuum furnace system.

(b) Inside the vacuum furnace pressure chamber showing cylindrical aluminum oxide sample holder block and three test specimen sections.

Figure 34: Oxy-Gon model C700 vacuum furnace.

selected for x-ray diffraction. Cross-sectioned and mounted samples were further analyzed using the SEM to examine the microstructure and composition. In following sub-sections, the equipment that was used for the test specimen evaluation, including microscopic evaluation and x-ray diffraction analysis, is listed, including a description of equipment used in the preparation of cross-sectional samples.

4.5.1 Microscopic Evaluation

Microscopic evaluation of the surface and cross-sectional features of as-received and heat-treated Hastelloy-X substrate material, together with as-deposited and heat treated MCrAlY-coated substrates, was performed using both optical and secondary electron microscopes. Surface features of all samples were observed without any prior sample preparation, whereas all cross-sectioned samples required further sectioning, mounting, grinding, and polishing before viewing. The following sub-sections describe the cross-sectional sample preparation, followed by a listing of optical and scanning electron microscopes, as well as energy dispersive spectrum analysis equipment used

Table 14: Summary of analysis techniques performed on test specimens.

Analysis	Technique	Test Specimens	Analysis
Surface features	• Optical microscope	• Hastelloy-X	• As-received (1), VHT (6), AHT (3)
	• SEM	• FeCrAlY (MS-PVD)	• As-deposited (1), VHT (6), AHT (3)
		• NiCrAlY (APS)	• As-deposited (1), VHT (6), AHT (3)
		• CoNiCrAlY (HVOF)	• As-deposited (1), VHT (6), AHT (3)
Cross-sectional features		• Hastelloy-X	• As-received (1), VHT (6), AHT (3)
	• SEM	• FeCrAlY (MS-PVD)	• As-deposited (1), VHT (6), AHT (3)
		• NiCrAlY (APS)	• As-deposited (1), VHT (6), AHT (3)
		• CoNiCrAlY (HVOF)	• As-deposited (1), VHT (6), AHT (3)
Composition	• EDS	• Hastelloy-X	• EDS: As-received/as-deposited (4), VHT (24), AHT (12)
	• XRD	• FeCrAlY (MS-PVD)	• XRD: As-received/deposited (4), VHT [1100°C/1 hour] (4), AHT [1050°C/5 hours] (4)
		• NiCrAlY (APS)	
		• CoNiCrAlY (HVOF)	

(N): N test specimens per condition

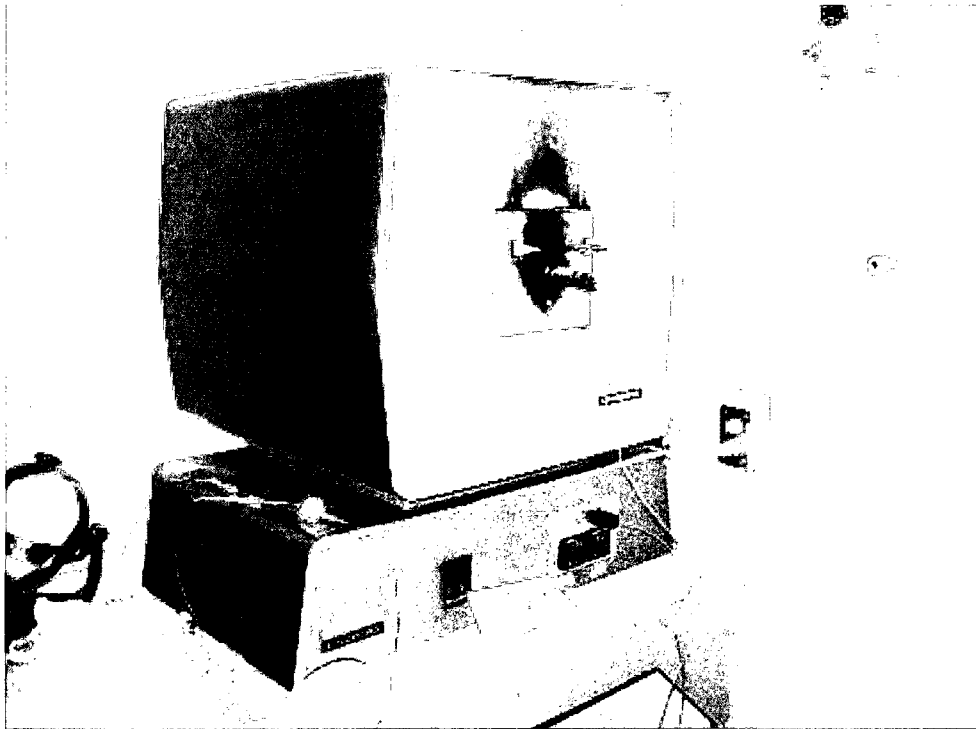


Figure 35: Lindberg model 51232 box furnace with Lindberg model 59554 furnace controller.

in this work, with a brief discussion regarding the limitations of the latter.

Cross-sectional Sample Preparation

For ease of microscopic analysis of cross-sectional features, all samples were sectioned and mounted using both hot and cold mounting techniques. Hot mounting was used for all thermally-sprayed samples as well as as-received and heat treated Hastelloy-X specimens. All as-deposited and heat treated FeCrAlY-coated samples were cold mounted due to concerns regarding the retention of the coating after deposition and the porous thermally-grown oxide that resulted from the subsequent heat treatments. This sub-section lists and describes the use of all materials used in the metallographic sample preparation of the cross-sectioned samples, beginning with test specimen sectioning, followed by hot and cold mounting, and finally, grinding and polishing.

Sample preparation was performed using controlled and consistent conditions. PVD-coated substrates were sectioned using a Buehler Isomet 2000 precision saw equipped with a Beta Diamond sectioning blade. The samples were positioned so that the coating surface faced into the blade rotation. The coating surface was protected from sample holding clamp abrasion with cotton wadding. The bare Hastelloy-X specimens and the thermal spray-coated specimens were cut using a Buehler Samplomet II abrasive cutter, equipped with a Buehler abrasive cut-off wheel for non-ferrous materials.

Hot mounting of the sectioned samples was performed using a Streuers LaboPress 3 and mounted in Buehler PhenoCure 640 or Transoptic powders. The Buehler Transoptic powders were used primarily to facilitate correct sample placement under the microscope due to the simplified identification of the mounted samples' coated surface. Samples were supported using metallic Buehler Sampl-Klip or plastic Buehler Uniclip sample supports. Delicate sectioned samples were cold mounted using an epoxy cold mounting procedure. Reusable plastic cold mounting moulds (Buehler Sampl-Kup) were first coated in release agent, then the supported sample was placed into the mould and coated with an epoxy resin/hardener mixture. The mixture consisted of a 10:1 ratio of Hysol RE2038 epoxy resin to Hysol HD3404 resin hardener. The filled moulds were then transferred to a Streuers Epovac apparatus for vacuum hardening treatment at 800 mbar (80 kPa) gauge pressure until cured.

Mounted samples were wet ground from 180, 240, 320, 400 and 600 grit using Buehler-Met II silicon carbide paper on a Buehler Ecomet 4 automatic grinding/polishing machine with an Automet 2 power head. Intermediate polishing was performed using Beta Diamond Products KDM-KG2040 diamond suspensions of 9-, 6-, 3-, and 1- μm average particle diameter on Streuers MD-Rondo adaptor backed Buehler Texmet 2000 polishing cloths. Diamond suspensions were supplemented using water-soluble Buehler Metadi extender fluid. Final polishing of mounted samples

was accomplished with Buehler Mastermet colloidal silica polishing suspension on a Streuers MD-Rondo adaptor backed Buehler Chemomet polishing cloth. Each intermediate and final polishing stage was followed by ultrasonic cleaning in Buehler Ultramet II ultrasonic cleaning solution and distilled water for 10 minutes to minimize carry-over of abrasive particles into each consecutive polishing stage.

Optical Microscopy

Low and medium magnification microscopy was performed using a Nikon SMZ 1000 stereo-microscope allowing for examination of samples at magnifications between 10x and 40x. Medium-magnification (50x–500x) microscopy work was performed using an Olympus PMG3 optical microscope.

Scanning Electron Microscopy (SEM) and Energy Dispersive Spectrum (EDS) Analysis

High-magnification microscopic examination (500x–40,000x) was carried out using two individual scanning electron microscope (SEM) units to generate secondary electron (SE), backscattering electron (BSE) images, and energy dispersive x-ray spectrometry data. Approximately half of the SEM evaluation was performed on a Philips XL30S Schottky-based field emission gun (FEG) SEM (Figure 36) coupled with a Phoenix EDS detector system with the capability of detecting oxygen. The latter half was performed using a Hitachi S-570 tungsten filament thermionic emission gun SEM (Figure 37) coupled with a Link Systems LX-5 model 5697 EDS detector that is controlled by a Mektech EDS Ultra Rapid Spectrum Analyzer system.

The EDS systems used in this work were subject to several critical limitations. The EDS system integrated with the Hitachi microscope cannot detect oxygen at all, however the newer EDS system coupled to the Philips SEM has this ability. The second limitation, common to both systems, is the use of standardless quantification.

Using a standardless approach for quantification means that the detected spectrum is compared to a model that serves as the standard, instead of applying an improved Castaing standards/matrix corrections method. Using a standardless approach may lead to the introduction of relative errors of approximately $\pm 25\%$ for 95% of the analyses [73]. A third limitation stems from inherent operating characteristics of an EDS system. A two-dimensional representation of a pear-shaped ionization diagram is illustrated in Figure 38, illustrating the relative penetration depth of various signal-types probing a solid surface. The EDS system coupled to both the Philips and Hitachi SEM, exhibits a spot size (for an EDS spot scan) of approximately $0.5 \mu\text{m}$ in diameter with a pear width of approximately $5 \mu\text{m}$ and a penetration depth of the characteristic x-rays of approximately $10 \mu\text{m}$ [73–75]. Since the thermally-grown oxide films have thicknesses of a few microns, it is probable that the EDS spectra obtained from surface features contained information pertaining to both the oxide layer as well as the underlying material. Due to these limitations and characteristics of the EDS systems used, accurate quantification and identification of coating or oxide constituent phases was not possible with EDS alone, requiring other analytical tools such as XRD for positive identification. EDS can, however, give a qualitative indication of the element (or elements) associated with a particular morphological structure in the sample.

4.5.2 X-ray Diffraction (XRD) Analysis

For this work, XRD analysis was used in a qualitative capacity in conjunction with EDS surface results for the respective samples. The EDS results were used to estimate the possible oxide compositions, allowing for spectrum comparison between powder diffraction file (PDF) standards (Appendix B) and published XRD spectra.

XRD analysis was performed at NRC's Institute for Chemical Process and Environmental Technology (NRC-ICPET) using a Bruker AXS D8 Discover diffractometer



Figure 36: Philips XL30S FEG SEM with Phoenix EDS detector system.

controlled with General Area Detector Diffractometer Software (GADDS). Samples were cut into 15 mm x 20 mm x 2.8 mm pieces and scanned in parallel-beam mode with 40 kV Cu-generated x-rays from angles in the range of $20\text{-}100^\circ 2\theta$.

XRD analysis was performed on a selection of test specimens at specific specimen conditions. The spectra from the as-deposited conditions of the three MCrAlY-coated specimens were used as a baseline of comparison to the spectra of two heat treatment conditions: vacuum heat treatment of 1100°C for 1 hour, and air furnace heat treatment of 1050°C for 5 hours. In addition, the Hastelloy-X substrate was also analyzed in the same conditions as previously mentioned, with one difference. Rather than using the as-received material as a baseline for comparison, a bare Hastelloy-X specimen was first air furnace heat treated at 1000°C for 10 hours and subsequently ground with 1200 grit silicon carbide paper to remove all visible traces of surface oxides. This was done to precipitate secondary phases, such as carbides, which tend to form

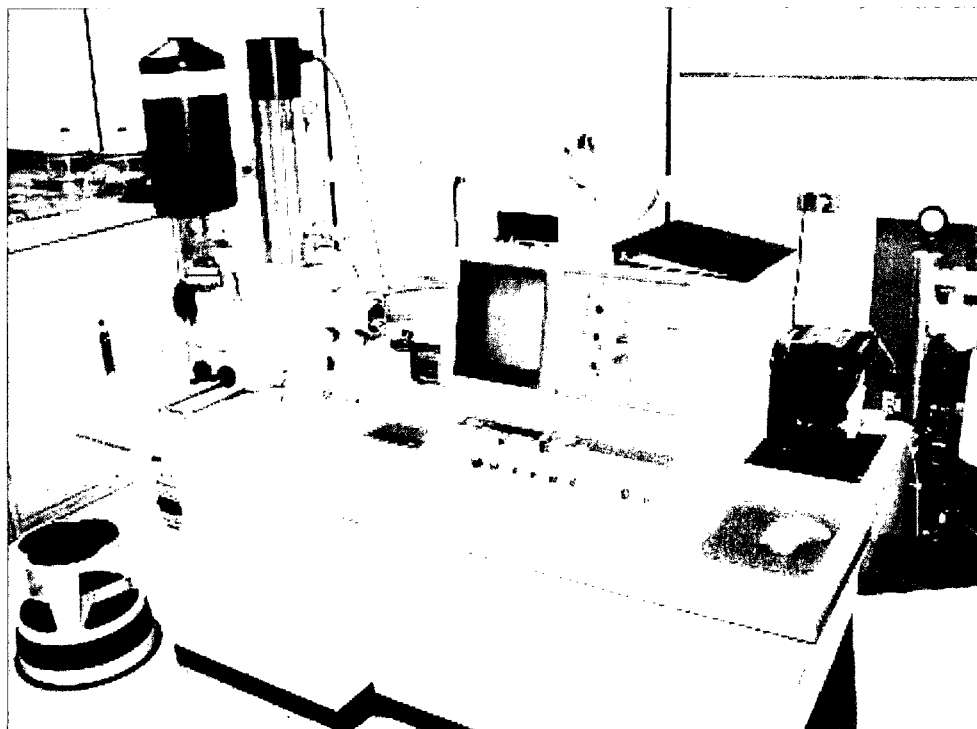


Figure 37: Hitachi S-570 tungsten filament thermionic emission gun SEM with Link Systems LX-5 model 5697 EDS detector system.

between 538–1093°C [57]. This heat-treated baseline XRD spectrum, with secondary phases but without surface oxides, was necessary as there was no PDF standard or otherwise published XRD spectrum for Hastelloy-X known to the author at the time of writing.

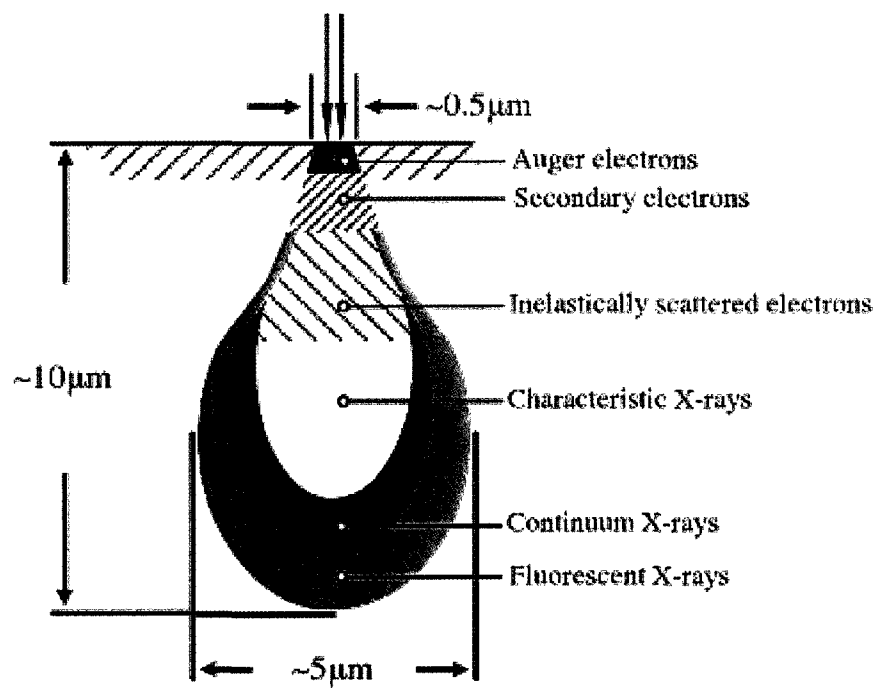


Figure 38: Characterizing pear-shaped ionization diagram for relative penetration volumes for various incident energy beam types. Adapted from [76].

Chapter 5

Results and Discussion

This chapter presents the results of both PVD FeCrAlY coating trials and the pre-oxidation heat treatment results for the MCrAlY-coated Hastelloy-X substrates. The results presented in this chapter are based on scanning electron microscopy (SEM), energy dispersive spectroscopy (EDS), and X-ray diffraction (XRD) analysis of the substrates and MCrAlY-coated test specimens in as-received/as-deposited condition, together with those subject to both vacuum and air furnace pre-oxidation heat treatments. SEM analysis was used to generate secondary electron (SE) and backscattering electron (BSE) micrograph images of surface and cross-sectional features present in the test specimens. EDS analysis was used, in conjunction with SEM, to correlate relative compositional information with the morphological features seen in the SEM micrographs. EDS spot scan locations are marked in the micrographs containing the measured feature with a circular label. The square labels in the micrographs indicate features of note, which do not have any associated compositional EDS data. XRD analysis was used to provide through-surface crystalline structure information in terms of the phases present in the specimens that could be further correlated to both SEM and EDS results.

As two different SEM/EDS systems were used to obtain the results presented in this work (see **Materials and Experimental Procedures** chapter), an attempt was

made to normalize the data to make comparison across these two systems feasible. Differences in the capability of the two different SEM/EDS systems include significant variation in SEM micrograph image quality and format, as well as differences in EDS detector accuracy and the ability of the EDS detector to measure the presence of oxygen. To overcome the differences in SEM micrograph format, a common micrograph image size was chosen. Where at all possible, comparable image magnification rates were maintained to allow for direct comparison of microstructural features on the test specimen surface and in the specimen cross-section. To overcome differences in EDS system capabilities, only the metallic elements present in the EDS spectra were quantified and tabulated with an exception in the case that the EDS spectrum contains peaks pertaining to the presence of only one metallic and one non-metallic element. When non-metallic elements are present in the EDS spectrum, their presence is noted in the table containing the quantified element concentrations. Although one of the EDS systems used cannot detect the presence of oxygen, it is assumed that oxygen is present in both the as-deposited thermally-sprayed test specimens and all test specimens that have been subjected to a heat treatment in a vacuum or air environment.

This chapter begins with an examination of the as-received Hastelloy-X substrate material in order to establish a baseline for comparison to the pre-oxidation heat treated test specimens. The Hastelloy-X substrate material was also analyzed after select vacuum and air furnace heat treatments for comparison with the results yielded by the heat treated MCrAlY-coated test specimens.

After examination of the substrate material, the results for both cathodic arc (CA) and magnetron sputtering (MS) PVD coating trials, performed in NRC-IAR's PVD coating facility, are presented. The failed CA-PVD FeCrAlY deposition trial and the limited success of the MS-PVD FeCrAlY deposition trial are listed and discussed in terms of the process parameters varied during the coating trials, the problems

encountered, and possible explanations for the occurrence of these problems. In addition, the deposited MS-PVD FeCrAlY bond coat layer is characterized.

Finally, the results for the MCrAlY-coated test specimens, in both as-deposited and in heat treated conditions are presented. The results are presented by means of SEM micrographs of microstructural features on the test specimen surface and cross-section. The distribution of elements on both specimen surface and cross-section was provided by means of EDS surface area scan and spot scan measurement data. The test specimens consisted of Hastelloy-X substrates that were coated with the following MCrAlY bond coats:

- magnetron sputtering PVD-deposited FeCrAlY,
- air-plasma sprayed (APS) NiCrAlY
- high-velocity oxy-fuel (HVOF) sprayed CoNiCrAlY.

A total of 9 heat treatment conditions were applied to each of the three different MCrAlY-coated test specimens. The results from each heat treatment series are presented individually, and a summary concludes each respective heat treatment series sub-section, listing the trends observed. The six vacuum furnace pre-oxidation heat treatments (VHTs) consisted of the following conditions:

- 1000°C for 10 and 15 hours
- 1050°C for 5 and 10 hours
- 1100°C for 1 and 5 hours

The 3 air furnace pre-oxidation heat treatments (AHTs) consisted of the following conditions:

- 1000°C for 10 hours

- 1050°C for 5 hours
- 1100°C for 1 hour

Finally, XRD analysis results are presented for the three different types of MCrAlY-coated test specimens. Three conditions were selected:

- as-deposited condition
- VHT of 1100°C for 1 hour
- AHT of 1050°C for 5 hour

5.1 Hastelloy-X Substrate

The Hastelloy-X substrate material was examined in as-received and heat treated conditions to establish a baseline for comparison when interpreting the results from the MCrAlY-coated test specimens. Exposing Hastelloy-X to vacuum and air furnace heat treatments also allowed for the examination of the native thermally-grown oxides (TGOs) that are typically formed when the high-temperature structural alloy is exposed to these conditions.

The surface and cross-sectional properties were investigated through SEM and EDS analysis in the following four conditions:

- as-received condition
- vacuum furnace heat treatments of 1000°C for 15 hours and 1100°C for 1 hour
- air furnace heat treatment of 1000°C for 10 hours

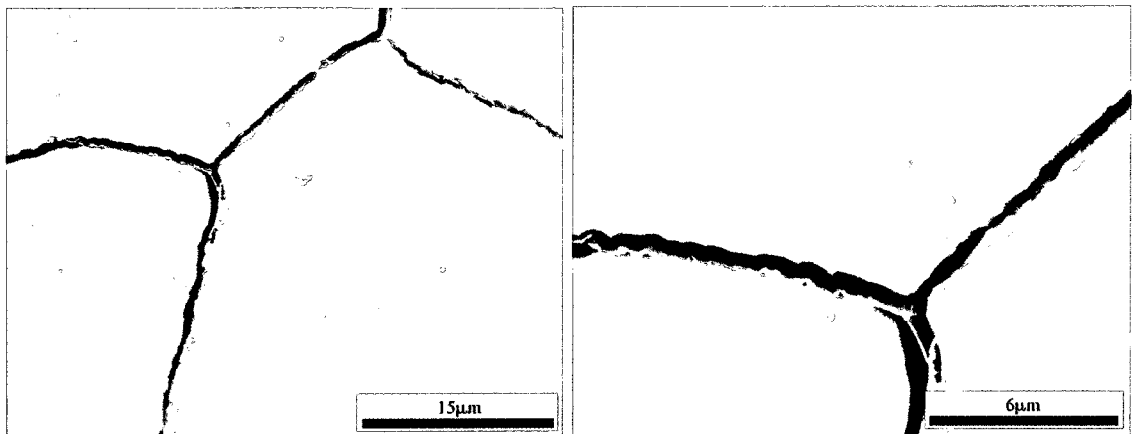
5.1.1 As-received Condition

The as-received Hastelloy-X substrate material was polished and lightly etched with a mild acid solution to expose the grain boundaries. A SE micrograph of this condition is shown in Figure 39. As expected, the wrought, as-received Hastelloy-X exhibits a single phase microstructure in its solution-treated condition. The solution heat treatment, which involves holding the material at a temperature of 1177°C, is used to dissolve all precipitates. A subsequent rapid cooling sequence is then applied, which prevents the precipitation of carbide phases that tend to decrease toughness and corrosion resistance of the material [57].

The composition of the as-received Hastelloy-X material, as listed in Table 15 is quite similar to the standard nominal composition provided by the manufacturer (Table 4), with small discrepancies in the measured values that can be accounted for due to the known inaccuracy of the EDS equipment. While minor alloying elements such as cobalt, tungsten, carbon, manganese, silicon, and boron are likely present in the composition, their relative concentrations are below the detection threshold of the EDS equipment used.

Table 15: EDS surface area scan data for region shown in Figure 39a (in wt%).

Ni	Cr	Fe	Mo
54.73	22.22	16.97	6.07



(a) A SE micrograph showing the microstructure of the as-received substrate material.

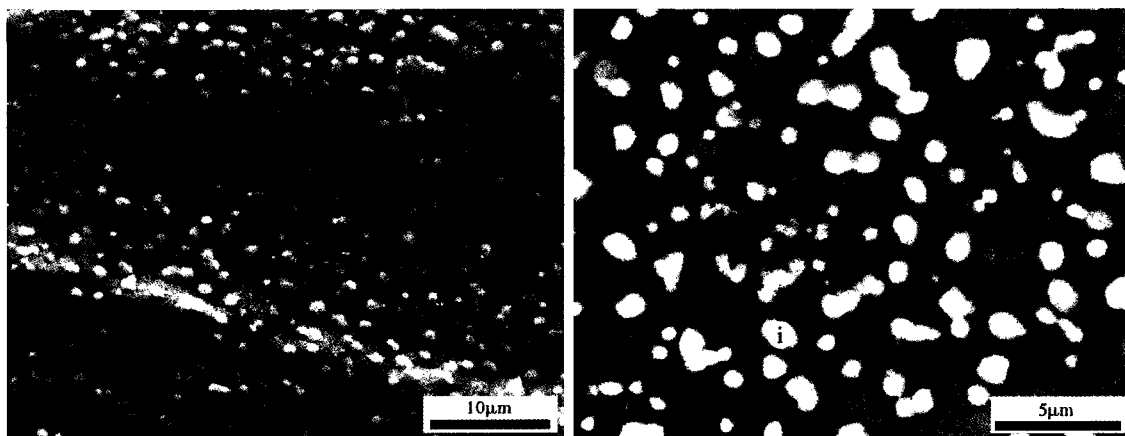
(b) A detailed view of the grain boundaries of the as-received substrate material.

Figure 39: Hastelloy-X substrate material in as-received condition, etched with a mild acid solution to expose grain boundaries.

5.1.2 Vacuum Furnace Heat Treatments

After a vacuum heat treatment (VHT) of 1000°C for 15 hours, the surface of the Hastelloy-X is covered by fine, evenly dispersed, globular particles that tend to preferentially form along the grain boundaries of the Hastelloy-X material, as shown in Figure 40. Macroscopically, the heat-treated specimen presented a dull, matte surface in contrast to the polished surface finish that existed before the heat treatment. EDS spot scan data for the location marked in Figure 40b, listed in Table 16, indicates that these particles are more rich in molybdenum and silicon than the average surface composition of the test specimen, suggesting the preferential oxidation of both molybdenum and silicon to MoO_2 and SiO_2 , respectively. Even though the heat treatments were performed in a vacuum (between 10^{-6} and 10^{-5} torr) environment, there was still sufficient oxygen remaining to react with some components of the Hastelloy-X material.

A cross-sectional micrograph of a Hastelloy-X specimen that has been subjected to a VHT of 1100°C for 1 hour (Figure 41) shows the lack of any visible TGO growth. The cross-section does, however, show the precipitation of darker, spherical secondary phases in the bulk specimen material that are thought to be precipitated carbides, as is expected as a result of heating above 538°C [59]. Although the VHT temperature of 1100°C is adequate to solutionize the Hastelloy-X material, it is believed that the slow cooling after heat treatment is gradual enough to allow for the precipitation of these carbide phases.



(a) A SE micrograph showing molybdenum-rich particles that appear to grow on the surface of the Hastelloy-X material. (b) A high-magnification BSE micrograph showing the bright molybdenum-rich particles on Hastelloy-X material. Marker (i) indicates EDS spot scan location.

Figure 40: Surface features on the Hastelloy-X substrate material after a VHT of 1000°C for 15 hours.

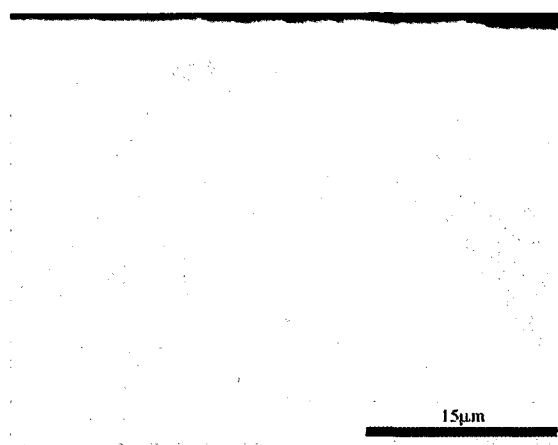


Figure 41: A cross-sectional SE micrograph showing the microstructure of the Hastelloy-X substrate material after VHT of 1100°C for 1 hour. The brightening effect visible along the specimen surface is attributed to an edge effect.

Table 16: EDS surface area scan data for region shown in Figure 40a and spot scan data for location marked in Figure 40b (in wt%).

	Ni	Cr	Fe	Mo	Co	Si
surface	44.97	19.57	16.97	15.29	1.76	1.45
(i)	24.28	13.84	7.18	48.82	1.53	4.35

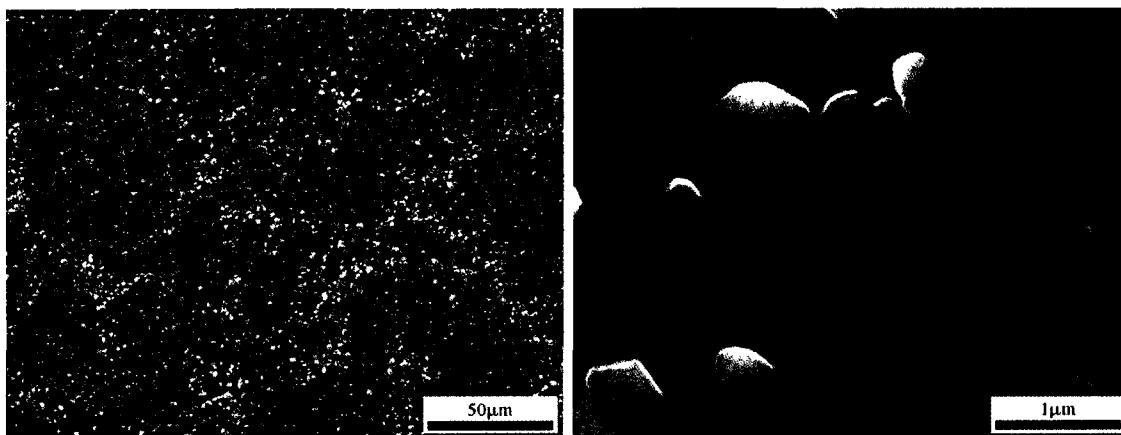
Note: While not quantified, the EDS spectra also indicate presence of O in both cases.

5.1.3 Air Furnace Heat Treatments

Exposure of Hastelloy-X to an air furnace heat treatment (AHT) of 1000°C for 10 hours produces a black, dense, and adherent TGO layer, as shown in Figure 42a. The micrograph clearly shows preferential oxide growth along the grain boundaries of the underlying Hastelloy-X material. The high-magnification micrograph in Figure 42b) shows the dense globular structure of the TGO. EDS surface area scan data (Table 17) indicates the exclusive presence of chromium and oxygen, leading to the assumption of Cr_2O_3 TGO formation.

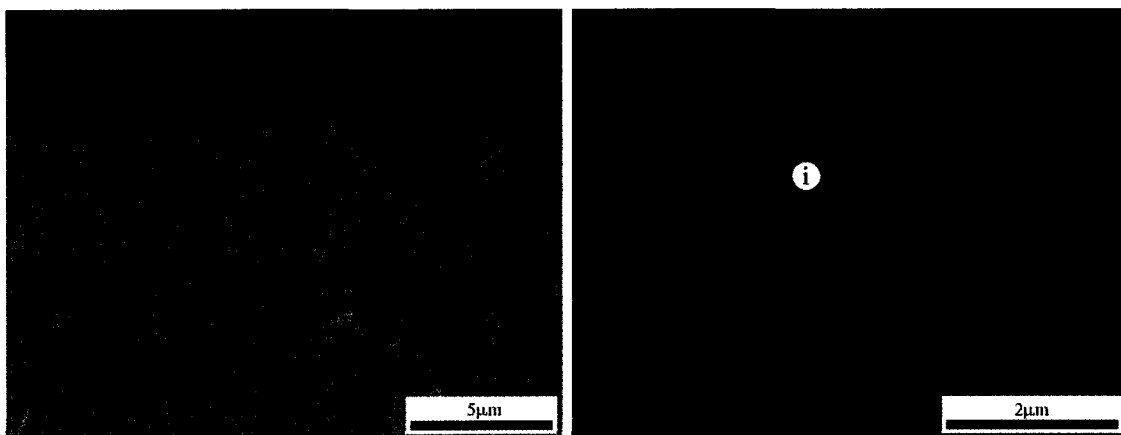
A cross-sectional view of the 1000°C/10 hr AHT Hastelloy-X specimen (Figure 43) shows the presence of a dense and continuous TGO with an average thickness of 2.6 μm . Table 18 lists the compositional EDS spot scan data for the location marked in Figure 43b, indicating the exclusive presence of chromium and oxygen, which agrees with the surface composition of the TGO. The high-magnification micrograph in Figure 43b also indicates the presence of what appears to be a second phase between the Hastelloy-X substrate and the Cr_2O_3 TGO. It was not possible, however, to further confirm the composition of the second phase as it was too small (less than 0.5 μm in thickness) to be detected accurately using available analysis techniques.

Although the Cr_2O_3 TGO layer is dense, continuous, and adherent, it is not suitable for use as both an electrically insulating and an oxidation-resistant bond coat layer at temperatures above 900°C. Above this temperature, the Cr_2O_3 layer forms volatile CrO_3 , that evaporates away, thinning the corrosion-resistant layer. In addition, at temperatures above 1000°C, the electrical resistivity steadily decreases from $1 \times 10^2 \Omega\text{-cm}$ [15], as opposed to an Al_2O_3 layer that maintains an electrical resistivity of $1 \times 10^{14} \Omega\text{-cm}$ at this temperature.



(a) A low-magnification SE micrograph of the TGO, showing larger oxide particles along the former grain boundaries of the Hastelloy-X material. (b) A high-magnification SE micrograph showing the globular morphology of the TGO.

Figure 42: Surface features on the Hastelloy-X substrate material after an AHT of 1000°C for 10 hours.



(a) A SE micrograph showing a dense and continuous TGO layer with average thickness of 2.6 µm. (b) A high-magnification SE micrograph showing the presence of a second oxide phase between the predominant oxide phase of the TGO and the Hastelloy-X substrate. Marker (i) indicates EDS spot scan location.

Figure 43: Cross-sectional features on the TGO layer on the Hastelloy-X substrate material after an AHT of 1000°C for 10 hours.

Table 17: EDS surface area scan data for region shown in Figure 42a (in wt%).

	Cr	O
	67.05	32.95

Table 18: EDS spot scan data for region shown in Figure 43b (in wt%).

	Cr	O
i	67.59	32.41

5.1.4 XRD Results

XRD spectra for the following Hastelloy-X sample conditions are shown in Figure 44:

- an AHT at 1000°C for 10 hours followed by thorough removal of surface oxides
- a VHT of 1100°C for 1 hour
- an AHT of 1050°C for 5 hours

The test specimen that was subjected to an AHT of 1000°C for 10 hours, followed by thorough oxide removal, was devised to yield a microstructure in the Hastelloy-X that included the secondary phases (carbides such as M_6C and $M_{23}C_6$) and the σ -phase that precipitate as a result of heat treatment above at least 538°C and subsequent slow furnace cooling. The σ -phase is an embrittling, chromium/molybdenum-rich phase that belongs to the Fe-Cr-Mo alloy system [77, 78]. As a published XRD spectrum was not available to the author, this specimen was intended to serve as a reference in order to discern the peaks belonging to the Hastelloy-X substrate and those of the overlaid MCrAlY bond coats. The XRD spectrum for this specimen shows the main peaks associated with (A) the parent γ -nickel phase of the Hastelloy-X material, together with several very small peaks that are thought to belong to (B) secondary carbides and/or the σ -phase.

The XRD spectrum for the 1100°C/1 hr VHT test specimen also shows the same predominant γ -nickel phase (A) peaks, together with peaks of the secondary Hastelloy-X phases (B), as seen in the previous reference specimen. In addition, there are three unidentifiable peaks. Although EDS spot scan data for the TGO particles on the sample surface (Table 16) indicate a molybdenum- and silicon-rich composition, no matching peaks for either MoO_2 and SiO_2 can be found.

For the test specimen subjected to an AHT of 1050°C for 5 hours, the XRD spectrum shows (A) the attenuated γ -nickel peaks for the Hastelloy-X substrate material

together with strong peaks belonging to two oxides: (C) CrO and (D) Cr₂O₃ TGO. This correlates with the compositional EDS spot scan data for the surface TGO layer shown in Figure 43b.

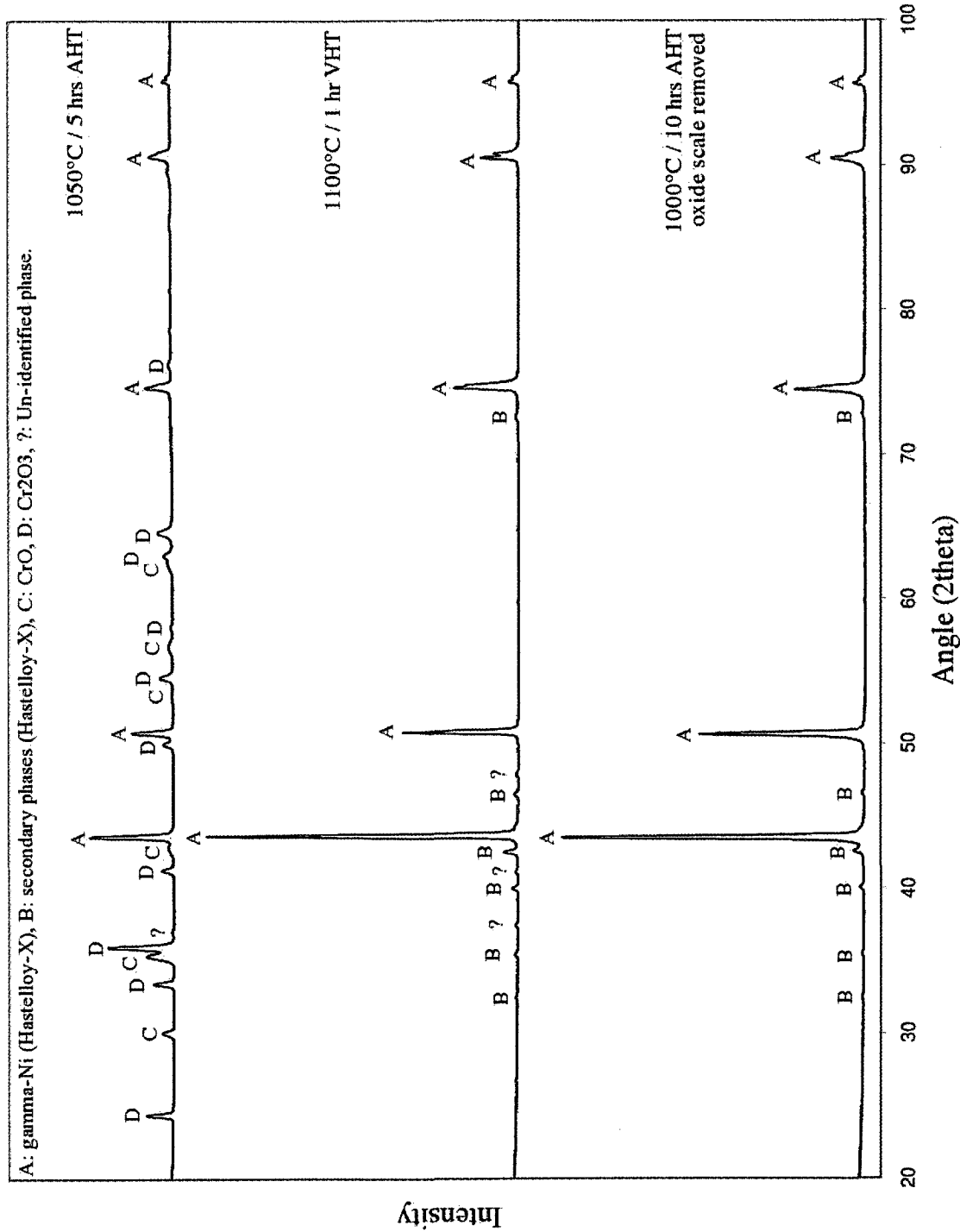


Figure 44: XRD spectra for the bare Hastelloy-X test specimens in the following conditions: AHT of 1000°C for 10 hours (followed by complete oxide scale removal), VHT of 1100°C for 1 hour, and AHT of 1050°C for 5 hours.

5.2 PVD FeCrAlY Bond Coat Deposition

Both cathodic arc and magnetron sputtering physical vapour deposition processes were used to attempt to deposit a suitable FeCrAlY bond coat (BC) layer onto Hastelloy-X substrates. The PVD coating deposition trials were performed using equipment described in the **Materials and Experimental Procedures** chapter. The following sub-sections present the results of both the cathodic arc and magnetron sputtering deposition trials.

5.2.1 Cathodic Arc PVD

The cathodic arc physical vapour deposition (CA-PVD) process was selected for the deposition of a FeCrAlY bond coat onto the Hastelloy-X substrate. The FeCrAlY BC layer was intended to act both as an oxidation / corrosion barrier, as well as an electrical insulation layer for NRC's proposed thin film sensor layer structure, because of its ability to act as a strong α -Al₂O₃ thermally-grown oxide (TGO) former. Detailed information about the CA-PVD equipment used in this work can be found in the **Materials and Experimental Procedures** chapter.

In practice, CA-PVD coatings have shown to be superior in terms of coating density and adhesion to the substrate when compared to thermally sprayed BCs. In previous work by Leontiev et al. [70] and Knotek et al. [79], CA-PVD has been investigated as an alternative to thermal spray (TS) deposition processes by demonstrating the ability to deposit multi-constituent BC materials that are more dense and adherent than coatings produced through TS techniques, and at sufficiently high deposition rates and volumes to make cathodic arc PVD a commercially competitive alternative.

An extensive set of coating trials were performed in this study. During these test

runs, three operating variables of the cathodic arc coating equipment were manipulated: base pressure, operating pressure, and arc current. Base pressure was varied between 2.9×10^{-3} and 7.3×10^{-3} mtorr (3.9×10^{-4} and 9.7×10^{-4} Pa), operating pressure was varied between 7.5 and 37.5 mtorr (1 and 5 Pa), and arc current was varied between 15 and 80 A. All attempted combinations of the preceding operating variables resulted in a failure to produce a suitable coating due to the following complications: unstable arc generation and arc travel leading to preferential evaporation of circular cathode edge, excessive macroparticle ejection, and arcing to stainless steel cathode heat shield. While the coating quality itself was only directly impacted by the formation of excessive macroparticles, the issues of arc instability, undesirable arcing with the cathode heat shield, and the premature cathode degradation prevented the deposition process itself from completion. An example of preferential evaporation of the cathode edge and fusion resulting from arcing to the stainless steel cathode heat shield is shown in Figure 46a, where the severely degraded cathode is compared to a fresh, un-used cathode.

Unstable arc travel and macroparticle ejection can be attributed to a relatively non-homogeneous cathode composition resulting in preferential and explosive evaporation of the lower melting point constituents (such as aluminum or FeCrAlY) in the cathode material, leading to macroparticle formation. It has been shown that inhomogeneities such as pores and poorly distributed cathode alloy phases can lead to consistent arcing of a particular location [80]. This consistent arcing in the same location leads to the formation of craters on the cathode surface, resulting in an unstable arcing behaviour and uneven cathode evaporation. It has also been observed that the arc will preferentially travel along grain boundaries, also resulting in unstable arc behaviour [80]. Similar premature cathode degradation was noted by Knotek et al [79] in a high-chromium MCrAlY cathode after 20 hours of evaporation, where the cathode erosion behaviour was attributed to the hot isostatic pressing (HIP)

treatment used in the manufacture of these cathodes. The HIP treatment can result in a non-homogeneous structure around the periphery of the circular cathode [79]. The majority of cathodes tested by Knotek et al [79], however, showed that it was possible to achieve stable and largely even evaporation of multicomponent cathode compositions using the CA-PVD process.

The FeCrAlY cathodes used for CA-PVD in this work were also vacuum-cast and then subsequently hot isostatically-pressed (HIPed) before machining to final cathode shape. An axial section of the cylindrical FeCrAlY cathode material used in this study is shown in Figure 45. The sputtered surface of this section reveals the grains structure of the cathode as a result of the casting operation, clearly showing the columnar grains that formed radially inward along the solidification front, with a region of coarse, equiaxed grains in the center of the cathode [81]. It is thought that this microstructure might contribute to the problem of unstable arc travel and the exasperation of macroparticle ejection. This microstructure could be improved through a homogenizing heat treatment to attempt to produce a more uniform microstructure throughout the cathode material.

During the course of troubleshooting the arc instability issues, it was also discovered that the FeCrAlY cathode material is inherently ferromagnetic. This ferromagnetic property is thought to also interfere with arc travel as the arc used to evaporate the cathode is sensitive to magnetic fields, causing the arc to preferentially travel along the periphery of the cathode. The CA-PVD coater used in this work makes use of permanent ring magnets that have been strategically placed on the backside of each cathode in order to control arc travel on the cathode surface. During several coating trials, it was attempted to change the magnetic field by the addition of commercially-available rare earth magnets together with the complete removal of the coater's permanent ring magnets. None of the modifications applied to the permanent magnet configuration made any discernible improvement over arc travel and arc

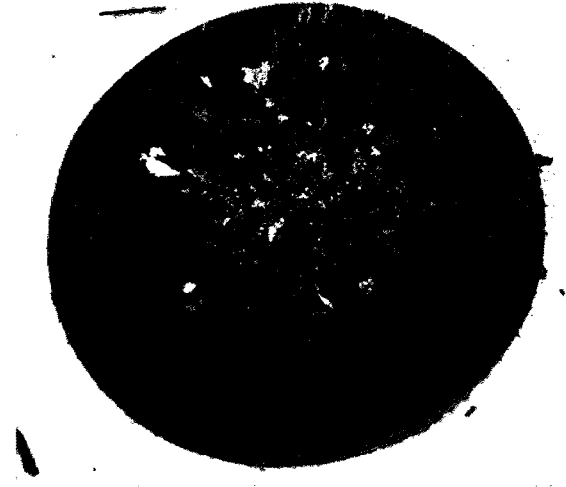
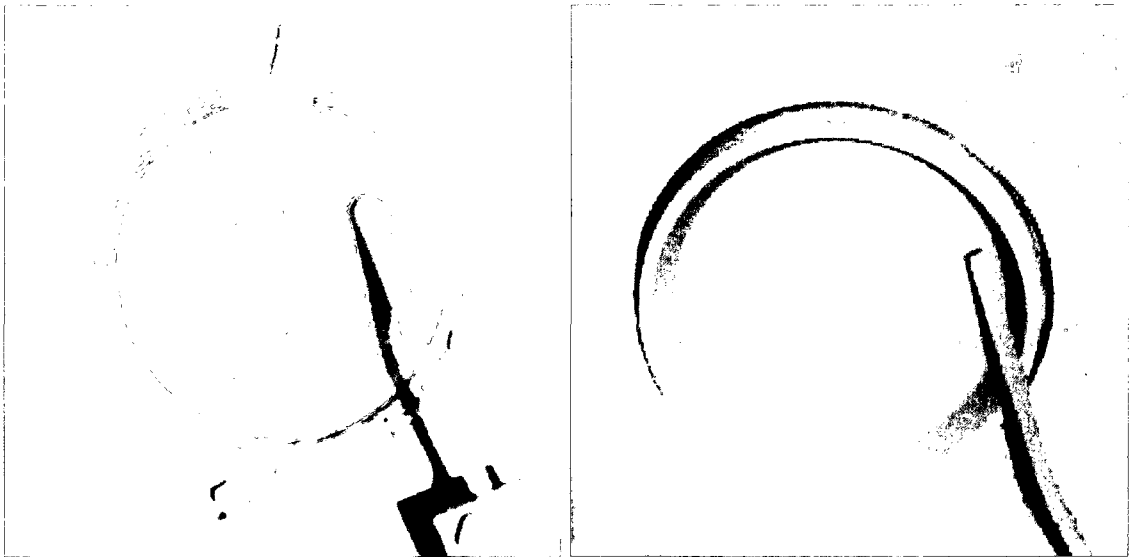


Figure 45: A sputter-polished section of the FeCrAlY cathode material showing the as-cast microstructure.

stability during the coating process.

At higher arc currents (greater than 40 A), it was also noted that arcing had occurred between the cathode and the stainless steel cathode heat shield, causing subsequent fusion between the two components. The result of this phenomena is shown in Figure 46a. Again, this effect is thought to be caused due to the distortion of the 'standard' magnetic field imparted to the permanent ring magnets through the influence of the FeCrAlY cathode material's ferromagnetic properties.

The demonstrated incompatibility of the ferromagnetic FeCrAlY cathode material and the CA-PVD process led to the decision to use an alternative deposition method that was also available at NRC's coating facility. An alternative method of deposition would have to be insensitive to FeCrAlY's ferromagnetic properties while still being able to deposit a dense and adherent bond coat layer onto the Hastelloy-X substrate. This alternative method chosen was the magnetron sputtering PVD process, which is elaborated upon in the following sub-section.



(a) Cathode degradation after only few hours of use. Note fusion of cathode material to stainless steel heat shield and eroded cathode rim.

(b) Standard geometry of a fresh cathode.

Figure 46: Comparison of a severely degraded FeCrAlY cathode to a fresh cathode. Arc-striking mechanism of the CA-PVD coater is shown in the foreground (images courtesy of Q. Yang/R. McKellar, NRC).

5.2.2 Magnetron Sputtering PVD

While magnetron sputtering physical vapour deposition (MS-PVD) can be used to deposit thin, dense, and adherent films, this method has considerably slower material deposition rates on the order of $0.5 \mu\text{m/hr}$ in comparison to CA-PVD deposition rates around $25 \mu\text{m/hr}$. The MS-PVD equipment used also did not have a substrate heater that could be used to decrease the coating stresses that result from the deposition. On a beneficial note, the MS-PVD coatings exhibit a greater density than their CA-PVD counterparts, and the MS-PVD process does not suffer from macroparticle formation problems.

To avoid having to purchase a FeCrAlY sputtering target at considerable cost and lead time, a composite target was devised, making use of available materials. The composite target consisted of a standard aluminum sputtering target to which thin FeCrAlY wafers were adhered in a square pattern. Detailed information about the MS-PVD equipment and target arrangement used in this work is described in greater detail in the **Materials and Experimental Procedures** chapter. The following sub-sections will describe the deposition process of the MS-PVD FeCrAlY bond coat onto the Hastelloy-X substrate material, as well as the properties of the as-deposited coating using SEM and EDS tools.

Deposition Process

The evaluation of a coating run was generally based on the criteria that the run had to make it through the complete deposition program without run stoppage and that the coating had to show no obvious signs of spallation after removal from the PVD chamber.

The greatest impediment to running a complete PVD program was that the magnetron reached excessive voltages while trying to meet the desired current settings,

generally resulting in automatic shut-down of the coating system in order to prevent potential damage to the magnetron. In the cases where the desired deposition current could be reached, there was often significant unstable current pulsing, whose cause has not been explained.

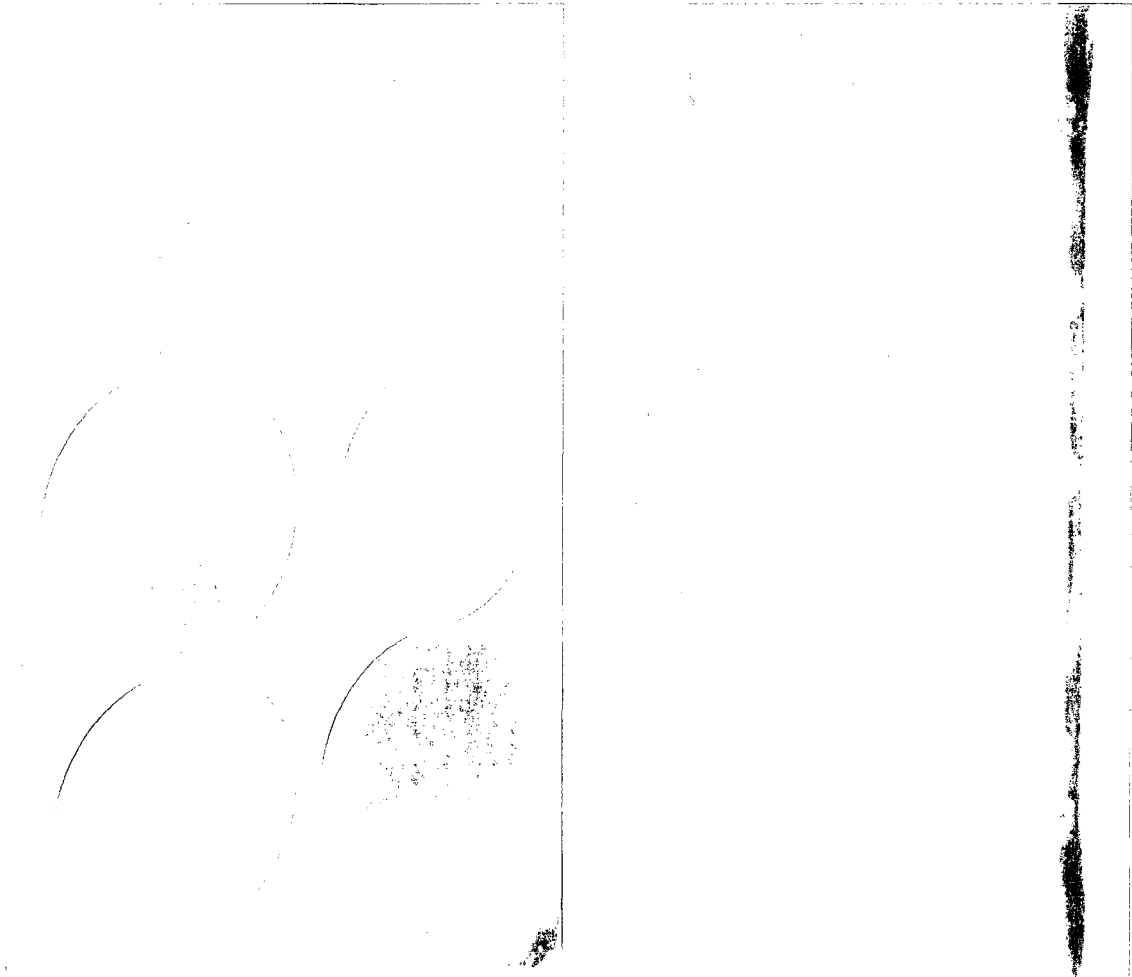
Attempting to run the coater with currents in excess of 1 A resulted in a breakdown in magnetic attraction that supported the circular FeCrAlY wafers on the aluminum magnetron target. This caused the FeCrAlY wafers to slide down the vertical face of the aluminum sputtering target and fall to the bottom of the deposition chamber, moving them from the influence of the magnetically-confined plasma region. Removing the FeCrAlY wafers from the plasma region effectively excluded them from participation in the sputtering process, resulting in the evaporation of just the aluminum target.

Additionally, it was extremely difficult to repeat the results of a previous successful coating run. This was attributed to the constantly-changing geometry and relative composition of the hybrid FeCrAlY+Al target as a result of un-even evaporation during the sputtering process. Figure 47 provides a comparison between the geometry of the fresh hybrid FeCrAlY+Al and another configuration used for a later deposition run. As the sputtering time for a given target assembly elapsed, the FeCrAlY wafers began to lose thickness and the previously sharp edges of the wafer periphery became rounded. This is in contrast to what would occur during the evaporation of a purpose-manufactured planar magnetron sputtering target, which typically wears at a relatively even rate in the vicinity of the oval-shaped, magnetically-confined plasma region. Eventually, the now very thin FeCrAlY wafers became permanently fused to the backing aluminum sputtering target, as shown in Figure 47, requiring that additional fresh wafers be placed on top of them to continue the deposition experiments. These significant changes in target geometry required constant adjustment of the processing parameters to obtain a stable deposition run, making it difficult

to ascertain the effects of each process parameter on the outcome of the deposited coating.

Of the coating runs whose deposition program was able to go to completion, a significant number of test specimens suffered from spallation of the coating. In some cases, the coating had separated from the substrate even before the removal of the coated specimen from the PVD chamber, and in other cases, the coating spalled off at some time after removal from the chamber but before further processing. Further processing of the test specimens for heat treatment and analysis required sectioning of the coated substrate into smaller pieces using a diamond sectioning saw (see **Materials and Experimental Procedures** chapter). The vibration caused by this sectioning process seemed to also lead to coating spallation. The exact cause of the premature coating spallation is not known, but several factors are thought to contribute. These factors include excessive internal stresses between the coating and the substrate as a result of the deposition process and the presence of contamination on the substrate surface as a result of pre-deposition surface processing and/or insufficient cleaning of the substrate before coating deposition.

A small quantity of the MS-PVD FeCrAlY-coated test specimens were suitable for further heat treatment processing and analysis. The MS-PVD processing parameters for the successful coating runs are listed in Table 19. The following sub-section describes the as-deposited MS-PVD FeCrAlY coating structure.



(a) Four fresh FeCrAlY wafers mounted on a lightly-used aluminum magnetron sputtering target, showing oval sputtering wear track. (b) Six partially depleted FeCrAlY wafers placed on top of four expended wafers, mounted to the aluminum magnetron sputtering target.

Figure 47: Comparison of geometry changes in the hybrid FeCrAlY+Al target with use (images courtesy of Q. Yang/R. McKellar, NRC).

Table 19: Magnetron sputtering PVD process parameters for successful coating runs.

	M081118a	M090119a	M090225a
Run Time	36 hrs		
Base Pressure	1.7×10^{-6} torr	1.6×10^{-6} torr	1.7×10^{-6} torr
Operating Pressure	2.8×10^{-3} torr	2.8×10^{-3} torr	1.8×10^{-3} torr
Ar Flow Rate	25 sccm		
Magnetron Current	1 A		
Magnetron Voltage	635 V	635 V	638 V
Substrate Bias	-25 V		

Coating Characterization

Following a successful coating run, after which it was possible to section the FeCrAlY-coated test specimen without spallation, the test specimens were examined using SEM, EDS, and XRD analysis techniques. It is important to note that the average coating composition varied for reasons explained in the previous sub-section. General coating structures, however, appear to be largely similar for all three successful coating runs. In this sub-section, the results of the as-deposited test specimen analysis for coating run M081119a are described in terms of surface and cross-sectional features of the test specimen.

SEM/EDS examination of the magnetron sputtering PVD FeCrAlY bond coat surface indicates a continuous and dense layer with the the surface morphology shown in Figure 48. The compositional EDS area scan results for this surface are listed in Table 20. A thorough examination of the coating surface did not yield any coating imperfections such as cracking, macroparticle inclusion, foreign debris, or other defects. The surface composition of the FeCrAlY coating is significantly higher in aluminum and chromium contents and lower in iron contents than the cathode feedstock originally purchased for the CA-PVD coating trials (see Table 5. This higher aluminum contents was expected due to the use of the hybrid FeCrAlY+Al sputtering target. This target arrangement resulted in a higher proportion of aluminum-containing material to be placed in contact with the magnetically-confined plasma region, the region where the sputtering process predominantly takes place. This, in turn, will result in the deposition of higher amounts of aluminum onto the substrate. While yttrium is likely present in the as-deposited BC layer, its concentrations fall below the detection limit of the EDS equipment used. Also, a significant presence of an argon peak in the EDS surface scan spectrum was noticed. The effects of this plasma-forming argon sputtering gas inclusion into the FeCrAlY coating structure and its effects on the

outcome of the pre-oxidation heat treatments of the test specimens will be further examined in a subsequent section.

A cross-sectional examination of the as-deposited FeCrAlY coating yields an average coating thickness of approximately 20 μm after a 36 hour deposition time for an average material deposition rate of 0.56 $\mu\text{m/hr}$. It can be seen in cross-sectional micrographs in Figure 49 that the coating microstructure varies as a function of location across the width of the 20 mm substrate. At substrate mid-width (Figure 49c) there appears to be a distinct fir-tree pattern, with angles approximately $30^\circ/150^\circ$. It can be seen that in both Figure 49b and Figure 49d, that one growth pattern direction predominates over the other, depending on the proximity to either of the substrate edges. In both cases, the predominant growth pattern tends to slant away from the edge of the substrate. This change in coating microstructure has been thought to be caused due to the effects of the proximity to the relatively sharp substrate edges that modify the local deposition conditions. The cross-sectional micrographs of Figure 49 also show several distinct horizontal lines, with the most obvious near the top of the coating. These horizontal lines are thought to be due to unexplained fluctuations in the coating processing parameters during the deposition run.

The results of a cross-sectional EDS area scan survey of the regions labeled in Figure 49a and partially shown in Figures 49b-d are listed in Table 21. The compositional changes between the EDS scan locations indicate a symmetrical trend about the vertical substrate centreline, mirroring about the central location (iii). While taking into account the error in the EDS measurement equipment, there is still a noticeable change in composition between the sample centre and the edge locations to either side. Again, it must be noted that a significant argon peak was present in all five cross-sectional EDS spectra, although it was not quantified.

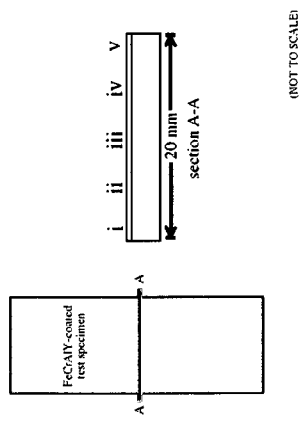
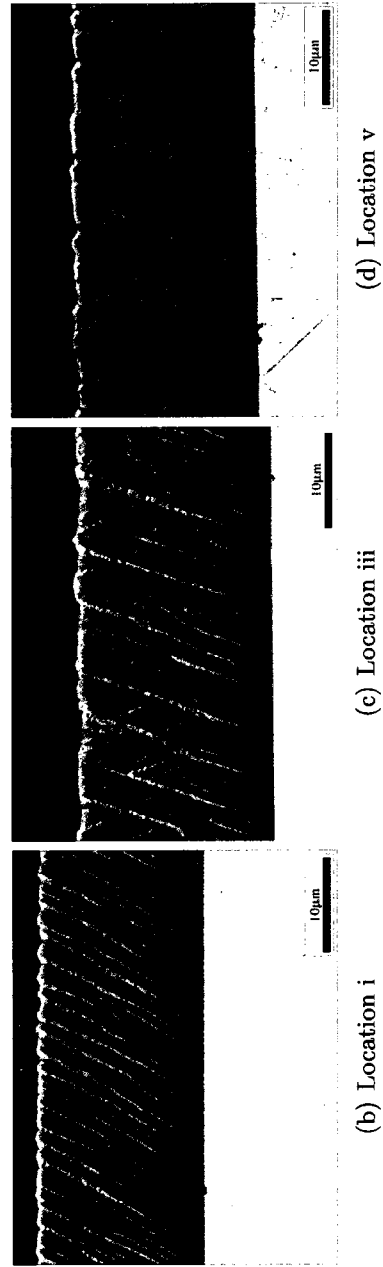
Figure 50 provides a further examination of the light- and dark-shaded coating constituents that make up the fir tree pattern. EDS spot scan data for the locations



Figure 48: A high-magnification SE micrograph showing the surface texture of the MS-PVD deposited FeCrAlY coating for sample number M081119a.

marked in Figure 50 is listed in 23. The EDS spectra indicate only a very small compositional difference between the two coating constituents where the light-shaded regions in Figure 50 contain slightly more chromium and iron than the dark-shaded regions, while the dark-shaded regions contain a slightly higher relative amount of aluminum.

The XRD spectrum for the as-deposited M081119a sample (Figure 75) is quite noisy and shows only two readily identifiable peaks: one at $43.8^\circ 2\theta$ that has been identified as the $\langle 110 \rangle$ peak, and the other at $80.4^\circ 2\theta$ that has been identified as the $\langle 211 \rangle$ peak, both belonging to the α -(Fe,Cr)Al phase of the FeCrAlY material. The lack of other peaks may suggest that the magnetron sputtering PVD process produces preferential growth of the FeCrAlY coating structure in those two directions. The presence of only two peaks pertaining to the same phase indicates that the coating constitutes of just a single phase rather than two phases, as might be suggested by presence of two seemingly different coating constituents that form the fir-tree pattern in Figure 50.



(a) Schematic of sample section location and SEM/EDS analysis locations.

Figure 49: Cross-sectional BSE micrographs showing the different coating microstructures as a function of distance across the substrate width, showing selected views. Average coating thickness is 20 μm .



Figure 50: A high-magnification BSE micrograph showing a detailed view of the light (i) and dark (ii) coating constituents present in the as-deposited MS-PVD FeCrAlY layer. Markers also indicate EDS spot scan locations.

Table 20: EDS surface area scan data for region shown in Figure 48 (in wt%).

Fe	Cr	Al
54.22	29.19	16.59

Note: While not quantified, the EDS spectrum also indicates presence of Ar.

Table 21: Cross-sectional EDS area scan data for the locations shown in Figures 49a with select cross-sectional views shown in Figures 49b-d (in wt%).

	Fe	Cr	Al
i	59.26	20.07	20.65
ii	55.29	18.33	26.38
iii	55.46	18.75	25.80
iv	55.50	18.84	25.65
v	59.39	20.47	20.15

Note: While not quantified, the EDS spectra also indicate the presence of Ar in all cases.

Table 22: EDS spot scan data for locations shown in Figure 50 (in wt%).

	Fe	Cr	Al
i	60.88	21.26	17.86
ii	56.27	19.92	23.81

Note: While not quantified, the EDS spectra also indicate the presence of Ar in all cases.

5.3 Magnetron Sputtering PVD FeCrAlY

In this section, the results of the pre-oxidation heat treatments (both VHT and AHT) on the MS-PVD FeCrAlY-coated test specimens are presented. The results for the VHT and AHT series are listed in a separate sub-section, classified according to ascending temperature and time variables of each heat treatment in the series. Each series is concluded with a summary of the overall trends for each heat treatment series. Heat treatment results are followed by XRD analysis of selected test specimen conditions.

The section begins with an examination of the as-deposited condition of the test specimens produced in the coating run M090225a. The specimens from this coating run are unique to those produced by all other successful coating runs (such as M081119a, presented in an earlier section) in that the Hastelloy-X substrates were not polished to either a 1200 grit or 1 μm surface finish. The substrates used for this particular coating run retained the original surface finish of the as-received Hastelloy-X coupons, which had parallel ridges and grooves in the surface that are thought to have been produced by a surface grinding tool. All MS-PVD FeCrAlY-coated test specimens that underwent the various pre-oxidation heat treatments were deposited in coating run M090225a. For this reason, the surface and cross-sectional features of the as-deposited M090225a are presented additionally to that of M081119a, in order to compare the results of the pre-oxidation heat treatments with that of the as-deposited test specimen condition.

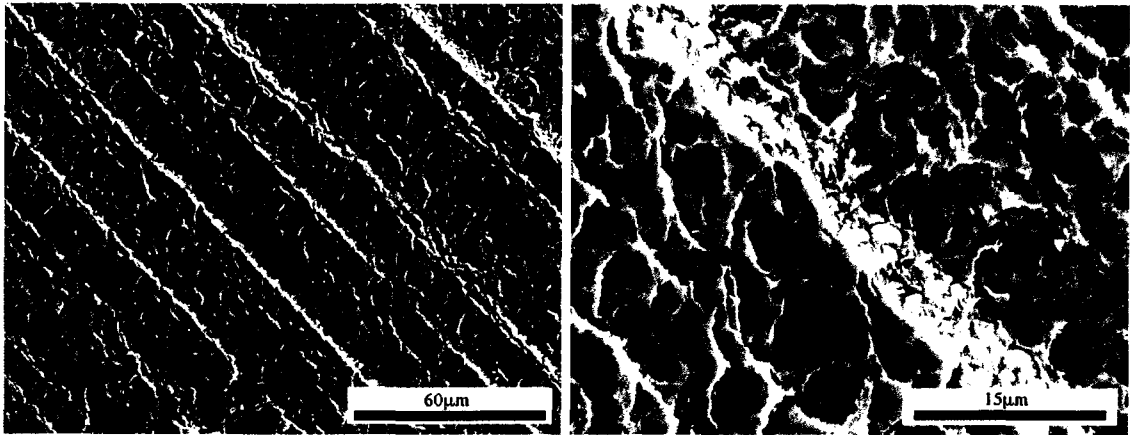
5.3.1 As-deposited Condition

Surface examination of the as-deposited MS-PVD FeCrAlY-coated test specimen (Figure 51) shows an apparent dense and continuous coating layer with a lightly

scalloped surface texture, without any visible coating defects such as cracking or foreign debris. The parallel ridges and grooves that appear to run at an approximate angle of 45° to the horizontal of the micrograph frame are thought to be caused due to machining marks produced by a surface grinding tool on the Hastelloy-X substrate surface. Because the MS-PVD deposition process involves the evaporation, transfer, and deposition of individual atoms from the sputtering target to the substrate, the uniformly-deposited surface will follow the profile of the substrate surface, re-creating the parallel ridge and groove pattern.

EDS surface data for the region shown in Figure 51a (listed in Table 23) indicates that the average composition of the FeCrAlY surface is significantly higher in aluminum concentration than the feedstock FeCrAlY cathode material, which is expected due to the use of the hybrid FeCrAlY+Al sputtering target. Although yttrium is likely present in the deposited coating material, its concentration is below the detection limit of the EDS equipment. The surface composition of this specimen is quite similar to that measured for M081119a, listed in Table 20.

Cross-sectional examination of the as-deposited MS-PVD FeCrAlY-coating test specimen (Figure 52) shows the typical fir-tree patterned coating structure, although somewhat less pronounced than the coating structure shown in the cross-sections from coating run M081119a (Figure 49). The coating layer appears to be dense and adherent, without any visible coating defects in either the substrate/coating interface, inside the coating, or near the coating surface. The average coating thickness is measured to be approximately $30\ \mu\text{m}$, giving an average deposition rate of approximately $0.83\ \mu\text{m/hr}$ over a total deposition time of 36 hours. Compositional data for the specimen cross-section (Table 24) closely agrees with that for the specimen surface (Table 23). It is important to note that both coating surface and cross-sectional EDS spectra indicate a significant presence of argon sputtering gas, the consequences of which will become apparent in the following pre-oxidation heat treatment results.



(a) A SE micrograph showing the general surface features of the as-deposited coating layer. (b) A high-magnification SE micrograph showing the detail of the scalloped surface of the as-deposited coating layer.

Figure 51: Surface features of the as-deposited MS-PVD FeCrAlY (M090225a).

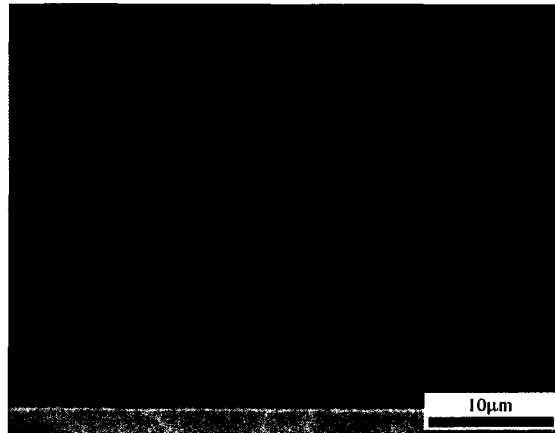


Figure 52: A cross-sectional BSE micrograph showing the coating microstructure of the as-deposited MS-PVD FeCrAlY layer (M090225a). Average coating thickness is 30 μm .

Table 23: EDS surface area scan data for region shown in Figure 51a (in wt%).

Fe	Cr	Al
54.12	29.04	16.84

Note: While not quantified, the EDS spectrum also indicates the presence of Ar.

Table 24: EDS surface area scan data for the cross-sectional area shown in Figure 52 (in wt%).

Fe	Cr	Al
54.37	28.98	16.65

Note: While not quantified, the EDS spectrum also indicates the presence of Ar.

5.3.2 Vacuum Furnace Heat Treatments

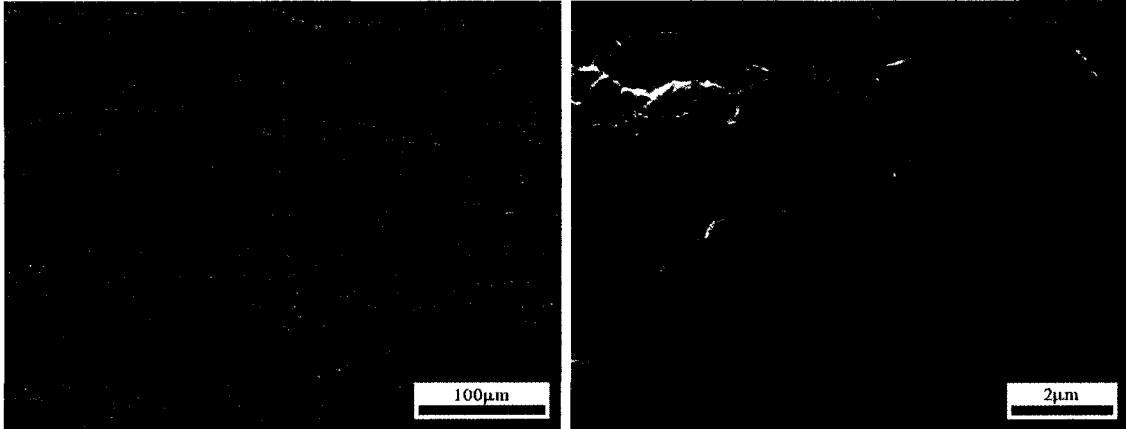
This sub-section outlines the SEM/EDS analysis results in terms of the microstructural features present both on the surface and in the cross-sections of the MS-PVD FeCrAlY-coated test specimens that have been subjected to the pre-oxidation VHTs. The sub-section is concluded with a summary of the trends in the results of the VHT series. The 6 VHT conditions examined are:

- 1000C for 10 and 15 hours
- 1050C for 5 and 10 hours
- 1100C for 1 and 5 hours

1000°C / 10 Hours

After a VHT of 1000°C for 10 hours, the surface of the MS-PVD FeCrAlY-coated test specimen (Figure 53a) shows a highly porous surface across the entire specimen. A high-magnification micrograph of the coating surface (Figure 53b) further confirms the porous nature of the surface. Also present on the specimen surface is the formation of through-thickness cracks in the former BC which seem to form parallel and along the tops of the coating ridges.

Compositional data for the (i) light- and (ii) dark-shaded TGO constituents, shown in the micrograph in Figure 54, is listed in Table 25. The dark-shaded constituent appears to contain higher amounts of aluminum than that of the as-deposited coating composition (Table 25, whereas the light-shaded component contains more iron. EDS spot scan measurement locations (i) and (ii) in Figure 54 both indicate the presence of nickel, while (i) also contains molybdenum. Nickel and molybdenum have diffused from the Hastelloy-X substrate to the specimen surface as a result of the heat treatment. It is important to note that the argon peaks are no longer present in the EDS spectra, in contrast to the as-deposited surface composition.



(a) A SE micrograph showing the general surface condition of the FeCrAlY layer after VHT. Note the details of the TGO surface. (b) A high-magnification SE micrograph showing the formation of bubbling along the coating ridges, together with coating cracking and rupture.

Figure 53: Surface features of the MS-PVD deposited FeCrAlY bond coat after VHT of 1000°C for 10 hours.

A cross-sectional micrograph of the specimen (Figure 55) shows the formation of a multi-layered structure consisting of a (i) highly porous top layer (formerly the bond coat layer), followed by (ii) an interdiffusion layer. In some instances, (vi) large voids have separated the porous top layer completely from the interdiffusion layer and even (iv) the substrate. This porous structure, together with the formation of large voids between the top layer and the rest of the specimen structure, is attributed to the coalescence of argon sputtering gas that was entrapped during the MS-PVD deposition process. A chromium-rich top (σ) phase (iii) has also formed between the interdiffusion layer and the Hastelloy-X substrate. The large white patches (vii) visible in the substrate material consist of a tungsten-rich phase that is frequently present in all specimen cross-sections, regardless of heat treatment condition or MCrAlY coating. Also visible in the substrate is the segregation of heavier (light-shaded) phases to the grain boundaries of the Hastelloy-X material.

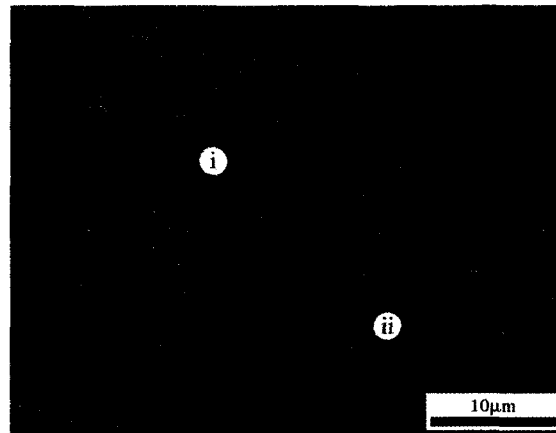


Figure 54: A BSE micrograph showing the two predominant surface oxide constituents typically present on the FeCrALY layer as a result of a VHT of 1000°C for 10 hours: (i) a 'light' iron- and chromium-rich component and (ii) a 'dark' aluminum-rich component. Markers also show EDS spot scan locations.

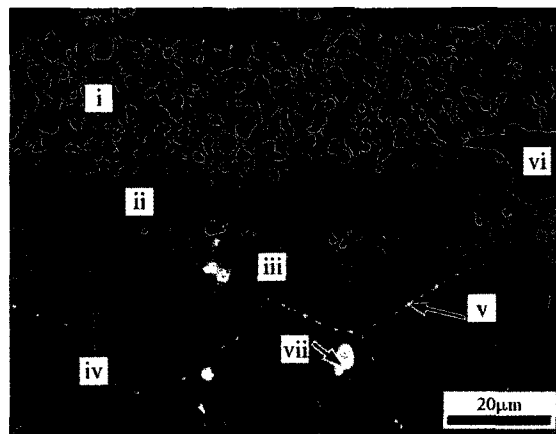


Figure 55: A cross-sectional BSE micrograph showing the formation of three different layers as a result of a VHT of 1000°C for 10 hours: (i) the porous top layer (former BC layer), (ii) an interdiffusion layer, and (iii) an Cr-rich tcp (σ) phase region above (iv) the Hastelloy-X substrate. Also shown is (v) the diffusion of heavier elements to the Hastelloy-X grain boundaries, (vi) voids, and (vii) tungsten-rich patches that are frequently present in the substrate material.

Table 25: EDS surface area scan data for locations shown in Figure 54 (in wt%).

	Fe	Cr	Al	Ni	Mo
i	57.77	21.44	13.88	5.08	1.83
ii	46.52	17.51	29.28	5.68	-

Note: While not quantified, the EDS spectra also indicates the presence of O in both cases.

Table 26: EDS surface area scan data for region shown in Figure 56a (in wt%).

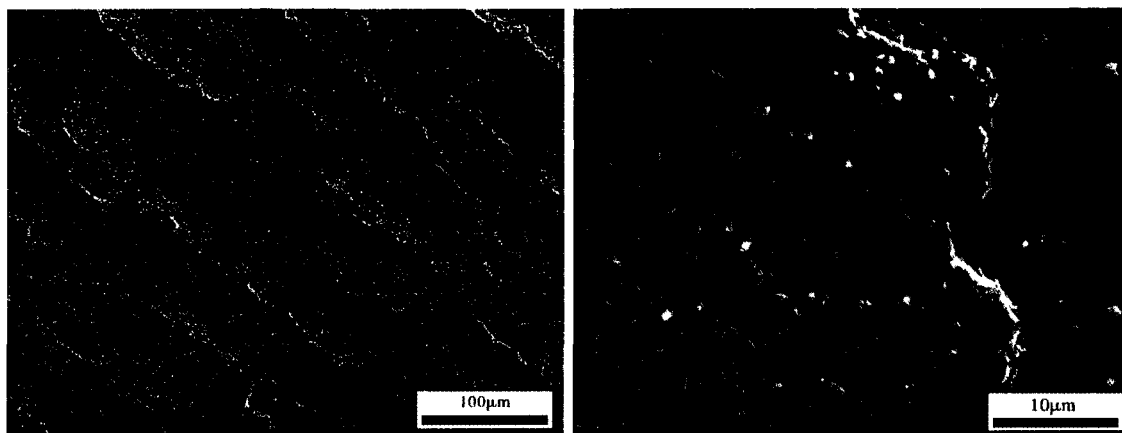
Fe	Cr	Al	Ni	Mo
41.81	24.33	21.52	10.15	2.19

Note: While not quantified, the EDS spectrum also indicates the presence of O.

1000°C / 15 Hours

The surface morphology of the MS-PVD FeCrAlY-coated test specimen that has been subjected to a VHT of 1000°C for 15 hours (Figure 56a) shows a porous layer. Additionally, through-coating cracks are visible that tend to form along the tops of ridges and run parallel to them, although through-coating cracks appear to be less prevalent than that for the 1000°C/10 hr VHT specimen. A high-magnification micrograph of the specimen surface (Figure 56b) provides a detailed view of the porous nature of the surface layer. EDS surface scan data for region shown in Figure 56a, listed in Table 26, indicates a significantly higher proportion of aluminum than present on the as-deposited FeCrAlY coating surface (Table 23). The surface composition also includes both molybdenum and nickel, which have diffused to the TGO surface from the Hastelloy-X substrate. In contrast to the as-deposited surface composition of the FeCrAlY layer, the argon peaks are no longer present.

A cross-sectional micrograph of the test specimen after a VHT of 1000°C for 15 hours (Figure 57) shows a layered structure with three distinct layers: (i) an outer, highly porous top layer (former BC layer) above (ii) an interdiffusion layer, followed by (iii) a layer consisting of a chromium-rich top phase between the interdiffusion layer and (iv) the Hastelloy-X substrate. As in the previous VHT condition, the porosity in the top layer is attributed to the coalescence of escaping argon sputtering gas as a result of the heat treatment. The light-shaded, irregularly-shaped particles (v) that extend between the substrate and the σ -phase are tungsten-rich particles, thought to be refractory phases that are typically present in wrought Hastelloy-X material.



(a) A SE micrograph showing the general surface structure of the TGO. Parallel ridges in the coating surface follow the profile of surface finish machining marks present on the substrate material prior to deposition. (b) A high-magnification SE micrograph showing a detailed view of the porous TGO surface.

Figure 56: Surface features of the MS-PVD FeCrAlY coated test specimen after VHT of 1000°C for 15 hours.

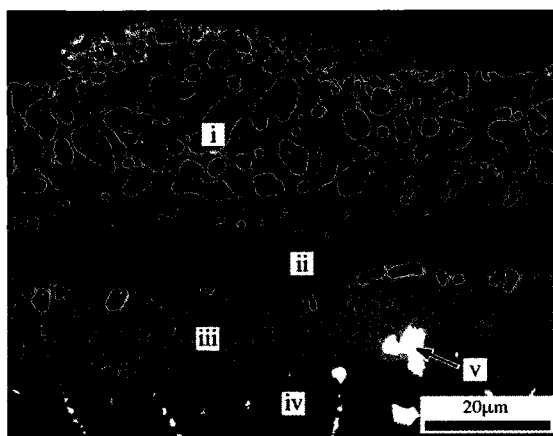


Figure 57: A cross-sectional BSE micrograph showing the formation of three different layers as a result of a VHT of 1000°C for 15 hours: (i) a porous top layer, (ii) an interdiffusion layer, and (iii) a Cr-rich top phase layer between the interdiffusion layer and (iv) substrate material. Light-shaded particles (v) in the substrate material are tungsten-rich.

1050°C / 5 Hours

The surface micrograph of the MS-PVD FeCrAlY-coated test specimen that was subjected to a VHT of 1050°C for 5 hours (Figure 58a) shows a porous surface with surface cracks running parallel along the coating ridges. Although not shown in this micrograph, through-cracks are also present in the sample. A high-magnification micrograph of the coating surface (Figure 58b) shows the presence of porosity in the surface of the test specimen. The compositional EDS surface area data for the region shown in Figure 58a, listed in Table 27, indicates a higher proportion of aluminum in relation to the as-deposited surface composition (Table 23). In contrast to the as-deposited surface composition of the FeCrAlY-coated test specimens, this heat treated specimen does not contain any measurable presence of the argon sputtering gas. Also present on the surface is molybdenum and nickel which have diffused up to the surface from the Hastelloy-X substrate.

A cross-sectional micrograph of the test specimen (Figure 59) shows a layer structure with three distinct layers: (i) a highly porous TGO layer on top (ii) the as-deposited FeCrAlY BC layer, followed by (iii) a porous diffusion layer between the as-deposited FeCrAlY layer and (iv) the Hastelloy-X substrate. EDS spot scan compositional data is listed in Table 28. The porous top layer (i), formerly the bond coat layer, contains predominantly iron and chromium, together with nickel and molybdenum that have diffused to the sample surface from the Hastelloy-X substrate. The interdiffusion layer (ii) contains predominantly nickel that has diffused here from the Hastelloy-X substrate, with remnants of iron, chromium, and aluminum from the as-deposited BC layer. Traces of molybdenum are also present, which have diffused upward from the substrate. The porous structure in the top layer and the interdiffusion layer are attributed to the coalescence of the argon sputtering gas that was

Table 27: EDS surface area scan data for region shown in Figure 58a (in wt%).

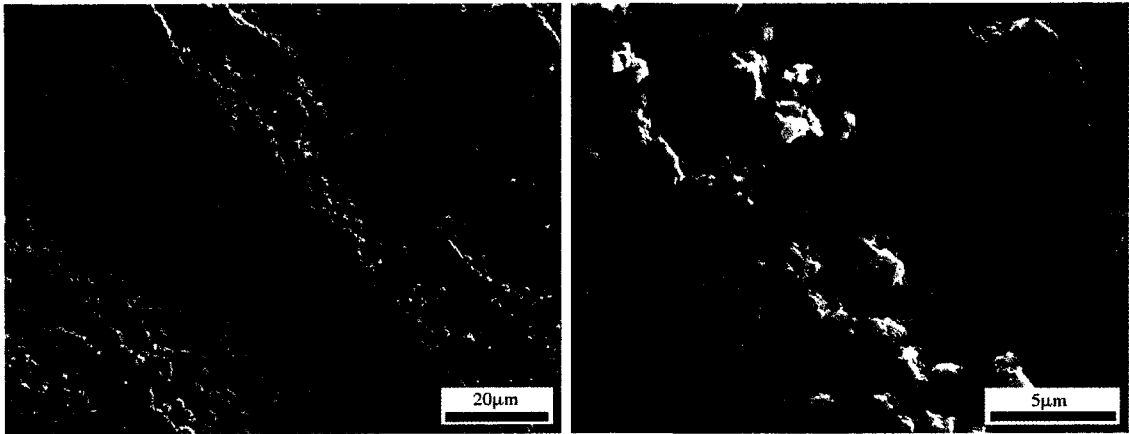
Fe	Cr	Al	Ni	Mo
45.30	22.10	21.31	9.14	2.15

Note: While not quantified, the EDS spectrum also indicates the presence of O.

included in the coating structure during BC deposition. In contrast to the cross-sectional as-deposited composition of the FeCrAlY BC layer (Table 24), the EDS spot scan spectra of all four measurement locations does not indicate any presence of the argon sputtering gas. It is thought that the through-coating cracks are as a result of the coalescence of argon into large voids which bubble up through the coating layer to the specimen surface.

The tcp (σ) phase layer (iii) contains a significant proportion of chromium, iron, and molybdenum, suggesting the downward diffusion of iron and chromium from the as-deposited coating layer, and the upward diffusion of the molybdenum into the diffusion layer from the Hastelloy-X substrate. As indicated in micrographs of preceding heat treatment conditions, the light-shaded particles present in the substrate and the diffusion layer are tungsten-rich phases, a typical constituent found in the wrought Hastelloy-X material used in this work.

The carbon constituent present in all four measurement locations is thought to be due to organic contamination in the porous structure as a result from the SEM sample preparation process where residual grinding and polishing media was not successfully removed after final specimen cleaning.



(a) A SE micrograph showing general TGO surface structure. (b) A high-magnification SE micrograph showing the details of the porous TGO surface structure.

Figure 58: Surface features of the MS-PVD FeCrAlY-coated test specimens after VHT of 1050°C for 5 hours.

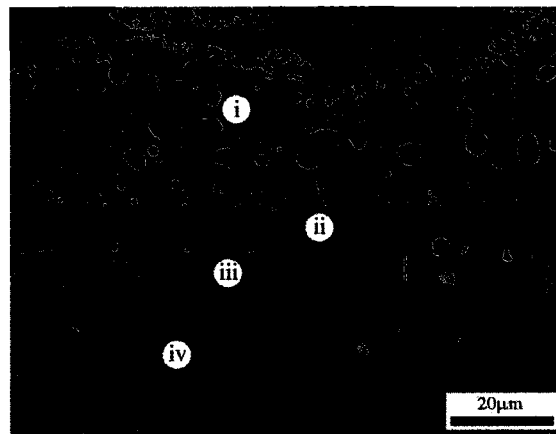


Figure 59: A cross-sectional BSE micrograph showing the four layers present in the MS-PVD FeCrAlY-coated test specimen after VHT of 1050°C for 5 hours: (i) a porous top layer, (ii) an interdiffusion layer, and (iii) a Cr-rich top-phase layer between the interdiffusion layer and (iv) the Hastelloy-X substrate material. Markers also indicate EDS spot scan locations.

Table 28: EDS spot scan data for locations shown in Figure 59 (in wt%).

	Fe	Cr	Al	Ni	Mo	Si	C
i	53.47	24.06	3.46	6.90	3.28	-	8.83
ii	14.49	6.13	19.19	47.13	0.83	-	12.24
iii	34.31	29.80	1.39	9.37	16.32	0.95	7.86
iv	17.53	20.87	0.26	44.79	8.21	0.56	7.78

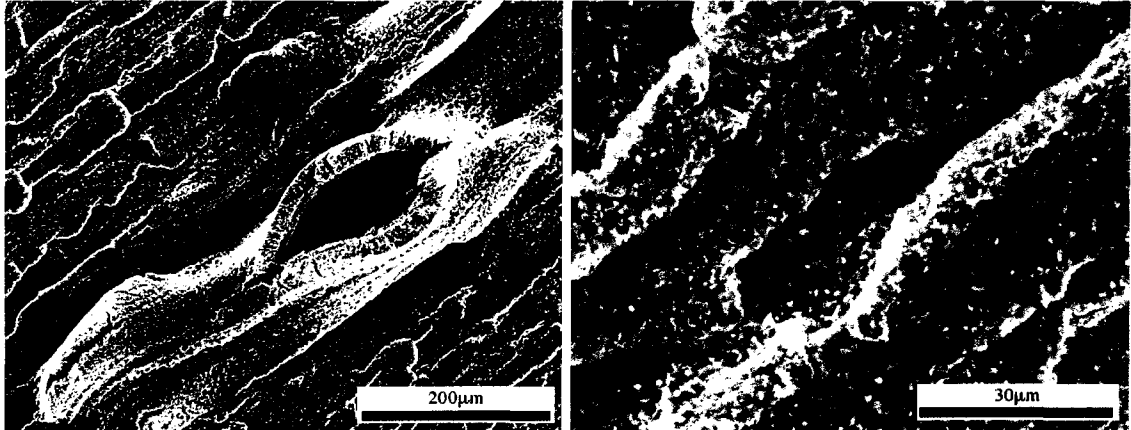
Note: While not quantified, the EDS spectra also indicate the presence of O in all cases.

1050°C / 10 Hours

The surface micrograph of the MS-PVD FeCrAlY-coated specimen that was subjected to a VHT of 1050°C for 10 hours (Figure 60a) shows the presence of a porous surface that is regularly interrupted by the presence of through-coating cracks that tend to form parallel to and on top of the ridges on the specimen surface. Figure 60b shows a high-magnification micrograph providing a detailed view of porous surface. The compositional EDS surface area scan data for the region shown in Figure 60a, listed in Table 29, indicates an increased proportion of chromium and nickel concentrations. Both nickel and chromium are thought to have diffused upwards to the specimen surface from the Hastelloy-X substrate material.

A cross-sectional micrograph of the test specimen (Figure 61) shows the presence of (i) a porous top layer (former as-deposited BC) above (ii) an interdiffusion layer, followed by (iii) a Cr-rich top (σ) phase layer between the diffusion layer and (iv) the Hastelloy-X substrate. The compositional EDS spot scan data for locations marked in Figure 61 are listed in Table 30. The highly porous top layer (i) contains traces of nickel and molybdenum that have diffused upward from the Hastelloy-X substrate together with increased proportions of chromium and iron when compared to the as-deposited surface compositions (Table 23). The interdiffusion layer (ii) is composed primarily of upward-diffused nickel, together with the remaining portions of the downward-diffused FeCrAlY layer constituents of iron, chromium, and aluminum. The σ -phase layer (iii) contains a significant proportion of chromium, indicating diffusion of chromium from both the as-deposited BC layer downward, and from the Hastelloy-X substrate upward.

In contrast to the as-deposited coating composition (Table 24), all EDS spot scan spectra for the locations listed in Table 30 do not contain even a trace of the argon sputtering gas. This contributes to the hypothesis, also mentioned to support the



(a) A SE micrograph showing the general features of the TGO layer after VHT. Note the presence of bubbling along coating ridges and cracking and rupture along the tops of the bubbles. (b) A high-magnification SE micrograph showing a detailed view of the porous TGO surface.

Figure 60: Surface features of the MS-PVD FeCrAlY-coated test specimen after VHT of 1050°C for 10 hours.

Table 29: EDS surface area scan data for region shown in Figure 60a (in wt%).

Fe	Cr	Al	Ni
32.35	34.09	18.47	15.08

results of previous heat treatment conditions, that the porous nature of the top layer (i) and the interdiffusion layer (ii) are likely due to the coalescence of the argon sputtering gas as a result of the heat treatment, leading to void formation and, ultimately, through-coating crack formation.

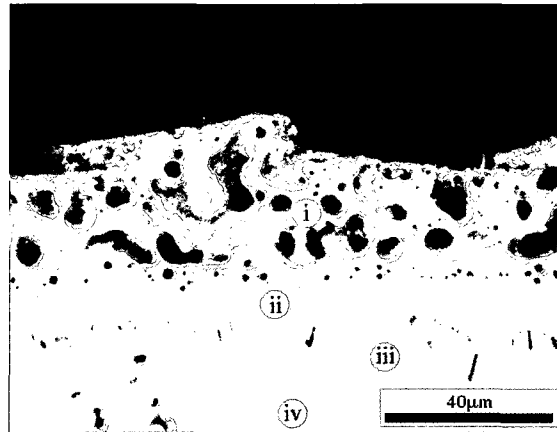


Figure 61: A cross-sectional BSE micrograph showing the formation of three different layers in the MS-PVD FeCrAlY-coated test specimen as a result of a VHT of 1050°C for 10 hours: (i) a porous top layer, (ii) an interdiffusion layer, and (iii) σ -phase layer that forms between the interdiffusion layer and (iv) the Hastelloy-X substrate material.

Table 30: EDS spot scan data for locations shown in Figure 61 (in wt%).

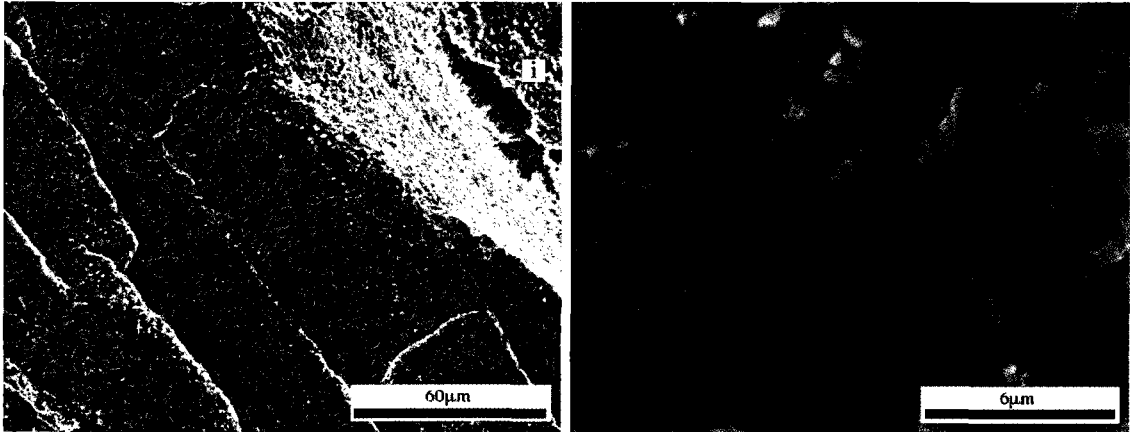
	Fe	Cr	Al	Ni	Mo
i	40.90	34.29	-	22.34	2.46
ii	15.37	6.09	14.56	63.97	-
iii	29.31	44.96	-	15.97	9.76
iv	16.16	30.63	-	49.42	3.78

1100°C / 1 Hour

The surface micrograph of the MS-PVD FeCrAlY-coated specimen that was subjected to a VHT of 1100°C for 1 hour (Figure 62a) shows the presence of a porous surface that is regularly interrupted by the presence of (i) through-coating cracks that tend to form parallel to and on top of the ridges on the specimen surface. Figure 62b shows a high-magnification micrograph providing a detailed view of porous surface. The compositional EDS surface area scan data for the region shown in Figure 62a, listed in Table 31, indicates a significantly increased proportion of aluminum in comparison to the as-deposited surface composition (Table 23). Trace amounts of nickel are also present due to upward diffusion from the Hastelloy-X substrate material.

A cross-sectional micrograph of the test specimen (Figure 63) shows the presence of (i) a porous top layer (former as-deposited BC layer) above (ii) an interdiffusion layer, followed by (iii) tcp-phase layer between the interdiffusion layer and the Hastelloy-X substrate. The compositional EDS spot scan data for locations marked in Figure 63 are listed in Table 32. The highly porous top layer (i) contains nickel and molybdenum that have diffused upward from the Hastelloy-X substrate together with an increased proportion of chromium when compared to the as-deposited surface compositions (Table 24). The as-interdiffusion layer (ii) is composed primarily of upward-diffused nickel, together with the remaining portions of the former FeCrAlY BC layer constituents of iron, aluminum, and traces of chromium. The tcp (σ) phase layer (iii) contains a significant proportion of chromium, indicating diffusion of chromium from either (or both) the as-deposited BC layer downward, and from the Hastelloy-X substrate upward.

In contrast to the as-deposited coating composition (Table 24), all EDS spot scan spectra for the locations listed in Table 32 do not contain as much as a trace of the argon sputtering gas. This contributes to the hypothesis, also mentioned to



(a) A SE micrograph showing the general features of the porous TGO surface after VHT. Note the presence of coating bubbling along the side of coating ridge with (i) cracking. (b) A high-magnification SE micrograph showing the detail of the porous TGO layer surface.

Figure 62: Surface features of the MS-PVD FeCrAlY-coated test specimen after VHT of 1100°C for 1 hour.

Table 31: EDS surface area scan data for region shown in Figure 62a (in wt%).

Fe	Cr	Al	Ni
39.95	31.46	22.81	5.78

support the results of previous heat treatment conditions, that the porous nature of the top layer (i) and the upper part of the interdiffusion layer (ii) are likely due to the coalescence of the argon sputtering gas as a result of the heat treatment, leading to void formation and, ultimately, through-coating crack formation.

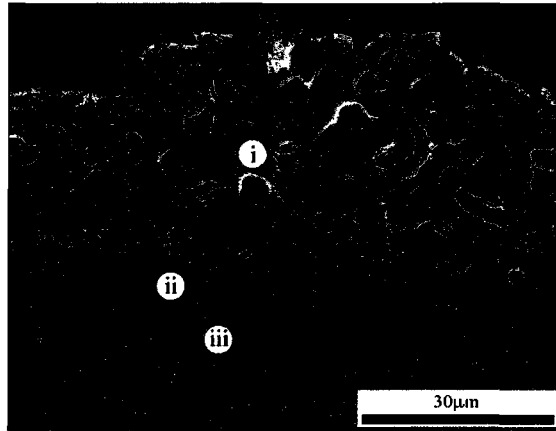


Figure 63: A cross-sectional BSE micrograph showing the formation of three different layers in the MS-PVD FeCrAlY-coated test specimen as a result of a VHT of 1100°C for 1 hour: (i) a porous top layer, (ii) an interdiffusion layer, and (iii) a σ phase-containing layer that forms between the interdiffusion layer and the Hastelloy-X substrate material. Markers also indicate EDS spot scan locations.

Table 32: EDS spot scan data for locations shown in Figure 63 (in wt%).

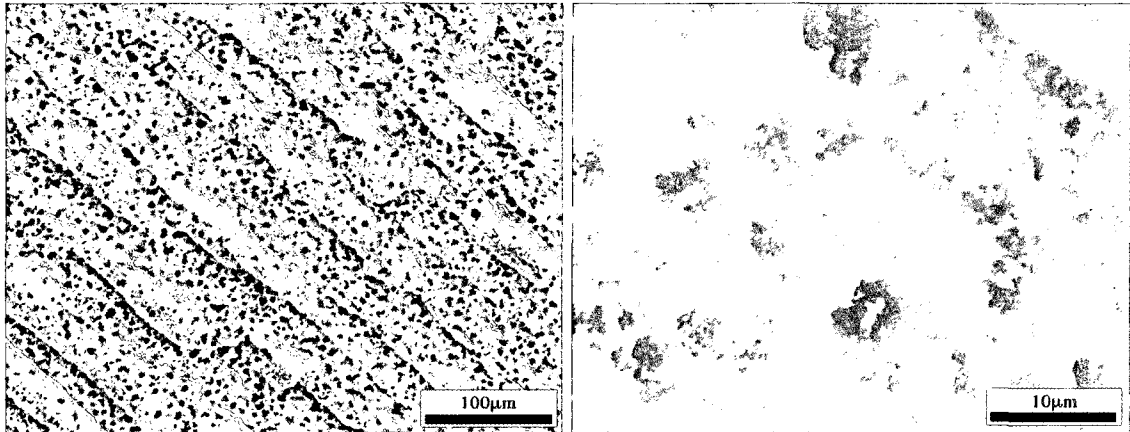
	Fe	Cr	Al	Ni	Mo
i	52.23	33.71	4.97	7.36	1.73
ii	15.58	5.44	19.39	59.58	-
iii	9.74	69.66	-	11.02	9.57

1100°C / 5 Hours

The surface micrograph of the MS-PVD FeCrAlY-coated specimen that was subjected to a VHT of 1100°C for 5 hours (Figure 64a) shows the presence of a porous surface. Unlike the test specimen surfaces of the previous VHT conditions, there does not appear to be a presence of coating cracks. Figure 64b shows a high-magnification micrograph providing a detailed view of porous surface. The compositional EDS surface area scan data for the region shown in Figure 64a, listed in Table 33, indicates a significantly increased proportion of aluminum in comparison to the as-deposited surface composition (Table 23). Nickel and molybdenum are also present due to upward diffusion from the Hastelloy-X substrate material.

A cross-sectional micrograph of the test specimen (Figure 65) shows the presence of (i) a porous top layer above (ii) an interdiffusion layer, which is followed by (iii) a σ phase-containing layer which has formed between the interdiffusion layer and the Hastelloy-X substrate. The compositional EDS spot scan data for locations marked in Figure 65 are listed in Table 34. The highly porous top layer (i) contains nickel and molybdenum that have diffused upward from the Hastelloy-X substrate together with an increased proportion of chromium when compared to the as-deposited surface compositions (Table 24). The interdiffusion layer (ii) is composed primarily of upward-diffused nickel and traces of molybdenum, together with the remaining portions of the as-deposited FeCrAlY BC layer constituents of iron, aluminum, and traces of chromium. The tcp-phase layer (iii) contains significant proportions of chromium, iron, molybdenum, and nickel as a result of a combination of both upward diffusion from the substrate and downward diffusion from the as-deposited BC layer.

In contrast to the as-deposited coating composition (Table 24), all EDS spot scan spectra for the locations listed in Table 34 do not contain even a trace of the argon sputtering gas. This contributes to the hypothesis, also mentioned to support the



(a) A SE micrograph showing the general surface features of the porous TGO layer after VHT. (b) A high-magnification SE micrograph showing a detailed view of the porous TGO layer surface.

Figure 64: Surface features of the MS-PVD FeCrAlY-coated test specimen after VHT of 1100°C for 5 hours.

Table 33: EDS surface area scan data for region shown in Figure 64a (in wt%).

Fe	Cr	Al	Ni	Mo
36.85	20.06	20.37	18.11	4.61

Note: While not quantified, the EDS spectrum also indicates the presence of O.

results of previous heat treatment conditions, that the porous nature of the top layer (i) and the upper part of the diffusion layer (ii) are likely due to the coalescence of the argon sputtering gas as a result of the heat treatment, leading to the formation of porosity.

Table 34: EDS spot scan data for locations shown in Figure 65 (in wt%).

	Fe	Cr	Al	Ni	Mo	Si
i	42.14	24.74	5.44	18.79	8.89	-
ii	18.78	5.81	20.22	53.91	1.28	-
iii	37.49	26.45	4.31	19.21	11.70	0.85



Figure 65: A cross-sectional BSE micrograph showing the formation of three different layers in the MS-PVD FeCrAlY-coated test specimen as a result of a VHT of 1100°C for 5 hours: (i) a porous top layer, (ii) an interdiffusion layer, and (iii) a Cr-rich σ phase-containing layer that forms between the diffusion layer and the Hastelloy-X substrate material. Markers also indicate EDS spot scan locations.

VHT Summary

As presented in the summary table of the MS-PVD FeCrAlY-coated test specimen surfaces as a result of the VHT series (Table 35), it can be seen that all VHT conditions led to the formation of a porous top layer on the specimen surface. All VHT conditions also led to the formation of large voids between the interdiffusion layer and the porous top layer, predominantly along the tops of the coating ridges, which have ultimately led to cracking through the former as-deposited FeCrAlY BC layer.

A summary of EDS surface area scan data for the 6 VHT conditions (Figure 66) shows a general increase in the proportion of aluminum on the specimen surfaces, possibly indicating the presence of a very thin aluminum oxide surface TGO layer. Also evident from Figure 66 is the additional presence of nickel and molybdenum on the surface for the majority of VHT conditions. These elements are thought to have diffused upward to the specimen surface from the Hastelloy-X substrate. In contrast to the as-deposited surface composition, all VHT specimens lack the presence of the argon sputtering gas in the EDS surface scan measurements.

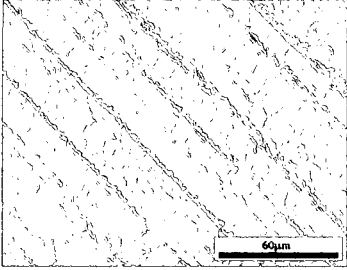
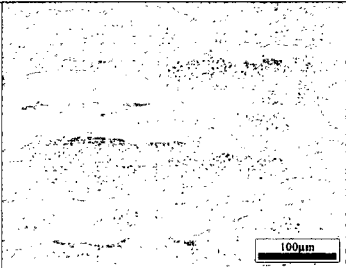
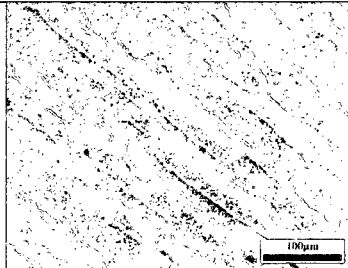
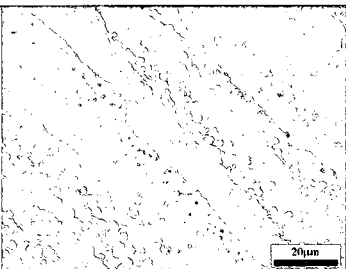
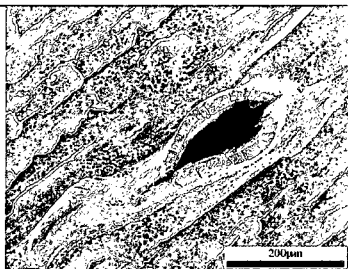
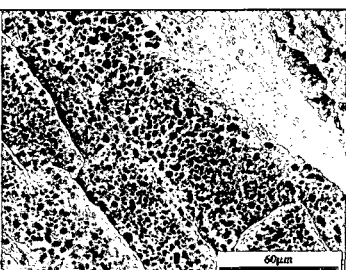
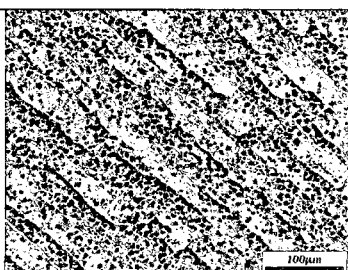
As shown in the summary table of the MS-PVD FeCrAlY-coated test specimen cross-sectional features as a result of the VHT series (Table 36), it can be seen that all VHT conditions led to the formation of a multi-layered structure in the test specimen that consisted of a highly porous top layer, an interdiffusion layer, and a σ -phase layer that is present between the interdiffusion layer and the Hastelloy-X substrate. In contrast to the as-deposited MS-PVD FeCrAlY BC composition (prior to any heat treatment), the compositional data from all cross-sectional features in the VHT-exposed test specimens lack the presence of the argon sputtering gas in the EDS spot scan measurements.

The porous top layer is generally found to be iron- and chromium-rich in comparison to the as-deposited composition. This differs from the general trend of the surface

composition, which indicates an increased proportion of aluminum in comparison to the as-deposited composition. This indicates the presence two different constituents: one on the specimen surface (a very thin aluminum oxide TGO) and the second that consists of the porous top layer, as shown in Table 36. The porosity in both the top layer and the upper portion of the interdiffusion layer are thought to be caused by the coalescence of the argon gas which results the formation of porosity, larger voids, and ultimately in through-cracks in the former FeCrAlY BC layer. The argon sputtering gas is entrapped in the deposited FeCrAlY BC as a result of the MS-PVD process.

The σ phase-containing layer in the vacuum furnace heat treated test specimens consists primarily of chromium with some iron and molybdenum. The voids present in this layer are thought to be caused by cracking as a result of the formation of the σ -phase, which is accompanied by a detrimental volume change.

Table 35: A summary of MS-PVD FeCrAlY-coated test specimen surface after VHT.

As-deposited		
1000°C for 10 & 15 hrs		
1050°C for 5 & 10 hrs		
1100°C for 1 & 5 hrs		

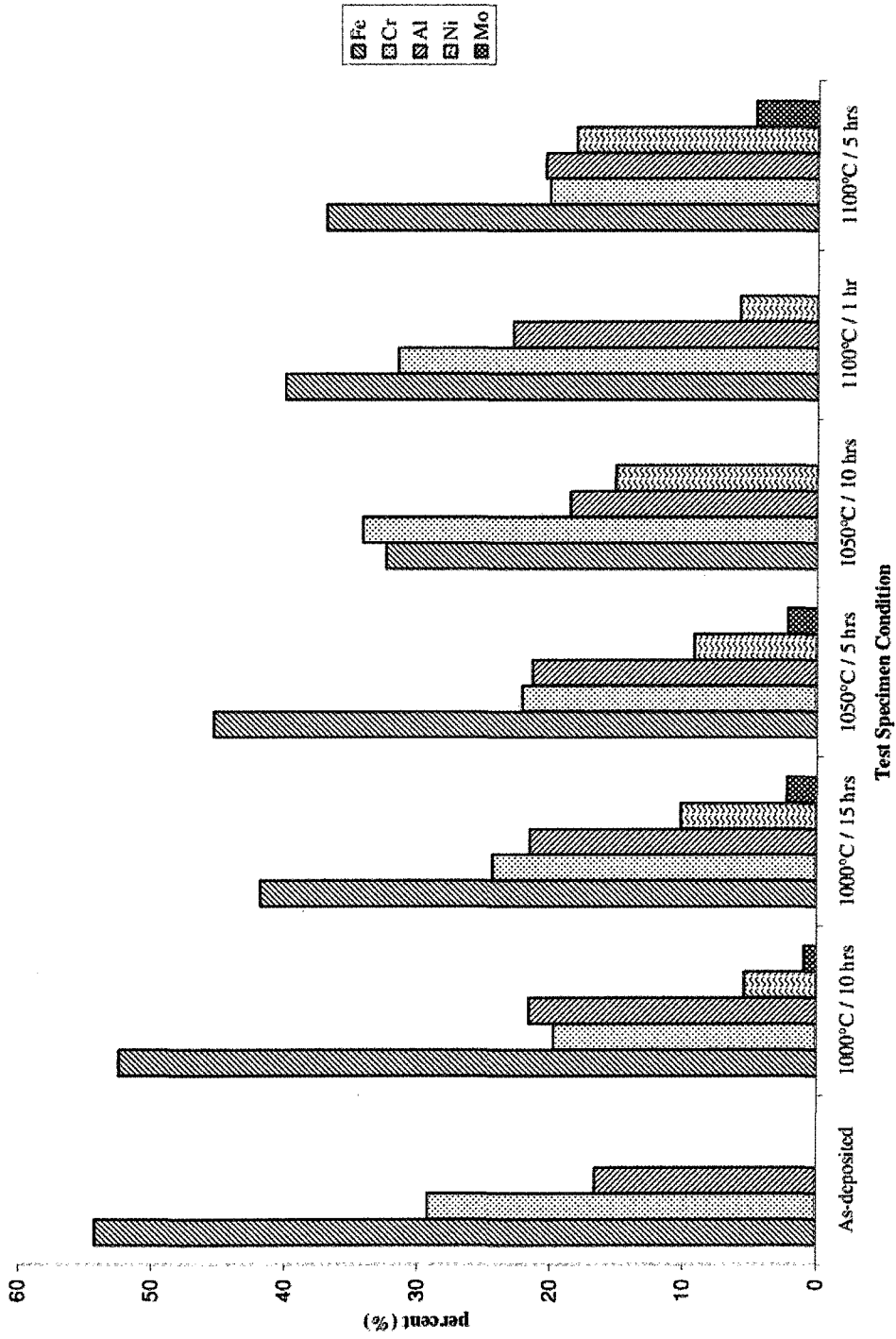
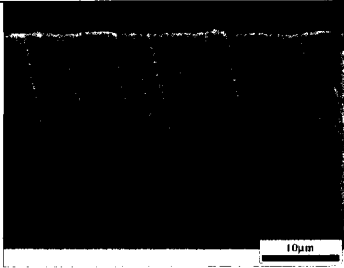
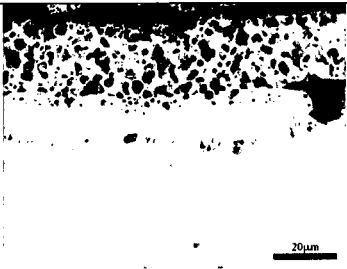
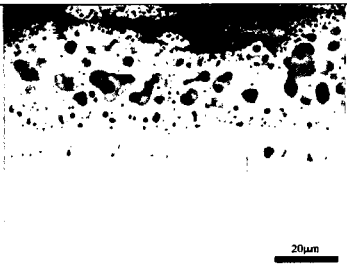
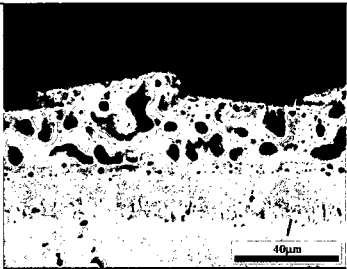
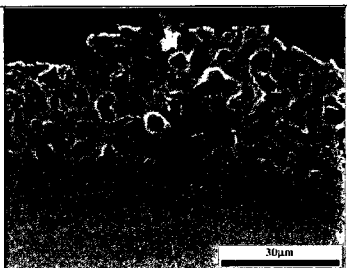
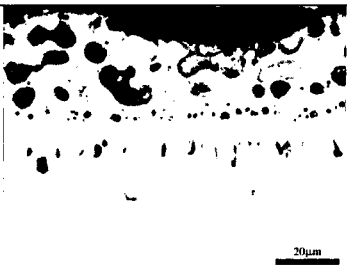


Figure 66: EDS area scan data for the MS-PVD FeCrAlY-coated test specimen surface composition (in wt%) as a function of specimen condition.

Table 36: A summary of MS-PVD FeCrAlY-coated test specimen cross-sections after VHT.

<p>As-deposited</p>		
<p>1000°C for 10 & 15 hrs</p>		
<p>1050°C for 5 & 10 hrs</p>		
<p>1100°C for 1 & 5 hrs</p>		

5.3.3 Air Furnace Heat Treatments

This sub-section outlines the SEM/EDS analysis results in terms of the microstructural features present both on the surface and in the cross-sections of the MS-PVD FeCrAlY-coated test specimens that have been subjected to the pre-oxidation AHTs. The sub-section is concluded with a summary of the trends in the results of the AHT series. The 3 AHT conditions examined are:

- 1000C for 10 hours
- 1050C for 5 hours
- 1100C for 1 hour

1000°C / 10 Hours

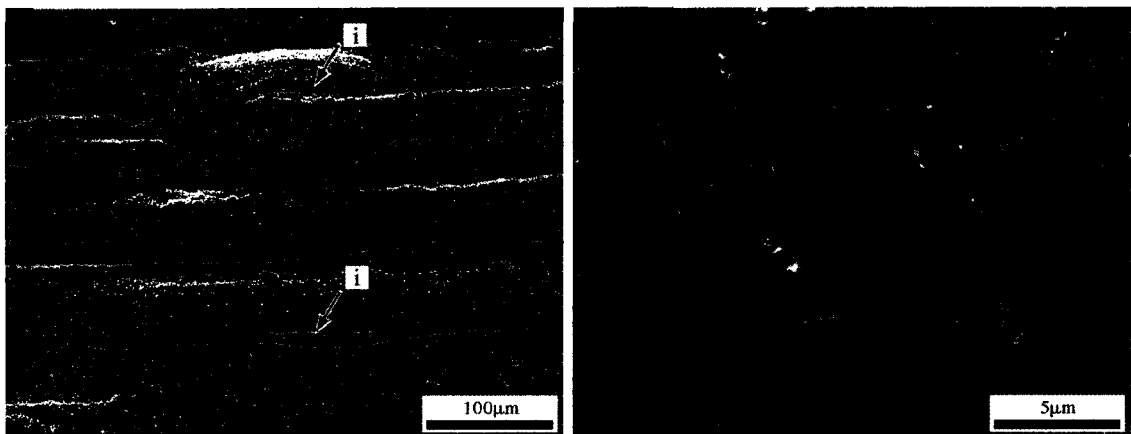
The surface micrograph of the MS-PVD FeCrAlY-coated specimen that was subjected to an AHT of 1000°C for 10 hours (Figure 67a) shows the presence of a porous TGO surface that is frequently interrupted by the presence of (i) through-coating cracks that tend to form parallel to and on top of the ridges on the specimen surface. The compositional EDS surface area scan data for the region shown in Figure 67a, listed in Table 37, indicates a significant proportion of aluminum in comparison to the as-deposited surface composition (Table 23). This strong presence of aluminum in the EDS spectrum is thought to be due to the presence of a predominantly aluminum-containing TGO layer. Figure 67b shows a high-magnification micrograph providing a detailed view of aluminum-rich, whisker-shaped TGO that predominantly populates the test specimen surface. This morphology of aluminum oxide has been associated with the θ -Al₂O₃ phase in studies performed by Hesnawi et al [17] (see Figure 12).

A cross-sectional micrograph of the test specimen (Figure 68) shows the presence of (i) a porous top layer (former as-deposited FeCrAlY BC) above (ii) an interdiffusion

layer, followed by (iii+iv) a σ (tcp) phase-containing layer between the interdiffusion layer and (v) the Hastelloy-X substrate. In the micrograph, a seemingly continuous, sub- μm surface TGO layer is visible on top of the relatively thicker, more porous top layer (i). In comparison to the previously presented cross-sectional test specimen structures as a result of the VHT series, the thicker top layer has a greater average thickness and the porosity appears to have a much finer distribution of more plentiful and significantly smaller pores. The compositional EDS spot scan data for locations marked in Figure 68, together with the average surface composition of the test specimen, are listed in Table 38. The composition of the surface TGO layer and the underlying, highly porous top layer vary considerably: the surface layer contains predominantly aluminum, whereas the highly porous top layer (i) consists predominantly of iron and chromium, some aluminum, and traces of nickel and molybdenum. Both nickel and molybdenum have diffused upward into the top layer (i) from the Hastelloy-X substrate.

The interdiffusion layer (ii) is composed primarily of upward-diffused nickel and some aluminum, together with remnants of iron and chromium from the deposited FeCrAlY BC material. The σ phase-containing layer (iii+iv) contains significant proportions of molybdenum, tungsten, and cobalt, which have diffused upward from the substrate.

In contrast to the as-deposited coating composition (Table 24), all EDS spot scan spectra for the locations listed in Table 38 do not contain even a trace of the argon sputtering gas. This contributes to the hypothesis that the porous nature of the TGO is likely due to the coalescence of the argon sputtering gas as a result of the heat treatment, leading to the formation of porosity.



(a) A SE micrograph showing the general surface features of the TGO layer after AHT. Note the appearance of coating bubbling along coating ridges and (i) cracks along the tops of the bubbles. (b) A high-magnification SE micrograph showing a detailed view of the aluminum-rich, whisker-shaped TGO layer.

Figure 67: Surface features of the MS-PVD FeCrAlY-coated test specimen after an AHT of 1000°C for 10 hours.

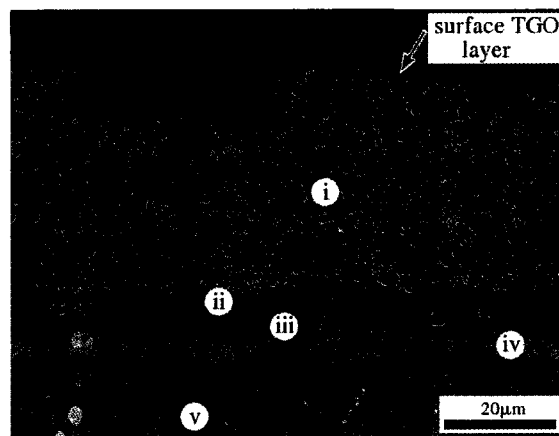


Figure 68: A cross-sectional BSE micrograph showing the formation of three different layers in the MS-PVD FeCrAlY-coated test specimen as a result of a AHT of 1000°C for 10 hours: (i) a porous top layer, (ii) an interdiffusion layer, and (iii+iv) σ phase-containing layer that forms between the interdiffusion layer and the (v) Hastelloy-X substrate material. Note the presence of a largely continuous, sub- μm TGO surface layer. Markers also indicate EDS spot scan locations.

Table 37: EDS surface area scan data for region shown in Figure 67a (in wt%).

Fe	Cr	Al
15.88	10.91	73.21

Note: While not quantified, the EDS spectrum also indicates the presence of O.

Table 38: EDS spot scan data for locations shown in Figure 68 (in wt%).

	Fe	Cr	Al	Ni	Mo	W	Co
surface	15.88	10.91	73.21	-	-	-	-
i	55.18	22.41	13.69	6.84	1.88	-	-
ii	11.60	3.55	20.87	63.97	-	-	-
iii	26.66	28.02	2.93	32.86	6.81	1.22	1.50
iv	25.72	28.39	1.47	19.10	19.26	3.98	2.07
v	18.74	21.31	0.31	45.96	9.89	1.89	1.90

1050°C / 5 Hours

The surface micrograph of the MS-PVD FeCrAlY-coated specimen that was subjected to an AHT of 1050°C for 5 hours (Figure 69) shows the presence of a TGO surface that is frequently interrupted by the presence of through-coating cracks that tend to form parallel to and on top of the ridges and bubbles on the specimen surface. The compositional EDS surface area scan data for the region shown in Figure 69, listed in Table 39, indicates a significant proportion of aluminum in comparison to the as-deposited surface composition (Table 23). The strong presence of aluminum in the EDS spectrum is thought to be due to the presence of a predominantly aluminum-containing TGO layer. Also present on the sample surface is nickel, which has diffused upward from the Hastelloy-X substrate. The high-magnification micrographs in Figure 70 provide detailed views of the aluminum-rich TGO surface morphology. These micrographs show a relatively dense clusters of a globular oxide.

The cross-sectional micrographs of the test specimen (Figure 71) shows the presence of (i) a porous top layer above an interdiffusion layer, followed by a top phase (σ) containing layer found between the diffusion layer and the Hastelloy-X substrate. In Figure 71b, a largely continuous, sub- μm surface TGO layer is visible on top of the relatively thicker, more porous top layer (i). The compositional EDS spot scan data for the location marked in Figure 71a is listed in Table 40. As in the results for the test specimen subjected to the previous AHT condition, both the surface TGO layer (ii) and the underlying, highly porous top layer (i) have contrasting compositions: the surface TGO layer consists of predominantly aluminum (possibly indicating an aluminum oxide layer) whereas the underlying highly porous top layer consists predominantly of iron and chromium. As noted in the previous AHT condition, in contrast to the previously presented cross-sectional test specimen structures as a result of the VHT series, the thicker top layer in this test specimen has a greater average

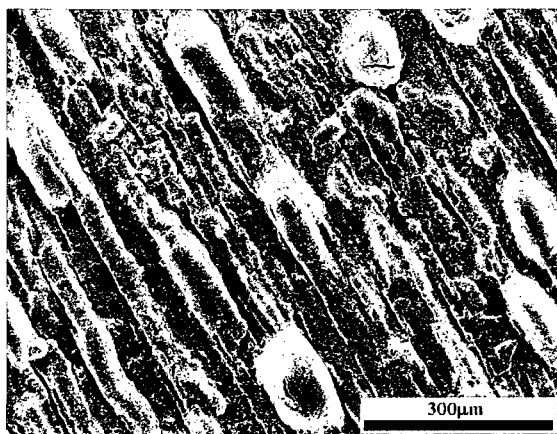


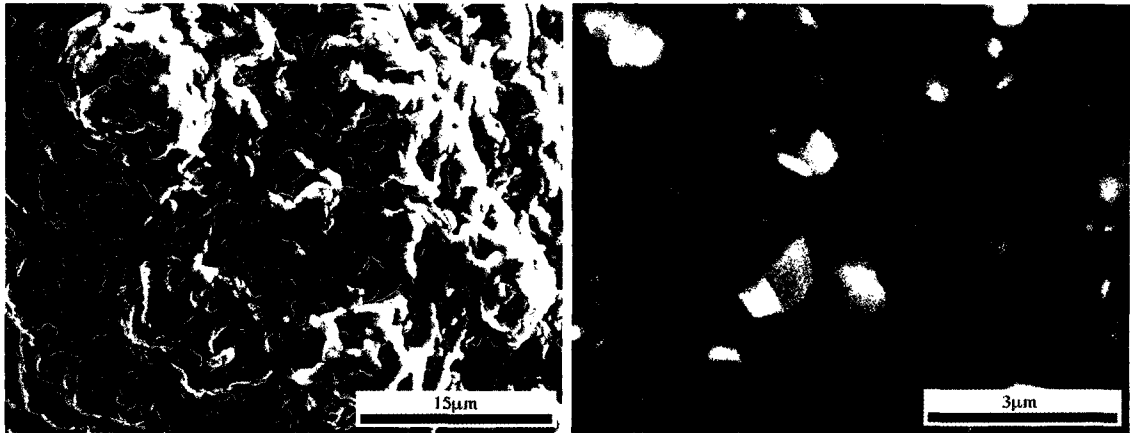
Figure 69: Surface features of the MS-PVD FeCrAlY-coated test specimen after an AHT of 1050°C for 5 hours. Note the presence of bubbling along coating ridges with some cracking along the highest points of the bubbles.

Table 39: EDS surface area scan data for region shown in Figure 69 (in wt%).

Fe	Cr	Al	Ni
20.15	20.51	57.89	1.44

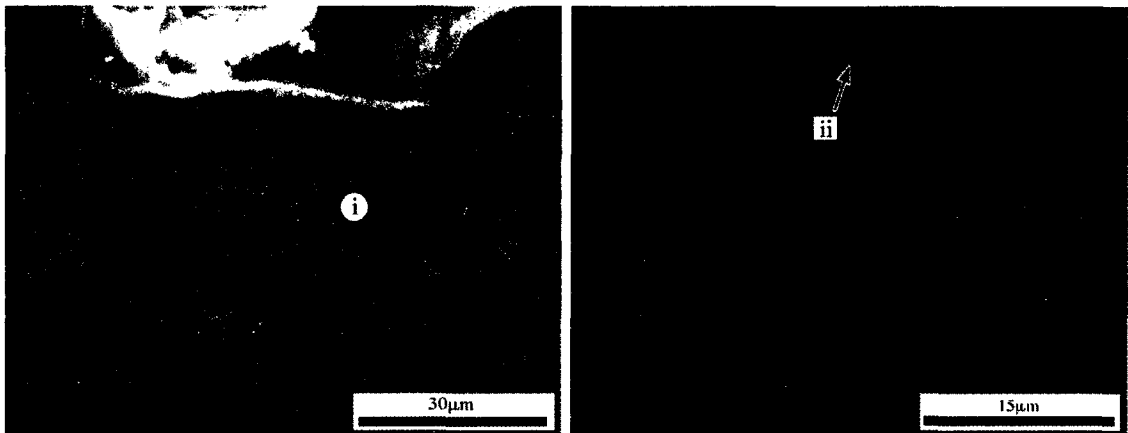
thickness and the porosity appears to consist of a much finer distribution of more plentiful and significantly smaller pores. The top phase-containing layer suffers from a large degree of void formation, likely due to a volume decrease associated in the formation of the σ -phase.

In contrast to the as-deposited coating composition (Table 24), the EDS spot scan spectra for the locations listed in Tables 39 and 40 do not contain even a trace of the argon sputtering gas. This contributes to the hypothesis, as previously stated for the preceding VHT and AHT conditions, that the porous nature of the top layer is likely due to the coalescence of the argon sputtering gas as a result of the heat treatment, leading to the formation of porosity.



(a) A SE micrograph showing the typical features of the TGO surface as a result of the AHT. (b) A high-magnification SE micrograph showing a detailed view of the TGO surface.

Figure 70: Detailed views of the TGO layer surface features on the MS-PVD FeCrAlY-coated test specimen after an AHT of 1050°C for 5 hours.



(a) A three-layer structure consisting of (i) a porous top layer (the as-deposited FeCrAlY BC containing layer), an interdiffusion layer, and a σ phase-face TGO layer. Marker also indicates EDS spot scan location. (b) A detailed view of the porous top layer showing the presence of (ii) a continuous, sub- μm surface TGO layer. Marker also indicates EDS spot scan location.

Figure 71: Cross-sectional SE micrographs of the MS-PVD FeCrAlY-coated test specimen as a result of a AHT of 1050°C for 5 hours.

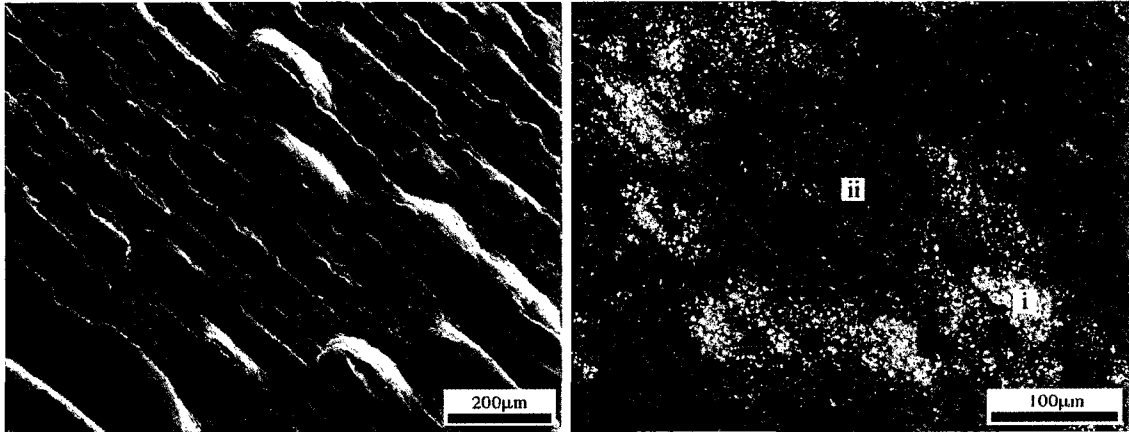
Table 40: EDS spot scan data for location shown in Figure 71 (in wt%).

	Fe	Cr	Al	Ni
i	47.96	32.91	11.33	7.78

1100°C / 1 Hour

The surface micrograph of the MS-PVD FeCrAlY-coated specimen that was subjected to an AHT of 1100°C for 1 hour (Figure 72a) shows the presence of a surface TGO layer that is frequently interrupted by the presence of through-coating cracks that tend to form parallel to and on top of the ridges and bubbles on the specimen surface. A detailed view of the the specimen surface (Figure 72b) shows the presence of clusters of (i) a light-shaded oxide phase in a matrix of a darker-shaded oxide phase. High-magnification micrographs of both light-shaded (i) and dark-shaded (ii) oxide phases are presented in Figure 73a and Figure 73b, respectively. Compositional EDS spot scan data for regions shown in Figure 73a and Figure 73b are listed in Table 41, indicating that the light-shaded oxide is predominantly iron-containing (suggesting iron oxide formation) and that the dark-shaded oxide is predominantly aluminum-containing (suggesting aluminum oxide formation). The aluminum-rich oxide phase shown in Figure 73b shares similarities with the aluminum-rich oxide surface TGO morphology shown in Figure 70a.

The cross-sectional micrographs of the test specimen (Figure 74) shows the presence of (i) a porous top layer above (ii) an interdiffusion layer, followed by (iii) a σ phase-containing layer between the diffusion layer and the Hastelloy-X substrate. As noted in the previous AHT condition, in contrast to the previously presented cross-sectional test specimen structures as a result of the VHT series, the thicker top layer in this specimen has a greater average thickness and the porosity appears to consist of a much finer distribution of more plentiful and significantly smaller pores. The significant presence of voids in the σ phase-containing layer (iii) is thought to be due to cracking as a result of tcp-phase formation in this location, which is accompanied by a volume change. The compositional EDS spot scan data for the locations marked in Figure 74 are listed in Table 42. The highly porous top layer contains

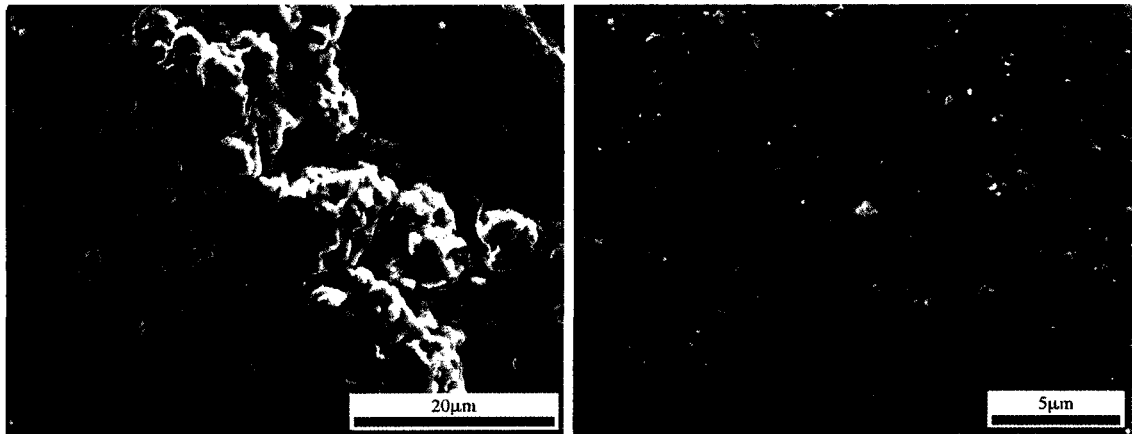


(a) A SE micrograph showing the general surface (b) A BSE micrograph showing (i) a lighter oxide phase and (ii) a darker oxide phase that are typically found on the specimen surface. Note the presence of coating bubbling, together with cracking on the highest points of the bubbles.

Figure 72: Surface features of the MS-PVD FeCrAlY-coated test specimen after an AHT of 1100°C for 1 hour. Note the presence of bubbling along coating ridges with some cracking along the highest points of the bubbles.

predominantly iron and chromium, with a presence of nickel and molybdenum that has diffused upwards towards the specimen surface from the Hastelloy-X substrate. The interdiffusion layer contains primarily nickel (also upward-diffused from the substrate) and remnants of the as-deposited FeCrAlY BC layer. The σ phase-containing layer is composed of significant proportions of aluminum and chromium, with a minor presence of iron, nickel, and molybdenum.

In contrast to the as-deposited coating composition (Table 24), the EDS spot scan spectra for the locations listed in Table 41 and 42 do not contain even a trace of the argon sputtering gas. This contributes to the hypothesis, as previously stated for the preceding VHT and AHT conditions, that the porous nature of the top layer and the upper portions of the interdiffusion layer are likely due to the coalescence of the argon sputtering gas as a result of the heat treatment, leading to the formation of porosity.



(a) The light-shaded mixed oxide phase. (b) The dark-shaded, aluminum-rich oxide phase.

Figure 73: High-magnification SE micrographs showing details of both light and dark phases present on the surface of the MS-PVD FeCrAlY-coated test specimen after an AHT of 1100°C for 1 hour.

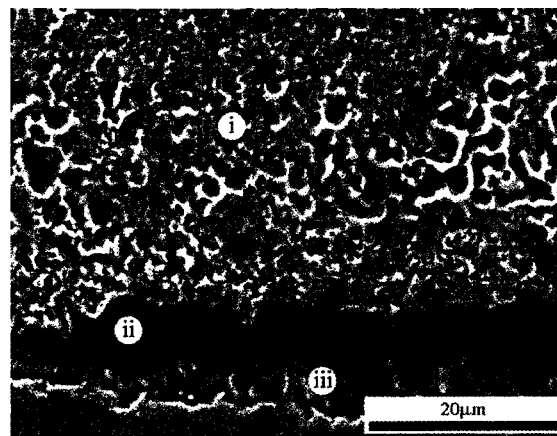


Figure 74: A cross-sectional SE micrograph showing the formation of three different layers in the MS-PVD FeCrAlY-coated test specimen as a result of a AHT of 1100°C for 1 hour: (i) a porous top layer, (ii) an interdiffusion layer, and (iii) a σ phase-containing layer that forms between the diffusion layer and the Hastelloy-X substrate material. Marker also indicates EDS spot scan location.

Table 41: EDS area scan data for both 'light' and 'dark' oxides shown in Figures 73a and b, respectively, (in wt%).

	Fe	Cr	Al
light	87.00	6.97	6.03
dark	28.53	13.90	57.59

Note: While not quantified, the EDS spectra also indicate the presence of O in both cases.

Table 42: EDS spot scan data for locations shown in Figure 74 (in wt%).

	Fe	Cr	Al	Ni	Mo
i	49.18	31.04	5.16	13.31	1.31
ii	19.36	11.67	11.41	57.56	-
iii	8.07	48.06	36.03	3.47	4.37

AHT Summary

The summary table of the MS-PVD FeCrAlY-coated test specimen surfaces as a result of the AHT series (Table 43) shows the similar formation of bubbles, voids, and cracking in the coating layer to the specimens subjected to the VHT series. In contrast to the as-deposited composition, all specimen surfaces in the AHT series lack the presence of argon. In contrast to the VHT series, the test specimens subjected to the AHT series generally exhibit the formation of significant aluminum-rich surface TGO layer, indicating the possible presence of an aluminum oxide surface TGO layer. An exception to this is the 1100°C/1 hr-heat treated specimen whose surface also contains the minor presence of an iron-rich oxide phase that forms on top of the predominantly aluminum-rich oxide.

The summary table of the MS-PVD FeCrAlY-coated test specimen cross-sections as a result of the AHT series (Table 44) shows a multi-layered structure consisting of a highly porous top layer, an interdiffusion layer, and a σ phase-containing layer that separates the diffusion layer and the Hastelloy-X substrate. This layered structure is similar to that exhibited by the specimens that were subjected to the VHT series, with the exception of the presence of an additional sub- μm aluminum-rich surface TGO layer on top of the highly porous top layer. In contrast to the as-deposited composition, all cross-sectional features present in the specimens subjected to the AHT series lack the presence of argon. The porous layer, however, exhibits a much finer porosity and an increase in layer thickness over those typical for the VHT series. Similar to the VHT series, the porous TGO layer in the AHT series consists predominantly of iron and chromium. This differs from the average surface composition of the specimens in the AHT series, which indicate the presence of a aluminum-rich surface TGO layer that lies on top of the porous iron- and chromium-rich layer. The porosity in both the iron- and chromium-rich layer and the upper part of the diffusion

layer is thought to occur due to the coalescence of the argon sputtering gas as a result of the AHT, resulting in bubble formation that ultimately leads to the formation of through-coating cracks.

In contrast to the VHT series, the composition of the σ phase-containing layer for the specimens subjected to the AHT series varies significantly with the heat treatment conditions. At 1000°C/10 hrs, the layer consists primarily of chromium, iron, molybdenum, and nickel. At 1100°C/1 hr, however, it consists primarily of chromium and aluminum, indicating the possible formation of a mixed chromium/aluminum oxide, rather than just a σ -phase. As present in the VHT series specimens, this layer present in the AHT series specimens also exhibits the formation of voids.

Table 43: A summary of MS-PVD FeCrAlY-coated test specimen surface condition after AHT.

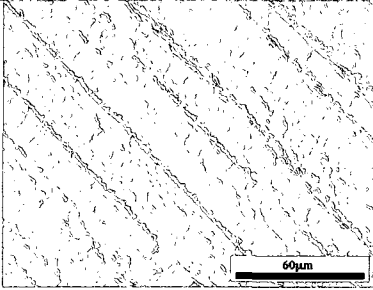
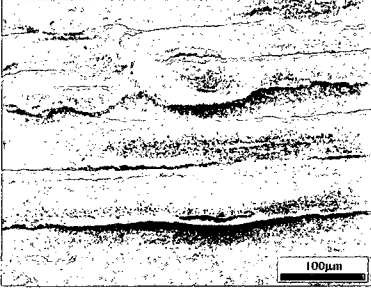
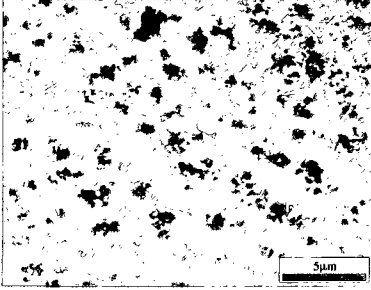
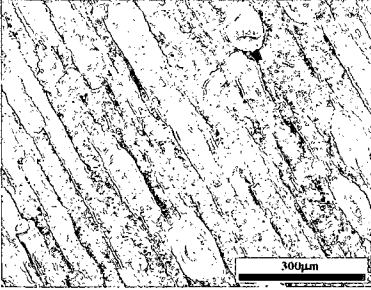
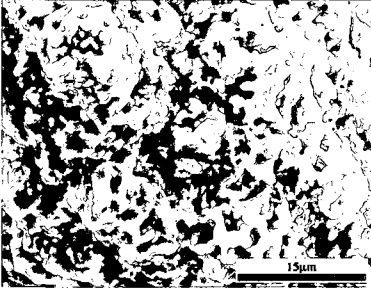
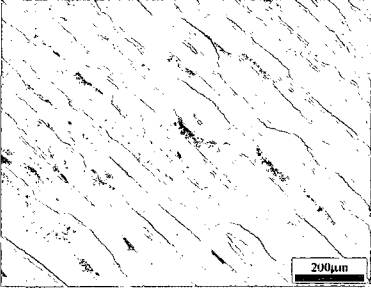
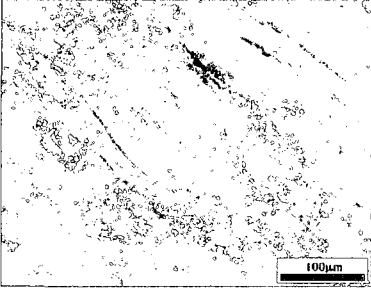
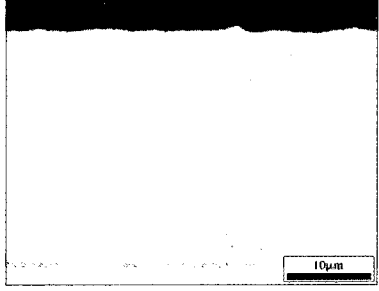
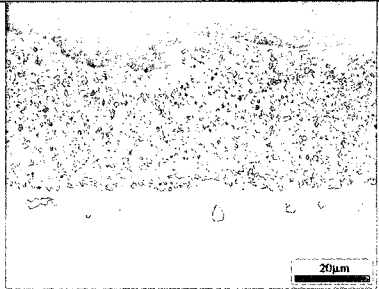
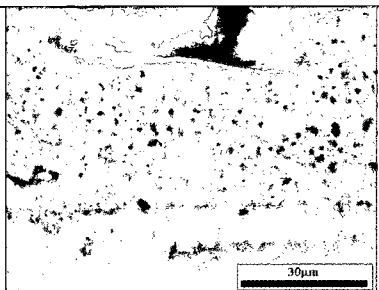
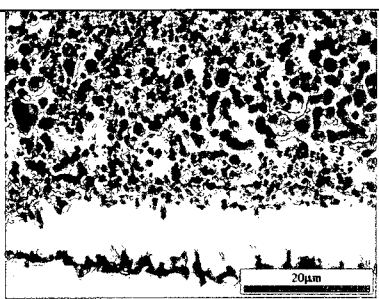
	General Surface Features	Oxide Morphology
As-deposited	 A micrograph showing the surface of an as-deposited specimen. The surface exhibits a series of parallel, diagonal striations or ridges running from the top-left to the bottom-right. A scale bar at the bottom right indicates 60 μm.	
1000°C for 10 hrs	 A micrograph showing the surface after 1000°C for 10 hours. The surface is characterized by several distinct, roughly horizontal layers or bands of varying thickness and texture. A scale bar at the bottom right indicates 100 μm.	 A micrograph showing the oxide morphology after 1000°C for 10 hours. The surface is covered with numerous small, dark, irregularly shaped spots or particles, indicating the formation of oxide. A scale bar at the bottom right indicates 5 μm.
1050°C for 5 hrs	 A micrograph showing the surface after 1050°C for 5 hours. The surface exhibits diagonal striations, similar to the as-deposited state, but with some additional texture and small features. A scale bar at the bottom right indicates 300 μm.	 A micrograph showing the oxide morphology after 1050°C for 5 hours. The surface shows larger, more irregular dark spots and clusters compared to the 1000°C condition. A scale bar at the bottom right indicates 15 μm.
1100°C for 1 hr	 A micrograph showing the surface after 1100°C for 1 hour. The surface exhibits diagonal striations, similar to the as-deposited state, but with some additional texture and small features. A scale bar at the bottom right indicates 200 μm.	 A micrograph showing the oxide morphology after 1100°C for 1 hour. The surface shows sparse, small dark spots and clusters, indicating the formation of oxide. A scale bar at the bottom right indicates 100 μm.

Table 44: A summary of MS-PVD FeCrAlY-coated test specimen cross-sections after AHT.

<p>As-deposited</p>	
<p>1000°C for 10 hrs</p>	
<p>1050°C for 5 hrs</p>	
<p>1100°C for 1 hr</p>	

5.3.4 XRD Results

This sub-section outlines the XRD analysis results (Figure 75) for the through-surface measurements of the MS-PVD FeCrAlY-coated test specimens that have been subjected to the following sample conditions:

- as-deposited condition
- a VHT of 1100°C for 1 hour
- an AHT of 1050°C for 5 hours.

The XRD spectrum for the as-deposited sample shows only two main peaks occurring at 43.8° and 81°, corresponding to (A) FeCrAlY α -phase peaks for crystal planes $\langle 110 \rangle$ and $\langle 211 \rangle$, respectively. The absence of other peaks in this spectrum leads to the assumption that the MS-PVD process used to make the test specimens tends favour deposition in $\langle 110 \rangle$ and $\langle 211 \rangle$ crystal planes. The width of the peaks may provide some indication of the lattice strains that exist in the as-deposited coating.

For the test specimen subjected to a VHT of 1100°C for 1 hour, the XRD spectrum shows the two main FeCrAlY α -phase peaks (A), as seen in the as-deposited XRD spectrum, although with narrowed peaks indicating strain relief as a result of the vacuum heat treatment. Also present in the spectrum is (B) the γ -phase that belongs to the Hastelloy-X substrate (see Figure 44). Due to the significant porosity in (C) the iron- and chromium-rich TGO layer layer (see Figure 63, location i), it is thought that the X-rays have penetrated through the layer structure and down to the substrate, thereby resulting in the presence of the characteristic Hastelloy-X peaks. Also present are several (D) α -Al₂O₃ peaks, together with several unidentifiable peaks.

For the test specimen subjected to an AHT of 1050°C for 5 hours, the XRD spectrum shows the predominant presence of (B) the characteristic main (γ -nickel)

and secondary Hastelloy-X peaks together with several smaller peaks that have been identified as (D) α -Al₂O₃, (E) NiCrO₄, and (F) FeCr₂O₄.

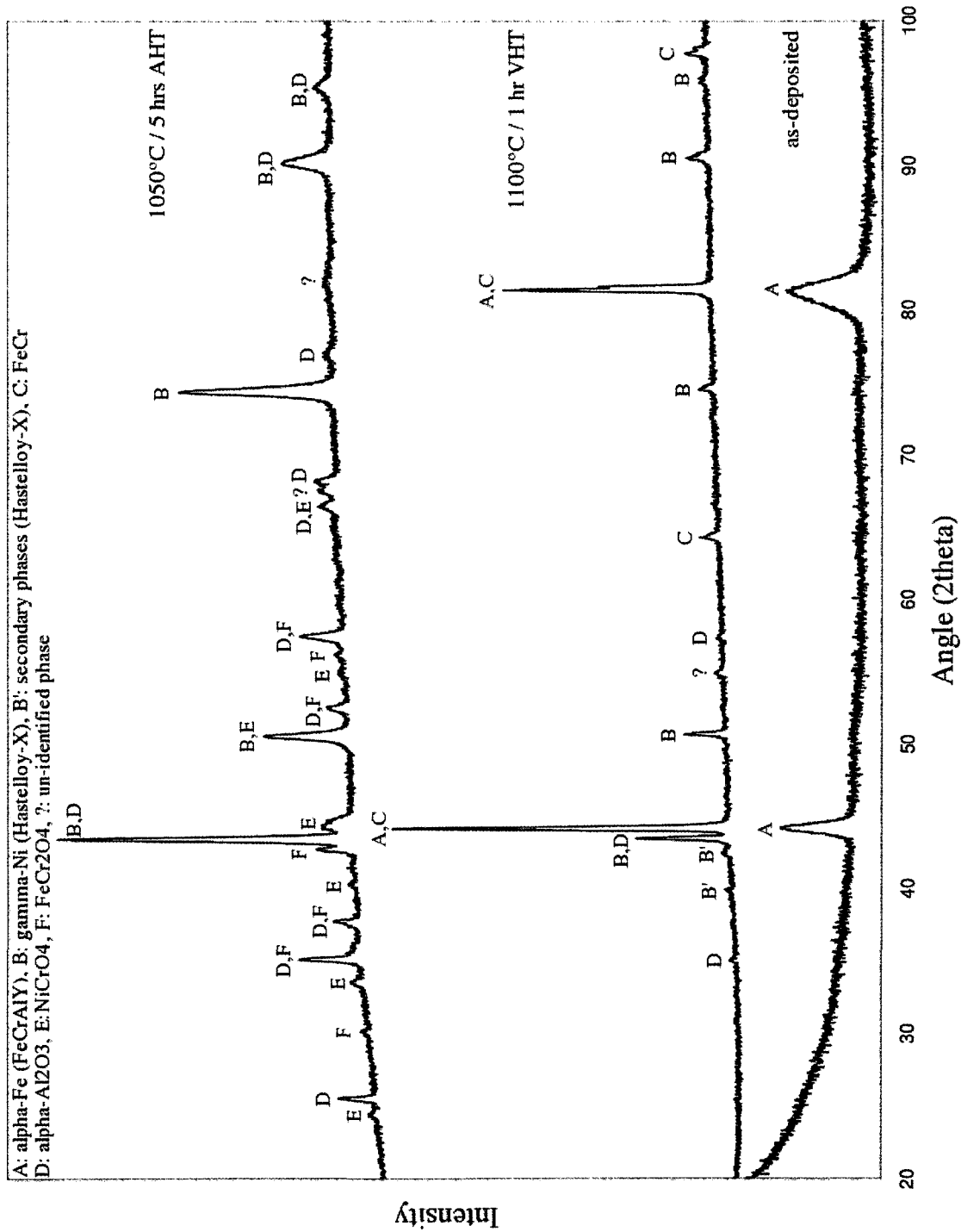


Figure 75: XRD spectra for the MS-PVD deposited FeCrAlY-coated Hastelloy-X test specimens in the following conditions: as-deposited, VHT of 1100°C for 1 hour, and AHT of 1050°C for 5 hours.

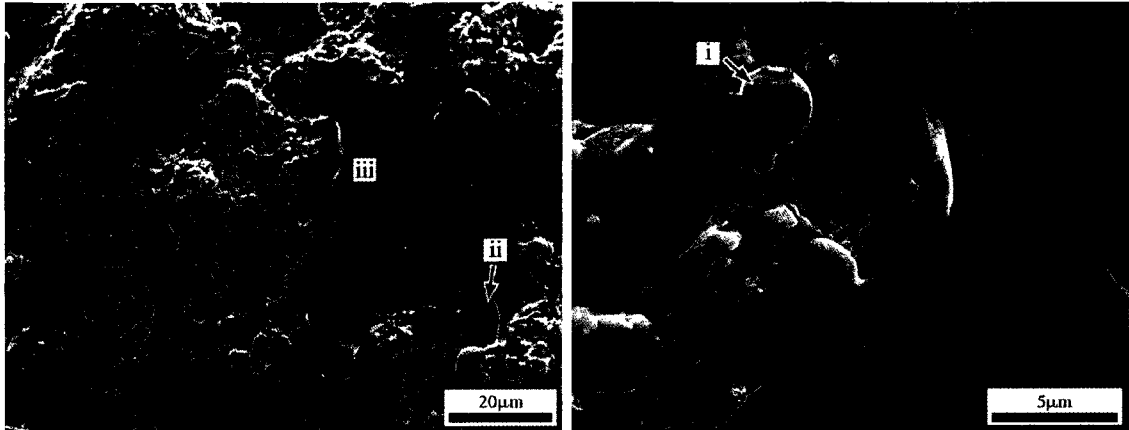
5.4 Air Plasma Spray Deposited NiCrAlY

In this section, the results of the pre-oxidation heat treatments (both VHT and AHT) on the APS NiCrAlY-coated test specimens are presented. The results for the VHT and AHT series are listed in a separate sub-section, classified according to ascending temperature and time variables of each heat treatment in the series. Each series is concluded with a summary of the overall trends for each heat treatment series. Heat treatment results are followed by XRD analysis of selected test specimen conditions. This section begins with a characterization of the as-deposited APS NiCrAlY coating, with analysis of microstructural features on both test specimen surface and cross-section.

5.4.1 As-deposited Condition

The surface of the as-deposited APS NiCrAlY-coated test specimen (Figure 76) shows the typical constituents that are present on a thermally-sprayed coating surface: coating splats, (i) un-melted particles, (ii) porosity, and (iii) glazed regions providing an indication of melting and re-solidification of the coating material. Composition EDS surface area scan data, together with the nominal feedstock powder composition, is listed in Table 45. Although not quantified, oxygen is present in the EDS spectrum and is attributed to the presence of oxide phases that inherently develop as part of the high-temperature APS process.

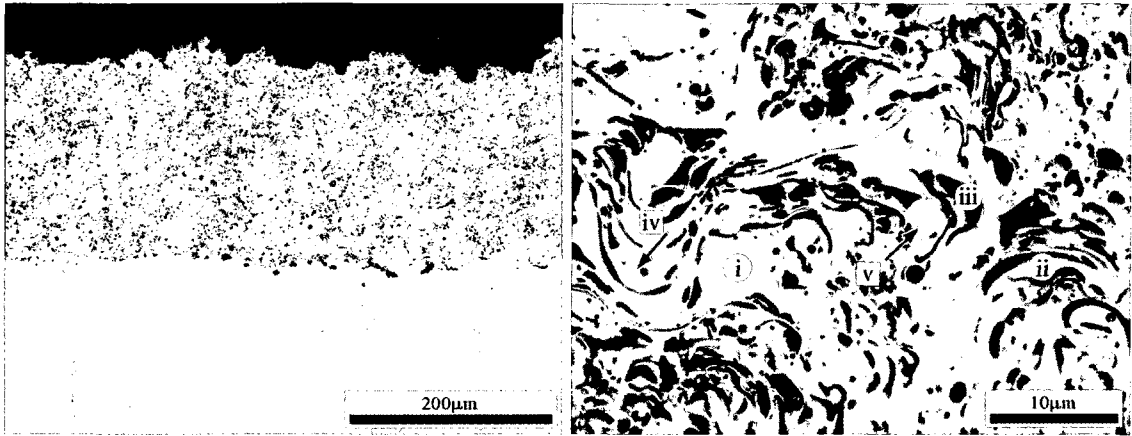
The cross-sectional micrograph of the as-deposited APS NiCrAlY-coated test specimen (Figure 77a) shows a typical coating microstructure for a thermally sprayed coating. The average coating thickness is approximately 200 μm . The dark constituents at the coating-substrate interface are embedded aluminum oxide particles remaining from the grit-blasting used to roughen the substrate surface to improve coating adhesion. The vertically-distributed, light-shaded particle ribbons on the



(a) A representative view of the surface morphology of the as-deposited BC surface, showing (ii) the coating surface features, including (i) an unporosity (iii) glazed areas indicating melting and re-solidification of the BC material.

Figure 76: SE micrographs showing the surface condition of the as-deposited APS NiCrAlY coated specimen.

substrate are a tungsten-rich refractory phase that is typically present in the wrought Hastelloy-X substrate material. Table 46 lists compositional data for an EDS area scan of the coating cross-section shown in Figure 77a, together with the EDS spot scan data for locations marked in Figure 77b. Both surface and cross-sectional composition correlate well. The micrograph in Figure 77b provides a detailed view of the thermally-sprayed APS microstructure, showing (i) material of average coating composition, (ii) a nickel-rich coating component, (iii) an oxide inclusion as a result of the APS process, (iv) a coating 'splat', and (v) an un-melted coating feedstock powder particle.



(a) A representative view of the as-deposited BC structure. Average coating thickness is 200 μm .

(b) A high-magnification view of the BC microstructure, showing typical constituents of a TS coating: (i) BC material, (ii) a nickel-rich coating constituent, (iii) oxide inclusions, (iv) coating splats, and (v) unmelted powder particles. Circular markers also indicate EDS spot scan locations.

Figure 77: Cross-sectional BSE micrographs showing the microstructural details of the as-deposited APS NiCrAlY-coated test specimen.

Table 45: EDS surface area scan data for region shown in Figure 76a (in wt%), with comparison to the nominal NiCrAlY powder (Sulzer Metco AMDRY 962) composition.

	Ni	Cr	Al	Y
surface	68.32	18.59	11.96	1.13
nominal	67	22	10	1

Note: While not quantified, the EDS spectrum also indicates the presence of O.

Table 46: EDS area scan data for region shown in Figure 77a and EDS spot scan data for locations shown in Figure 77b (in wt%), with the nominal NiCrAlY powder (AMDRY 962) composition for comparison.

	Ni	Cr	Al	Y
cross-section	67.93	17.74	12.37	1.96
nominal	67	22	10	1
i	68.41	21.36	9.73	0.50
ii	76.14	15.17	6.99	1.70
iii	31.30	28.96	30.85	8.89

Note: While not quantified, the EDS spectra also indicate the presence of O in all cases.

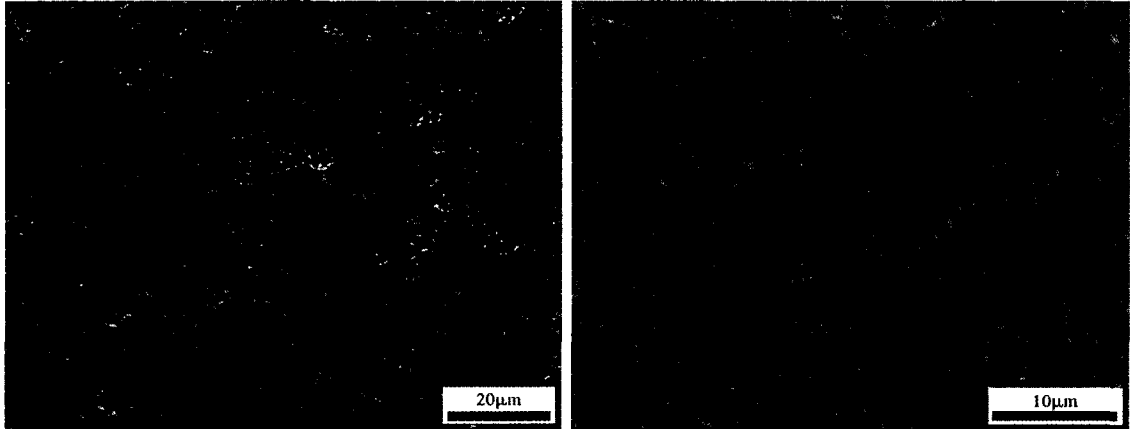
5.4.2 Vacuum Furnace Heat Treatments

This sub-section outlines the SEM/EDS analysis results in terms of the microstructural features present both on the surface and in the cross-sections of the APS NiCrAlY-coated test specimens that have been subjected to the pre-oxidation VHTs. The sub-section is concluded with a summary of the trends in the results of the VHT series. The 6 VHT conditions examined are:

- 1000C for 10 and 15 hours
- 1050C for 5 and 10 hours
- 1100C for 1 and 5 hours.

1000°C / 10 Hours

A micrograph of the APS NiCrAlY-coated test specimen that has undergone a VHT of 1000°C for 10 hours (Figure 78a) shows the formation of a relatively thin, smooth TGO layer that marginally covers the features of underlying NiCrAlY layer surface. Compositional EDS surface area scan data for the region shown in Figure 78a, listed in Table 47, indicates increased proportions of aluminum concentration in comparison to the as-deposited BC composition (Table 45), potentially as a result of the formation of a very thin aluminum oxide TGO layer. A high-magnification view of the sample surface (Figure 78b) shows the retention of typical TS coating features such as coating material splats, oxide inclusions and porosity that is still visible beneath the very thin aluminum-rich TGO layer. As the top surface of the coated test specimen was ground to a 1200 grit surface finish prior to VHT, the surface morphology does not resemble that of the as-deposited condition (as seen in Figure 76 and rather resembles more closely that of a ground and polished cross-sectional view of a TS coating.



(a) A SE micrograph showing a representative view of the test specimen surface after VHT. (b) A high-magnification BSE micrograph showing a detailed view of the test specimen surface after VHT. Typical features of a TS coating are retained.

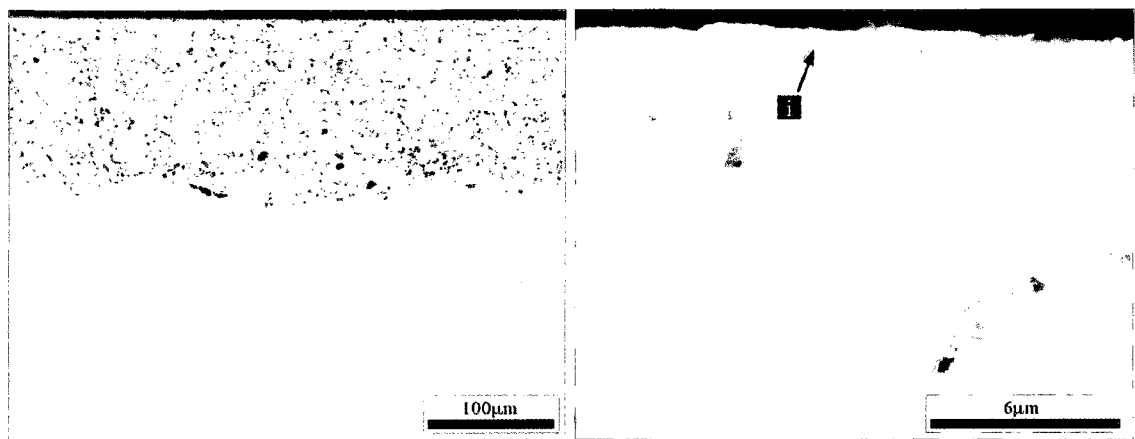
Figure 78: Surface features of the APS NiCrAlY-coated test specimen after VHT of 1000°C for 10 hours.

Table 47: EDS surface area scan data for region shown in Figure 78a (in wt%).

Ni	Cr	Al	Y
59.69	15.63	22.81	1.96

Note: While not quantified, the EDS spectrum also indicates the presence of O.

A micrograph showing a cross-sectional overview of the heat treated NiCrAlY-coated test specimen (Figure 79a) does not show significant change from the as-deposited condition, with exception of the ground specimen surface as a result of a pre-oxidation surface treatment. Hardly visible in the high-magnification micrograph (Figure 79b) is the existence of (i) a discontinuous TGO layer on the surface of the test specimen. This TGO layer is far too thin in size to be examined for elemental composition with the EDS equipment used in this work.



(a) A BSE micrograph showing a representative view of the typical post-heat treatment features. (b) A high-magnification SE micrograph providing a detailed view of the BC surface, showing the presence of (i) a discontinuous TGO layer.

Figure 79: Cross-sectional microstructural features of the APS NiCrAlY-coated test specimen after VHT of 1000°C for 10 hours.

1000°C / 15 Hours

A micrograph of the APS NiCrAlY-coated test specimen that has undergone a VHT of 1000°C for 15 hours (Figure 80) shows the formation of a relatively thin, smooth TGO layer that marginally covers the features of underlying NiCrAlY layer surface. In comparison to the previous VHT condition, it appears that the TGO layer has become more coarse. Compositional EDS surface area scan data for the region shown in Figure 80, listed in Table 48, indicates increased proportions of aluminum concentration in comparison to the as-deposited BC composition (Table 45), potentially as a result of the formation of a very thin aluminum oxide TGO layer.

High-magnification views of the same location on the sample surface (Figure 81) show the formation of a discontinuous TGO phase on the sample surface consisting predominantly of two constituents; (i) a darker-shaded aluminum-rich component and (ii) a lighter-shaded aluminum and nickel-rich component. The compositional EDS spot scan data for these two locations, marked in Figure 81b, is listed in Table 49.

A cross-sectional micrograph of the heat treated NiCrAlY-coated test specimen (Figure 82a) shows the retention of typical features of a TS coating as seen in the as-deposited condition (Figure 77) but with the addition of a discontinuous TGO on the surface of the test specimen. A high-magnification micrograph (Figure 82b) provides a detailed view of (i) the discontinuous TGO layer on the surface of the test specimen. Compositional EDS spot scan data for this location is listed in Table 50, indicating an aluminum-rich layer that can be attributed to the possible formation of an aluminum oxide TGO. In comparison to the previous VHT condition, although still discontinuous, the TGO has greater thickness with the increased VHT holding time from 10 to 15 hours.

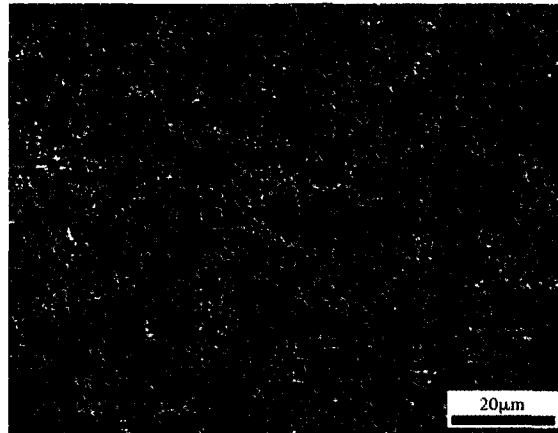
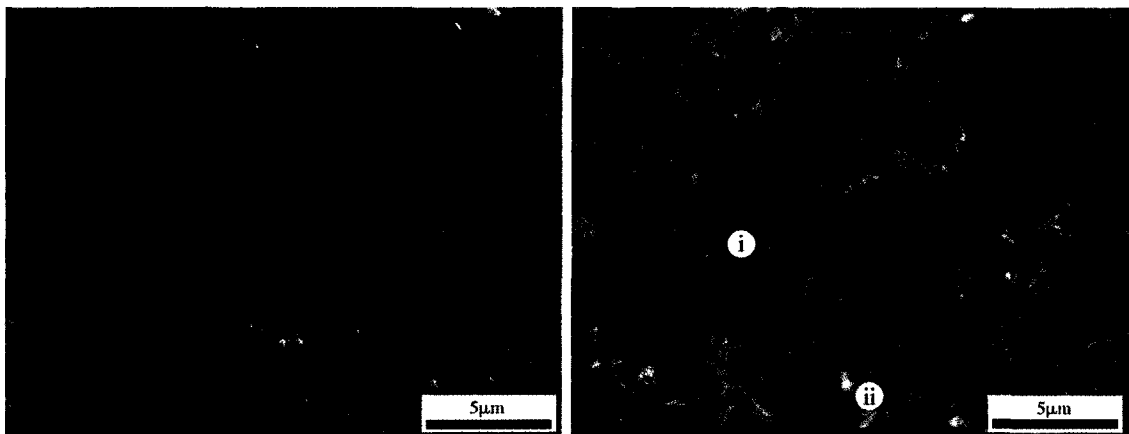


Figure 80: A SE micrograph showing the typical surface features of the APS NiCrAlY-coated test specimen after VHT of 1000°C for 15 hours.



(a) SE micrograph.

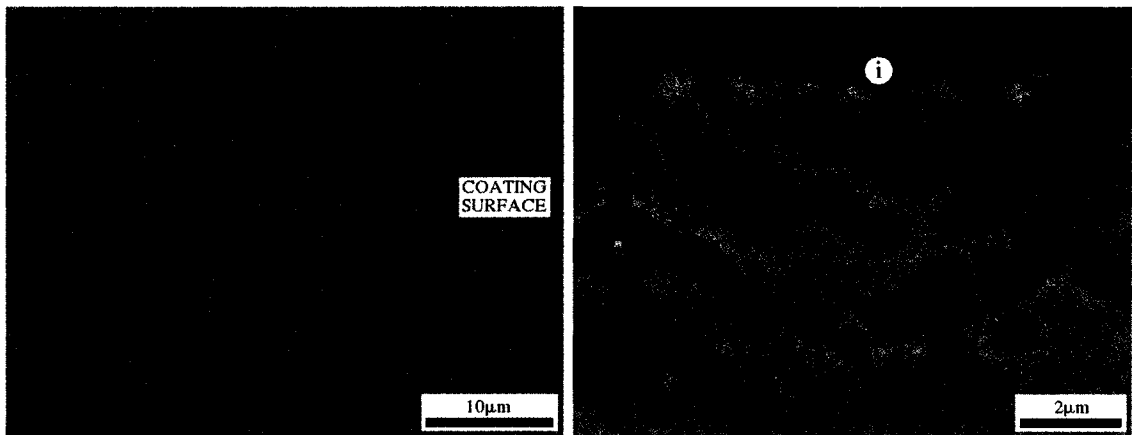
(b) BSE micrograph of same location as (a), showing (i) a dark-shaded, aluminum-rich oxide constituent and (ii) a light-shaded, nickel-rich oxide constituent. Markers also indicate EDS spot scan locations.

Figure 81: High-magnification micrographs showing the surface morphology of the two TGO constituents typically present on the APS NiCrAlY-coated test specimen surface after a VHT of 1000°C for 15 hours.

Table 48: EDS surface area scan data for region shown in Figure 80 (in wt%).

Ni	Cr	Al	Y
60.92	13.14	23.09	2.85

Note: While not quantified, the EDS spectrum also indicates the presence of O.



(a) A BSE micrograph showing a representative view of test specimen after VHT.

(b) A high-magnification BSE micrograph near the test specimen surface showing (i) a sub-micron, discontinuous TGO layer on top of the BC. Marker indicates EDS spot scan location.

Figure 82: Cross-sectional microstructural features of the APS NiCrAlY-coated test specimen after VHT of 1000°C for 15 hours. The sample was mounted face-to-face to ensure TGO retention throughout the metallographic preparation process.

Table 49: EDS spot scan data for locations shown in Figure 81b (in wt%).

	Ni	Cr	Al	Y
i	28.30	11.99	56.84	2.87
ii	50.29	13.84	34.86	1.01

Note: While not quantified, the EDS spectra also indicate the presence of O in both cases.

Table 50: EDS spot scan data for location shown in Figure 82b (in wt%).

	Ni	Cr	Al	Y
i	41.81	9.09	46.83	2.27

Note: While not quantified, the EDS spectrum also indicates the presence of O.

Table 51: EDS surface area scan data for region shown in Figure 83a (in wt%).

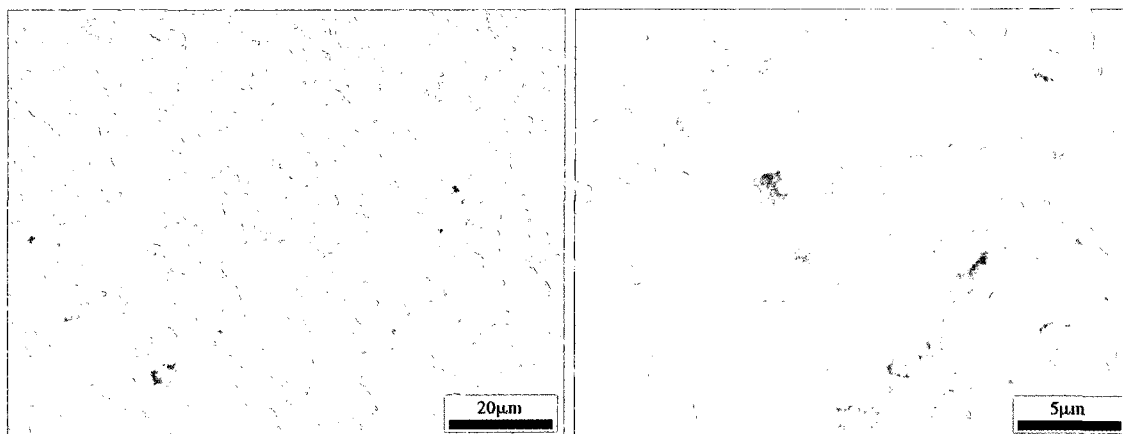
Ni	Cr	Al	Y
58.00	14.51	23.78	3.71

Note: While not quantified, the EDS spectrum also indicates the presence of O.

1050°C / 5 Hours

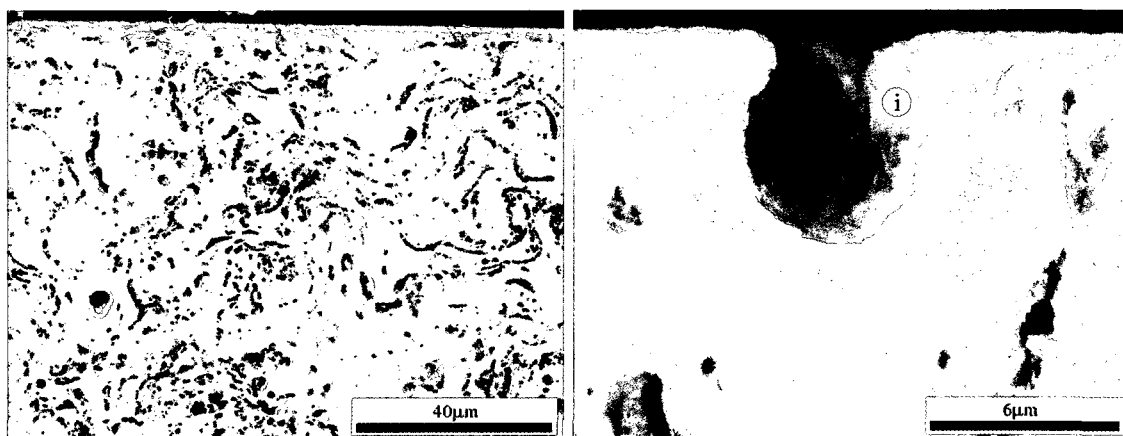
A micrograph of the APS NiCrAlY-coated test specimen that has undergone a VHT of 1050°C for 5 hours (Figure 83a) shows the formation of a relatively thin, smooth, and discontinuous TGO layer that marginally covers the features of underlying NiCrAlY layer surface. Compositional EDS surface area scan data for the region shown in Figure 83a, listed in Table 51, indicates increased proportions of aluminum and yttrium concentrations in comparison to the as-deposited BC composition (Table 45), potentially as a result of the formation of a very thin aluminum oxide TGO layer. A high-magnification view of the sample surface (Figure 83b) still shows some retention of typical TS coating features that are partially visible beneath the thin aluminum-rich surface TGO layer, as present in previous VHT conditions. The morphology of surface TGO components is very similar to those seen on the surface of the 1000°C/15 hr VHT test specimen (Figure 81a).

A micrograph showing a cross-sectional overview of the heat treated NiCrAlY-coated test specimen (Figure 84a) does not show significant change from the as-deposited condition (Figure 77), with exception of the ground specimen surface as a result of the pre-oxidation surface treatment. Hardly visible in the high-magnification micrograph (Figure 84b) is the existence of (i) a discontinuous TGO layer on the surface of the test specimen. Compositional EDS spot scan data for this location, listed in Table 52, indicates a significantly increased presence of both aluminum and yttrium in comparison to the as-deposited coating condition (Table 46).



(a) A SE micrograph showing a representative view of the test specimen surface after VHT. (b) A high-magnification SE micrograph providing a detailed view of the test specimen post heat treatment surface features.

Figure 83: Surface features of the APS NiCrAlY-coated test specimen after VHT of 1050°C for 5 hours.



(a) A SE micrograph showing the typical BC microstructure after VHT. (b) A high-magnification SE micrograph of a typical BC surface void. Marker indicates EDS spot scan location.

Figure 84: Cross-sectional microstructural features of the APS NiCrAlY-coated test specimen after VHT of 1050°C for 5 hours.

Table 52: EDS spot scan data for location shown in Figure 84b (in wt%).

	Ni	Cr	Al	Y	Fe
i	48.71	15.65	21.68	13.60	0.35

Table 53: EDS surface area scan data for region shown in Figure 85a (in wt%).

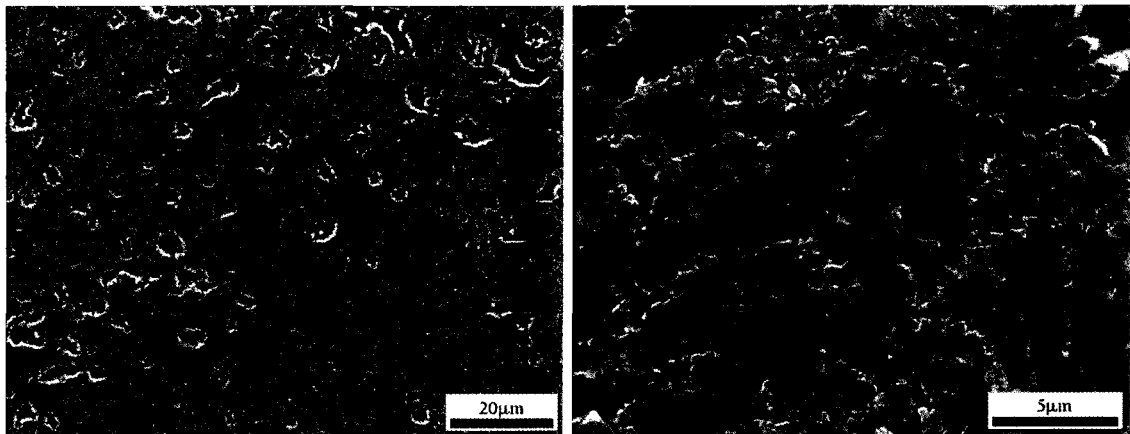
Ni	Cr	Al	Y
53.68	14.28	29.44	2.60

Note: While not quantified, the EDS spectrum also indicates the presence of O.

1050°C / 10 Hours

A micrograph of the APS NiCrAlY-coated test specimen that has undergone a VHT of 1050°C for 10 hours (Figure 85a) shows the formation of a very thin, and discontinuous TGO layer that marginally covers the features of underlying NiCrAlY layer surface. Compositional EDS surface area scan data for the region shown in Figure 85a, listed in Table 53, indicates significantly increased proportions of aluminum and yttrium concentrations in comparison to the as-deposited BC composition (Table 45), potentially as a result of the formation of a very thin aluminum oxide TGO layer. A high-magnification view of the sample surface (Figure 85b) still shows some retention of typical TS coating features that are partially visible beneath the very thin, discontinuous, aluminum-rich surface TGO layer, as present in previous VHT conditions. The morphology of surface TGO components is very similar to those seen on the surface of the 1050°C/5 hr VHT test specimen (Figure 83a), however, the TGO particles as a result of this VHT are slightly more coarse.

A micrograph showing a cross-sectional overview of the heat treated NiCrAlY-coated test specimen (Figure 86) does not show significant change from the as-deposited condition (Figure 77), with exception of the ground specimen surface as a result of the pre-oxidation surface treatment. Partly visible along the coating surface is the existence of (i) a discontinuous TGO layer on the surface of the test specimen. The thickness of the TGO layer, however, was too small to measure with the EDS equipment used in this work.



(a) A SE micrograph showing a representative view of the test specimen surface after VHT.

(b) A high-magnification SE micrograph providing a detailed view of the test specimen post-heat treatment surface features.

Figure 85: Surface features of the APS NiCrAlY-coated test specimen after VHT of 1050°C for 10 hours.

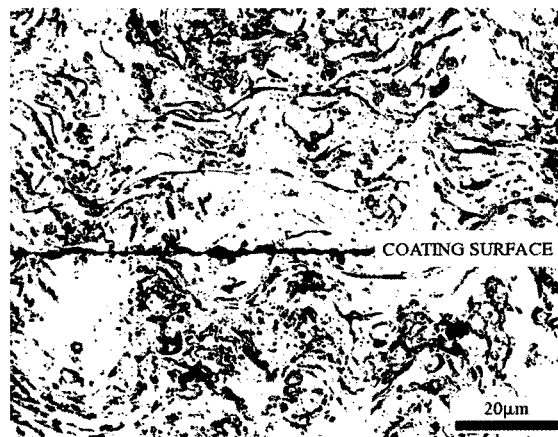


Figure 86: Cross-sectional microstructural features of the APS NiCrAlY-coated test specimen after VHT of 1050°C for 10 hours. The sample was mounted face-to-face to ensure TGO retention throughout the metallographic preparation process.

Table 54: EDS surface area scan data for region shown in Figure 87 (in wt%).

Ni	Cr	Al
62.36	20.01	17.62

1100°C / 1 Hour

A micrograph of the APS NiCrAlY-coated test specimen that has undergone a VHT of 1100°C for 1 hour (Figure 87) shows the presence of discontinuous TGO particles that barely cover the features of underlying NiCrAlY layer surface. Compositional EDS surface area scan data for the region shown in Figure 87, listed in Table 54, indicates only a minutely increased proportion of aluminum concentration in comparison to the as-deposited BC composition (Table 45). The test specimen surface still retains a variety of typical TS coating features that are partially visible beneath the very thin, discontinuous surface TGO layer, similar to those present in previous VHT conditions.

A micrograph showing a cross-sectional overview of the heat treated NiCrAlY-coated test specimen (Figure 88a) does not show significant change from the as-deposited condition (Figure 77), with exception of the ground specimen surface as a result of the pre-oxidation surface treatment. Typical features of a TS coating layer are retained. A high-magnification micrograph (Figure 88b) does not show any trace of a visible TGO layer to be present on the surface of the test specimen. By the absence of the TGO layer, it is evident that above temperatures of 1050°C, it is not possible to form a visible TGO in a vacuum environment.

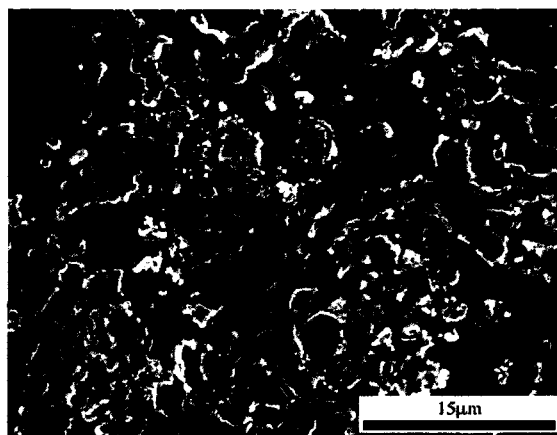
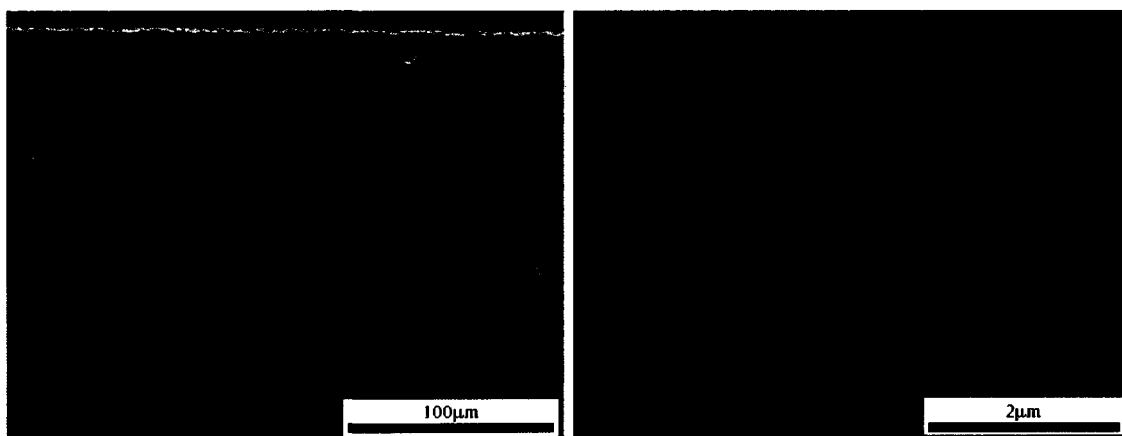
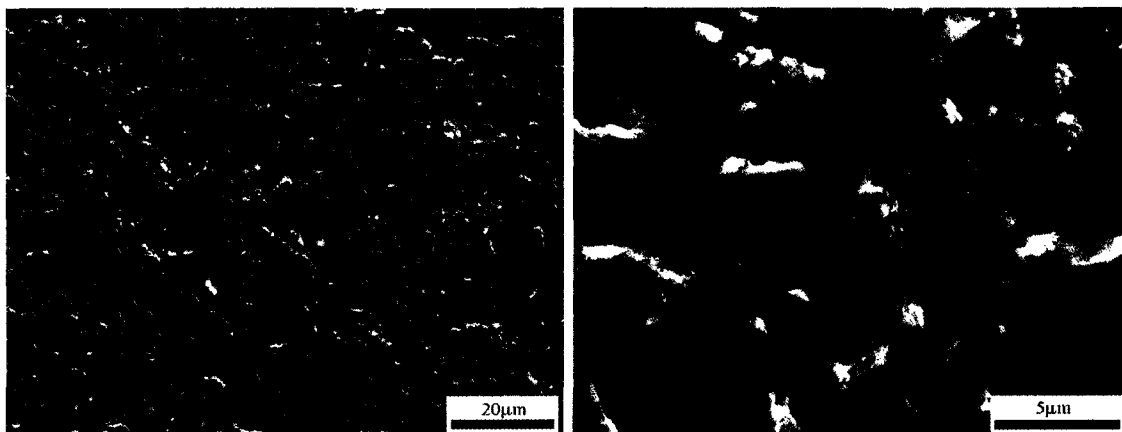


Figure 87: A SE micrograph showing the surface features of the APS NiCrAlY-coated test specimen after VHT of 1100°C for 1 hour.



(a) A SE micrograph showing the typical BC microstructure after VHT. (b) A high-magnification SE micrograph showing a detailed view of the BC surface after VHT.

Figure 88: Cross-sectional microstructural features of the APS NiCrAlY-coated test specimen after VHT of 1100°C for 1 hour.



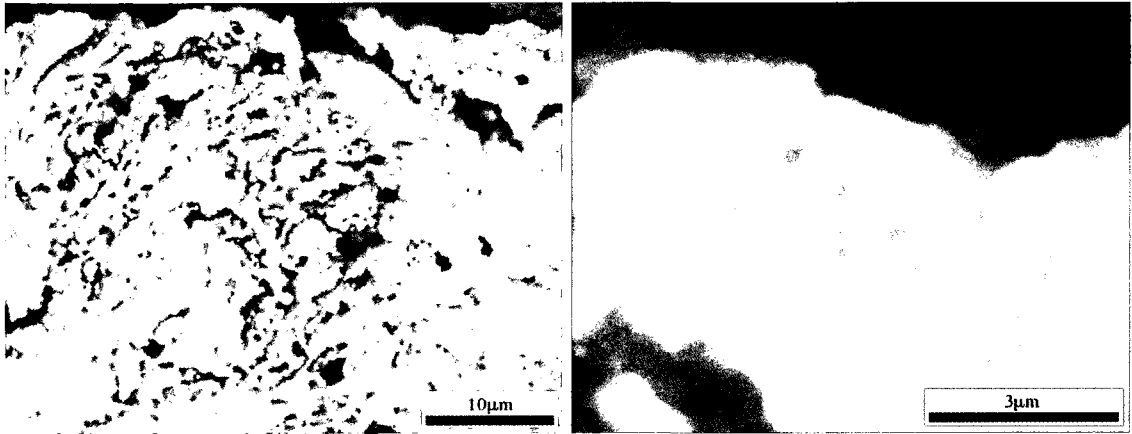
(a) A SE micrograph showing a representative view of the test specimen surface after VHT. (b) A high-magnification SE micrograph providing a detailed view of the test specimen post-heat treatment surface features.

Figure 89: Surface features of the APS NiCrAlY-coated test specimen after VHT of 1100°C for 5 hours.

1100°C / 5 Hours

The micrographs of the APS NiCrAlY-coated test specimen that has undergone a VHT of 1100°C for 5 hours (Figures 89a and b) show the formation of discontinuous TGO particles that sparsely cover the underlying NiCrAlY layer surface. Compositional EDS surface area scan data for the region shown in Figure 89a, listed in Table 55, indicates an increased proportion of yttrium concentration in comparison to the as-deposited BC composition (Table 45).

A micrograph showing a cross-sectional overview of the heat treated NiCrAlY-coated test specimen (Figure 90a) indicates the retention of typical TS coating features and does not show significant change from the as-deposited condition (Figure 77). A high-magnification micrograph (Figure 90b) does not show any trace of a visible TGO layer to be present on the surface of the test specimen.



(a) A BSE micrograph showing the typical BC microstructure after VHT.

(b) A high-magnification SE micrograph showing a detailed view of the BC surface after VHT, indicating the lack of an appreciable TGO layer.

Figure 90: Cross-sectional microstructural features of the APS NiCrAlY-coated test specimen after VHT of 1100°C for 5 hours.

Table 55: EDS surface area scan data for region shown in Figure 89a (in wt%).

Ni	Cr	Al	Y
65.03	11.93	18.12	4.92

Note: While not quantified, the EDS spectrum also indicates the presence of O.

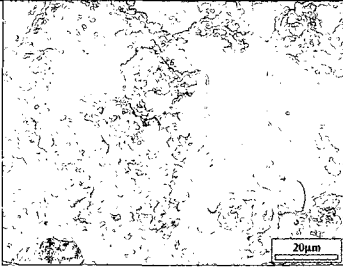
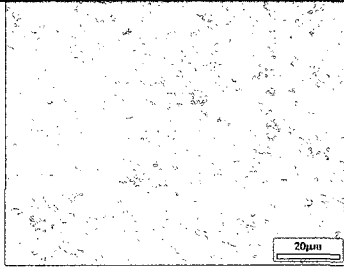
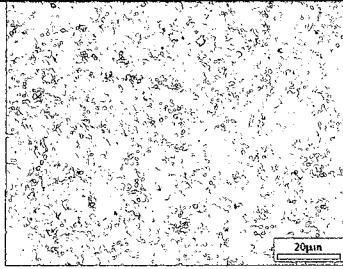
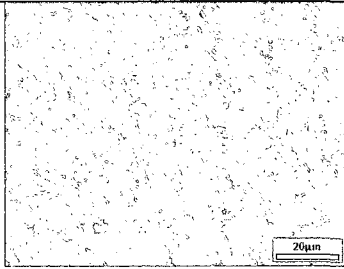
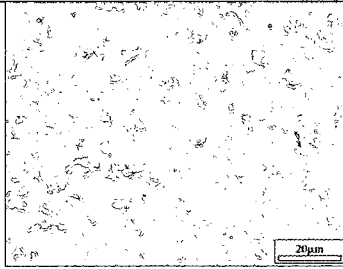
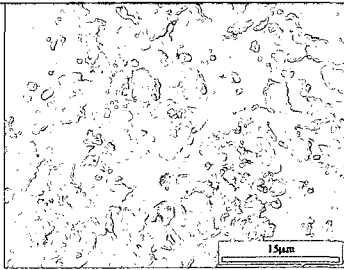
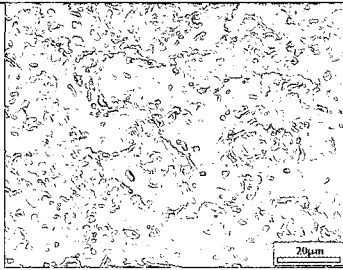
VHT Summary

The summary table of the APS NiCrAlY-coated test specimen surface conditions as a result of the VHT series (Table 56) shows the general trend of the formation of a very thin, discontinuous, and superficial layer of TGO particles up to the 1050°C/10 hrs VHT condition. At temperatures above 1050°C, the TGO particles become smaller in size and cover significantly less of the specimen surface.

A summary of the average surface composition of the specimens in the VHT series (Figure 91) supports this observation by indicating a steady rise, with increased heat treatment temperature and time, in the proportion of aluminum content on the specimen surface in comparison to the as-deposited condition. This higher proportion of aluminum on the specimen surfaces is thought to be due to the presence of a very thin aluminum oxide surface TGO layer. The heat treatment condition that exhibits the largest increase in the proportion of aluminum is the 1050°C/10 hrs VHT condition.

The summary table of the APS NiCrAlY-coated test specimen cross-sectional features as a result of the VHT series (Table 57) indicates that the heat treatment conditions that yield the most extensive formation of a surface TGO layer are that of the 1000°C for 10 and 15 hours. Both VHT conditions, however, produce a discontinuous, sub-micron TGO layer. Where it was possible to measure the composition of the TGO, it was shown to be aluminum-rich, suggesting the possible presence of an aluminum oxide TGO.

Table 56: A summary of APS NiCrAlY-coated test specimen surface conditions after VHT.

As-deposited		
1000°C for 10 & 15 hrs		
1050°C for 5 & 10 hrs		
1100°C for 1 & 5 hrs		

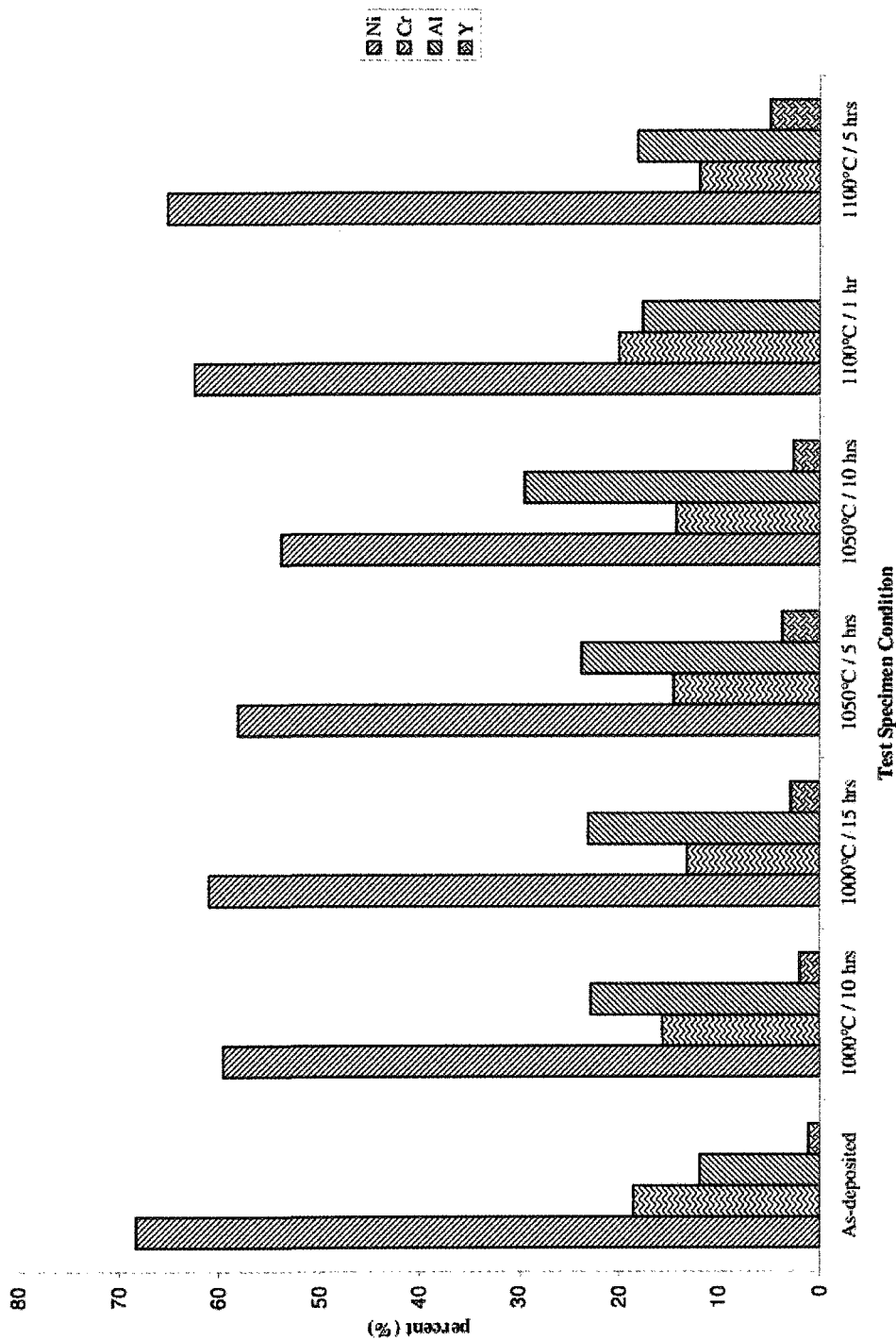
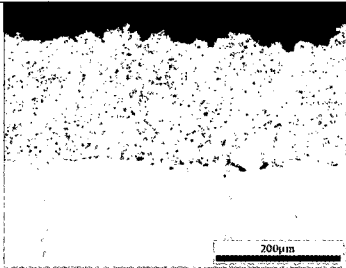
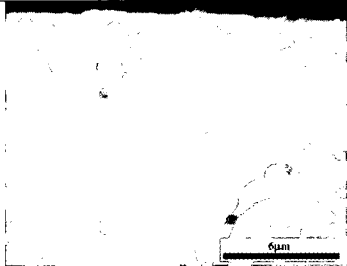
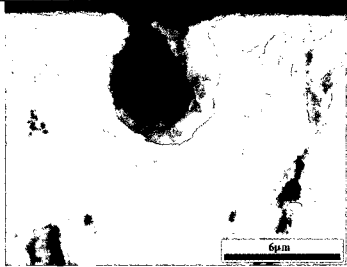
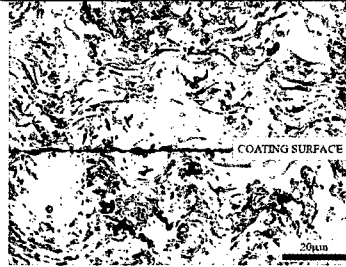
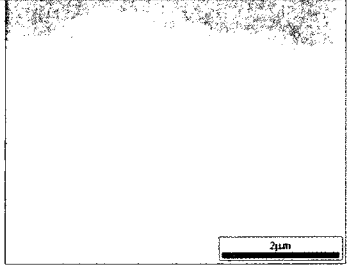
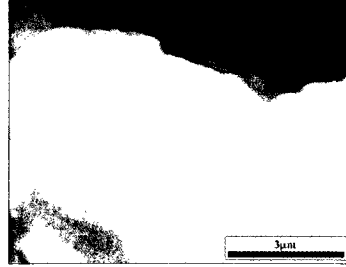


Figure 91: EDS area scan data for the APS NiCrAlY-coated test specimen surface composition (in wt%) as a function of specimen condition.

Table 57: A summary APS NiCrAlY-coated test specimen cross-sections after VHT.

<p>As-deposited</p>		
<p>1000°C for 10 & 15 hrs</p>		
<p>1050°C for 5 & 10 hrs</p>		
<p>1100°C for 1 & 5 hrs</p>		

5.4.3 Air Furnace Heat Treatments

This sub-section outlines the SEM/EDS analysis results in terms of the microstructural features present both on the surface and in the cross-sections of the APS NiCrAlY-coated test specimens that have been subjected to the pre-oxidation AHTs. The sub-section is concluded with a summary of the trends in the results of the AHT series. The 3 AHT conditions examined are:

- 1000C for 10 hours
- 1050C for 5 hours
- 1100C for 1 hour

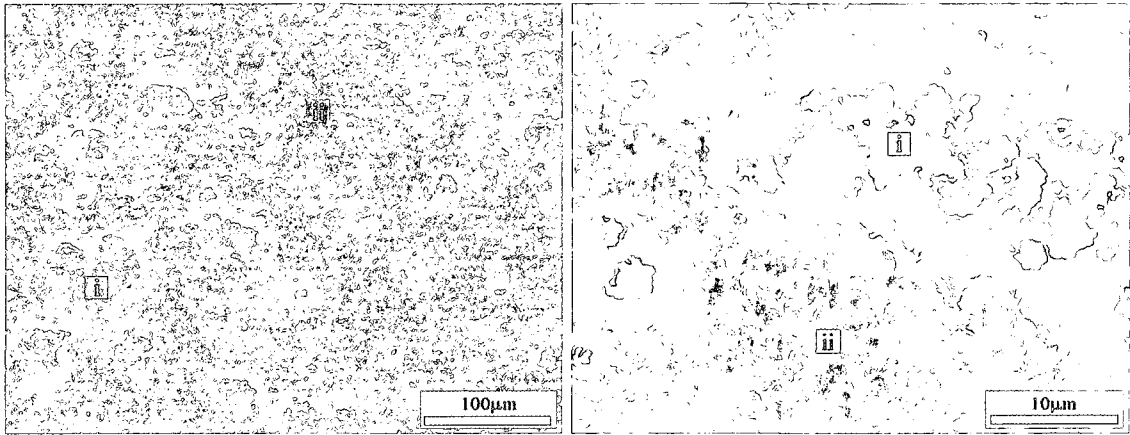
1000°C / 10 Hours

The surface of the APS NiCrAlY-coated test specimen that has been subjected to an AHT of 1000°C for 10 hours (Figure 92a) shows the formation of two different oxide phases: (i) a dense, globular mixed oxide phase that forms cluster islands in a matrix of (ii) a porous, whisker-shaped oxide phase. Figure 92b shows a detailed view of the test specimen surface morphology, clearly showing the interaction between the two different oxide phases (i and ii). Figure 93a shows a detailed view of the porous, whisker-shaped oxide structure. The compositional EDS spot scan data for the whisker-shaped oxide phase shown in Figure 93a, listed in Table 58, indicates a significant proportion of aluminum in comparison to the as-deposited coating composition. This whisker-shaped, aluminum-rich oxide morphology has been identified in previous work by Hesnawi et al [17] (see Figure 12) as θ -Al₂O₃, a transitional phase of aluminum oxide. Figure 93b shows a detailed view of the dense, globular oxide structure. The compositional EDS spot scan data for the globular-shaped oxide phase shown in Figure 93b, listed in Table 58, indicates a significant proportion of nickel in comparison to the as-deposited coating composition.

Table 58: EDS spot scan data for locations shown in Figure 93a (i) and Figure 93b (ii) (in wt%).

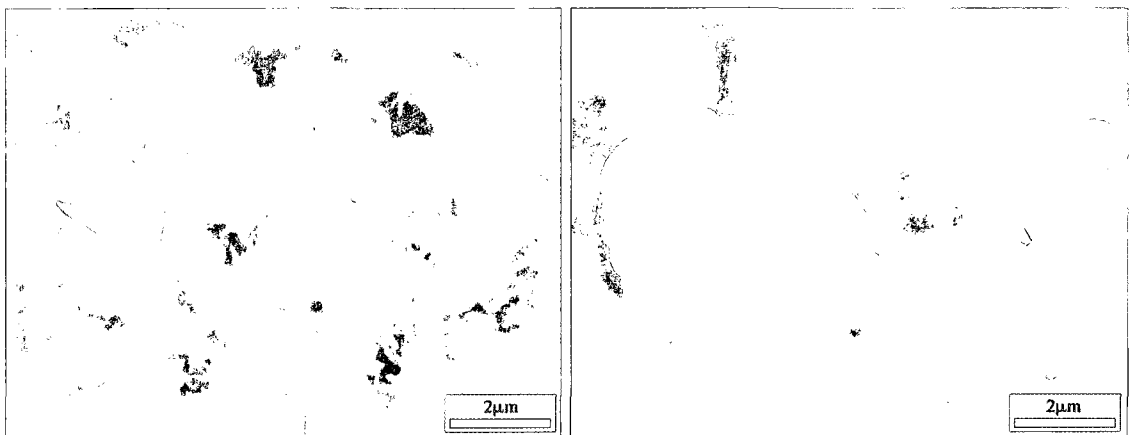
	Ni	Cr	Al
i	16.76	8.44	74.80
ii	91.51	5.27	3.22

A cross-sectional micrograph of the APS NiCrAlY-coated test specimen (Figure 94) shows the little noticeable change in sub-surface coating microstructure in comparison to the as-deposited coating microstructure (Figure 77). On the sample surface, however, the formation of (i) a continuous TGO layer can be seen with an average thickness of approximately 3 μm . This TGO is often interrupted by the presence of (ii) mixed-oxide cluster outcroppings that protrude through the TGO (i) from the as-deposited BC material. A detailed view of the TGO layer (i) is shown in Figure 95a. EDS spot scan data (Table 59) indicates a significantly increased proportion of aluminum concentration in comparison to the as-deposited coating composition, possibly due to the formation of an aluminum oxide surface TGO layer. This surface TGO layer is sporadically interrupted by outcroppings of a combination of two different oxide phases, as shown in the high-magnification micrograph in Figure 95b. Compositional EDS spot scan data for the locations marked in Figure 95b, listed in Table 59, indicates that the (ii) lighter-shaded mixed oxide constituent contains a greater proportion of nickel concentration, and (iii) the darker-shaded mixed oxide constituent contains a greater proportion of chromium concentration in comparison to the as-deposited coating composition (Table 46). It appears that these transition metal oxides (lighter mixed oxide constituents) grow from within the interior of the as-deposited NiCrAlY microstructure and through the aluminum oxide surface TGO layer.



(a) A SE micrograph showing the distribution of oxide phases on the surface of the test specimen after AHT: (i) a globular oxide islands in a matrix consisting of (ii) a whisker-shaped oxide phase. (b) A high-magnification BSE micrograph showing a detailed view of the two distinct oxide morphologies present on the sample surface: (i) globular oxide islands and (ii) a whisker-shaped oxide phase.

Figure 92: Surface features of the APS NiCrAlY-coated test specimen after an AHT of 1000°C for 10 hours.



(a) Porous, aluminum-rich, whisker-shaped oxide phase. (b) Dense, nickel-rich, globular-shaped oxide phase.

Figure 93: High-magnification SE micrographs providing detailed views of the surface morphology of the two predominant oxide phases that are typically found on the surface of the APS NiCrAlY-coated test specimen after an AHT of 1000°C for 10 hours.

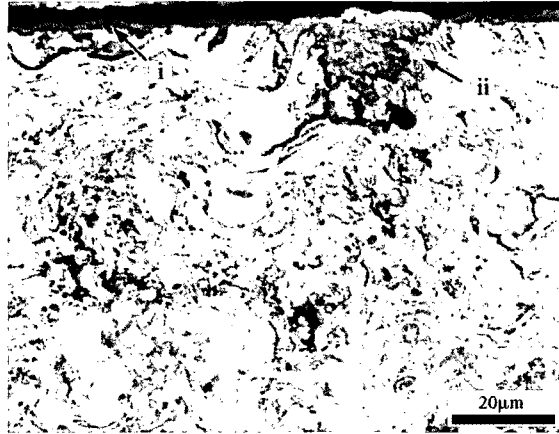
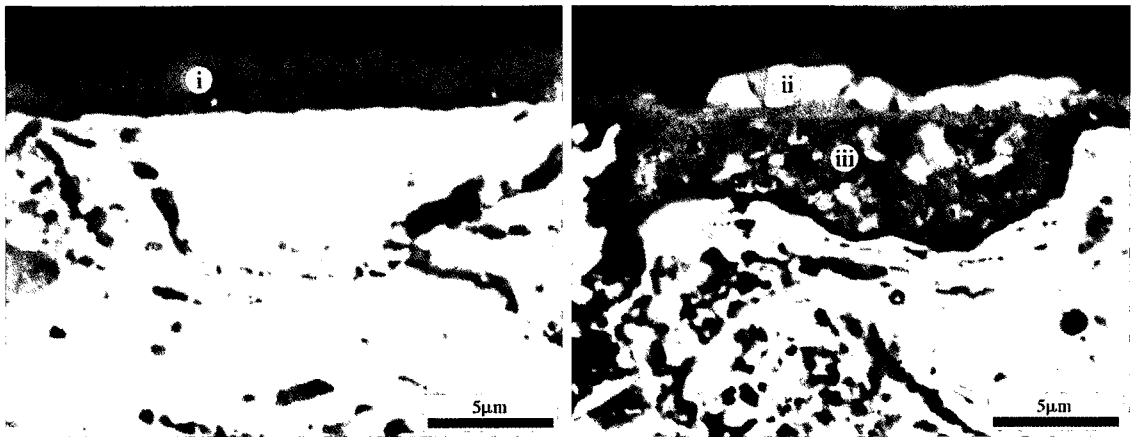


Figure 94: A BSE micrograph showing the typical cross-sectional microstructural features of the APS NiCrAlY-coated test specimen after an AHT of 1000°C for 10 hours, showing (i) a largely continuous oxide layer that is sporadically broken by (ii) outcroppings of a second oxide phase.



(a) A SE micrograph showing a detailed view of (i) the largely continuous, aluminum-rich oxide phase. (b) A BSE micrograph showing a detailed view of a mixed-oxide outcropping that consists of (ii) an upper nickel-rich phase and (iii) a lower chromium-rich phase.

Figure 95: High-magnification micrographs providing a detailed view of the three different oxide phases typically present on the surface of the APS NiCrAlY-coated test specimen after an AHT of 1000°C for 10 hours. Markers also indicate EDS spot scan locations.

Table 59: EDS spot scan data for locations shown in Figure 95 (in wt%).

	Ni	Cr	Al
i	11.02	7.74	81.24
ii	95.69	4.31	-
iii	21.19	47.31	31.5

Note: While not quantified, the EDS spectra also indicates the presence of O in all cases.

1050°C / 5 Hours

The surface of the APS NiCrAlY-coated test specimen that has been subjected to an AHT of 1050°C for 5 hours (Figure 96) shows the formation of two different oxide phases: (i) a dense, globular oxide phase that forms cluster islands in a matrix of (ii) a porous, whisker-shaped oxide phase. Compositional EDS surface scan data for region shown in Figure 96, listed in Table 60, indicates an overall significantly increased proportion of aluminum concentration when compared to the as-deposited surface composition (Table 45).

Figure 97 shows a detailed view of the porous, whisker-shaped oxide phase. The compositional EDS spot scan data for the whisker-shaped oxide phase, listed in Table 61, indicates a significant proportion of aluminum in comparison to the as-deposited coating composition. This high proportion of aluminum concentration is thought to be due to the formation of a θ -Al₂O₃ surface layer, of which a similar whisker-shaped morphology has been reported by Hesnawi et al [17] (see Figure 12).

Figure 98 shows a detailed view of two typical variants of the dense, globular oxide phase found on the test specimen surface. The compositional EDS spot scan data for both morphologies shown in Figure 98, listed in Table 62, indicates a significant proportion of nickel, suggesting the formation of a transition metal oxide phase consisting predominantly of nickel oxide.

A cross-sectional micrograph of the APS NiCrAlY-coated test specimen (Figure 99) shows the little noticeable change in the coating microstructure in comparison to the as-deposited coating microstructure (Figure 77) with the exception of some thickening of oxide inclusions in the as-deposited coating layer due to internal oxidation. On the sample surface, however, the formation of (i) a continuous surface TGO layer can be seen with an average thickness of approximately 2 μ m. This TGO is frequently interrupted by the presence of (ii) transition metal oxide cluster outcroppings that

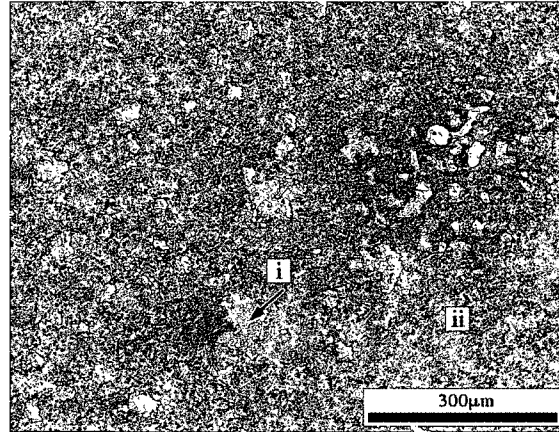


Figure 96: A SE micrograph showing the distribution of oxide phases on the surface of the APS NiCrAlY-coated test specimen after an AHT of 1050°C for 5 hours: (i) a globular oxide islands in a matrix consisting of (ii) a whisker-shaped oxide phase.

Table 60: EDS surface area scan data for region shown in Figure 96 (in wt%).

Ni	Cr	Al
35.51	20.87	43.61

protrude through the TGO (i) from the as-deposited BC material.

EDS spot scan data for locations marked in Figure 99, listed in Table 63, indicate a significantly increased proportion of aluminum concentration in the surface TGO layer (i) in comparison to the as-deposited coating composition (Table 46). The transition metal oxide cluster (ii), on the other hand, contains predominantly nickel and chromium, with some aluminum that is thought to be due to the inclusion of peripheral material to the spot scan measurement location. It appears that these transition metal oxides clusters (ii) grow from within the interior of the as-deposited NiCrAlY microstructure and through the aluminum oxide surface TGO layer (i).

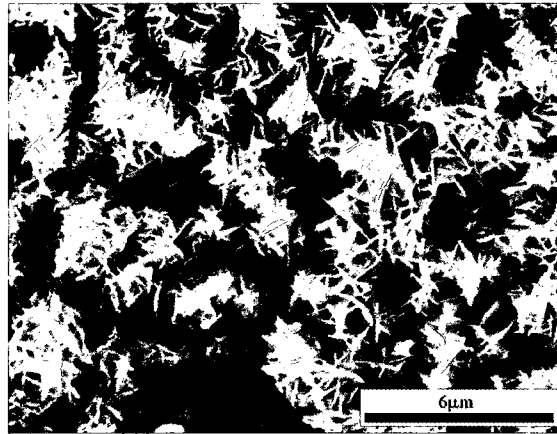
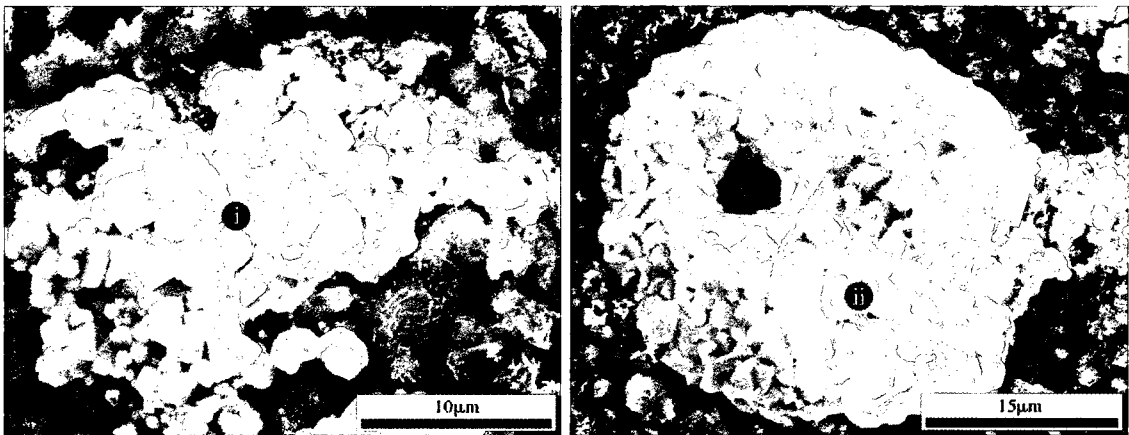


Figure 97: A high-magnification SE micrograph showing the surface morphology of the aluminum-rich, whisker-shaped oxide phase that is present on the surface of the APS NiCrAlY-coated test specimen after an AHT of 1050°C for 5.



(a) Variant 1.

(b) Variant 2.

Figure 98: High-magnification SE micrographs showing the surface morphology of the two variants of the globular, nickel-rich oxide phase that are typically present on the surface of the APS NiCrAlY-coated test specimen after an AHT of 1050°C for 5 hours. Markers show EDS spot scan measurement locations.

Table 61: EDS spot scan data for region shown in Figure 97 (in wt%).

Ni	Cr	Al
19.61	11.83	68.54

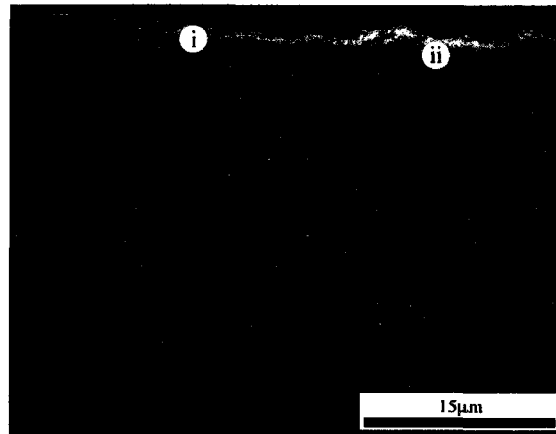


Figure 99: A SE micrograph showing the typical cross-sectional microstructural features of the APS NiCrAlY-coated test specimen after an AHT of 1050°C for 5 hours, showing (i) a largely continuous oxide layer that is sporadically broken by (ii) outcroppings of a second oxide phase. Markers also indicate EDS spot scan locations.

Table 62: EDS spot scan data for regions shown in Figure 98 (in wt%).

	Ni	Cr
i	95.34	4.65
ii	96.35	3.64

Table 63: EDS spot scan data for regions shown in Figure 99 (in wt%).

	Ni	Cr	Al
i	14.04	14.45	71.51
ii	44.59	31.25	24.16

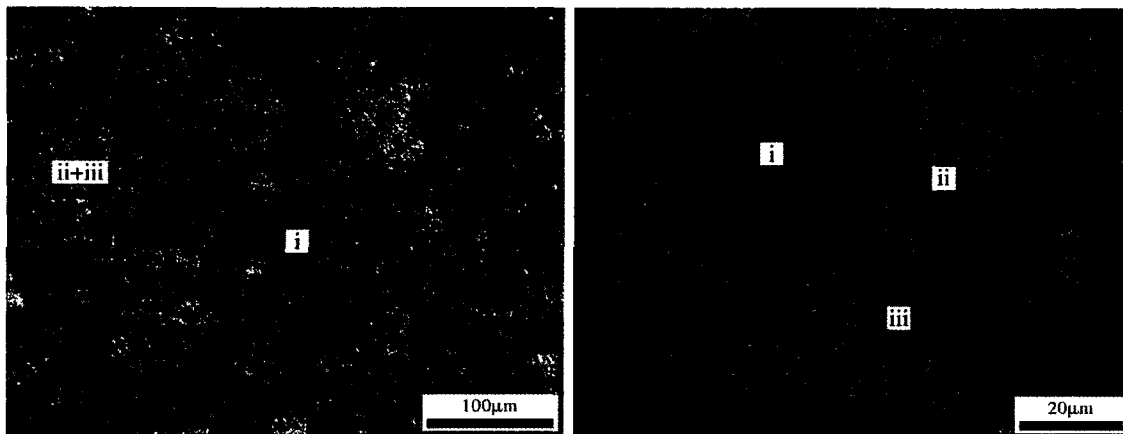
1100°C / 1 Hour

The surface of the APS NiCrAlY-coated test specimen that has been subjected to an AHT of 1100°C for 1 hour (Figure 100a) shows the formation of three different oxide phases: (ii+iii) a dense, light-shaded oxide clusters that form islands in a matrix of (i) a porous, whisker-shaped oxide phase. In comparison to the 1000°C/10hr AHT condition (Figure 92a), the light-shaded oxide clusters are much larger and cover a greater proportion of the test specimen surface. Figure 100b provides a detailed view of the three different surface oxide morphologies, showing that the dense, light-shaded oxide clusters are actually differentiable into (ii) a larger, globular-shaped oxide phase and (iii) a smaller, nodular-shaped oxide phase.

Figure 101a shows a detailed view of the porous, whisker-shaped oxide phase. The compositional EDS spot scan data for the whisker-shaped oxide phase, listed in Table 64, indicates a significant proportion of aluminum in comparison to the as-deposited coating composition. This high proportion of aluminum concentration is thought to be due to the formation of a θ -Al₂O₃ surface layer, of which a similar whisker-shaped morphology has been reported by Hesnawi et al [17] (see Figure 12).

Figure 101b shows a detailed views of two different oxide phases that make up the bright transition metal oxide cluster islands found on the test specimen surface. The compositional EDS spot scan data for the locations marked in Figure 101b is listed in Table 64. In comparison to the as-deposited coating composition (Table 46), the larger, globular-shaped oxide phase (ii) consists predominantly of nickel, possibly indicating an oxide consisting mainly of nickel oxide. The smaller, nodular-shaped oxide phase (iii), on the other hand, consists primarily of chromium and nickel, indicating the presence of a mixed transition metal oxide.

The high-magnification, cross-sectional micrographs of the APS NiCrAlY-coated test specimen (Figure 102) provide a detailed view of the features typically found



(a) A SE micrograph showing typical features of the APS NiCrAlY-coated test specimen after an AHT of 1100°C for 1 hour, showing (i) a whisker-shaped oxide layer that is broken by (ii and iii) outcroppings of a second mixed-oxide phase. (b) A high-magnification SE micrograph providing a detailed view of the three distinct oxide morphologies present on the test specimen surface after the AHT: (i) whisker-shaped constituent, (ii) a larger, globular-shaped constituent, and (iii) a smaller, nodular-shaped constituent.

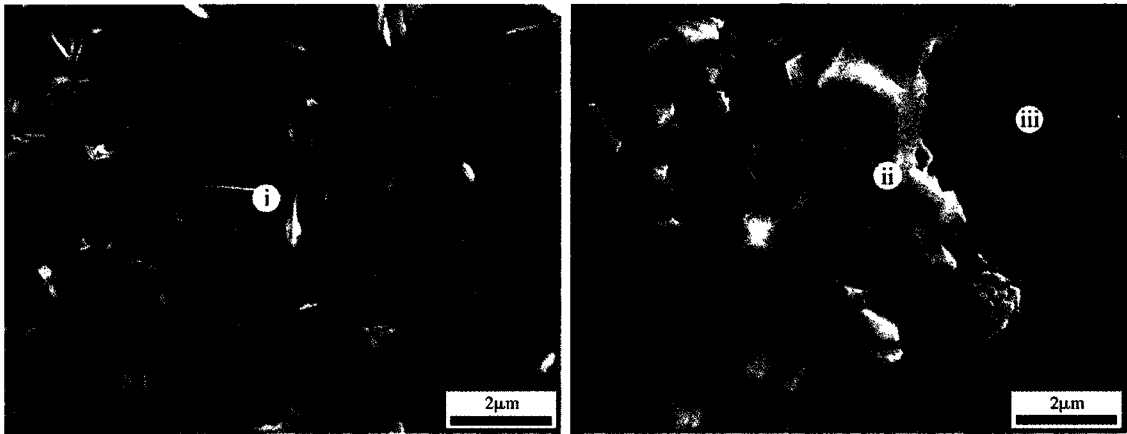
Figure 100: Surface features of the APS NiCrAlY-coated test specimen after an AHT of 1100°C for 1 hour.

near the surface of the heat treated test specimen. It shows the presence of (i) a surface TGO layer with an approximate average thickness of 1 μm and is frequently interrupted by the presence of (ii) oxide clusters. These oxide clusters appear to grow from within the interior of the as-deposited NiCrAlY microstructure and through the surface TGO layer .

Table 64: EDS spot scan data for regions shown in Figure 101 (in wt%).

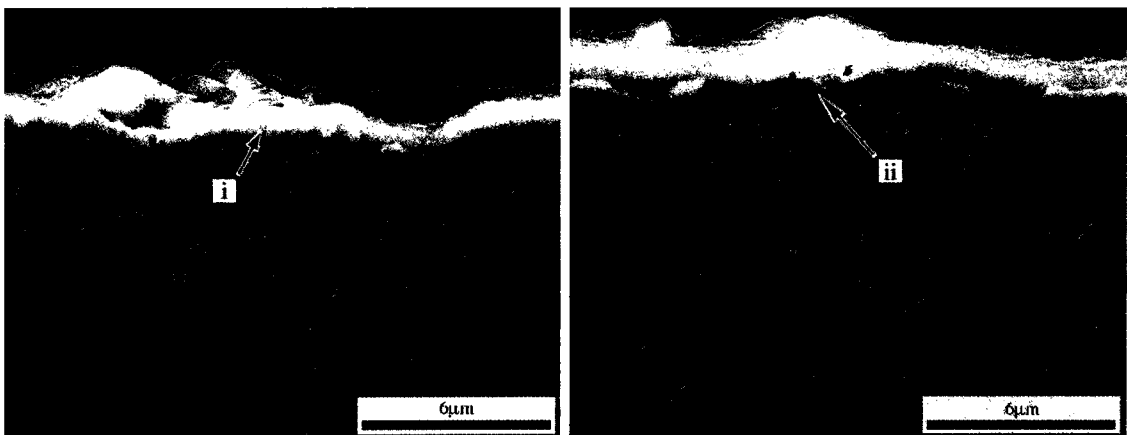
	Ni	Cr	Al
i	20.95	12.08	66.97
ii	71.90	8.15	1.96
iii	33.30	55.00	11.70

Note: While not quantified, the EDS spectra also indicates the presence of O in both cases.



(a) (i) Aluminum-rich, whisker-shaped oxide. (b) (ii) Larger, nickel-rich, globular-shaped oxide phase and (iii) smaller, chromium-rich, nodular-shaped oxide phase.

Figure 101: High-magnification SE micrographs showing the surface morphology of the three different oxide morphologies that are typically present on the surface of the APS NiCrAlY-coated test specimen after an AHT of 1100°C for 1 hour. Markers also indicate EDS spot scan locations.



(a) Aluminum-rich oxide layer (i). (b) Nickel- and chromium-rich mixed-oxide cluster (ii).

Figure 102: High-magnification SE micrographs providing a detailed view of the two TGO constituents typically present in the cross-section of the APS NiCrAlY-coated test specimen after an AHT of 1100°C for 1 hour: (a) an aluminum-rich layer that is frequently interrupted by (b) nickel- and chromium-rich mixed-oxide clusters.

AHT Summary

The summary table of the APS NiCrAlY-coated test specimen surface conditions as a result of the AHT series (Table 65) shows the general trend of the formation of light-shaded, nickel-rich, globular-shaped oxide cluster islands that are dispersed in a matrix consisting of a darker-shaded, whisker-shaped aluminum oxide surface TGO layer. The whisker-shaped aluminum oxide morphology is identified as θ -Al₂O₃. The 1100°C/1 hr AHT condition, however, forms a different light-shaded oxide cluster that appears to be a transition metal oxide that is nickel- and chromium-rich. As the heat treatment temperature increases and hold time decreases, the light-shaded oxide phase clusters increase in size, leading to greater coverage of the specimen surface.

The summary table of the APS NiCrAlY-coated test specimen cross-sectional features as a result of the AHT series (Table 66) supports the surface trends, noting the general formation of a continuous, aluminum-rich surface TGO layer that includes the frequent occurrence of nickel- and chromium-rich transition metal oxide clusters islands that appear to form from inside the as-deposited NiCrAlY BC layer and penetrate through the aluminum oxide surface TGO layer. As heat treatment temperature increases and the hold time decreases, the average aluminum oxide surface TGO layer thickness decreases from approximately 3 μm for the 1000°C/10 hrs AHT condition to approximately 1 μm for the 1100°C/1 hr AHT condition. While the temperature increase between the 1000°C/10 hrs AHT condition and that of the 1100°C/1 hr AHT condition will increase the oxidation rate, resulting in a TGO of greater average thickness, the shorter hold time in the latter condition limits the TGO growth. EDS spot scan measurements of the surface TGO layer present as a result of all three AHT conditions indicate an aluminum-rich composition, suggesting the formation of an aluminum oxide surface TGO layer.

Table 65: A summary of APS NiCrAlY-coated test specimen surfaces after AHT.

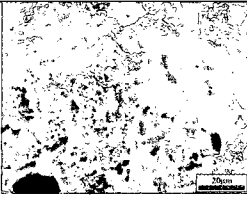
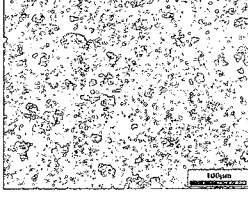
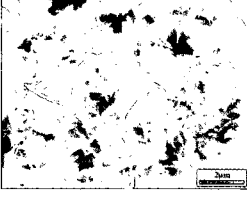
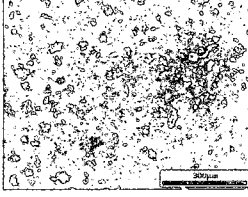
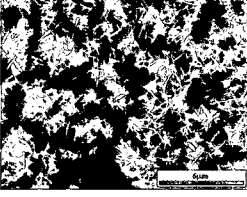
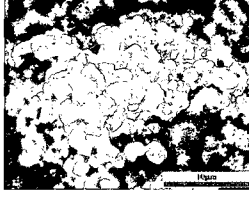
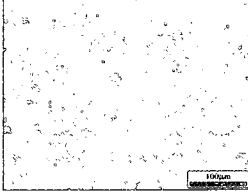
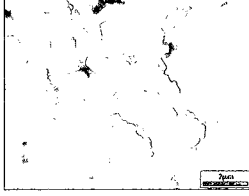
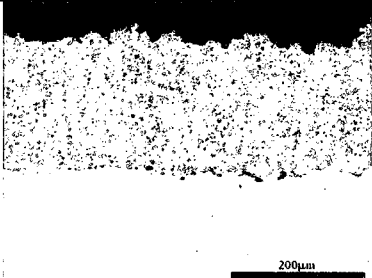
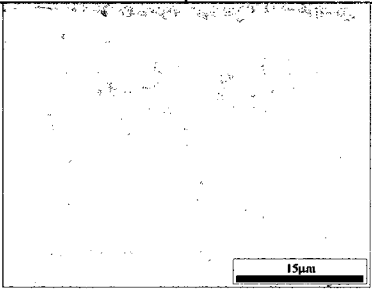
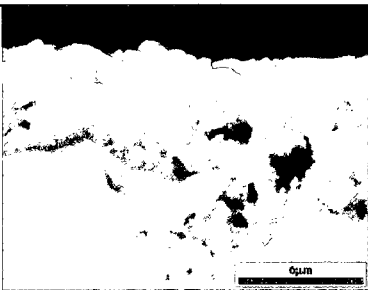
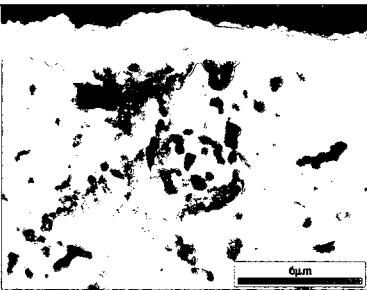
	General Features	Oxide Morphology	
As-deposited			
1000°C for 10 hrs			
1050°C for 5 hrs			
1100°C for 1 hr			

Table 66: A summary of APS NiCrAlY-coated test specimen cross-sections after AHT.

<p>As-deposited</p>		
<p>1000°C for 10 hrs</p>		
<p>1050°C for 5 hrs</p>		
<p>1100°C for 1 hr</p>		

5.4.4 XRD Results

This sub-section outlines the XRD analysis results (Figure 103) for the through-surface measurements of the APS NiCrAlY-coated test specimens that have been subjected to the following sample conditions:

- as-deposited condition
- a VHT of 1100°C for 1 hour
- an AHT of 1050°C for 5 hours

The XRD spectrum for the as-deposited sample shows the expected main peaks for NiCrAlY material. It consists of the γ -Ni (A) and γ' -Ni₃Al (B) components of the BC material.

For the test specimen subjected to a VHT of 1100°C for 1 hour, the XRD spectrum shows the strong presence of the γ' -Ni₃Al (B) phase belonging to the NiCrAlY BC layer, together with presence of very faint peaks associated with α -Al₂O₃ (C), and three other very small, unidentifiable peaks. The γ -Ni (A) phase that was present in the as-deposited condition is not present anymore.

For the test specimen subjected to an AHT of 1050°C for 5 hours, the XRD spectrum shows a strong presence of the γ' -Ni₃Al (B) phase, as well as the presence of peaks associated with α -Al₂O₃ (C), and NiO (D). The γ -Ni (A) phase that was present in the as-deposited condition is not present anymore.

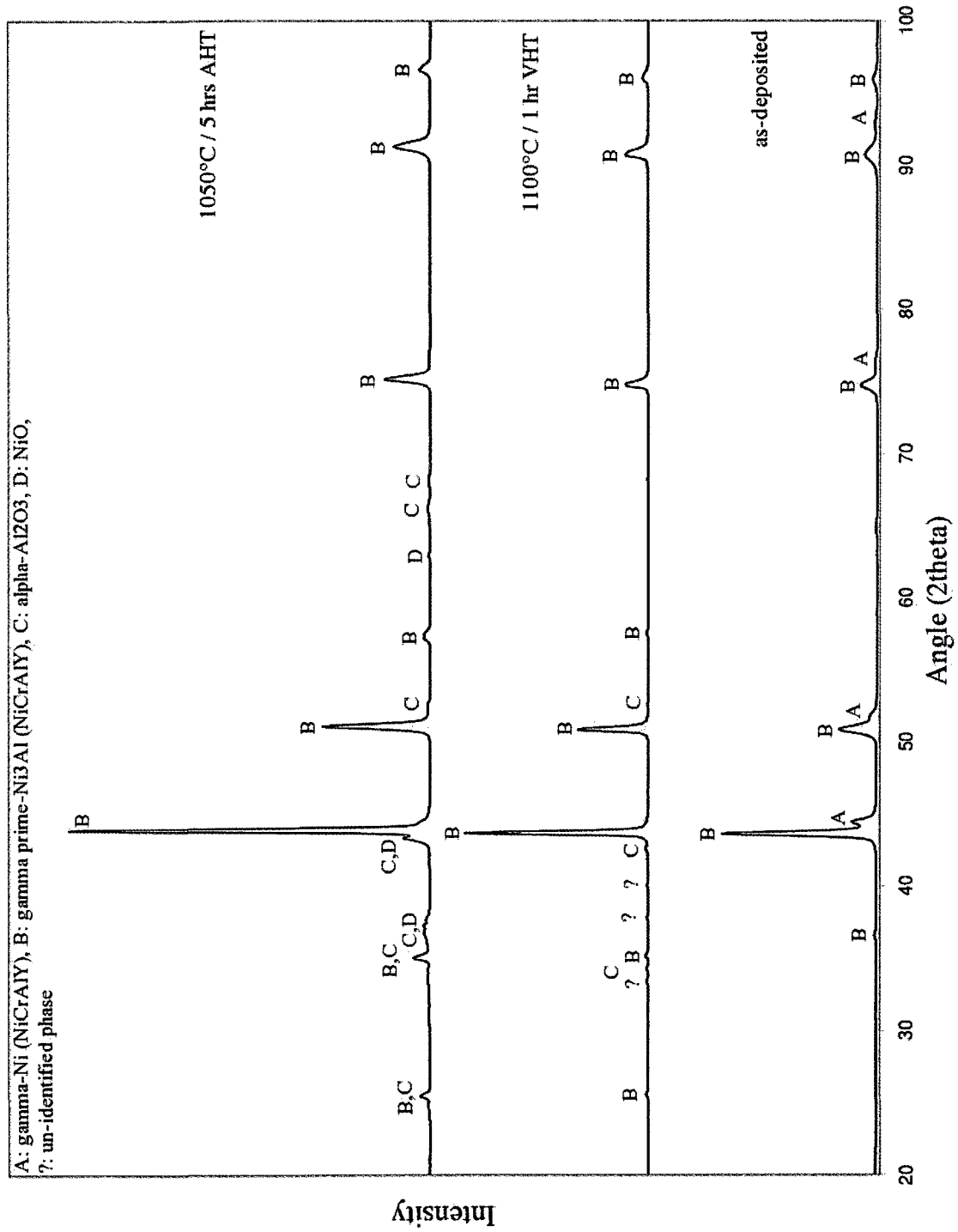


Figure 103: XRD spectra for the APS-sprayed NiCrAlY-coated Hastelloy-X test specimens in the following conditions: as-deposited, VHT of 1100°C for 1 hour, and AHT of 1050°C for 5 hours.

5.5 High-velocity Oxy-fuel Sprayed CoNiCrAlY

In this section, the results of the pre-oxidation heat treatments (both VHT and AHT) on the HVOF CoNiCrAlY-coated test specimens are presented. The results for the VHT and AHT series are listed in a separate sub-section, classified according to ascending temperature and time variables of each heat treatment in the series. Each series is concluded with a summary of the overall trends for each heat treatment series. Heat treatment results are followed by XRD analysis of selected test specimen conditions. This section begins with a characterization of the as-deposited HVOF CoNiCrAlY coating, with analysis of microstructural features on both test specimen surface and cross-section.

5.5.1 As-deposited Condition

The surface of the as-deposited HVOF CoNiCrAlY-coated test specimen (Figure 104) shows the typical constituents that are present on a thermally-sprayed coating surface: (i) impacted coating 'splats', (ii) porosity, and (iii) glazed areas indicating melting and re-solidification. Compositional EDS surface area scan data for the region shown in Figure 104a is listed in Table 67, together with the nominal CoNiCrAlY coating feedstock powder composition (see Table 5). The measured composition agrees well with the nominal composition of the feedstock powder. Oxygen is present in the EDS spectrum, indicating the presence of oxide inclusions as a result of the HVOF deposition process. Yttrium is likely also present in the coating, however, its relative concentration falls below the detection limits of the EDS equipment.

The cross-sectional micrograph of the as-deposited HVOF CoNiCrAlY-coated test specimen (Figure 105a) shows a coating microstructure that is characteristic of a thermally sprayed coating with an average coating thickness of approximately 90 μm . Compositional EDS area scan data for coating region shown in Figure 105a, listed in

Table 67: EDS surface area scan data for region shown in Figure 104a (in wt%), with comparison to the nominal CoNiCrAlY powder (Sulzer Metco AMDRY 4700) composition.

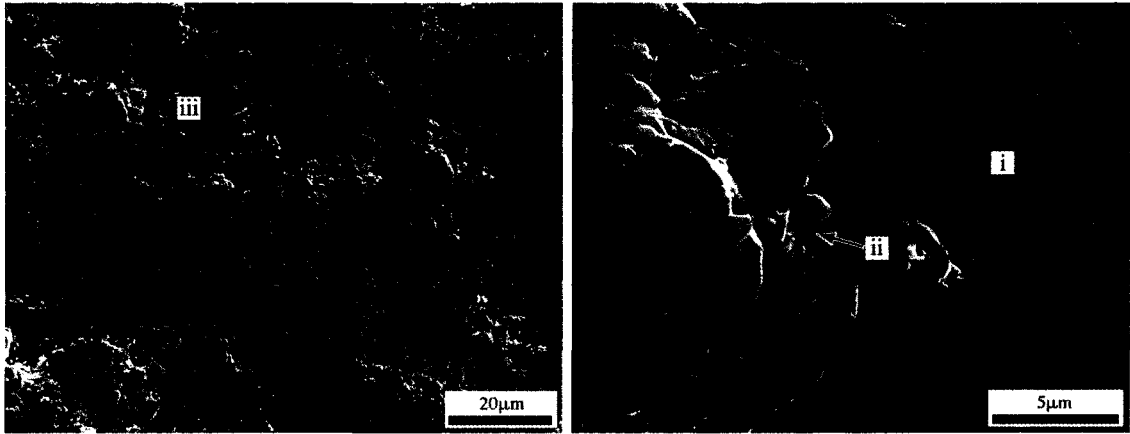
	Co	Ni	Cr	Al	Y
surface	36.84	32.35	21.10	9.71	-
nominal	38.5	32	21	8	0.5

Note: While not quantified, the EDS spectrum also indicates the presence of O.

Table 68, indicates good correlation with the average surface composition of the test specimen.

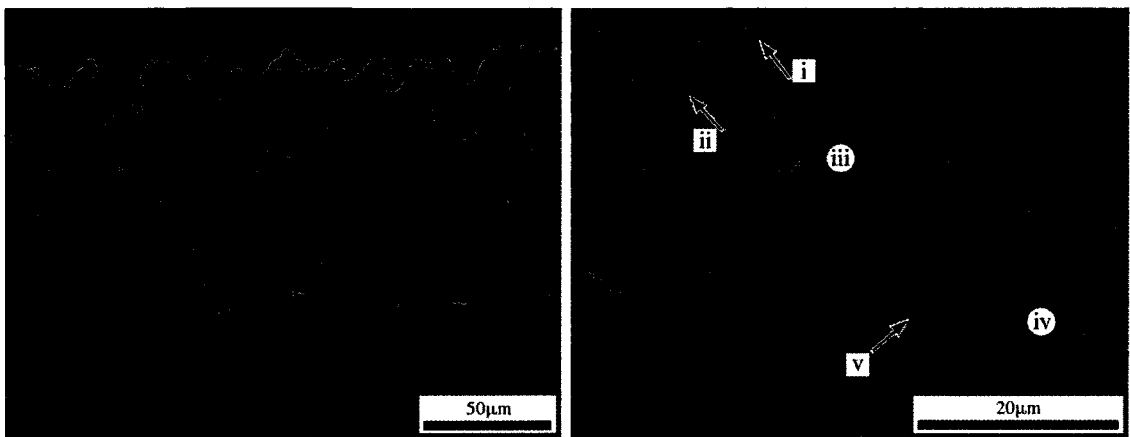
The dark-shaded constituents at the coating-substrate interface are embedded aluminum oxide particles left over from the grit-blasting used to roughen the substrate surface to improve coating adhesion. It should be noted that some Hastelloy-X substrates were ground and polished instead of being subject to a grit-blasting treatment with aluminum oxide before CoNiCrAlY BC deposition, and these samples do not have these left-over grit-blasting particles. The light-shaded, blot-shaped particles on the substrate are a tungsten-rich refractory phase that is typically present in the wrought Hastelloy-X substrate material.

A high-magnification view of the as-deposited coating microstructure (Figure 105b) shows typical constituents present in TS coatings: (i) porosity, (ii) oxide inclusions, (iii) coating material of average coating composition, (iv) a cobalt- and nickel-rich coating constituent, and (v) an un-melted coating feedstock powder particle. Compositional EDS spot scan data for the locations marked in Figure 105b are listed in Table 68.



(a) A representative view of the surface morphology of the as-deposited BC surface, showing (iii) glazed areas indicating melting and re-solidification of the BC material. (b) A high-magnification view showing details of the coating surface features, including (i) a coating material splat and (ii) porosity.

Figure 104: SE micrographs showing the surface condition of the as-deposited HVOF NiCrAlY-coated specimen.



(a) A representative view of the as-deposited BC structure. Average coating thickness is $92 \mu\text{m}$. (b) A high-magnification view of the BC microstructure, showing typical constituents of a TS coating: (i) porosity, (ii) oxide inclusion, (iii) coating material of average composition, and (iv) a nickel-rich coating component. Circular markers also indicate EDS spot scan locations.

Figure 105: Cross-sectional BSE micrographs showing the microstructural details of the as-deposited HVOF CoNiCrAlY-coated test specimen.

Table 68: EDS area scan data for region shown in Figure 105a and EDS spot scan data for locations shown in Figure 105b (in wt%), with the nominal CoNiCrAlY powder (AMDRY 4700) composition for comparison.

	Co	Ni	Cr	Al	Y
cross-section	37.41	32.63	20.71	9.25	-
nominal	38.5	32	21	8	0.5
iii	37.25	34.90	19.23	8.52	-
iv	40.36	44.96	11.36	3.31	-

Note: While not quantified, the EDS spectra also indicates the presence of O in both cases.

5.5.2 Vacuum Furnace Heat Treatments

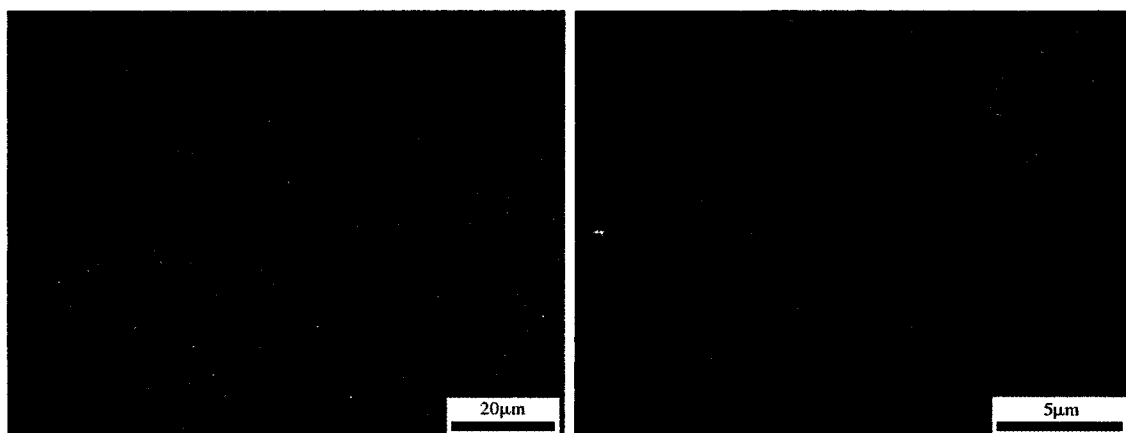
This sub-section outlines the SEM/EDS analysis results in terms of the microstructural features present both on the surface and in the cross-sections of the HVOF CoNiCrAlY-coated test specimens that have been subjected to the pre-oxidation VHTs. The sub-section is concluded with a summary of the trends in the results of the VHT series. The 6 VHT conditions examined are:

- 1000C for 10 and 15 hours
- 1050C for 5 and 10 hours
- 1100C for 1 and 5 hours

1000°C / 10 Hours

A micrograph of the HVOF CoNiCrAlY-coated test specimen that has undergone a VHT of 1000°C for 10 hours (Figure 106a) shows the formation of a relatively thin, smooth TGO layer that partially covers the specimen surface. This TGO morphology is very similar to that present in the VHT NiCrAlY-coated test specimens that were subjected to the same VHT conditions (see Figure 78a). Compositional EDS surface area scan data for the region shown in Figure 106a, listed in Table 69, indicates the presence of an increased proportion of aluminum concentration in comparison to the as-deposited BC composition (Table 67), potentially as a result of the formation of a very thin aluminum oxide TGO layer. Also present on the surface of the test specimen are traces of iron and molybdenum, both of which have diffused upwards from the Hastelloy-X substrate. A high-magnification view of the test specimen surface (Figure 106b) provides a detailed view of the TGO particles that have formed a discontinuous layer on the specimen surface.

A cross-sectional micrograph of the heat treated CoNiCrAlY-coated test specimen (Figure 107) provides a detailed view of (i) the discontinuous, sub-micron surface



(a) A representative SE micrograph of the post-AHT test specimen surface condition. (b) A high-magnification SE micrograph providing a detailed view of the post-AHT test specimen surface morphology.

Figure 106: Typical surface features present on the HVOF CoNiCrAlY-coated test specimen after a VHT of 1000°C for 10 hours.

Table 69: EDS surface area scan data for region shown in Figure 106a (in wt%).

Co	Ni	Cr	Al	Fe	Mo
27.33	30.59	17.53	20.84	2.25	1.46

Note: While not quantified, the EDS spectrum also indicates the presence of O.

TGO layer that has formed as a result of the heat treatment. The test specimen sections were mounted surface-to-surface in an attempt to assure the retention of the TGO layer. Compositional EDS spot scan data for the location marked in Figure 107, listed in Table 70, indicates that the layer consists principally of aluminum, which is a further indication that the TGO surface layer is likely aluminum oxide. Because the surface TGO layer is relatively thin, it is very likely that the compositional data obtained by the EDS system contains significant contributions from surrounding BC material.

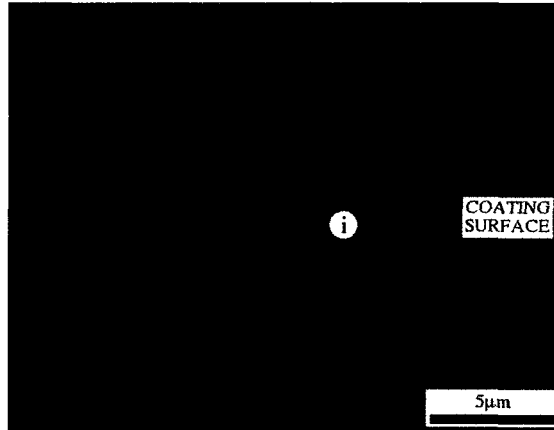


Figure 107: A cross-sectional BSE micrograph showing the typical microstructural features of the HVOF CoNiCrAlY-coated test specimen after a VHT of 1000°C for 10 hours. Note the presence of (i) a discontinuous, sub-micron TGO layer on the BC surface. Marker also indicates EDS spot scan location.

Table 70: EDS spot scan data for location shown in Figure 107 (in wt%).

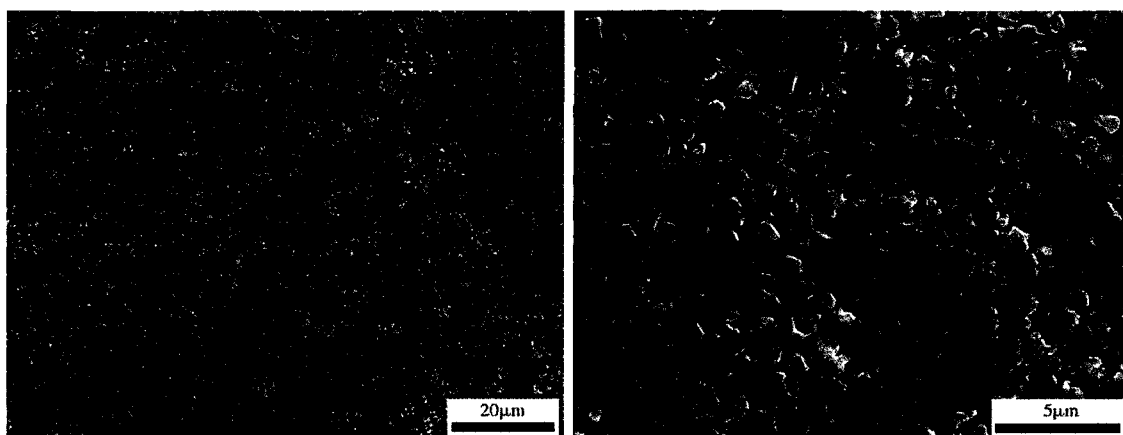
	Co	Ni	Cr	Al	Fe
i	23.83	24.93	18.09	30.26	2.89

Note: While not quantified, the EDS spectrum also indicates the presence of O.

1000°C / 15 Hours

A micrograph of the HVOF CoNiCrAlY-coated test specimen that has undergone a VHT of 1000°C for 15 hours (Figure 108a) shows the formation of a relatively thin TGO layer consisting of discontinuous oxide particles that cover the specimen surface. This TGO morphology is very similar to that present on the surface of the previous specimen (see Figure 106a), however, it appears that the oxide particles are smaller in size. Compositional EDS surface area scan data for the region shown in Figure 108a, listed in Table 71, indicates the presence of an increased proportion of aluminum concentration in comparison to the as-deposited BC composition (Table 67). This increase in the proportion of aluminum is attributed to the possible formation of a very thin aluminum oxide TGO layer. Also present on the surface of the test specimen are traces of iron and molybdenum, both of which have diffused upwards from the Hastelloy-X substrate. A high-magnification view of the test specimen surface (Figure 108b) provides a detailed view of the TGO particle distribution on the specimen surface. Another high-magnification view (Figure 109) provides a detailed view of (i) the surface TGO particle morphology, emphasizing their discontinuous nature. Compositional EDS spot scan data for the location marked in Figure 109, listed in Table 72, indicates that the TGO particles consist primarily of aluminum, further supporting the presence of an aluminum oxide TGO on the specimen surface. As the TGO particles are less than 1 μm in size, it is very likely that a substantial contribution from the compositional constituents of surrounding material is included in the measurement.

A cross-sectional micrograph of the heat treated CoNiCrAlY-coated test specimen (Figure 110) provides a detailed view of (i+ii) the discontinuous, sub-micron surface TGO layer that has formed as a result of the heat treatment. The test specimen sections were mounted surface-to-surface in an attempt to assure the retention of the



(a) A representative SE micrograph of the post-VHT test specimen surface condition. (b) A high-magnification SE micrograph providing a detailed view of the post-VHT test specimen surface morphology.

Figure 108: Typical surface features present on the HVOF CoNiCrAlY-coated test specimen after a VHT of 1000°C for 15 hours.

Table 71: EDS surface area scan data for region shown in Figure 108a (in wt%).

Co	Ni	Cr	Al	Fe	Mo
21.39	35.01	16.61	19.80	5.37	1.82

Note: While not quantified, the EDS spectrum also indicates the presence of O.

TGO layer. Compositional EDS spot scan data for the locations marked in Figure 110, listed in Table 73, indicate that the surface TGO layer consists principally of aluminum, which is a further indication that the TGO surface layer is likely aluminum oxide. Because the surface TGO layer is relatively thin, it is very likely that the compositional data obtained by the EDS system contains significant contributions from surrounding BC material. Also present in this micrograph are relatively large, dark-shaded masses at the coating-substrate interface which are embedded aluminum oxide particles remaining from the pre-deposition grit-blasting process used to roughen the substrate surface to improve the mechanical interlocking of the coating to the substrate.



Figure 109: A SE micrograph providing a detailed view of the TGO particles present on the HVOF CoNiCrAlY-coated test specimen after a VHT of 1000°C for 15 hours. Marker (i) indicates EDS spot scan location.

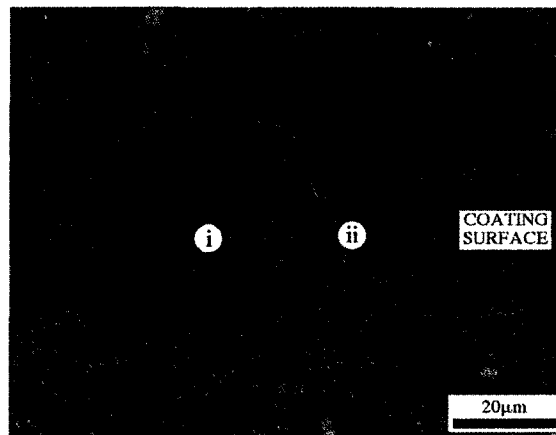


Figure 110: A cross-sectional BSE micrograph showing the typical microstructural features of the HVOF CoNiCrAlY-coated test specimen after a VHT of 1000°C for 15 hours. Note the presence of (i+ii) a largely continuous, sub-micron TGO layer on the BC surface. Markers also indicate EDS spot scan location. The sample was mounted face-to-face to ensure TGO retention throughout the metallographic preparation process.

Table 72: EDS spot scan data for location shown in Figure 109 (in wt%).

	Co	Ni	Cr	Al	Fe	Mo
i	15.82	23.52	13.12	41.36	4.26	1.92

Note: While not quantified, the EDS spectrum also indicates the presence of O.

Table 73: EDS spots can data for locations shown in Figure 110 (in wt%).

	Co	Ni	Cr	Al	Fe	Mo
i	23.83	24.93	18.09	30.26	2.89	-
ii	19.41	23.55	16.08	35.23	3.71	2.02

Note: While not quantified, the EDS spectra also indicate the presence of O in both cases.

Table 74: EDS surface area scan data for region shown in Figure 111a (in wt%).

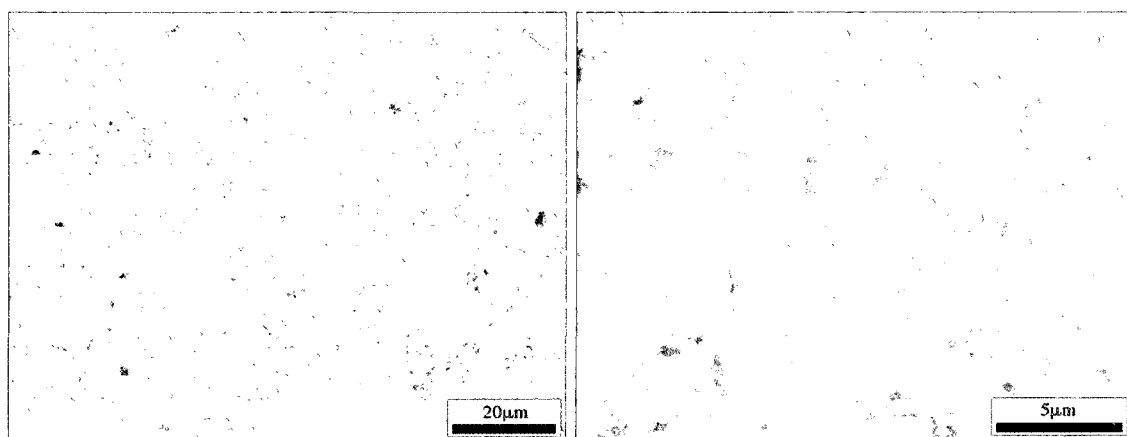
Co	Ni	Cr	Al	Y	Fe	Mo
25.28	33.84	17.96	15.77	0.72	4.42	2.01

Note: While not quantified, the EDS spectrum also indicates the presence of O.

1050°C / 5 Hours

A micrograph of the HVOF CoNiCrAlY-coated test specimen that has undergone a VHT of 1050°C for 5 hours (Figure 111a) shows the formation of a relatively thin TGO layer consisting of discontinuous oxide particles that cover the specimen surface. This TGO morphology is very similar to that present on the surface of the previous specimen (see Figure 108a), however, it appears that the oxide particles are smaller in size but are more densely packed. Compositional EDS surface area scan data for the region shown in Figure 111a, listed in Table 74, indicates the presence of an increased proportion of aluminum concentration in comparison to the as-deposited BC composition (Table 67). This increase in the proportion of aluminum is attributed to the possible formation of a thin aluminum oxide TGO layer. Also present on the surface of the test specimen are traces of iron and molybdenum, both of which have diffused upwards from the Hastelloy-X substrate. A high-magnification view of the test specimen surface (Figure 111b) provides a detailed view of the TGO particle distribution on the specimen surface.

A cross-sectional micrograph of the heat treated CoNiCrAlY-coated test specimen (Figure 112) provides a detailed view of the partially visible, discontinuous, sub-micron surface TGO layer that has formed along the test specimen surface as a result of the heat treatment. The test specimen sections were mounted surface-to-surface in an attempt to assure the retention of the TGO layer. In this case, it was not possible to obtain an EDS spot scan measurement due to the small size of the surface TGO layer.



(a) A representative SE micrograph of the post-VHT test specimen surface condition.

(b) A high-magnification SE micrograph providing a detailed view of the post-VHT test specimen surface morphology.

Figure 111: Typical surface features present on the HVOF CoNiCrAlY-coated test specimen after a VHT of 1050°C for 5 hours.

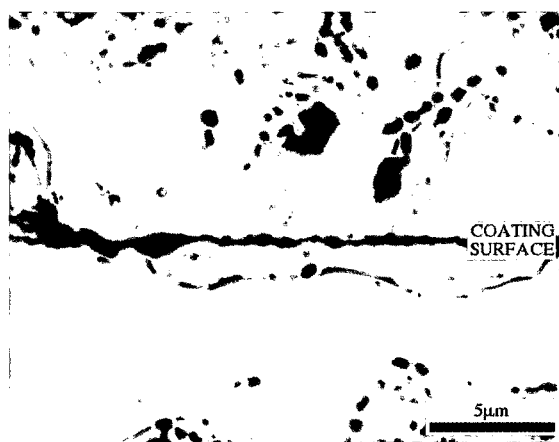
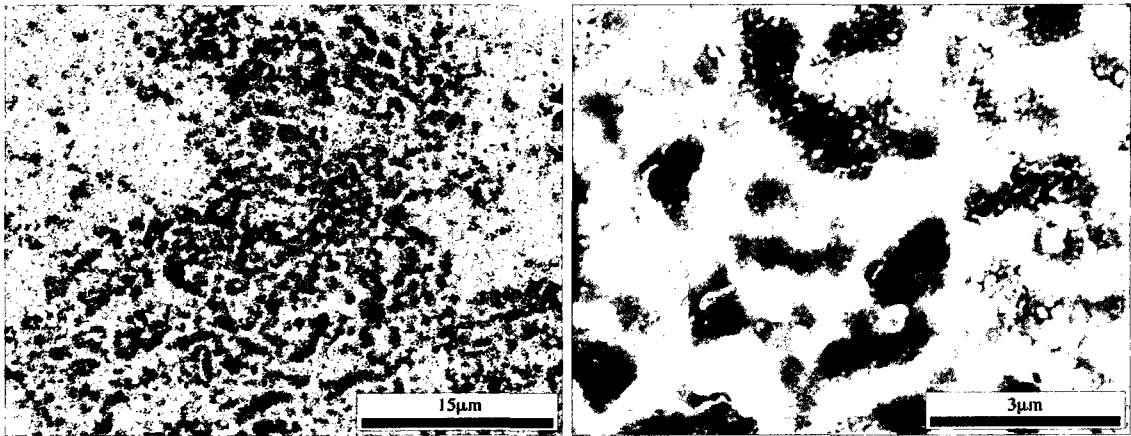


Figure 112: A cross-sectional, high-magnification BSE micrograph showing the typical microstructural features present in the HVOF CoNiCrAlY-coated test specimen after a VHT of 1050°C for 5 hours. The sample was mounted face-to-face to ensure TGO retention throughout the metallographic preparation process.

1050°C / 10 Hours

A micrograph of the HVOF CoNiCrAlY-coated test specimen that has undergone a VHT of 1050°C for 10 hours (Figure 113a) shows the formation of a relatively thin TGO layer consisting of discontinuous oxide particles that cover the specimen surface. Compositional EDS surface area scan data for the region shown in Figure 111a, listed in Table 75, indicates the presence of increased proportions of aluminum and yttrium concentrations in comparison to the as-deposited BC composition (Table 67). This increase in the proportion of aluminum is attributed to the possible formation of a thin aluminum oxide TGO layer. Also present on the surface of the test specimen is a trace of iron which has diffused upwards from the Hastelloy-X substrate. A high-magnification view of the test specimen surface (Figure 113b) provides a detailed view of the TGO particle distribution on the specimen surface. This TGO morphology is comparable to that present on the surface of the previous specimen (see Figure 111b) as it appears that the oxide particles are similar in size but are more densely packed.

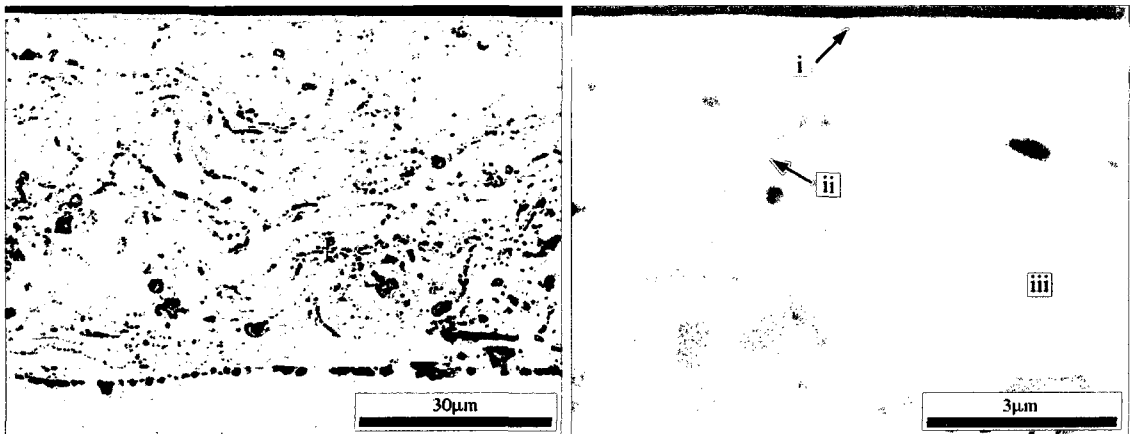
A cross-sectional micrograph of the heat treated CoNiCrAlY-coated test specimen (Figure 114a) shows coating microstructure as a result of the VHT. The top half of the BC presents signs of aluminum depletion as a result of diffusion to the surface to form the aluminum oxide TGO and β -NiAl phase coarsening. This specimen was not grit-blasted prior to BC deposition as is evident by the relatively flat coating-substrate interface and the aluminum-rich inclusions forming along this interface. A high-magnification micrograph (Figure 114b) providing a detailed view of the test specimen surface indicates the presence of: (i) a discontinuous, sub-micron surface TGO layer, (ii) a coarsened β -NiAl coating constituent, and (iii) the γ -Ni₃Al coating matrix. In this case, it was not possible to obtain an EDS spot scan measurement due to the small size of the surface TGO layer.



(a) A representative SE micrograph of the post-AHT test specimen surface condition.

(b) A high-magnification SE micrograph providing a detailed view of the post-VHT test specimen surface morphology.

Figure 113: Typical surface features present on the HVOF CoNiCrAlY-coated test specimen after a VHT of 1050°C for 10 hours.



(a) A representative SE micrograph showing the post-VHT microstructure.

(b) A high-magnification SE micrograph providing a detailed view of the microstructural features near the BC surface, showing (i) a largely continuous, sub-micron TGO, (ii) a coarsened β -NiAl grain, in a (iii) γ -Ni₃Al matrix of CoNiCrAlY BC material.

Figure 114: Cross-sectional micrographs showing the typical microstructural features present in the HVOF CoNiCrAlY-coated test specimen after a VHT of 1050°C for 10 hours.

Table 75: EDS surface area scan data for region shown in Figure 113a (in wt%).

Co	Ni	Cr	Al	Y	Fe
24.10	24.78	25.23	21.11	3.25	0.52

Table 76: EDS surface area scan data for region shown in Figure 115 (in wt%).

Co	Ni	Cr	Al
26.70	28.13	26.50	18.66

1100°C / 1 Hour

A micrograph of the HVOF CoNiCrAlY-coated test specimen that has undergone a VHT of 1100°C for 1 hour (Figure 115) shows the formation of a relatively thin TGO layer consisting of discontinuous oxide particles that cover the specimen surface. Also present in this micrograph is the development of a substantial void in the specimen surface which is thought to be a result of the transformation of Cr_2O_3 to volatile CrO_3 . Compositional EDS surface area scan data for the region shown in Figure 115, listed in Table 76, indicates the presence of increased proportions of aluminum and chromium concentrations in comparison to the as-deposited BC composition (Table 67). This increase in the proportion of aluminum and chromium is attributed to the possible formation of a mixed aluminum/chromium oxide TGO layer.

A cross-sectional micrograph of the heat treated CoNiCrAlY-coated test specimen (Figure 116a) shows coating microstructure as a result of the VHT. This specimen was not grit-blasted prior to BC deposition as is evident by the relatively flat coating-substrate interface and the aluminum-rich inclusions forming along this interface. A high-magnification micrograph (Figure 116b) providing a detailed view of the test specimen surface shows the complete absence of a visible surface TGO layer. By the absence of the TGO layer, it is evident that above temperatures of 1050°C, it is not possible to form a visible TGO in a vacuum environment.

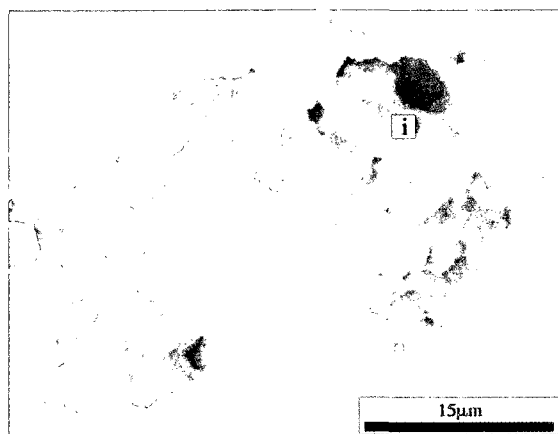
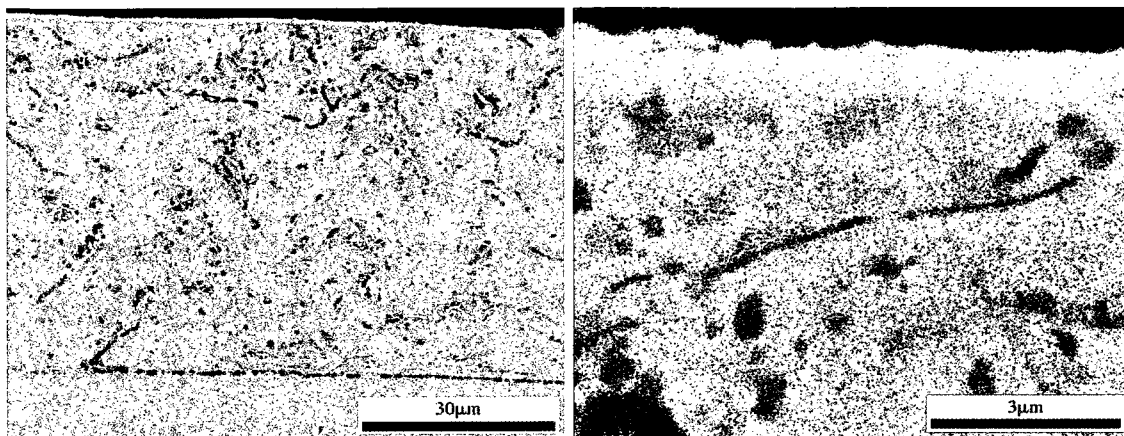


Figure 115: Typical surface features present on the HVOF CoNiCrAlY-coated test specimen after a VHT of 1100°C for 1 hour, showing (i) porosity in the BC layer.



(a) A representative SE micrograph showing the post-VHT microstructure.

(b) A high-magnification SE micrograph providing a detailed view of the microstructural features near the BC surface.

Figure 116: Cross-sectional micrographs showing the typical microstructural features present in the HVOF CoNiCrAlY-coated test specimen after a VHT of 1100°C for 1 hour.

Table 77: EDS surface area scan data for region shown in Figure 117a (in wt%).

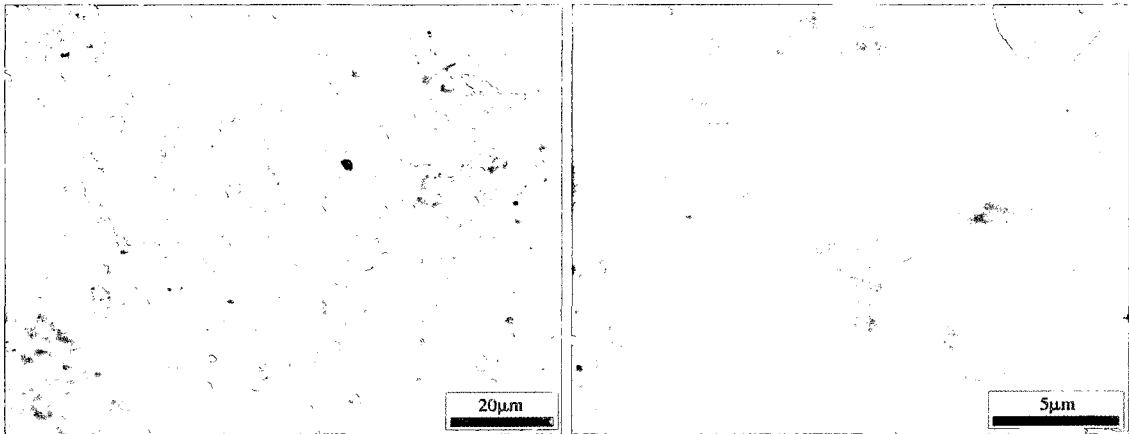
Co	Ni	Cr	Al	Y	Fe	Mo
26.29	38.44	14.72	7.53	3.14	6.44	3.44

Note: While not quantified, the EDS spectrum also indicates the presence of O.

1100°C / 5 Hours

A micrograph of the HVOF CoNiCrAlY-coated test specimen that has undergone a VHT of 1100°C for 5 hours (Figure 117a) shows the formation of a cellular, striated morphology on the specimen surface. Compositional EDS surface area scan data for the region shown in Figure 117a is listed in Table 77. The compositional distribution shows a general decrease in proportion of all BC elements, with a significant addition of iron and molybdenum. In contrast to previous test specimens in this VHT series, there is no indication of a predominantly aluminum-rich TGO scale. The presence of iron and molybdenum on the specimen surface is attributed to the upward diffusion of these elements from the Hastelloy-X substrate. A high-magnification micrograph (Figure 117b) provides a detailed view of the striated cellular morphology present on the specimen surface.

A cross-sectional micrograph of the heat treated CoNiCrAlY-coated test specimen (Figure 118) shows coating microstructure as a result of the VHT. There appears to be a general absence of a discernible TGO layer on the surface of the specimen. This specimen was not grit-blasted prior to BC deposition as is evident by the relatively flat coating-substrate interface and the aluminum-rich inclusions forming along this interface.



(a) A representative SE micrograph of the post-VHT test specimen surface condition.

(b) A high-magnification SE micrograph providing a detailed view of the post-VHT test specimen surface morphology.

Figure 117: Typical surface features present on the HVOF CoNiCrAlY-coated test specimen after a VHT of 1100°C for 5 hours.

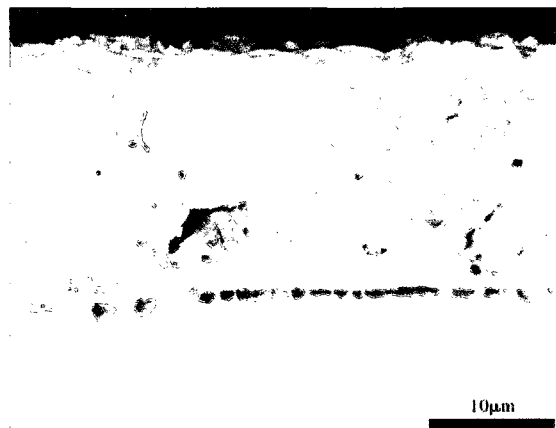


Figure 118: A cross-sectional BSE micrograph showing the typical microstructural features present in the HVOF CoNiCrAlY-coated test specimen after a VHT of 1100°C for 5 hours.

VHT Summary

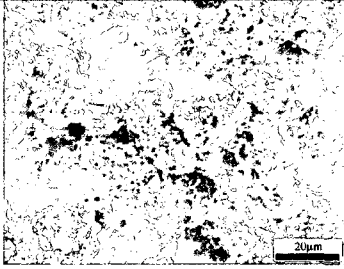
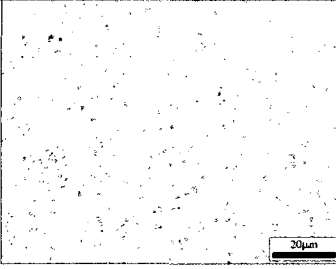
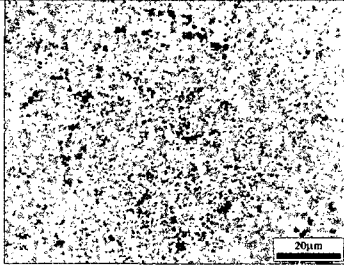
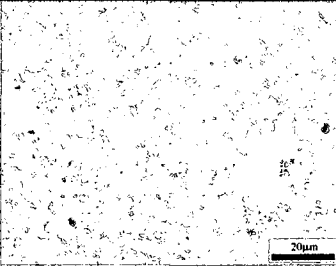
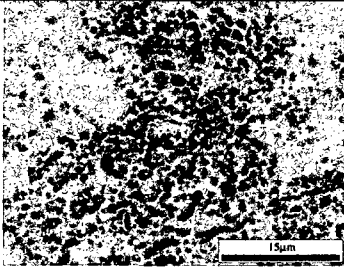
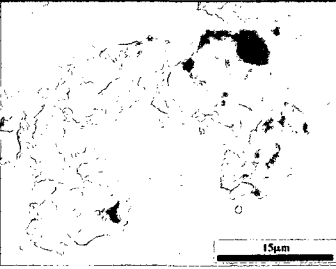
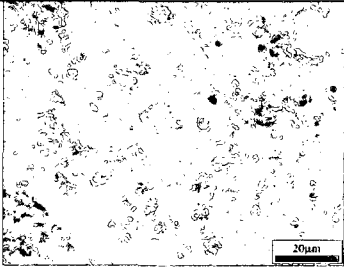
The summary table of the HVOF CoNiCrAlY-coated test specimen surface conditions as a result of the VHT series (Table 78) shows the general trend of the formation of a very thin, discontinuous, and superficial layer of TGO particles up the 1050°C/10 hrs VHT condition. At temperatures above 1050°C, the TGO particles become smaller in size and cover significantly less of the specimen surface.

A summary of the average surface composition of the specimens in the VHT series (Figure 119) supports this observation by indicating a rise in the proportion of aluminum content on the specimen surface in comparison to the as-deposited condition. This higher proportion of aluminum on the specimen surfaces is thought to be due to the presence of a very thin aluminum oxide surface TGO layer. The heat treatment conditions that exhibit the largest increase in the proportion of aluminum on the specimen surface are the 1000°C/10 hrs VHT and 1050°C/10 hrs VHT conditions. At temperatures and hold times above 1050°C/10 hrs, the proportion of aluminum decreases steadily with the 1100°C/5 hr VHT condition containing a lower proportion of aluminum than that of the as-deposited condition. The majority of the test specimen surfaces subject to the VHT series also contain traces of iron and molybdenum, which are thought to have diffused upward from the Hastelloy-X substrate. At both the 1050°C for 10 hrs VHT and 1100°C for 5 hrs VHT, there also appears to be a slight increase in the proportion of chromium together with measurable traces of yttrium on the specimen surface. In contrast to the other surface conditions of the test specimens in the VHT series, the surface morphology of the 1100°C/5 hrs condition indicates the possible formation of a cellular, nickel- and cobalt-rich transition metal oxide.

The summary table of the HVOF CoNiCrAlY-coated test specimen cross-sectional

features as a result of the VHT series (Table 79) shows the development of a discernible, discontinuous, sub-micron surface TGO layer in the VHT conditions up to 1050°C/10 hrs. At temperatures above 1050°C, no surface TGO layer is visible along the sample surface. This correlates with the observation of an increase in aluminum proportion on test specimen surface at all VHT conditions up to 1050°C/10 hrs. Where it was possible to measure the composition of the TGO, it was shown to be aluminum-rich, suggesting the possible presence of an aluminum oxide TGO.

Table 78: A summary of HVOF CoNiCrAlY-coated test specimen surface condition after VHT.

<p>As-deposited</p>		
<p>1000°C for 10 & 15 hrs</p>		
<p>1050°C for 5 & 10 hrs</p>		
<p>1100°C for 1 & 5 hrs</p>		

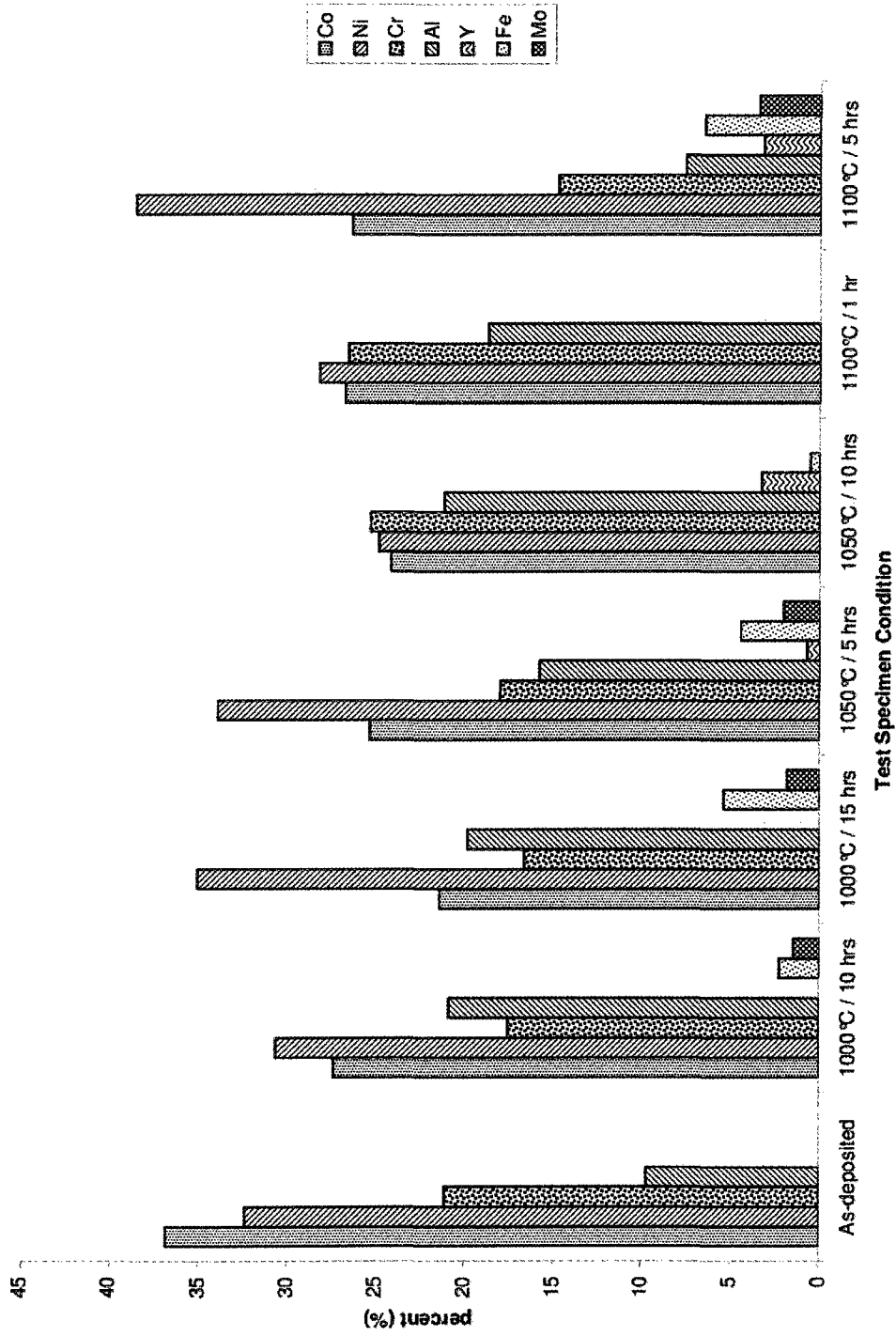
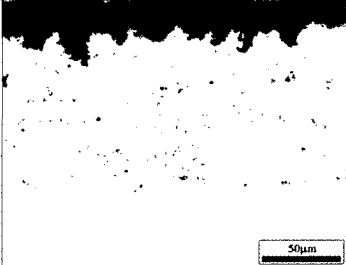
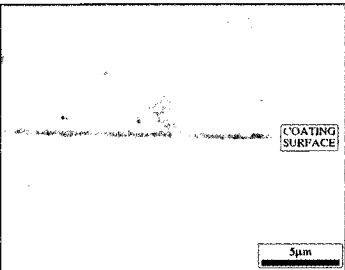
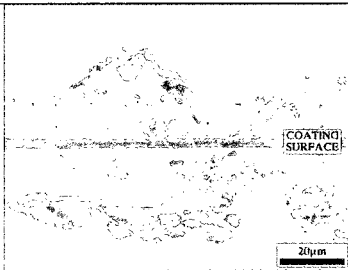
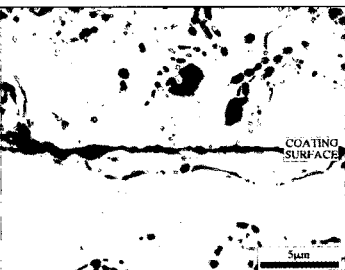
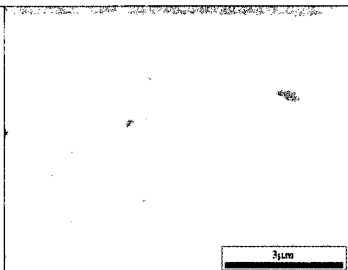
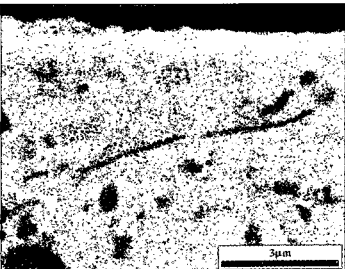
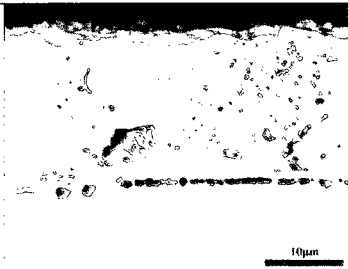


Figure 119: EDS area scan data for the HVOF CoNiCrAlY-coated test specimen surface composition (in wt%) as a function of specimen condition.

Table 79: A summary of HVOF CoNiCrAlY-coated test specimen cross-sections after VHT.

<p>As-deposited</p>		
<p>1000°C for 10 & 15 hrs</p>		
<p>1050°C for 5 & 10 hrs</p>		
<p>1100°C for 1 & 5 hrs</p>		

5.5.3 Air Furnace Heat Treatments

This sub-section outlines the SEM/EDS analysis results in terms of the microstructural features present both on the surface and in the cross-sections of the HVOF CoNiCrAlY-coated test specimens that have been subjected to the pre-oxidation AHTs. The sub-section is concluded with a summary of the trends in the results of the AHT series. The 3 AHT conditions examined are:

- 1000C for 10 hours
- 1050C for 5 hours
- 1100C for 1 hours

1000°C / 10 Hours

The surface of the HVOF CoNiCrAlY-coated test specimen that has been subjected to an AHT of 1000°C for 10 hours (Figure 120a) shows the presence of a light-shaded oxide phase that is finely distributed in the form of oxide cluster islands in a matrix of a darker-shaded oxide phase. In contrast to the NiCrAlY-coated test specimen that was subjected to the same AHT conditions (Figure 92a), the HVOF-coated test specimen possesses a much finer distribution of light-shaded oxide phases in the darker-shaded oxide matrix. Figure 120b provides an overview of the interaction between the two different oxide phases: (i) the light-shaded, globular oxide phase and (ii) the coarse, dark-shaded oxide phase.

The high-magnification micrograph in Figure 121a shows a detailed view of (i) a light-shaded, globular, nickel- and cobalt-rich transition metal oxide island which is surrounded by (ii) a smooth, darker-shaded mixed oxide phase that contains predominantly aluminum, followed by cobalt, nickel, and chromium. Figure 121b shows a detailed view of (iii) the coarse, whisker-shaped, predominantly aluminum-containing

Table 80: EDS spot scan data for locations shown in Figure 121 (in wt%).

	Co	Ni	Cr	Al
i	35.01	56.71	6.02	2.26
ii	18.90	15.57	11.38	54.15
iii	15.66	10.66	9.94	63.74

Note: While not quantified, the EDS spectra also indicate the presence of O in all cases.

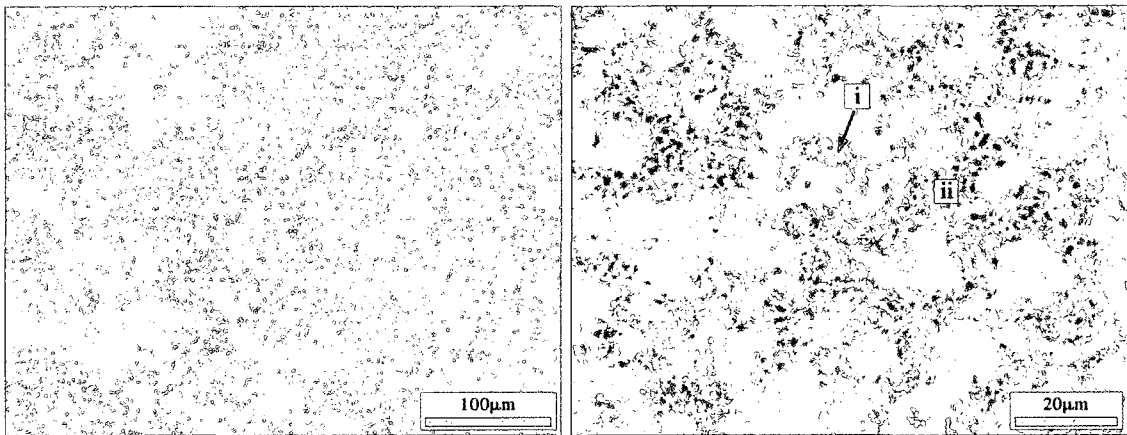
Table 81: EDS spot scan data for location shown in Figure 122b (in wt%).

	Co	Ni	Cr	Al
i	5.75	4.82	6.01	83.42

Note: While not quantified, the EDS spectrum also indicates the presence of O.

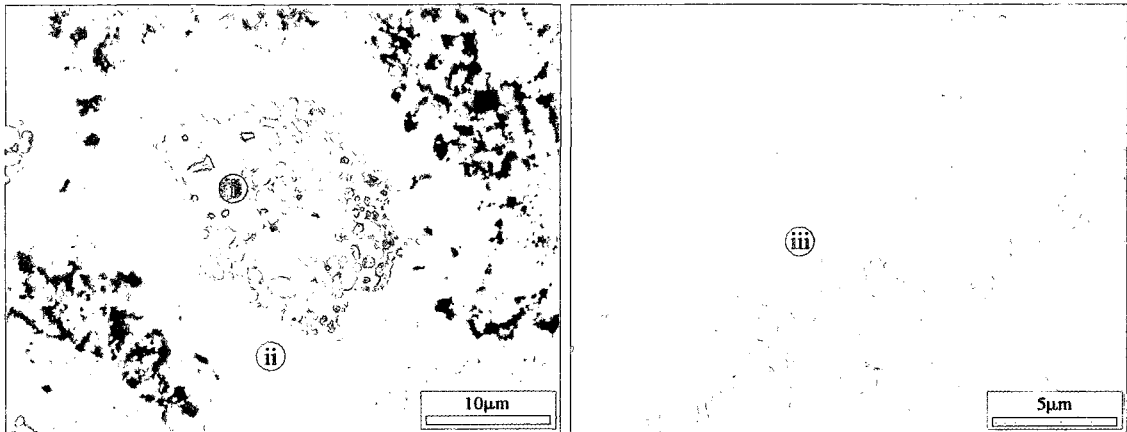
oxide phase. Compositional EDS spot scan data for locations marked in Figure 121 are listed in Table 80.

A cross-sectional micrograph of the HVOF CoNiCrAlY-coated test specimen (Figure 122a) shows the microstructural changes in the coating and substrate as a result of the heat treatment where the as-deposited BC material shows evidence of aluminum depletion near the surface of the test specimen and β -phase coarsening in the middle-portion of the BC material. The high-magnification micrograph (Figure 122b) provides a detailed view of the test specimen surface showing the presence of (i) a continuous surface TGO layer with an approximate average thickness of 2 μm . Compositional EDS spot scan data for the location marked in Figure 122b, listed in Table 81, indicates the presence of a predominantly aluminum-containing layer, suggesting the presence of an aluminum oxide surface TGO. After thorough inspection of the test specimen cross-section, it was not possible to find any of the bright, globular transition metal oxide cluster islands, as shown in Figure 120b. This is likely due to small percentage and fine distribution of these phases in the aluminum oxide matrix, as shown in Figure 120a.



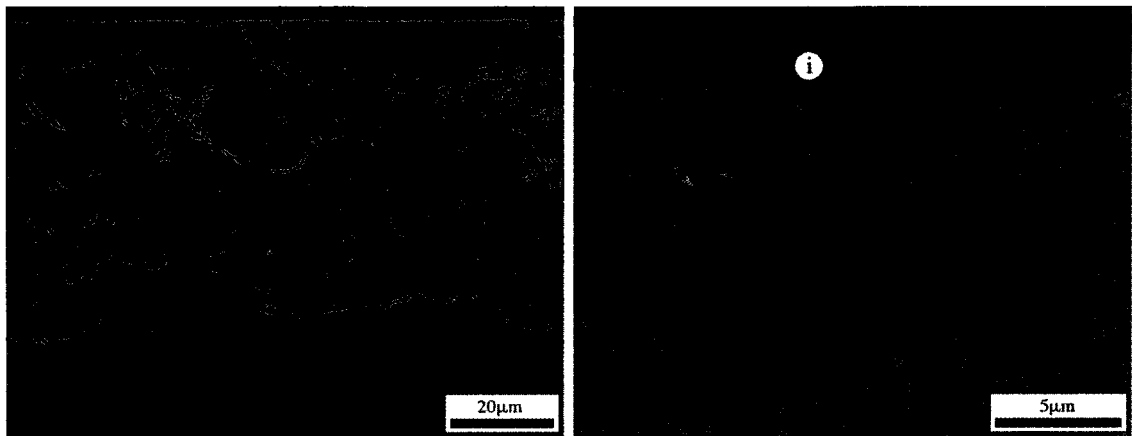
(a) A representative SE micrograph showing the fine distribution of globular oxide clusters in a matrix of a coarse, whisker-shaped oxide phase. (b) A high-magnification BSE micrograph showing the two predominant TGO constituents present on the test specimen surface after AHT: (i) globular, mixed-oxide islands, surrounded by a coarse, whisker-shaped oxide phase.

Figure 120: Typical surface features present on the HVOF CoNiCrAlY-coated test specimen after an AHT of 1000°C for 10 hours.



(a) A BSE micrograph showing the surface morphology of the (i) light-shaded cobalt- and nickel-rich, globular oxide island, surrounded by (ii) oxide phase. (b) A SE micrograph showing the surface morphology of (iii) the more coarse, aluminum-rich oxide phase.

Figure 121: High-magnification micrographs providing detailed views of the three oxide phases typically found on the surface of the the HVOF CoNiCrAlY-coated test specimen after an AHT of 1000°C for 10 hours. Markers also indicate EDS spot scan locations.



(a) A representative BSE micrograph of the post-AHT test specimen microstructure.

(b) A high-magnification BSE micrograph providing a detailed view of the BC surface, showing the presence of (i) a continuous TGO layer with an average coating thickness of $2\ \mu\text{m}$. Marker also indicates spot scan location.

Figure 122: Typical cross-sectional microstructural features present in the HVOF CoNiCrAlY-coated test specimen after an AHT of 1000°C for 10 hours.

1050°C / 5 Hours

The surface of the HVOF CoNiCrAlY-coated test specimen that has been subjected to an AHT of 1050°C for 5 hours (Figure 123) shows the presence of a light-shaded oxide phase that is finely distributed in the form of oxide cluster islands in a matrix of a darker-shaded oxide phase. Compositional EDS surface area scan data for region shown in Figure 123, listed in Table 82, indicates a significantly increased proportion of aluminum concentration in comparison to the as-deposited composition (Table 67). This suggests the possible formation of a TGO that consists predominantly of aluminum oxide.

The high-magnification micrograph in Figure 124a provides a detailed view of (i) the globular, light-shaded transition metal oxide phase that consists predominantly of nickel and cobalt with a trace of chromium. The high-magnification micrograph in Figure 124b provides a detailed view of (ii) the aluminum-rich, dense, nodular oxide phase. The morphology of the aluminum-rich, nodular oxide phase is similar to that identified by Kiyohara et al [28] as α -Al₂O₃ (see Figure 11b). Compositional EDS spot scan data for locations marked in Figure 124 are listed in Table 83.

A cross-sectional micrograph of the HVOF CoNiCrAlY-coated test specimen (Figure 125a) shows the microstructural changes in the BC material as a result of the heat treatment. The as-deposited BC material shows evidence of aluminum depletion near the surface of the test specimen and β -phase coarsening in the middle-portion of the BC material. Present on the sample surface is the formation of a continuous surface TGO layer. The high-magnification micrograph (Figure 125b) provides a detailed view of the test specimen surface showing the presence of (i) a continuous surface TGO layer with an approximate average thickness of 1.5 μ m. Compositional EDS spot scan data for the location marked in (Figure 125b), listed in Table 84, indicates the presence of a predominantly aluminum-containing layer, suggesting the presence

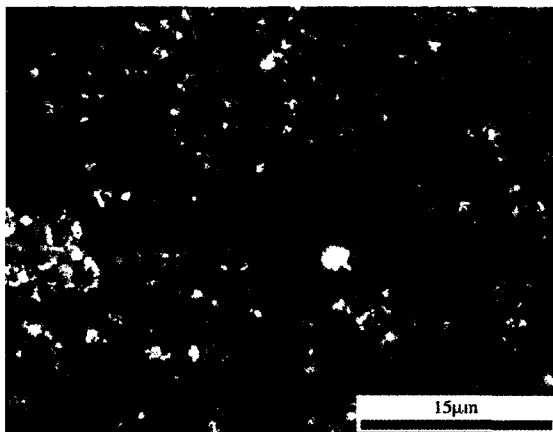


Figure 123: A SE micrograph showing the typical surface features present on the HVOF CoNiCrAlY-coated test specimen after an AHT of 1050°C for 5 hours.

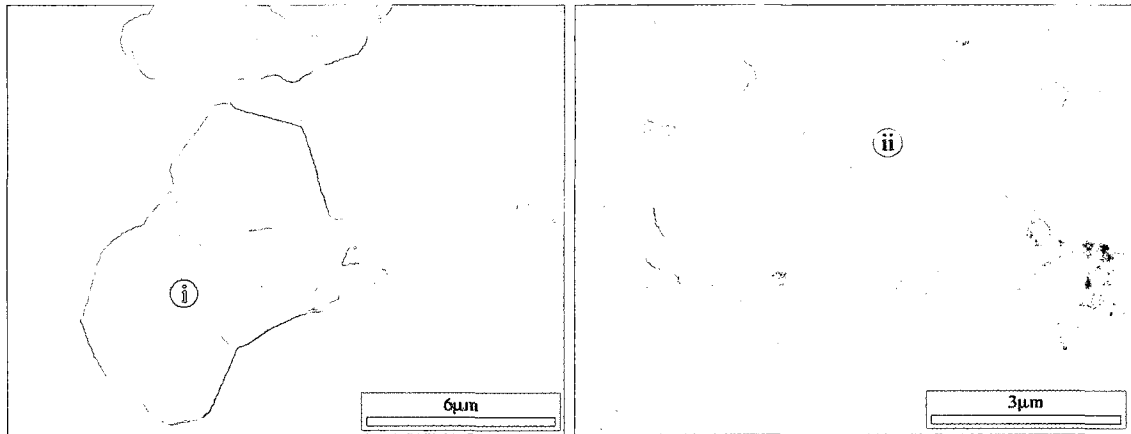
Table 82: EDS surface area scan data for region shown in Figure 123 (in wt%).

Co	Ni	Cr	Al
15.66	14.93	16.72	52.66

of an aluminum oxide surface TGO. Due to the small size of the surface TGO layer, it is likely that compositional information from the surrounding material is included in the presented values.

Table 83: EDS spot scan data for locations shown in Figure 124 (in wt%).

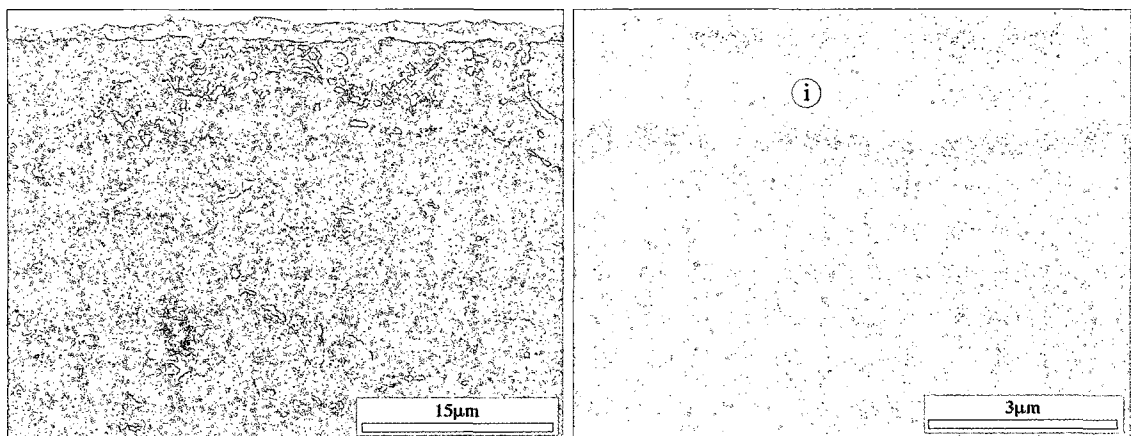
	Co	Ni	Cr	Al
i	34.86	61.92	3.22	-
ii	7.18	7.31	10.89	74.62



(a) A SE micrograph showing the surface morphology of the (i) light-shaded cobalt- and nickel-rich, globular oxide island.

(b) A SE micrograph showing the surface morphology of (ii) the more coarse, nodular, aluminum-rich oxide phase.

Figure 124: High-magnification micrographs providing detailed views of the two oxide phases typically found on the surface of the the HVOF CoNiCrAlY-coated test specimen after an AHT of 1050°C for 5 hours. Markers also indicate EDS spot scan locations.



(a) A representative BSE micrograph of the post-AHT test specimen microstructure.

(b) A high-magnification BSE micrograph providing a detailed view of the BC surface, showing the presence of (i) a continuous TGO layer with an average coating thickness of 1.5 μm . Marker also indicates spot scan location.

Figure 125: Typical cross-sectional microstructural features present in the HVOF CoNiCrAlY-coated test specimen after an AHT of 1050°C for 5 hours.

Table 84: EDS spot scan data for location shown in Figure 125b (in wt%).

	Co	Ni	Cr	Al
i	14.16	8.43	36.35	41.06

1100°C / 1 Hour

The surface of the HVOF CoNiCrAlY-coated test specimen that has been subjected to an AHT of 1100°C for 1 hour (Figure 126) shows the presence of a light-shaded oxide phase that is sparsely distributed in the form of oxide cluster islands in a matrix of (ii) a darker-shaded oxide phase. In comparison to the surface conditions of the preceding CoNiCrAlY-coated test specimen in the AHT series, this specimen exhibits the most sparse distribution of the light-shaded oxide islands.

The high-magnification micrograph in Figure 127a provides a detailed view of (i) the globular, light-shaded transition metal oxide phase that consists predominantly of nickel and cobalt. The high-magnification micrograph in Figure 127b provides a detailed view of (ii) the aluminum-rich, dense, nodular oxide phase. The morphology of the aluminum-rich, nodular oxide phase is similar to that identified by Kiyohara et al [28] as α -Al₂O₃ (see Figure 11b). Compositional EDS spot scan data for locations marked in Figure 127 are listed in Table 85.

A cross-sectional micrograph of the HVOF CoNiCrAlY-coated test specimen (Figure 128) shows the microstructural changes in the specimen as a result of the heat treatment. Present on the specimen surface is the formation of a continuous surface TGO layer with an approximate average thickness of 1 μ m. Compositional EDS spot scan data for the location marked in (Figure 128), listed in Table 86, indicates the presence of a predominantly aluminum-containing layer, suggesting the presence of an aluminum oxide surface TGO. Due to the small size of the surface TGO layer, it is likely that compositional information from the surrounding material is included in the presented values. Figure 128 also shows that the as-deposited BC material shows evidence of (ii) aluminum depletion near the surface of the test specimen and (iii) β -phase coarsening in the middle-portion of the BC material.

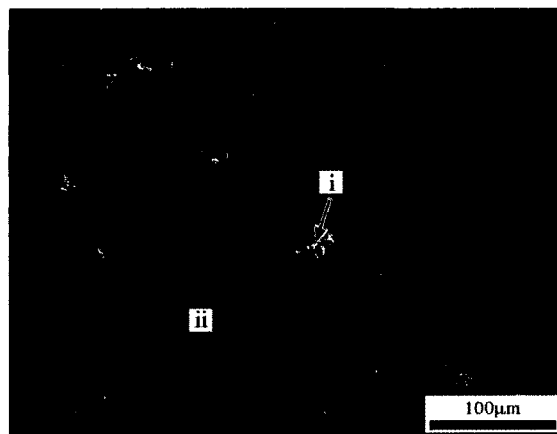
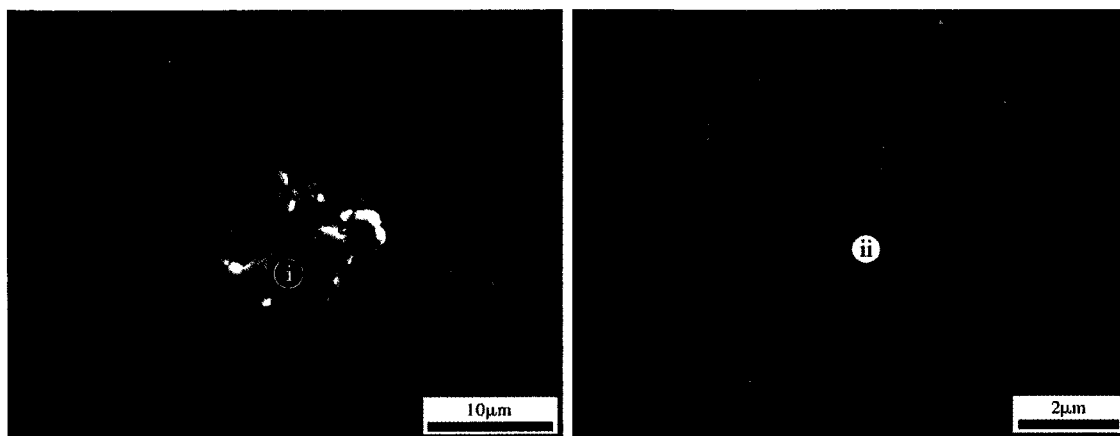


Figure 126: A SE micrograph showing the typical surface features present on the HVOF CoNiCrAlY-coated test specimen after an AHT of 1100°C for 1 hour: (i) globular, mixed-oxide islands in widely interspersed in (ii) a dense, nodular oxide matrix.



(a) A SE micrograph showing the surface morphology of the (i) light-shaded cobalt- and nickel-rich, globular oxide island.

(b) A SE micrograph showing the surface morphology of the (ii) dark-shaded, more coarse, and nodular aluminum-rich oxide phase.

Figure 127: High-magnification micrographs providing detailed views of the two oxide phases typically found on the surface of the the HVOF CoNiCrAlY-coated test specimen after an AHT of 1100°C for 1 hour. Markers also indicate EDS spot scan locations.

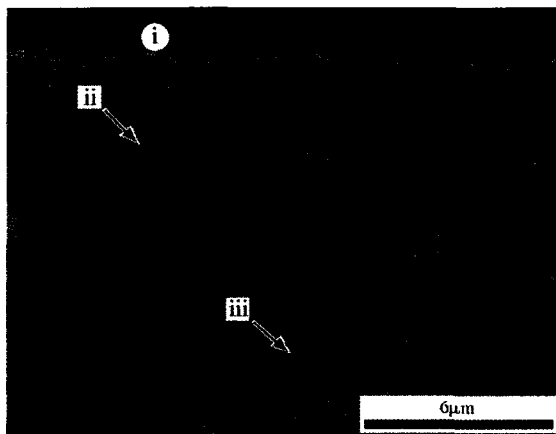


Figure 128: A cross-sectional SE micrograph showing the typical microstructural features present in the HVOF CoNiCrAlY-coated test specimen after an AHT of 1100°C for 1 hour, indicating the presence of (i) a continuous TGO layer with an average thickness of 1 μm . Marker also indicates spot scan location.

Table 85: EDS spot scan data for locations shown in Figure 127 (in wt%).

	Co	Ni	Cr	Al
i	42.59	52.62	3.30	1.49
ii	22.41	14.58	14.10	45.36

Table 86: EDS spot scan data for location shown in Figure 128 (in wt%).

	Co	Ni	Cr	Al	Mo
i	12.94	12.38	15.84	57.36	1.48

AHT Summary

The summary table of the HVOF CoNiCrAlY-coated test specimen surface conditions as a result of the AHT series (Table 87) shows general trend of the formation of light-shaded, nickel- and cobalt-rich transition metal oxide clusters that are widely dispersed in a matrix consisting of a dark-shaded, nodular, aluminum-rich surface TGO layer. In comparison to the APS NiCrAlY-coated test specimens that have been subjected to the same AHT series, the HVOF CoNiCrAlY-coated test specimens exhibit a much finer distribution of the mixed oxide clusters, in contrast to the larger, more prevalent islands of nickel- and chromium-rich mixed oxide cluster islands (Table 65). Of the CoNiCrAlY-coated test specimens subjected to the AHT series, the 1100°C/1 hr condition shows the most sparse distribution of mixed oxide clusters present on the specimen surface, however, the clusters are also the largest. In contrast, the 1000°C/10 hrs AHT condition exhibits a greater proportion of transition metal oxide clusters on the specimen surface, albeit of a much smaller cluster size.

The morphology of the dark-shaded aluminum-rich surface TGO layer is identified as α -Al₂O₃, with the coarse, whisker-shaped morphology also present on the surface of the 1000°C/10 hrs AHT specimen identified as θ -Al₂O₃ that is undergoing transformation to stable α -Al₂O₃.

The summary table of the HVOF CoNiCrAlY-coated test specimen cross-sectional features as a result of the AHT series (Table 88) supports the specimen surface observations in showing the formation of a continuous surface TGO layer along the test specimen surface for each AHT condition. The average thickness of the surface TGO layer decreases as the heat treatment temperature increases and hold time decreases: the 1000°C/10 hrs AHT yielding an approximate thickness of 2 μ m, the 1050°C/5 hrs AHT yielding an approximate thickness of 1.5 μ m, and the 1100°C/1 hr AHT yielding an approximate thickness of 1 μ m. EDS spot scan measurements of the surface TGO

layer present as a result of all three AHT conditions indicate an aluminum-rich composition, suggesting the formation of an aluminum oxide surface TGO layer. While the temperature increase between the 1000°C/10 hrs AHT condition and that of the 1100°C/1 hr AHT condition will increase the oxidation rate, resulting in a TGO of greater average thickness, the shorter hold time in the latter condition limits the TGO growth.

Table 87: A summary of HVOF CoNiCrAlY-coated test specimen surfaces after AHT.

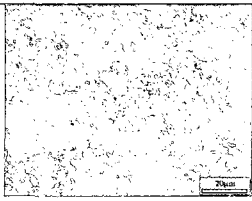
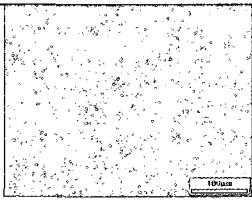
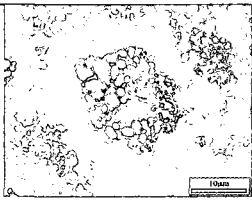
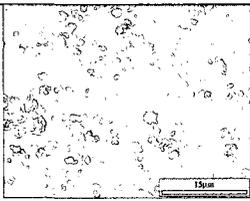
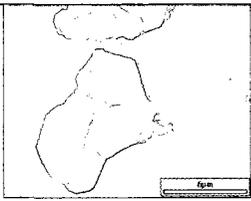
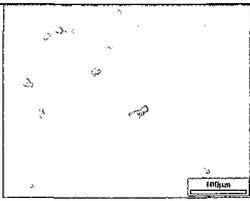
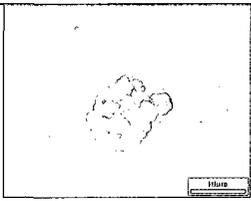
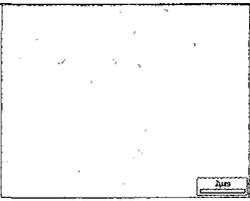
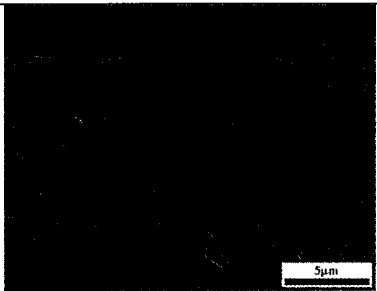
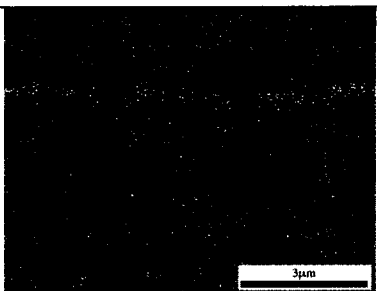
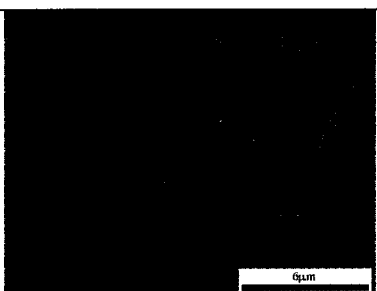
	General Features	Oxide Morphology	
As-deposited			
1000°C for 10 hrs			
1050°C for 5 hrs			
1100°C for 1 hr			

Table 88: A summary of HVOF CoNiCrAlY-coated test specimen cross-sections after AHT.

As-deposited	
1000°C for 10 hrs	
1050°C for 5 hrs	
1100°C for 1 hr	

5.5.4 XRD Results

This sub-section outlines the XRD analysis results (Figure 129) for the through-surface measurements of the HVOF spray-deposited CoNiCrAlY coated Hastelloy-X samples that have been subjected to the following sample conditions:

- as-deposited condition
- a VHT of 1100°C for 1 hour
- an AHT of 1050°C for 5 hours.

For the as-deposited test specimen the XRD spectrum contains the expected peaks belonging to the γ -(Co/Ni) (A) and γ' -(Co/Ni)₃Al phases (B) of the CoNiCrAlY material. Peaks belonging to the β -(Ni,Co)Al phase (C) are not evident in this spectrum, likely due to the supersaturation of the γ' -phase as a result of the high cooling rates inherent in the HVOF deposition process. This supersaturation phenomena is evident in the presence of the stepped peak between 43.7° and 44.4° 2θ

For the test specimen subjected to a VHT of 1100°C for 1 hour, the XRD spectrum again contains both γ -(Co/Ni) (A) and γ' -(Co/Ni)₃Al phases (B) of the CoNiCrAlY material, as well as peaks belonging to the β -(Ni,Co)Al phase (C). These β -(Ni,Co)Al phase peaks are now visible due the dissociation of the supersaturated γ' -(Co/Ni)₃Al phase into γ -(Co/Ni) (A) and stable β -(Ni,Co)Al (C) as a result of the heat treatment. Also present in the spectrum are traces of α -Al₂O₃ (D) and AlCr₂ (E).

For the test specimen subjected to the AHT of 1050°C for 5 hours, the XRD spectrum contains usual peaks associated with the CoNiCrAlY BC material (γ -(Co/Ni) (A), γ' -(Co/Ni)₃Al (B), and β -(Ni,Co)Al (C)), together with an increase in α -Al₂O₃ (D) peak intensity. Also present in the XRD spectrum are traces of (Co/Ni)Cr₂O₄ (F).

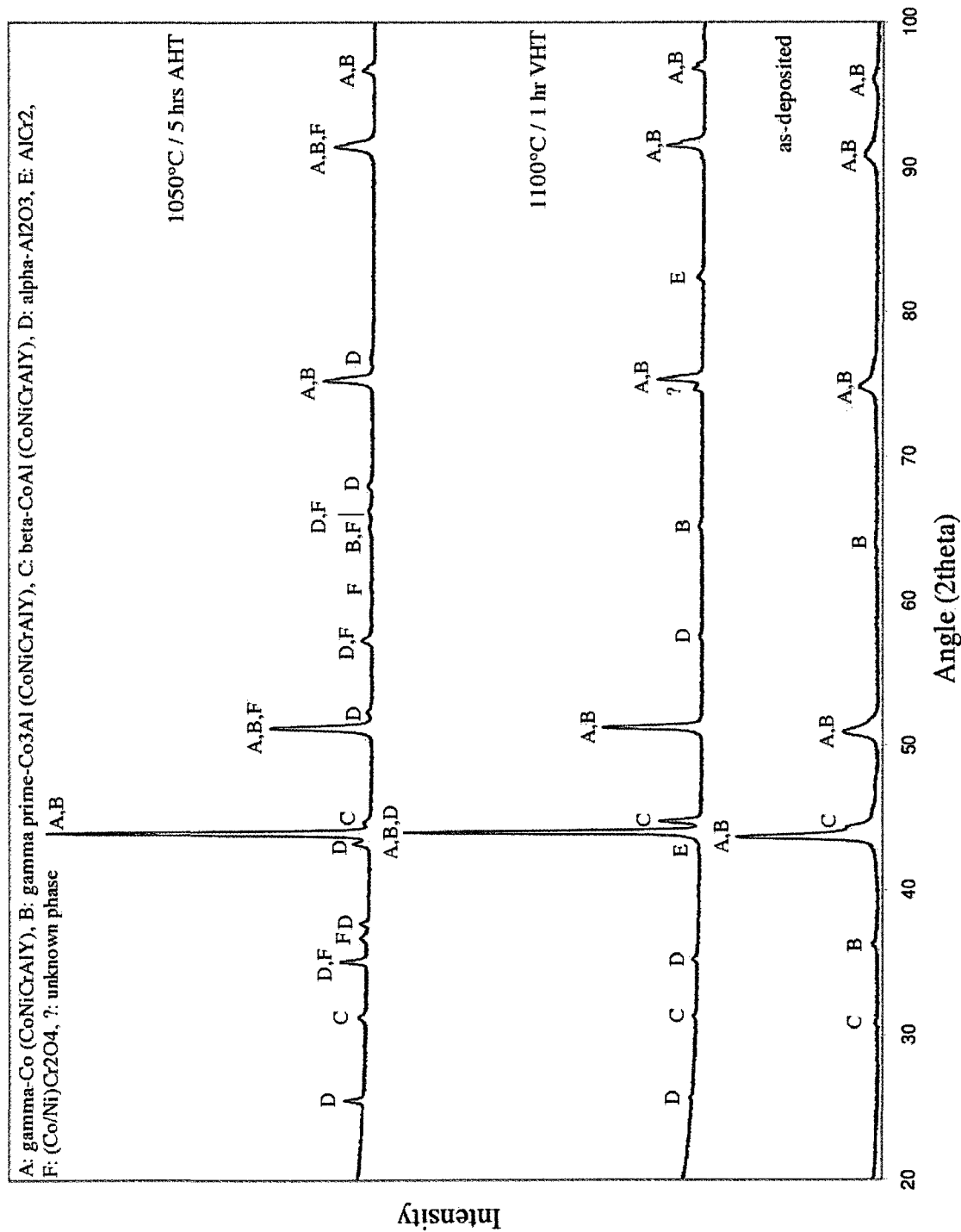


Figure 129: XRD spectra for the HVOF-sprayed CoNiCrAlY-coated Hastelloy-X test specimens in the following conditions: as-deposited, VHT of 1100°C for 1 hour, and AHT of 1050°C for 5 hours.

Chapter 6

Conclusions and Recommendations

6.1 Conclusions

In support of the objectives for the presented work, as listed in the **Research Objectives** chapter, the following conclusions were drawn from experimental results:

6.1.1 MS-PVD FeCrAlY

After both vacuum and air furnace heat treatments, the MS-PVD FeCrAlY-coated test specimens exhibited the formation of a highly porous TGO layer of complex composition in between the as-deposited coating layer and the specimen surface. The porosity in these test specimens was attributed to the escape of the argon sputtering gas from the as-deposited coating layer, which became entrapped as a consequence of the MS-PVD process. The coalescence of the argon sputtering gas into bubbles caused the formation of critical porosity, voids, and through-coating cracks. In consequence to the formation of an unfavourable specimen structure, the MS-PVD FeCrAlY-coated test specimens produced and heat treated under the procedures outlined in this work are not suitable for use as part of a high temperature thin film sensor assembly.

6.1.2 APS NiCrAlY

The exposure of APS NiCrAlY-coated test specimens to vacuum furnace heat treatment resulted, at best, in the formation of a superficial TGO layer consisting of discontinuous, sub-micron aluminum oxide particles. The heat treatment that resulted in the most abundant formation of the aluminum oxide TGO was the 1000°C/15 hour VHT. The inability to form a continuous aluminum oxide TGO layer with an average thickness of at least 2-3 μm makes the vacuum furnace heat treated APS NiCrAlY test specimens unsuitable in a high temperature thin film sensor application.

The exposure of APS NiCrAlY-coated test specimens to air furnace heat treatments resulted in the formation of a continuous surface TGO layer consisting predominantly of aluminum oxide. The aluminum oxide layer is, however, frequently interrupted by the presence of transition metal oxide clusters that originate from the as-deposited bond coat and protrude through the aluminum oxide layer. The greatest average aluminum oxide surface TGO layer achieved was approximately 3 μm as a result of the 1000°C/10 hour AHT. This heat treatment condition also yielded the lowest proportion and smallest size of transition metal oxide cluster islands on the specimen surface for this heat treatment series. The formation of excessive, fast-growing transition metal oxide clusters, however, makes the air furnace heat treated APS NiCrAlY test specimens unsuitable for high temperature thin film sensor application due to their limited insulating capability in comparison to the desired aluminum oxide layer.

6.1.3 HVOF CoNiCrAlY

Similar to the APS NiCrAlY-coated specimens, the exposure of HVOF CoNiCrAlY-coated test specimens to vacuum furnace heat treatment resulted, at best, in the formation of a superficial TGO layer consisting of discontinuous, sub-micron aluminum oxide particles. The heat treatment that resulted in the most abundant formation of

the aluminum oxide TGO was the 1000°C/10 hour VHT. Due to the insufficient formation of a continuous aluminum oxide TGO layer, the vacuum furnace heat treated HVOF CoNiCrAlY test specimens are unsuitable for a high temperature thin film sensor application.

As was observed for the APS NiCrAlY-coated specimens, the exposure of HVOF CoNiCrAlY-coated test specimens to air furnace heat treatments resulted in the formation of a continuous surface TGO layer consisting predominantly of aluminum oxide. The aluminum oxide layer was also intermittently broken by the presence of islands consisting of transition metal oxide clusters that originate from the as-deposited bond coat and protrude through the aluminum oxide layer. In contrast to the APS NiCrAlY-coated specimens, however, the HVOF CoNiCrAlY-coated test specimens exhibited the lowest quantity and the most sparse distribution of transition metal oxide cluster islands.

The most ideal specimen surface condition was produced by an AHT of 1100°C for 1 hour. Although this heat treatment condition exhibited an average aluminum oxide surface layer thickness of only 1 μm , the general surface TGO condition is better suited as a bond coat and electrically-insulating layer for use in a high temperature thin film sensor application. This is in contrast to the 1000°C for 10 hours AHT that resulted in a thicker average aluminum oxide TGO layer (3 μm) but contained a greater proportion of transition metal oxide cluster islands on the specimen surface.

6.2 Recommendations for Future Work

The presented experimental results reveal several directions for continued research:

1. To prepare additional HVOF CoNiCrAlY-coated Hastelloy-X test specimens and subject them to a pre-oxidation air furnace heat treatment of 1100°C for 1 hour or longer to form an aluminum oxide TGO layer of greater thickness (up

to 2–3 μm). After application of thin film sensing elements onto the aluminum oxide surface layer, subject instrumented test specimens to cyclic and isothermal loading in an air furnace to evaluate sensing capability and durability.

2. Examine the feasibility of supplementing the thermally-grown aluminum oxide layer with additional APS- or PVD-deposited aluminum oxide to increase the layer thickness to achieve the desired level of electrical insulation required by the thin film sensor system.
3. Continue pre-oxidation heat treatment trials with the APS NiCrAlY- and HVOF CoNiCrAlY-coated test specimens in an environment in which the oxygen partial pressure can be varied, such as O_2+Ar or O_2+He , in order to evaluate the effects of oxygen partial pressure on the properties of the aluminum oxide surface TGO layer.
4. Explore the effects on NiCrAlY- and CoNiCrAlY-coated test specimens that have been deposited via other PVD processes (such as electron beam PVD or pulsed laser PVD) and then subjected to vacuum and air furnace heat treatments.

List of References

- [1] L. Zhao and P. Patnaik, "Final report on functional thin films for gas turbine sensing applications - review of thin film strain gauges for gas turbine engine applications," National Research Council Canada, Tech. Rep., 2007.
- [2] Ibid., "Final report on functional thin films for gas turbine sensing applications - review of thin film thermocouples for gas turbine engine applications," National Research Council Canada, Tech. Rep., 2007.
- [3] T. Pollock and S. Tin, "Nickel-based superalloys for advanced turbine engines: Chemistry, microstructure, and properties," *Journal of Propulsion and Power*, vol. 22, pp. 361–374, March-April 2006.
- [4] G. Meetham, "High temperature materials in gas turbine engines," *Materials and Design*, vol. 9, pp. 213–219, 1988.
- [5] C. Soares, *Gas Turbines: A Handbook of Air, Land, and Sea Applications*. Oxford, UK: Elsevier, 2008.
- [6] H. Saravanamuttoo, G. Rogers, and H. Cohen, *Gas Turbine Theory, 5th Edition*. Essex, UK: Pearson/Prentice-Hall, 2001.
- [7] A. Koul, V. Parameswaran, J.-P. Immarigeon, and W. Wallace, Eds., *Advances in High Temperature Structural Materials and Protective Coatings*. Ottawa, Canada: National Research Council Canada, 1994.
- [8] R. Sivakumar and B. Mordike, "High temperature coatings for gas turbine blades: A review," *Surface and Coatings Technology*, vol. 37, pp. 139–160, 1989.
- [9] K. H. Stern, Ed., *Metallurgical and Ceramic Protective Coatings*. Chapman and Hall, 1996.
- [10] B. Gleeson, "Thermal barrier coatings for aeroengine applications," *Journal of Propulsion and Power*, vol. 22, no. 2, pp. 375–383, 2006.

- [11] H. Oskarsson, "Material challenges in industrial gas turbines," in *Proceedings of Sino-Sweedish Structural Materials Symposium*, 2007, pp. 11–14.
- [12] C. Sims, N. Stoloff, and W. Hagel, *Superalloys II*. New York, USA: Wiley, 1986.
- [13] M. Durand-Charre, *The Microstructure of Superalloys*. Amsterdam, NL: Gordon and Breach, 1997.
- [14] F. Versnyder and M. Shank, "Development of columnar grain and single crystal high-temperature materials through directional solidification," *Materials Science and Engineering*, vol. 6, pp. 213–247, 1970.
- [15] G. Evans, D. Clarke, and C. Levi, "The influences of oxides on the performance of advanced gas turbines," *Journal of the European Ceramic Society*, vol. 28, pp. 1405–1419, 2008.
- [16] T. Rhys-Jones, "Coatings for blade and vane applications in gas turbines," *Corrosion Science*, vol. 29, pp. 623–646, 1989.
- [17] A. Hesnawi, H. Li, Z. Zhou, S. Gong, and H. Xu, "Effect of surface condition during pre-oxidation treatment on isothermal oxidation behaviour of MCrAlY bond coat prepared by EB-PVD," *Surface and Coatings Technology*, vol. 201, pp. 6793–6796, 2007.
- [18] W. Brandl, G. Marginean, D. Maghet, and D. Utu, "Effects on specimen treatment and surface preparation on the isothermal oxidation behaviour of the HVOF-sprayed MCrAlY coatings," *Surface and Coatings Technology*, vol. 188–189, pp. 20–26, 2004.
- [19] Y. Wu, M. Qin, Z. Feng, Y. Liang, C. Sun, and F. Wang, "Improved oxidation resistance of NiCrAlY coatings," *Materials Letters*, vol. 57, pp. 2404–2408, 2003.
- [20] J. Nicholls, N. Simms, W. Chan, and H. Evans, "Smart overlay coatings - concept and practice," *Surface and Coatings Technology*, vol. 149, pp. 236–244, 2002.
- [21] N. Eliaz, S. Shemesh, and R. Latanision, "Hot corrosion in gas turbine components," *Engineering Failure Analysis*, vol. 9, pp. 31–43, 2002.
- [22] J. Nicholls, "Designing oxidation-resistant coatings," *Journal of Metals*, pp. 28–35, 2000.
- [23] F. Stott, G. Wood, and J. Stringer, "The influence of alloying elements on the development and maintenance of protective scales," *Oxidation of Metals*, vol. 44, no. 1/2, pp. 113–145, 1995.

- [24] A. Rabiei and A. Evans, "Failure mechanisms associated with the thermally grown oxide in plasma-sprayed thermal barrier coatings," *Acta Materialia*, vol. 48, pp. 3963–3976, 2000.
- [25] R. Prescott and M. Graham, "The formation of aluminum oxide scales on high-temperature alloys," *Oxidation of Metals*, vol. 38, pp. 233–254, 1992.
- [26] J. Mueller and D. Neuschuetz, "Efficiency of alpha-alumina as diffusion barrier between bond coat and bulk material of gas turbine blades," *Vacuum: Surface Engineering, Surface Instrumentation and Vacuum Technology*, vol. 71, pp. 247–251, 2003.
- [27] H. El-Kadiri, R. Molins, Y. Bienvenu, and M. Horstemeyer, "Abnormal high growth rates of metastable aluminas on FeCrAl alloys," *Oxidation of Metals*, vol. 64, pp. 63–97, 2005.
- [28] P. Kiyohara, H. Santos, A. Vieira-Coelho, and P. D. Souza-Santos, "Structure, surface area and morphology of aluminas from thermal decomposition of $\text{Al}(\text{OH})(\text{CH}_3\text{COO})_2$ crystals," *Anais da Academia Brasileira de Ciencias*, vol. 72, pp. 471–495, 2000.
- [29] M. Warnes, "Improved aluminide/ MCrAlX coating systems for superalloys using CVD low activity aluminizing," *Surface and Coatings Technology*, pp. 163–164, 2003.
- [30] P. Hou, "Impurity effects on alumina scale growth," *Journal of the American Ceramic Society*, vol. 86, pp. 660–668, 2003.
- [31] A. Evans, D. Mumm, J. Hutchinson, G. Meier, and F. Pettit, "Mechanisms controlling the durability of thermal barrier coatings," *Progress in Materials Science*, vol. 46, pp. 505–553, 2001.
- [32] W. Lih, E. Chang, B. Wu, and H. Chao, "Effects of bond coat preoxidation on the properties of ZrO_2 -8wt.% Y_2O_3 /Ni-22Cr-10Al-1Y thermal-barrier coatings," *Oxidation of Metals*, vol. 36, no. 3/4, pp. 221–238, 1991.
- [33] T. Nijdam, G. Marijnissen, E. Vergeldt, A. Kloosterman, and W. Sloof, "Development of a pre-oxidation treatment to improve the adhesion between thermal barrier coatings and NiCoCrAlY bond coatings," *Oxidation of Metals*, vol. 66, no. 5/6, pp. 269–294, 2006.

- [34] W. Chen, X. Wu, B. Marple, R. Lima, and P. Patnaik, "Pre-oxidation and TGO growth behaviour of an air-plasma-sprayed thermal barrier coating," *Surface and Coatings Technology*, vol. 202, pp. 3787–3796, 2008.
- [35] D. Monceau, F. Crabos, A. Malie, and B. Pieraggi, "Effects of bond-coat preoxidation and surface finish on isothermal and cyclic oxidation, high temperature corrosion and thermal shock resistance of TBC systems," *Materials Science Forum*, vol. 369-372, no. 2, pp. 607–614, 2001.
- [36] H. Lau, C. Leyens, U. Schulz, and C. Friedrich, "Influence of bondcoat pretreatment and surface topology on the lifetime of EB-PVD TBCs," *Surface and Coatings Technology*, vol. 165, pp. 217–223, 2003.
- [37] J. Davies, Ed., *Handbook of Thermal Spray Technology*. Materials Park, OH: ASM International, 2004.
- [38] D. Almeida, C. Silva, M. Nono, and C. Cairo, "EB-PVD TBCs of zirconia co-doped with yttria and niobia, a microstructural investigation," *Surface and Coatings Technology*, vol. 200, pp. 2827–2833, 2006.
- [39] L. Martin, J. Wrbanek, and G. Fralick, "Thin film sensors for surface measurements," NASA, Tech. Rep. NASA-TM-2001-211149, 2001.
- [40] J. Lei, L. Martin, and H. Will, "Advances in thin film sensor technologies for engine applications," NASA, Tech. Rep. NASA-TM-1997-107418, 1997.
- [41] L. Martin, G. Fralick, and K. Taylor, "Advances in thin film thermocouple durability under high temperature and pressure testing," NASA, Tech. Rep. NASA-TM-1999-208812, 1999.
- [42] J. Lei and H. Will, "Thin-film thermocouples and strain-gauge technologies for engine applications," *Sensors and Actuators A: Physical*, vol. 65, pp. 187–193, March 1998.
- [43] P. Kayser, J. Godefroy, and L. Leca, "High-temperature thin-film strain gauges," *Sensors and Actuators A: Physical*, vol. 27-28, pp. 328–332, 1993.
- [44] J. Lei, H. Will, and L. Martin, "Microfabricated thin-film physical sensors for hostile environment," in *Proceedings of the 17th Digital Avionics Systems Conference*, 1998, pp. D13/1–D13/7.

- [45] W. Cullinane and R. Strange, "Gas turbine engine validation instrumentation: measurements, sensors and needs," in *SPIE Conference on Harsh Environment Sensors II*, September 1999.
- [46] AIAA. The versatile affordable advanced turbine engines (VAATE) initiative. [Online]. Available: <http://pdf.aiaa.org/downloads/publicpolicypositionpapers/VAATE.pdf>.
- [47] J. Litt, D. Simon, S. Garg, T. Guo, C. Mercer, R. Millar, A. Behbahani, A. Bajwa, and D. Jensen, "A survey of intelligent control and health management technologies for aircraft propulsion systems," *Journal of Aerospace Computing, Information and Communication*, vol. 1, December 2004.
- [48] K. Smega, "Embedded sensors for measurement of material properties - needs, direction, and technology," in *Proceedings of the 41st AIAA/ASME/SAE/ASEE Joint Propulsion Conference and Exhibit*, July 2005.
- [49] C. Holtz, G. Smith, and R. Friend, "Modernizing systems through data integration: A vision for EHM in the united states air force," AIAA, Tech. Rep. AIAA-2004-049-126, July 2004.
- [50] D. Carey, J. Littles, R. Morris, D. Harmon, B. Cowles, and R. Rajamani. Health management technologies enabling safety, affordability, and readiness enhancements for legacy engine fleets. [Online]. Available: http://mindef.gov.sg/imindef/mindef_websites/atozlistings/air_force/microsites/ats/2007/topics/Propulsion.-imindefPars-0032-DownloadFile.tmp/propulsion_paper_5.pdf.
- [51] S. Prakash, R. Budhani, and R. Bunshah, "Development of thin film sensors for high performance turbo-jet engines," *Materials Research Bulletin*, vol. 23, pp. 187–195, February 1988.
- [52] J. Kiser, M. Singh, J. Lei, and L. Martin, "Novel approach for positioning sensor lead wires on SiC-based monolithic ceramic and FRCMC components/subcomponents having flat and curved surfaces," NASA, Tech. Rep. NASA-TM-1999-209197, 1999.
- [53] L. Martin and R. Holanda, "Applications of thin film thermocouples for surface temperature measurement," NASA, Tech. Rep. NASA-TM-1995-106714, 1995.
- [54] M. Verrilli, L. Martin, and D. Brewer, "RQL sector rig testing for SiC/SiC combustor liners," NASA, Tech. Rep. NASA-TM-2002-0211509, 2002.

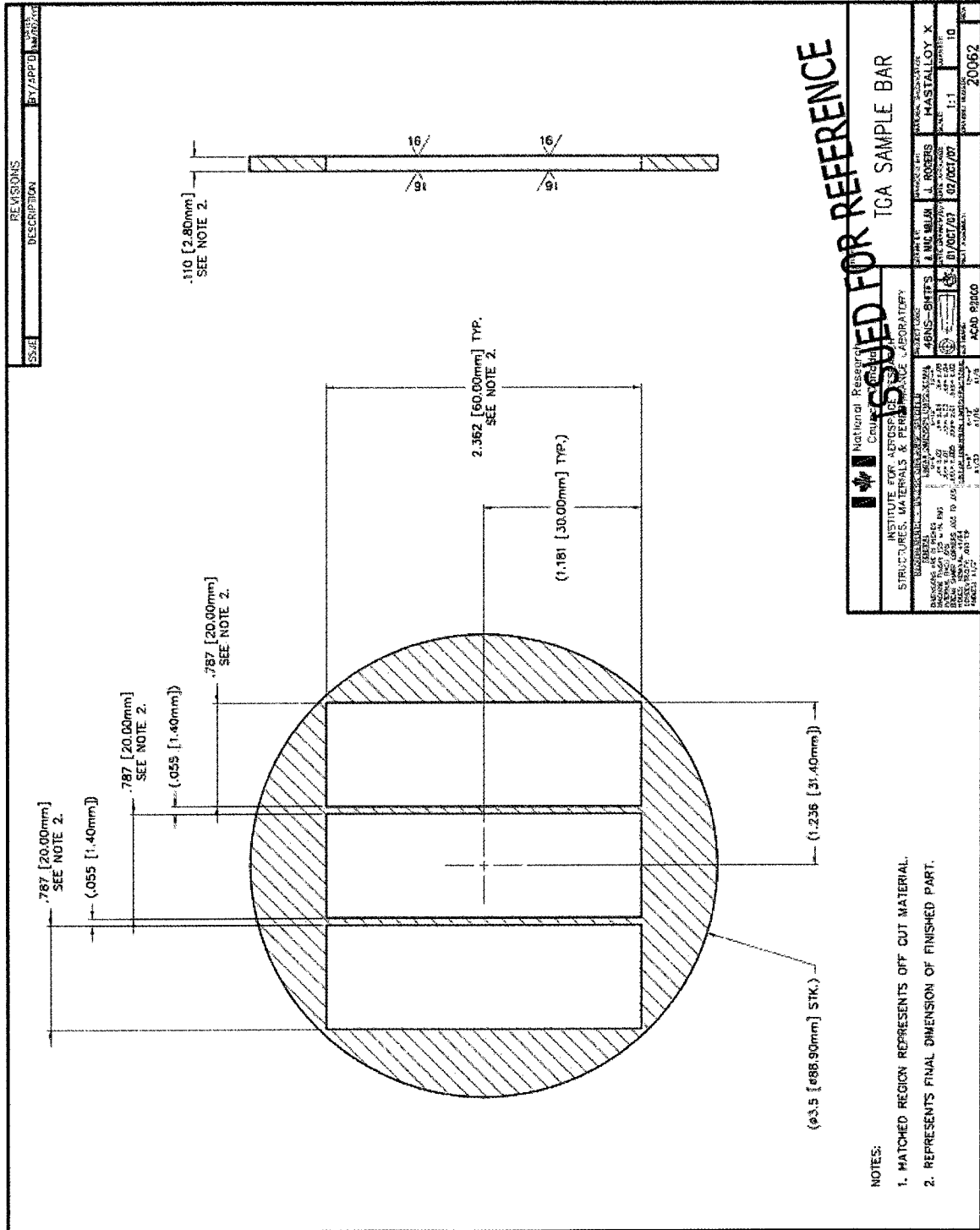
- [55] J. Wrbanek, G. Fralick, and J. Gonzales, "Thin film ceramic strain sensor development for high temperature environments," NASA, Tech. Rep. NASA-TM-2008-215256, 2008.
- [56] R. Holanda, "Development of thin film thermocouples on ceramic material for advanced propulsion system applications," NASA, Tech. Rep. NASA-TM-1993-106017, 1993.
- [57] W. Brown and S. Setlak, Eds., *Aerospace Structural Metals Handbook*, 38th ed. West Lafayette, IN, USA: CINDAS/USAF CRDA Handbooks Operation, 2004.
- [58] R. Viswanathan and S. Scheirer, "Materials technology for advanced land based gas turbines," in *POWERGEN*, December 1998.
- [59] H. International. Hastelloy X alloy (H-3009A). [Online]. Available: <http://www.haynesintl.com/pdf/h3009.pdf>.
- [60] P. Tortorelli and K. Natesan, "Critical factors affecting the high-temperature corrosion performance of iron aluminides," *Materials Science and Engineering*, vol. A258, pp. 115–125, 1998.
- [61] M. Pomeroy, "Coatings for gas turbine materials and long term stability issues," *Materials and Design*, vol. 26, pp. 223–231, 2005.
- [62] D. Naumenko, V. Kochubey, L. Niewolak, A. Dymiati, J. Mayer, L. Singheiser, and W. Quadackers, "Modification of alumina scale formation on FeCrAlY alloys by minor additions of group IVa elements," *Journal of Materials Science*, vol. 43, pp. 4550–4560, 2008.
- [63] G. Goward, "Progress in coatings for gas turbine airfoils," *Surface and Coatings Technology*, vol. 108-109, pp. 73–79, 1998.
- [64] C. Burman, T. Ericsson, I. Kvernes, and Y. Lindblom, "Coatings with lenticular oxides preventing interdiffusion," *Surface and Coatings Technology*, vol. 32, pp. 127–140, 1987.
- [65] Lindblohm, "Process for preparing high temperature materials," United States patent (4,687,678), August 1987.
- [66] Sulzer metco thermal spray materials guide. [Online]. Available: http://www.sulzermetco.com/en/PortalData/13/Resources/2_Products_Services/ThermalSpray_Materials_Guide_022006.pdf.

- [67] D. Mattox, *Handbook of Physical Vapor Deposition (PVD) Processing: Film Formation, Adhesion, Surface Preparation, and Contamination Control*. Westwood, NJ, USA: Noyes Publishing, 1998.
- [68] Ibid., *The foundations of vacuum coating technology*. Westwood, NJ, USA: Noyes Publishing, 2003.
- [69] D. Smith, *Thin-film Deposition: Principles and Practise*. New York, NY, USA: McGraw-Hill Inc., 1995.
- [70] K. Cooke, J. Hampshire, and D. Teer. Variations on the closed field unbalanced magnetron sputter ion plating configuration. [Online]. Available: <http://www.teercoatings.co.uk/documents/Kevin3.pdf>.
- [71] Sulzer metco - home. [Online]. Available: <http://www.sulzermetco.com>.
- [72] D. Seo, K. Ogawa, M. Tanno, T. Shoji, and S. Murata, "Influence of heat exposure time on isothermal degradation of plasma sprayed CoNiCrAlY coatings," *Surface and Coatings Technology*, vol. 201, pp. 7952–7960, 2007.
- [73] D. Newbury, "'standardless' qualitative electron beam x-ray microanalysis: The situation remains caveat emptor!" *Microscopic Microanalysis*, vol. 8, no. 1464CD-1465CD, 2002.
- [74] L. Zhao, "The particulars of EDS analysis 1," personal communication, July 2009.
- [75] D. Chow, "The particulars of EDS analysis 2," personal communication, July 2009.
- [76] W. Werner. Tutorial on quantitative surface analysis by means of electron spectroscopy. [Online]. Available: http://eaps4.iap.tuwien.ac.at/~werner/qes-tut_interact.html.
- [77] J.-C. Zhao, M. Larsen, and V. Ravikumar, "Phase precipitation and time-temperature-transformation diagram of Hastelloy-X," *Materials Science and Engineering*, vol. A293, pp. 112–119, 2000.
- [78] H. Tawancy, "Long-term ageing characteristics of Hastelloy alloy X," *Journal of Materials Science*, vol. 18, pp. 2976–2986, 1983.
- [79] O. Knotek, E. Lugscheider, F. Loeffler, W. Beele, and C. Barimani, "Arc evaporation of multicomponent MCrAlY cathodes," *Surface and Coatings Technology*, vol. 74-75, pp. 118–122, 1995.

- [80] J. Vetter, O. Knotek, J. Brandt, and W. Beele, "MCrAlY coatings deposited by cathodic vacuum arc evaporation," *Surface and Coatings Technology*, vol. 68-69, pp. 27-31, 1994.
- [81] S. Leontiev, V. Kuznetsov, A. Rybnikov, and I. Burov, "Structure and properties of protective coatings produced by vacuum arc deposition," *Surface and Coatings Technology*, vol. 76-77, pp. 41-46, 1995.

Appendix A

Hastelloy-X Substrate Coupon Drawing



Appendix B

XRD References

List of phases and their crystal structures

Phase	Crystal Structure	Cell Dimensions (Å)	Z	PDF File Number
CrO	cubic, F	8.36	-	06-0532
Cr ₂ O ₃	rhombohedral, R-3c	4.96 x 4.96 x 13.59	6	38-1479
Fe (α)	cubic, Im3m(229)	2.8664	2	06-0696
Ni (γ)	cubic, Fm3m(225)	3.5238	4	04-0850
Fe-Cr	cubic, Im3m(229)	2.8760	1	34-0396
Al ₂ O ₃ (α)	rhombohedral, R-3c(167)	4.7592 x 12.992	6	42-1484
NiCrO ₄	orthorhombic, Amam	6.15 x 8.24 x 5.48	4	21-0596
FeCr ₂ O ₄	cubic, Fd3m	8.38	8	34-0140
Ni ₃ Al (γ')	cubic, Pm3m(221)	3.572	1	09-0097
NiO	rhombohedral, R-3m	2.95 x 2.95 x 7.24	3	22-1189
Co (γ)	hexagonal, P63/mmc(194)	2.505 x 4.060	2	05-0727
CoAl (β)	cubic, Pm3m(221)	2.862	1	29-0021
AlCr ₂	tetragonal, P4/mmm(123)	3.001 x 8.637	2	29-0016
CoCr ₂ O ₄	cubic, Fd3m	8.33	8	22-1084